# SEISMIC BEHAVIOR OF BEAM COLUMN JOINTS STRENGTHENED WITH ULTRA HIGH PERFORMANCE CONCRETE

BY

**MUHAMMAD IRFAN KHAN**

A Thesis Presented to the
DEANSHIP OF GRADUATE STUDIES

**KING FAHD UNIVERSITY OF PETROLEUM & MINERALS**

DHAHRAN, SAUDI ARABIA

In Partial Fulfillment of the
Requirements for the Degree of

**MASTER OF SCIENCE**

In

**CIVIL ENGINEERING**

**MAY 2017**

KING FAHD UNIVERSITY OF PETROLEUM & MINERALS
DHAHRAN- 31261, SAUDI ARABIA
**DEANSHIP OF GRADUATE STUDIES**

This thesis, written by **MUHAMMAD IRFAN KHAN** under the direction of his thesis advisor and approved by his thesis committee, has been presented and accepted by the Dean of Graduate Studies, in partial fulfillment of the requirements for the degree of

**MASTER OF SCIENCE IN CIVIL ENGINEERING**

Dr. Salah U. Al-Dulaijan
Department Chairman

Dr. Mohammed Al-Osta
(Advisor)

Dr. Salam A. Zummo
Dean of Graduate Studies

Dr. Shamsad Ahmad
(Member)

8/6/17
Date

Kalimur Rahman
Dr. Muhammad K. Rahman
(Member)

*Dedicated to My Beloved Parents,*
*Brother and Sister*
*For their Love, Prayers, Support and*
*Encouragement*

# ACKNOWLEDGMENTS

First of all praise and adoration is due to Allah Almighty who is the most merciful and compassionate for bestowing me this opportunity and granting me the capabilities, knowledge, intellectual abilities and health to proceed successfully. May the peace, grace, blessings and supplications be upon the Last Messenger, Muhammad ﷺ who is the greatest benefactor of humanity, his family, and companions.

My sincere appreciation and gratitude to esteemed University, King Fahd University of Petroleum and Minerals for financial support and providing me a conducive academic and research environment. A great deal of thanks is due to Prainsa-Saudi Arabia Precast Concrete Company for providing the casting facility of normal concrete at their plant. Several companies including Saudi BASF, Saudi Ready-Mix Concrete Company, and Sika Saudi Arabia are also acknowledged for the provision of materials.

At the very outset, my deep gratitude and appreciation to my esteemed advisor, Dr. Mohammed Al-Osta for his warm encouragement, elucidation, thoughtful guidance, insightful decision, professional and technical advice, helpful suggestion and critical comments. My cordial thanks for grooming me as a master student. I am also thankful to Dr. Shamsad Ahmed for his assistance, intuition, perseverance, helpful suggestion and comments. Thanks are extended to Dr. Muhammad Kalimur Rehman for his constant support, valuable time, devotion, instructive comments and constructive criticism.

I am thankful to all Civil Engineering Department faculty and staff members for their kind support and assistance. I will also extend my gratitude to lab engineers including

Engr. Omer, Engr. Imran Ali and Engr. Najamuddin for their cordial support and cooperation during the experimental phase of this research.

I highly appreciate the contributions of senior colleagues and friends including Mr. Umar Khan, Mr. Saheed Kolawole Adekunl, Mr. Adil Ihsan, Mr. Sifatullah, Mr. Ashraf and Mr. Ahmed Jamil.

Finally, I would like to gratitude my parents, brother, and sister for allowing me to recognize my potential and support me throughout my stay at KFUPM for graduate studies. This degree would have not possible without their prayers, well wishes and encouragement.

# TABLE OF CONTENTS

# LIST OF TABLES

# LIST OF FIGURES

# LIST OF ABBREVIATIONS

| | | |
|---|---|---|
| **FRP** | : | Fiber Reinforced Polymer |
| **GFRP** | : | Glass Fiber Reinforced Polymer |
| **CFRP** | : | Carbon Fiber Reinforced Polymer |
| **BCJ** | : | Beam Column Joint |
| **UHPC** | : | Ultra-High Performance Concrete |
| **HCP** | : | Hybrid Composite Plate |
| **UHPFRC** | : | Ultra-High Performance Fiber Reinforced Concrete |
| **MARS** | : | Mending Application of Reinforced Sheet |
| **AFR** | : | Aramid Fiber Retrofitting |
| **MSCC** | : | Mutli-Scale Cement Composite |
| **CRC** | : | Compact Reinforced Composite |
| **RPC** | : | Reactive Powder Concrete |
| **NSM** | : | Near Surface Mounting |
| **NCSS** | : | Normal Concrete Substrate Surface |
| **CDP** | : | Concrete Damage Plasticity |

# ABSTRACT

**Full Name : MUHAMMAD IRFAN KHAN**

**Thesis Title : SEISMIC BEHAVIOR OF BEAM COLUMN JOINTS STRENGTHENED WITH ULTRA HIGH PERFORMANCE CONCRETE**

**Major Field : CIVIL ENGINEERING**

**Date of Degree : MAY 2017**

The destruction caused by past earthquakes fiercely indicated that beam-column joints (BCJs) are the most vulnerable and critical zone of RC moment resisting frames. In the past few decades, different strengthening techniques had been developed for strengthening the shear deficient BCJs. In the present research work, the effectiveness of UHPFRC jacket as a seismic strengthening solution for the damaged and undamaged exterior reinforced concrete (RC) BCJs having deficiencies in resisting the seismic action was experimentally studied and verified by generating the non-linear finite element models. The entire test matrix comprised of seven 1/3 scale exterior BCJ sub-assemblies with no stirrups in their joint region. The experimental work had been divided into two parts a) post-damage repairing b) pre-damage strengthening. The former set consisted of three damaged exterior BCJs with different column axial load (CAL). These specimens were repaired with a 30mm layer of UHPFRC and retested under monotonic loading. The efficiency of UHPFRC jacket was analyzed by evaluating the load-displacement response, max load carrying capacity, energy dissipation capacity, stiffness characteristics and comparison had been done with the corresponding values of the specimen in the virgin state. The second set comprised of four undamaged exterior BCJs. One of which was subjected to seismic excitation without strengthening in its as-built condition and considered as the control specimen. Two different methods used for strengthening consisted of: i) sandblasting the normal concrete substrate surface of BCJs and in-situ casting of a 30 mm thick UHPFRC jacket and ii) bonding 30 mm thick prefabricated UHPFRC plates to seismically deficient BCJ using epoxy resins and special fillers. The performance of UHPFRC jacketing in upgrading the BCJs was experimentally evaluated under reverse cyclic loading using displacement control approach keeping column axial load (CAL) constant at 150 kN. The results of upgraded BCJs included load carrying capacity, strength degradation, stiffness degradation, energy absorption and displacement ductility had been compared with the corresponding values of the control specimen. The analysis of test results showed that the first method of strengthening was highly effective in terms of shear capacity, deformation capacity, stiffness characteristics and energy dissipation capacity, as compared to the second method. Non-linear finite element models were developed using ABAQUS, which generated the results matching well with the respective experimental results.

## ملخص الرسالة

**الاسم الكامل:** محمد عرفان خان

**عنوان الرسالة:** السلوك الزلزالي للنقاط اتصال الجسور مع الاعمدة والمقواة باستخدام الخرسانة عالية الأداء والمقواة بالألياف الحديدية

**التخصص:** هندسة مدنية

**تاريخ الدرجة العلمية:** مايو 2017م

يشير الانهيارالناجم عن الزلازل السابقة إلى أن نقاط اتصال الجسور مع الاعمدة (BCJs) هي أكثر المناطق ضعفا وحرجا في الإطارات المقاومة للعزوم. ففي العقود القليلة الماضية، تم تطوير تقنيات تقوية مختلفة من أجل تعزيز الضعف في مقاومة القص لنقاط اتصال الجسور مع الاعمدة. في هذا البحث الحالي، تمت دراسة فعالية الخرسانة عالية الأداء والمقواة بالألياف الحديدية كسترة للتعزيز الزلزالي لنقاط اتصال الجسور مع الاعمدة التالفة وغير التالفة معمليا وحسابيا باستخدام النمذجة الغير خطية. حيث تم الاختبار على سبع عينات ذات مقاس 3/1 لنقاط اتصال الجسور مع الاعمدة الخارجية وبدون حديد تسليح في منطقة الاتصال. وقد تم تقسيم العمل التجريبي إلى قسمين أ) اصلاح عينات تالفة ب) اصلاح عينات غيرتالفة. تتألف المجموعة الاولى من ثلاثة عينات تالفة ومعرض العمود فيها الى حمل المحوري متغير (CAL). تم إصلاح هذه العينات بطبقة ذات سماكة 30مم من الخرسانة عالية الأداء والمقواة بالألياف الحديدية وإعادة اختبارها تحت تحميل متغير. تم تحليل فعالية استخدام الخرسانة عالية الأداء والمقواة بالألياف الحديدية كسترة من خلال تقييم علاقة استجابة الحمل مع الازاحة ، الحمولة القصوى ، وقدرة تبديد الطاقة، وخصائص الصلابة ومقارنتها بالعينة في حالتها الاولى. اما المجموعة الثانية فتتألف من أربعة عينات غير تالفة لنقاط اتصال الجسور مع الاعمدة. وكان تم تعريض أحد هذه العينات للاحمال الزلزالية بدون استخدام تعزيز اوتقوية واعتبارها كعينة تحكم.

في هذه المجموعة، تم استخدام اثنين من التقنيات (الطرق) المختلفة لتطبيق السترة الخرسانية العالية الأداء والمقواة بالألياف الحديدية. أ) الطريقة الاولى وذلك باستخدام الرمل تحت ضغط قوي لاعداد سطح العينة ومن ثم صب الخرسانة عالية الأداء. ب) الطريقة الثانية وذلك بربط ألواح ذات سماكة 30 مم من الخرسانة عالية الأداء والمسبق صبها عن طريق استخدام الايبوكسي لتثبيتها على العينة. وقد تم تقييم فعالية الخرسانة عالية الأداء في رفع كفاءة العينات عند تعريضها للتحميل الدوري العكسي. وكانت الاختبارات تتم تحت مايسمى بتحكم الازاحة وقد كان الحمل المحوري المطبق على العمود (CAL) ثابت طوال الاختبار عند قيمة 150 كيلو نيوتن. وقد تم مقارنة النتائج للعينات المقواة

بالخرسانة عالية الأداء مع عينة التحكم و ذلك من خلال القدرة على التحمل، وتدهور القوة، وتدهور الصلابة، وامتصاص الطاقة، وقابلية الازاحة. حيث أظهرت تحليل نتائج الاختبارات أن الطريقة الأولى للتقوية كانت فعالة جدا في مقاومة القص، وقدرة التشوه، وتأخير تدهور صلابة والقدرة على امتصاص الطاقة وذلك بالمقارنة مع الطريقة الثانية. تم تطوير نموذج باستخدام العناصر الغير الخطية والمحدودة باستخدام ABAQUS ، وقد كانت النتائج للنموذج مطابقة بشكل جيد مع النتائج التى تم الحصول عليها معمليا.

# CHAPTER 1

# INTRODUCTION

## 1.1 Prologue

The reinforced concrete (RC) exterior beam-column joints (BCJs) with a deficiency in resisting shear have been identified as the vulnerable and critical zone of RC frame structures when they are subjected to the large cyclic lateral loads (i.e., seismic loading). During the large seismic activity, the BCJ region is subjected to very high shear stresses as compared to the adjoining structural members. These joint shear stresses and the axial stresses in a column lead to the development of principal tensile and compressive stresses in the joint core, which results in the formation of diagonal cracking and crushing of concrete in the joint region. In this way, joints behave like the stress concentration points in RC frames. Therefore, BCJs should be designed for shear stresses to maintain the overall integrity and stability of the structures. Worldwide it is found that the majority of RC frame buildings were designed before the advent of seismic codes in early 1970's, and therefore, such structures with design deficiencies respond inadequately to lateral loads under the action of seismic forces. The first seismic design code was developed by ACI 352 committee in 1976[1].

Buildings constructed in between 1940 and 1970, have major defects in the BCJ region. The major defects that will cause the BCJ failure are: 1) Insufficient or no reinforcement in the joint panels, which is the potential plastic region, will lead to joint shear failure and this type of failure is the brittle in nature, result in the failure of the structure globally, as shown in Figure 1-1(a); 2) Large spacing between column ties that provide the little confinement to the concrete; 3) discontinues beam bottom reinforcement with short embedment length and the use of smooth bars in transverse and longitudinal reinforcement result into the bond and anchorage failure at joint, as shown in Figure 1-1(b); 4) construction joint above and below the beam; 5) lapped splices of column reinforcement just above the floor level[2]. These problems have been identified by the destruction caused by the catastrophic earthquakes in different regions of the world.


(a) (b)

**Figure 1-1 (a) Joint Shear Failure and (b) Anchorage Failure[3]**

In addition to that, the damage was also observed in so called modern construction RC buildings during the post-earthquake field investigation of Vast Earthquake 2011[4]. The majority of buildings were built after the development of seismic design codes.

## 1.2 Motivation

Post-earthquake field investigation of different earthquakes like Ecuador Earthquake (16 April 2016), Kathmandu and Gorkha Earthquake in Nepal (25 April 2015), Van

Earthquake in Turkey (23 October 2011), The Abruzzo Earthquake in Italy (6th April 2009) and Wenchuan earthquake in China (12 May 2008) fiercely indicated that the most of the RC buildings were not able to sustain the ground motion and most of the buildings were constructed after the development of seismic design codes. Post-earthquake reconnaissance team reported that BCJ failure of the RC framed structures was mainly due to lack of transverse reinforcement and inadequate confinement of joint core.

Three story RC frame structure collapsed partially when an earthquake struck Ecuador due to BCJ failure as shown in Figure 1-2. Nepal experienced a powerful earthquake in Gorkha and Kathmandu. Investigation team reported soft story collapse of RC building in Sitapaila, Kathmandu. They observed that no stirrups were provided in the joint region as shown in Figure 1-3. Several BCJ failures which resulted in the collapse of the structure, had been found by Serra Zerrin Korkmaz after Van Earthquake struck Turkey, as shown in Figure 1-4. Approximately, 2000 RC buildings had been affected due to Van Earthquake. BCJ failure in RC frame structures resulted in excessive drift or collapse of buildings. Post-earthquake investigation showed that these buildings were either collapsed or damaged beyond their repair.

**Figure 1-2 Collapse of three story RC frame structure due to BCJ Failure[5]**

Figure 1-3 Soft story collapse of building in Nepal [6]

a) b)

c) d)

**Figure 1-4 Several BCJ Failure during Van Earthquake Turkey[4]**

Many research works have been devoted to identifying the critical facts of non-seismically designed buildings and the methods of strengthening of such buildings. The strengthening of non-seismically designed joints in the seismic area is the challenging field. ACI 352-02 recommends that the shear deficient joints should be upgraded and strengthened by enhancing the effective confinement or by increasing the shear strength [7].

## 1.3 Seismicity of Kingdom

The Arabian plate hosts many countries like Saudi Arabia, Bahrain, The United Arab Emirates, Yemen, Oman, Jordan, Syria, and Kuwait. About 25 million years ago, the rocks that constitute the Arabian Peninsula, began to isolate from African Continent resulted in the formation of Arabian Plate [8] and since then the Arabian Plate has been moving toward the Eurasian Plate. The major part of Arabian plate consists of the Arabian Peninsula.

Seismicity in this region is controlled by the contact of the Arabian Plate with the Eurasian Plate along Bitlis Suture and Zagros Thrust, rifting and seafloor extending in the Red Sea and the Gulf of Aden and strike-slip faults along the Dead Sea Transform Fault and the Gulf of Aqaba, as shown in Figure 1-5.

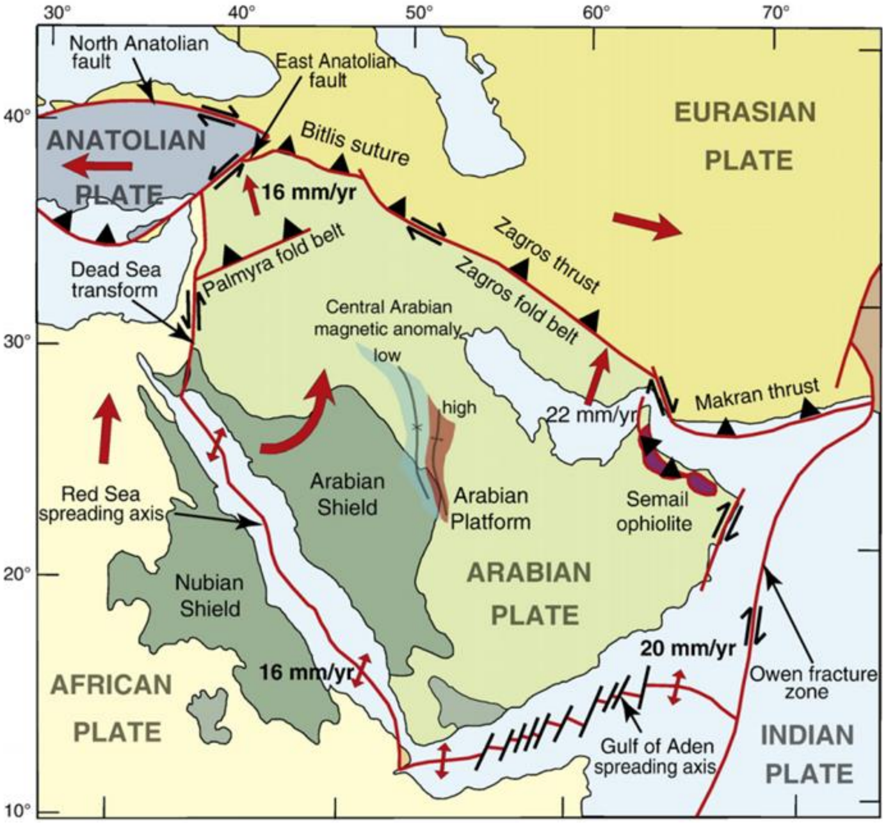

**Figure 1-5 Simplified map of Arabian Plate, with plate boundaries**[8]

According to Saudi Geological Survey (SGS), the most active seismic area is along the Gulf of Aqaba. The main threat to Kingdom regarding seismic activity is from the Gulf of Aqaba, as the various number of earthquakes struck to the Gulf of Aqaba in 1983, 1990, 1993, 1995 and 2004.

Along the Zagros Fold Belt, severe earthquakes of magnitude greater than five are very common due to the collision between the Arabian Plate and Eurasian Plate. The seismic wave lasts for 3 to 10 seconds, which is a potential threat to engineering structures. Due to strategic development projects and new urban society in the southwestern Arabian Shield and Southern Red Sea Region, this area has got attention regarding seismic hazards. Most of the earthquakes occurred along the axial trough of the Red Sea and four severe earthquakes occurred away from it [9].

An earthquake of magnitude 5.4, recorded by Saudi Geological Survey (SGS), struck the town of Al-Eis. The town is about 40 km from the city of Madinah. This earthquake caused structural damage and destroyed the infrastructure[10].

The responsibility of maintaining and monitoring the seismic activity in Saudi Arabia and surrounding area was assigned to SGS and Saudi Cabinet made this decision as per the council of ministers decision number 228. SGS has centers affiliated with King Abdul Aziz City for Science and Technology, King Abdul Aziz University, King Saud University and King Fahd University of Petroleum and Minerals.

Recent earthquake events in moderate seismic areas of Saudi Arabia have led to concern the safety of the RC frame structures having deficiencies in resisting the seismic action and designed only for gravity loads. Such buildings should be strengthened.

## 1.4 Need for Research

Several techniques have been reported in the literature for the strengthening of RC elements. Some of the conventional methods of strengthening and retrofitting of non-seismically detailed joints reported between 1975 and 2003 are epoxy repair, removal, and replacement, reinforced concrete jacketing, the addition of fiber reinforced polymer composites and external steel elements[11]. Recently, several novel techniques for the strengthening or repairing of BCJs have been reported including the repairing of non-seismically detailed BCJs using concrete cover together with CFRP jackets, mending application of reinforced sheet (MARS System), aramid fiber retrofitting system (AFR system)[12], strain hardening cementitious composites (SHCC) reinforced with CFRP, combination of GFRP sheet and steel cages, ferro-cement jackets, steel cages consist of steel angles and battens, steel prop and prefabricated hybrid composite (HCP) plates.

Some of these techniques are labor-intensive and require a different level of artful detailing, cost, disruption of building occupancy in terms of considerable loss of floor space and limited range of applicability. A major shortcoming of CFRP laminates is its premature brittle failure due to debonding. Mechanical anchorage was provided to fully utilize the strengthening potential of CFRP laminates, by avoiding the premature failure. The perforations in the concrete for anchoring the FRP sheets can damage the test units and anchorage zone becomes the stress concentration zone will lead to premature failure. Moreover, the strength degradation of epoxy adhesive used to apply the FRP laminates under high temperature makes them poor fire resistant and the long-term durability of FRP remains a matter of great concern. However, strengthening with steel elements suffered from various difficulties such as handling of heavy elements, corrosion, shear failure and requirement of the butt joint in limited space.

One of the main recent developments in concrete technology is the inception of ultra-high performance fiber reinforced concrete (UHPFRC). Recently, Martinola et al. [13] developed state of the art technique for the strengthening of RC beams involves the in-situ casting of 40 mm thick high-performance fiber reinforced concrete (HPFRC) jacket. In order to overcome the above-mentioned issues and shortcomings, the non-seismically designed joint will be repaired and strengthened by using the UHPFRC jacket.

## 1.5 Research Objectives

The primary objective of this research is to explore the effectiveness and efficiency of UHPFRC jacket in repairing and strengthening the structural and design deficient exterior BCJs, which is subjected to cyclic excitations. This study involves the experimental evaluation of hysteresis response, maximum strength, stiffness degradation, energy dissipation and displacement ductility of upgraded BCJs. The particular objectives are:

1. To evaluate the seismic response of seismically deficient damaged BCJs repaired with UHPFRC jacket.
2. To evaluate the seismic response of seismically deficient undamaged BCJs strengthened by using UHPFRC jacket.
3. To assess the efficiency of state of the art strengthening techniques in terms of their load-displacement response, strength degradation, deformation capacity, stiffness characteristics, energy dissipation capacity and displacement ductility and compare with the corresponding values of reference unit.
4. To develop a reliable and practically applicable rehabilitation technique for the upgradation of non-seismically designed BCJs.
5. Development and validation of FE model of BCJ sub-assemblies strengthened with UHPFRC using experimental results.

# CHAPTER 2

# LITERATURE REVIEW

## 2.1 Introduction

Because of destruction caused by earthquakes in the past few decades, RC frame structures, sub-assemblages and their response when subjected to reverse cyclic deformations have been the concern of various research projects. Post-earthquake investigations showed that BCJs in RC frame structures are fragile components when subjected to serious seismic shocks. The overall ductility of the structure is governed by the response of BCJs under cyclic loading. The brittle shear failure of BCJ results into the global failure of the structure even though all other structural members are conforming to the design requirements. As described earlier, the damage has also been observed in RC buildings constructed after the development of seismic codes. All structures that were designed according to GDL before or after the development of seismic-oriented design codes should be upgraded or strengthened as recommended by international codes.

This chapter aims at

1. Illustrating the different strengthening methods of strengthening the seismically deficit BCJs.
2. Development of UHPFRC and Material properties of UHPFRC.
3. Application of UHPFRC in strengthening different structural elements.

## 2.2 Recent studies on strengthening techniques of BCJs

Different methods of strengthening are reviewed with emphasis on their effectiveness, performance regarding load-displacement response, stiffness degradation, energy dissipation and displacement ductility which are the prime building blocks of advanced seismic design codes.

Saleh et al. ( 2010) [14] studied the seismic response of FRP-Upgraded exterior BCJs. The total experimental matrix consisted of 4 seismically deficit BCJs sub-assemblages. Of these, two specimens were strengthened with CFRP using two different schemes. In the first scheme, CFRP was wrapped with epoxy on joint, beam and column portions as shown in Figure 2-1, while in the second scheme, CFRP sheet was epoxy bonded on the joint region only and the author introduced the mechanical anchorages in order to provide the prevention against any possible de-bonding of CFRP from substrate (labeled as ES1 and ES2) as shown in Figure 2-2. The remaining two specimens were the control one (labeled as EC1 and EC2). Once damaged, repaired them under the above-mentioned schemes after filling the cracks with epoxy (labeled as ER1 and ER2). All specimens have same geometry and reinforcement detailing. All specimen were subjected to reverse cyclic loading. It was reported that the peak load for EC1 and EC2 was 47.08 kN and 45.8 kN respectively. These values become 62.34 kN and 58.11 kN for ES1 and ES2 specimens and the peak load reached to 81.79 kN and 58.63 kN for ER1 and ER2 specimens. Results showed the enhancement in the peak load values after strengthening and repairing of specimens. Stiffness degradation data showed that for scheme #1, the initial stiffness of retrofitted specimen was higher than the reference specimens, while in Scheme #2, these values were lower than their respected control specimens because, in Scheme #1 beam, column and joint were wrapped with CFRP. However, in Scheme #2 only joint portion is upgraded with CFRP. The displacement ductility of ES1, ES2, ER1 and ER2 was increased up to 34%, 11.4%, 39% and 61 % respectively than their respected control specimen.

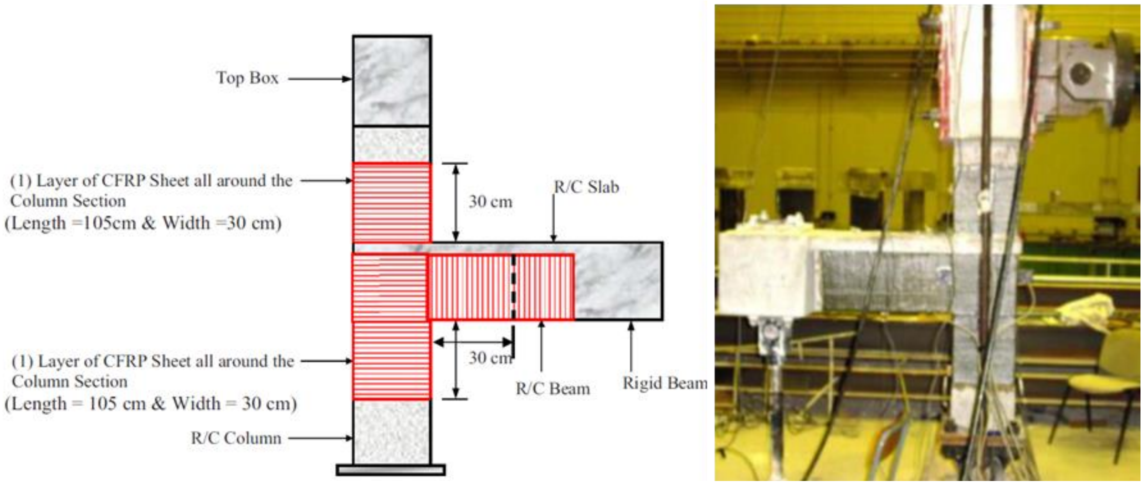

**Figure 2-1 Schematic representation of Scheme # 1 [14]**

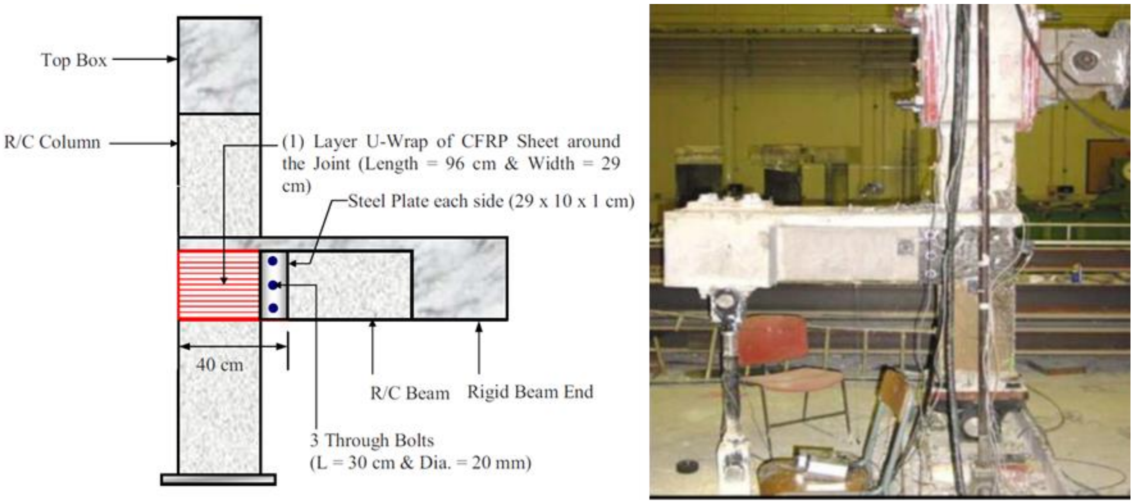

**Figure 2-2 Schematic representation of Scheme # 2 [14]**

Kazem et al. (2011)[15] experimentally investigated the performance of damaged RC exterior BCJ specimens repaired with steel elements including steel prop and curb. In this research work, different RC frames had been inspected and found out that their beam depths were less than the required depths based on the guidelines provided by design codes which resulted into the increasing drift under lateral loads and increasing vertical deflection against gravity loads. The author investigated that this method of retrofitting was suitable for such deficit frames. For this purpose, two half-scale exterior BCJs labeled as SC1 and SC2 used as reference specimens. Specimen SC2 had standard beam height. However, specimen SC1 had reduced beam height. These specimens were tested under reversed cyclic loading. Once damaged, repaired with the same type of concrete and then retrofitted with steel elements. These repaired specimens are designated as RSC1 and RSC2. Retrofitted schemes of these specimens are shown in Figure 2-3. The results showed that the average increase in the ultimate strength of specimen RSC1 relative to its control specimen was 86% and for specimen RSC2 this value reached to 156%. The ultimate rigidity of control specimens SC1 and SC2 were 0.17 and 0.19. By the up gradation of these specimens, the rigidity of these specimens increased up to 88% and 252% for the specimens RSC1 and RSC2 respectively. The author found that energy absorption of repaired specimens was more relative to control specimen because of no degradation during reversed cyclic loading, higher bearing capacity, and reduction in the pinching of hysteresis loops. With the reduction in the beam’s height at the joint, energy dissipation was reduced up to 26% and 44% for the control and retrofitted specimens.

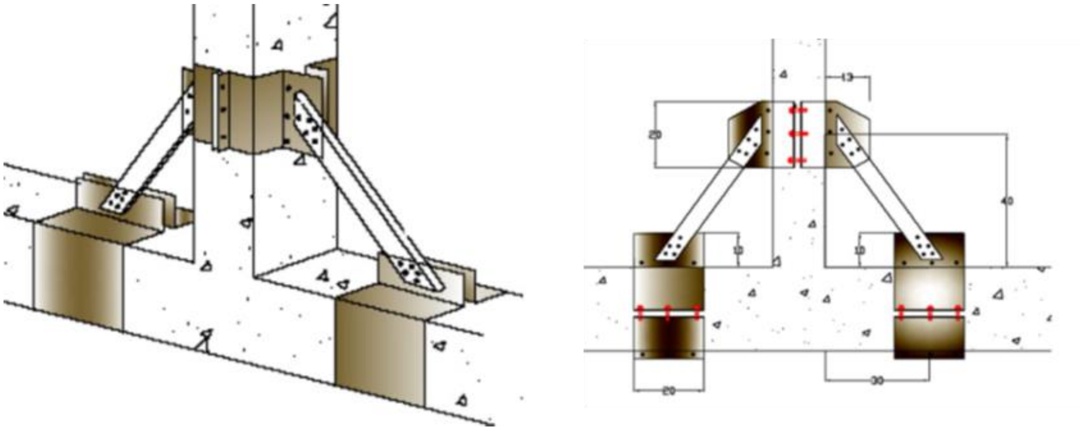

a) Three dimension view b) Two-dimensional view

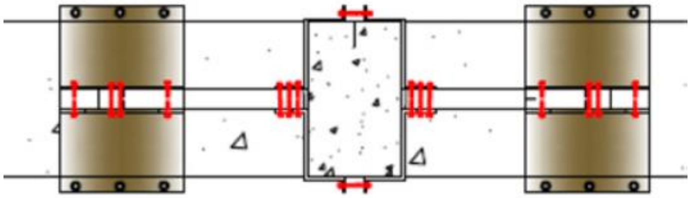

c) Plan view

**Figure 2-3 Pictorial view of retrofitted specimens RSC1 and RSC2 [15]**

Li et. al (2012) [16] proposed a method of strengthening the interior BCJs using Ferro-cement jackets with embedded diagonal reinforcement. Ferro-cement consists of mortar and wire mesh was used as the concrete cover. This experimental program includes four 2/3$^{rd}$ scale interior BCJs. One of them is control specimen and other three specimens were strengthened with Ferro-cement. All four specimens were tested under cyclic loading.

Three different kind mortar were used in Ferro-cement jacketing including cementitious mortar, cement-sand mortar, and epoxy-based mortar. The concrete cover in the joint area and plastic hinge zone was replaced with Ferro-cement. Before its application, the surface of concrete was made rough for proper bonding between substrate and mortar. The 30 mm Ferro-cement layer was applied for retrofitting contained properly folded two layers of wire mesh. The ferro-cement jacket was extended 300 mm from the joint region to the beam and column, which was equal to least dimension of the member as shown in Figure 2-4. The retrofitting solution improved the ultimate load carrying capacity. Experimental results showed improvement in ductility. The increase in the displacement ductility was 17%, 28% and 34% for the specimens S1, S2, and S3 respectively. Epoxy based mortar showed the best performance against seismic shocks. With the increase in the strength of Ferro-cement jacket, the energy dissipation capacity increased. At the initial stages, strengthened specimen showed larger stiffness. The author recommended high strength mortar for achieving high load carrying capacity, stiffness, energy dissipation and large displacement ductility.

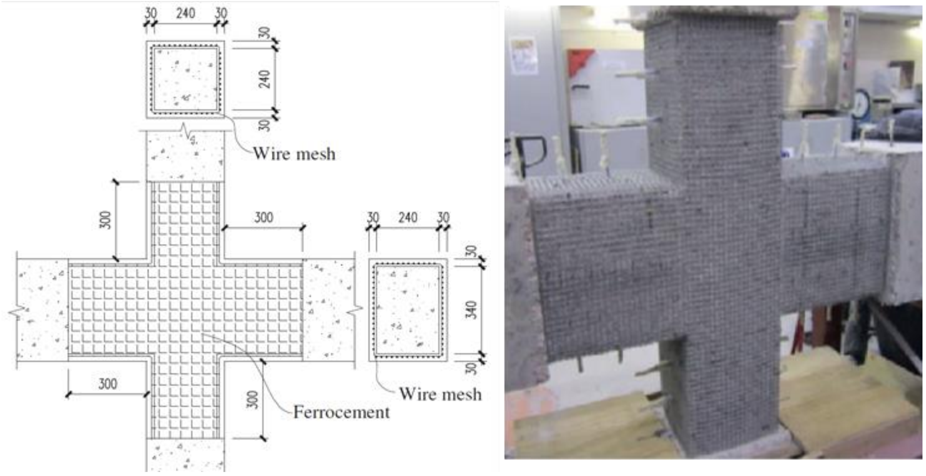

**Figure 2-4 Rehabilitation Scheme [16]**

Hadi et al. (2013) [17] studied the cyclic performance of two exterior T-connection strengthened and repaired with segmental circular concrete covers with CFRP jackets. The first specimen was glued to these segmental concrete cover to convert the square joint area to circular section and then it was strengthened with CFRP wrapping designated as TS. The formwork used to cast concrete covers is shown in Figure 2-5. The second specimen was tested first before strengthening it. A load was applied to cause serious damage and later on specimen was repaired using a segmental concrete cover with CFRP jackets designated as TR as shown in Figure 2-6. Both specimens were tested under cyclic loading. The author reported that segmental concrete cover not only enhanced the performance of CFRP but also helped in resisting the shear loads and worked as one unit with substrate concrete. The possibility of de-bonding of CFRP had been reduced due to modified circular section. Around the joints, the efficiency of CFRP reached a value of 32.4%. The performance of specimen TS is better (20 % in energy dissipation and 10% in maximum shear load) than TR specimen. This was attributed to yielding of beam reinforcement, concrete cracks which were filled with epoxy could not restore the full strength of concrete and the contact between reinforcement and concrete could not restore.

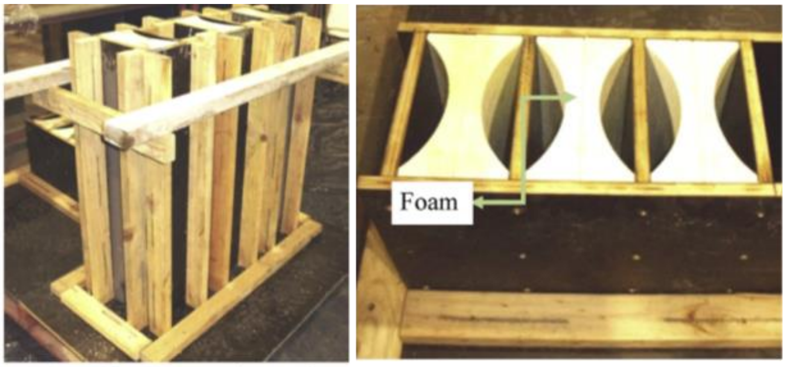

**Figure 2-5 Formwork for segmental concrete cover [17]**

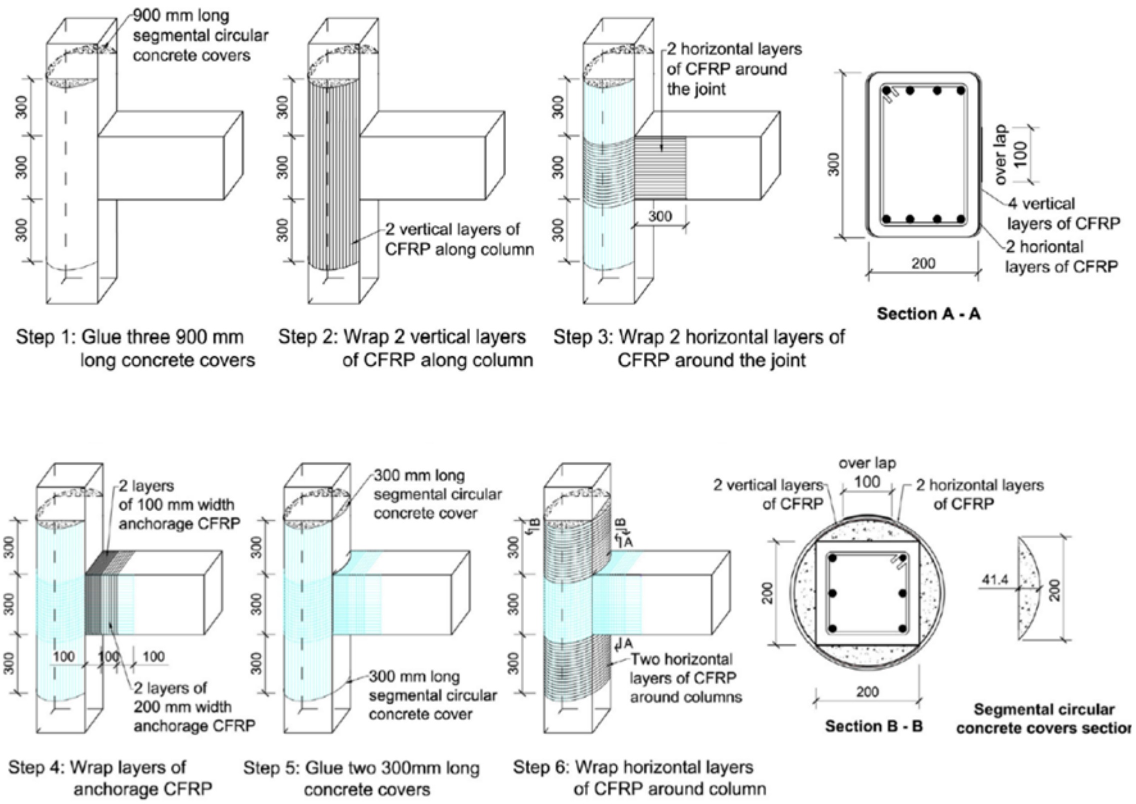

**Figure 2-6 Repairing Process [17]**

Roberto et al. (2013) [18] experimentally evaluated the seismic performance of RC BCJs with inadequate seismic details strengthened with FRP systems. The complete experimental program consisted of 8 full-scale specimens subjected to reversed cyclic loading at beam tip and keeping the CAL equal to 300 kN. Out of these eight specimens, six were strengthened with FRP by using different schemes. Of these, two specimens were controlled one. The complete experimental work consisted of two sets. Each set consisted of one control specimen and three specimens were upgraded with FRP. These control specimens have same geometry but different amount of longitudinal steel reinforcement in beam and column ensuring weak column but stronger than joint ensuring joint failure (Type 1) and strong column connection (Type 2) as shown in Figure 2-7.

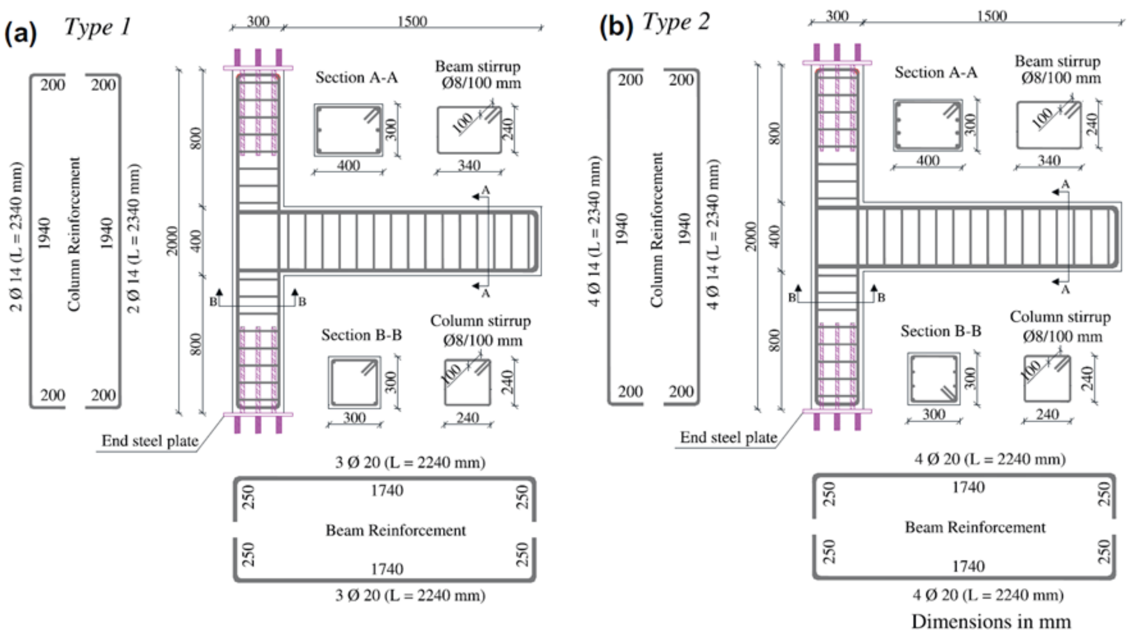

**Figure 2-7 Reinforcement detailing of specimens Type 1 and Type 2[18]**

Each set contained three strengthened specimens with different strengthening schemes as shown in Figure 2-8. The control specimens after damaging were also repaired/retrofitted and tested again under cyclic loading. One of the strengthened specimens once damaged, repaired it again and re-tested. The description of specimens is given in Table 2-1.

**Table 2-1 Description of Specimens**

| Set No. | Control Specimen | Strengthened Specimen | Repaired Specimen |
|---|---|---|---|
| Set 1 | J01 | J02, J03, J04 | J01-R, J02-R |
| Set 2 | J05 | J06, J07, J08 | J05R |

To avoid FRP delamination, FRP scheme was properly designed as for specimen J02. As a result, FRP delamination was delayed and with fully design FRP pattern, failure can be shifted to beam as for the specimen J04. Strength and ductility had been increased 72%

and 98% over the control specimen (Type 1). For Type 2 specimen, the experimental results showed that CFRP wrapping at the joint was sufficient to avoid premature column failure. Two different schemes of CFRP were used for this set. It was reported that X shape confinement and two vertical sheets on the joint exterior face was sufficient for providing efficient results. The experimental results of repaired specimens J01-R, J02-R and J05R showed the restoration of strength and prominent increase in the ductility of original members.

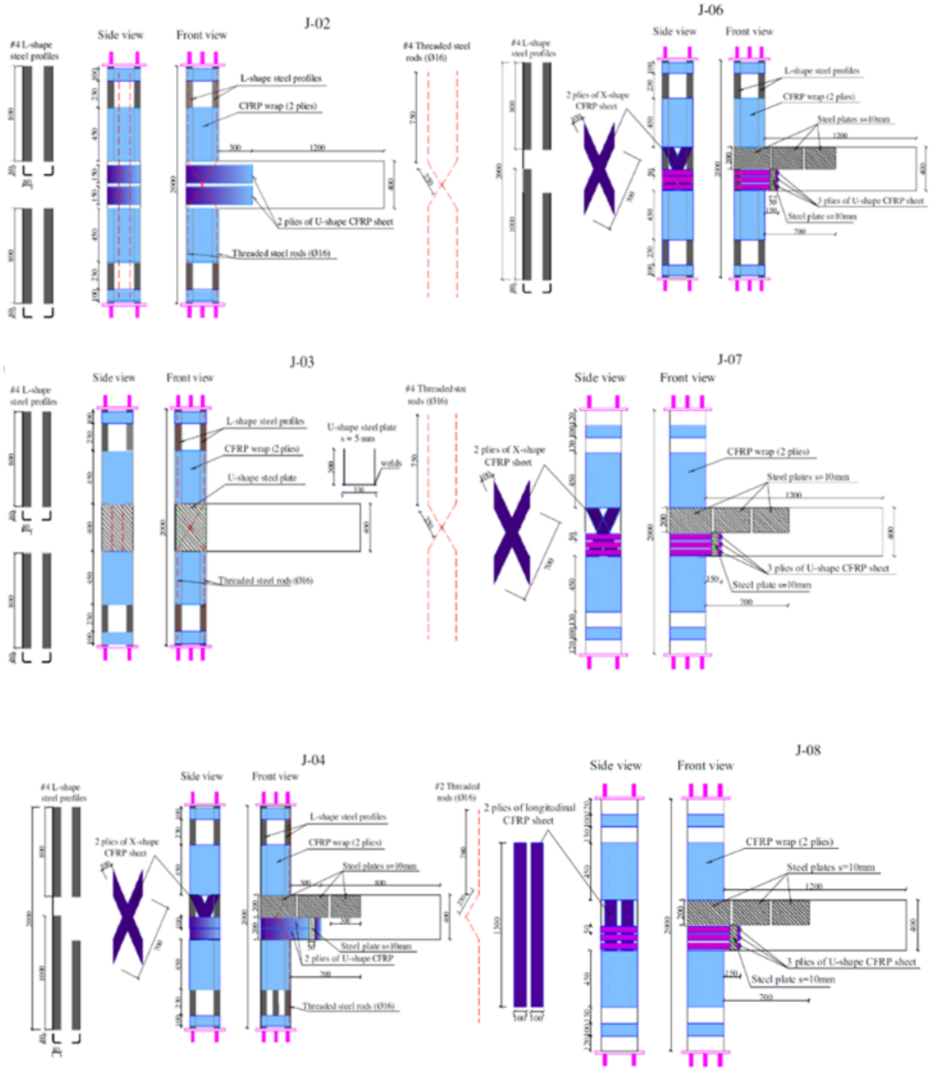

**Figure 2-8 Retrofitting schemes proposed by Roberto et al. [18]**

Esmaeel et al. (2014) [19] repaired the severely damaged full-scale interior BCJs using strain hardening cementitious composites (SHCC) reinforced with CFRP. The concrete cover in the joint area of the specimen was removed and replaced by SHCC. Self-compacting SHCC layer was reinforced with CFRP laminates. Two different schemes of CFRP laminates were used to retrofit the damaged specimen. In scheme #1, the CFRP laminates were applied on front and back faces of the specimen, designated as JPA3-R. While in Scheme #2 all four sides of joints were strengthened, designated as JPB-R. These retrofitting schemes are shown in Figure 2-9. These specimens were subjected to reverse cyclic loading. The load-displacement response showed that the lateral load carrying capacity has been restored. JPB-R specimen dissipated more energy than JPA3-R and hence more effective. At 4% of drift, JPA3-R could dissipate only 44.4 kN-m cumulative energy which was 5% more than the corresponding value in the virgin state. However, cumulative dissipated energy of JPB-R was 53.4 kN-m showing an increment of 95% in comparison with the specimen in undamaged condition.JPA3-R had higher secant stiffness as compared to specimen JPA3 between the drift of 0.13% and 1.67%. Later on, secant stiffness of JPA3-R and JPA3 was almost similar. For Scheme #2, after 0.13% drift value results showed a slower degradation in secant stiffness than its undamaged specimen. Hence Scheme #2 was more effective.

**Figure 2-9 Pictorial view of retrofitted specimens [19]**

Campione et al. (2014) [20] experimentally evaluated the effectiveness of steel cages in retrofitting the RC frames characterized by weak column and strong beam and transforming them into a strong column and weak. The experimental program consisted of 6 full-scale external RC BCJs. All BCJs had the same geometry and reinforcement details. One of the specimens was tested without strengthening and used as reference specimen (C1). All other five specimens were strengthened using steel cages constituted by battens (transverse reinforcement) and steel angles (longitudinal reinforcement) labeled as C2R, C1RR, C2RR, C3RR and C4RR. The C2R specimen was strengthened at the column and joint region while all other four specimens were reinforced in the beam, column and joint as shown in Figure 2-10.

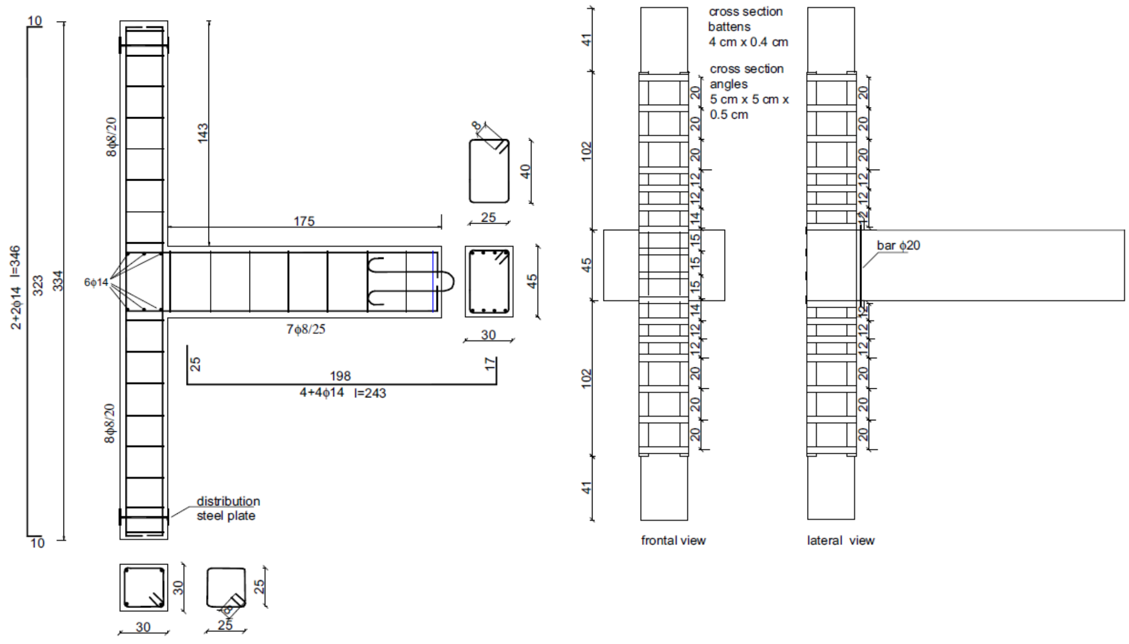

C1 C2R

**Figure 2-10 (Continued)**

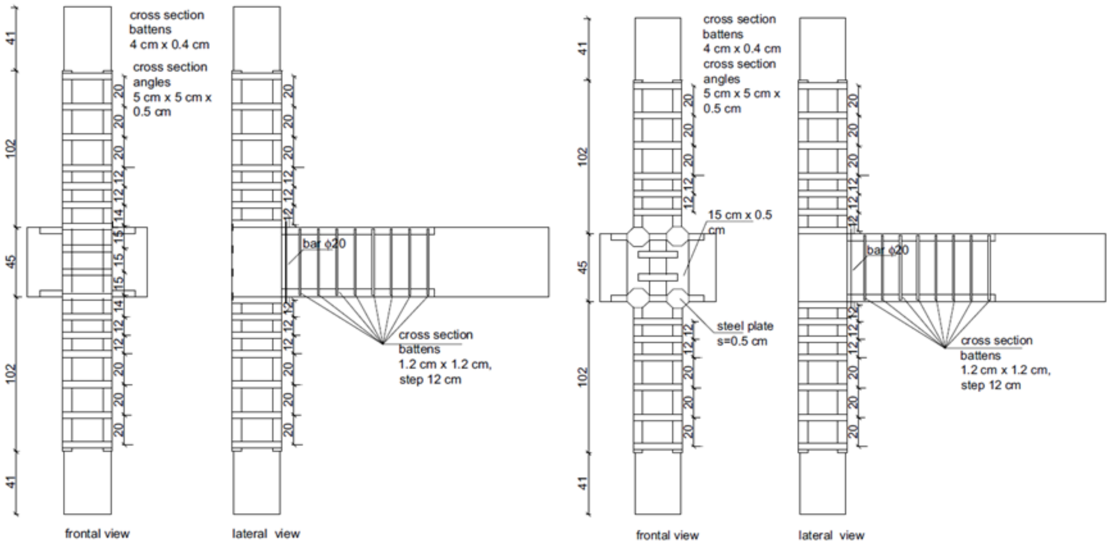

C1RR, C2RR, C3RR C4RR

**Figure 2-10 RC BCJ externally strengthened with steel cages [20]**

Results showed that this strengthening technique was very effective in transferring the undesired weak column strong beam frames characterized by brittle failure into a desirable strong column-weak beam frames. The response of reinforced specimens in terms of stiffness degradation and energy dissipation was promising. The author reported that special care had to be taken for welded section where brittle failure could occur under an elevated number of cycles.

Esmaeel et al. (2014) [21] introduced a new seismic retrofitting solution for the seismically deficit RC BCJs. The author experimentally investigated the effectiveness of pre-cast hybrid composite plates (HCP) in terms of their hysteresis response, energy dissipation, stiffness degradation and displacement ductility. HCP, prefabricated thin plate, was made of strain hardening cementitious composite (SHCC) reinforced with CFRP laminates. The research work comprised of 2 full-scale damaged interior BCJs. HCPs were bonded to damage specimens by means of epoxy resin and chemical anchors to cover these framed elements. Two different schemes had been used in this research work i.e; a) a cross shape HCPs according to near surface mounted method. b) L-shape configuration. The geometry and reinforcement details are shown in Figure 2-11 and specimens were designated as JPA0-R and JPC-R. Cross shape HCPs were attached to front and back faces of both damaged specimens. In repairing of JPC specimen, in addition of cross shape HCPs, L-shape HCPs were also attached to lateral faces of BCJs at each corner as shown in Figure 2-12.

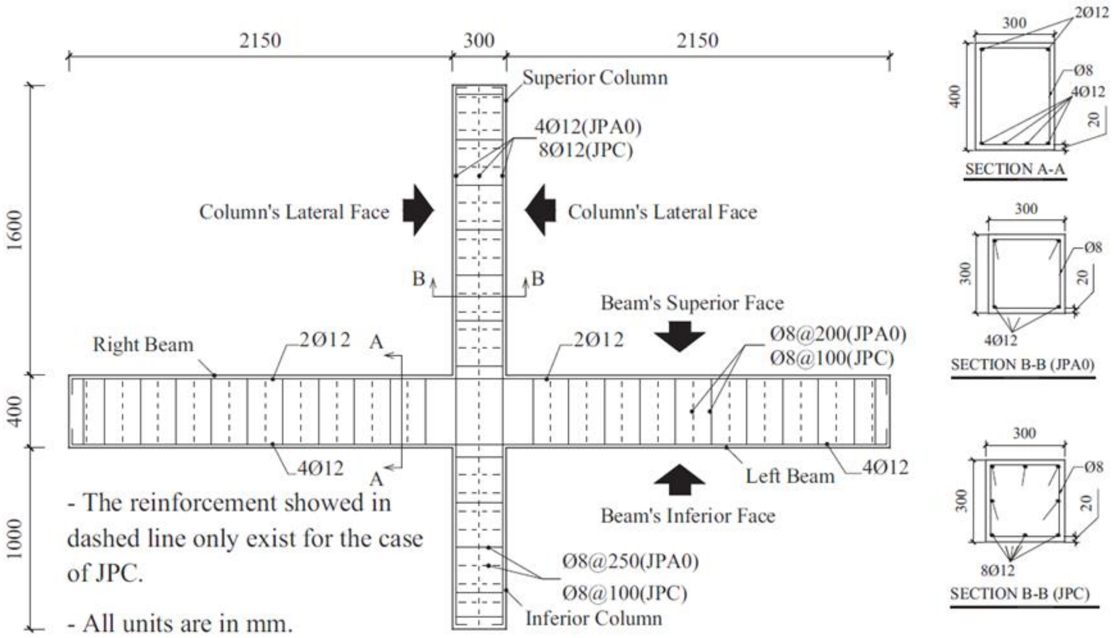

**Figure 2-11 Geometry and reinforcement configuration of interior BCJ [21]**

**Figure 2-12 Retrofitted scheme proposed by Esmaeel [21]**

The hysteresis response of retrofitted specimens showed that maximum strength of JPA0-R had been increased up to 18.2% and 25.5% for positive and negative directions respectively. However, corresponding values for the specimen JPC-R were 48.3% and 54.5% for the negative and positive excursions. The energy dissipated by the specimen JPA0-R 52.3kN-m at 4% drift which was 23% more than the energy dissipated by the specimen in the virgin state. However, JPC-R reached a value of 54.3 kN-m which was 84% more than energy dissipated in JPC. So strengthening scheme adopted for JPC specimen was more effective. Both specimens showed higher secant stiffness than in the virgin state up to 3% drift. The experimental results indicated that displacement ductility of JPA0-R was 22.66% more than the corresponding value of JPA0. This value was 18.2% more for the specimen JPC-R in comparison with JPC.

Esmaeel et al. (2016) [22] evaluated the seismic performance and effectiveness of the novel technique for the strengthening of exterior BCJs using bidirectional GFRP layers and anchorage was done with steel plates. Two 3D full-scale BCJs were constructed without transverse reinforcement in the joint region. One of the specimens was tested in its as-built condition, designated as TS. While the other specimen was subjected to reverse cyclic loading on the vertical and horizontal beams, as it is corner 3D full-scale joint, after that, it was retrofitted with the proposed scheme as shown in Figure 2-13 and designated as TSR.

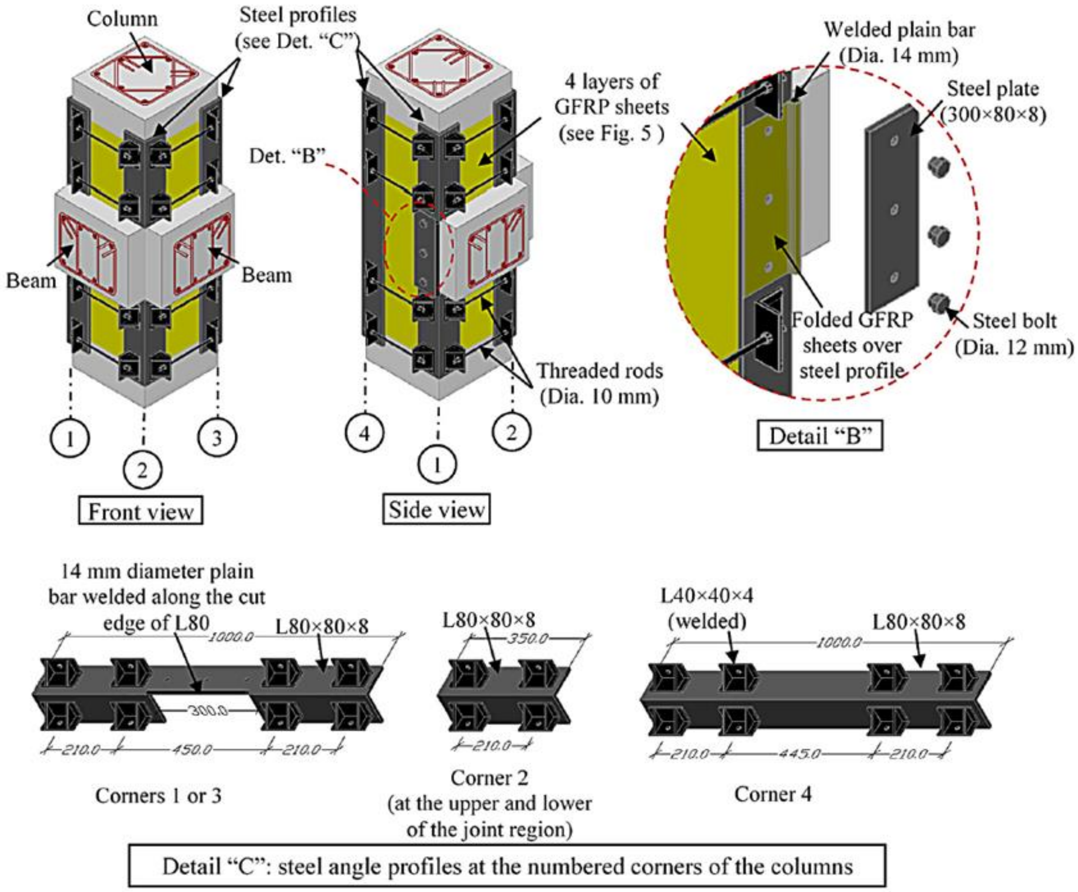

**Figure 2-13 Retrofitted Scheme proposed by Esmaeel (2016) [22]**

Experimental results showed that TS specimen achieved peak story shear of 35.5 kN in a vertical plane at drift angle of 1.6% and in a horizontal plane, this value was 38.6 kN. However, TSR specimen reached a value 47.8 kN and 45.7 kN at a drift angle of 1.6% and 2.4% in vertical and horizontal plane respectively. Experimental results showed that proposed technique achieved 28% higher displacement ductility than TS specimen. The energy dissipated by TSR specimen was 10.7 times more than TS specimen at the ultimate load point.

## 2.3 UHPFRC Material Properties

### 2.3.1 Background:

Different manufacturers in different countries have developed several types of UHPFRC. Of these, three fundamental types are Compact Reinforced Composite (CRC), Multi-Scale Cement Composite (MSCC) and Reactive Powder Concrete (RPC). The main difference between these types are the amount and the type of fibers used. One of the leading types of UHPFRC is RPC and French companies Lafrage, Bougues, and Rhodia launched one such product marked under the name Ductal®. Since RPC is commonly available, reliable and economically feasible type of UHPFRC.

### 2.3.2 Constituents of UHPFRC:

One of the main development in concrete technology is UHPFRC. The key factors behind the excellent mechanical properties and improved durability of UHPFRC are;

1. The formation of capillary pores is minimized due to the very low water-cement ratio of about 0.13-0.25 resulting into denser and stiff structure of hydration product.
2. The reduction in the water demand of fresh mix specifically results in a higher degree of particle packing density of fine grains in the binder matrix and enhancing the compressive strength.
3. The use of steel fibers prevents the growth and inter-connectivity of micro-cracks by absorbing the tensile stresses. The micro-cracks join together form macro-cracks [23].

**Cementitious materials:** As compared to conventional concrete and high-performance concrete (HPC), relatively high fractions of cement are used in UHPFR [24]. The compressive strength of UHPFRC increases with the increase of cement content but up to a certain limit known as optimum content, beyond this limit, the strength tends to reduce due to limited contribution of aggregates [25]. Cement with the calcium aluminates less than 6% is preferred due to its lower water demand. Cement content does not hydrate completely due to lower water-binder ratio, so the part of un-hydrated cement content can be replaced with silica fume, crush quartz or blast furnace slag without compromising the strength. Because of much finer particle size 0.1 to 10 µm, optimal spherical shape, and its pozzolanic reactions fill the gap between the relatively coarser particles and hence improve the workability and compressive strength [26].

**Water-binder ratio:** In order to achieve allowable spread flow and maximum relative density and the optimum water-binder ratio of 0.13-0.25 was suggested in the literature. Willey et. al 2011 achieved compressive strength of 150 MPa with w/b equals to 0.25[26]. In addition to w/b ratio, other strength governing parameters are properties of constituents, mixing procedure, mixer type, curing regime and curing type.

**Superplasticizer:** Water-binder (cement + silica fume) ratio much affect the workability of concrete. The much low workability of UHPFRC mixture, because of very low w/b ratio, can be enhanced by the use of effective superplasticizers (SP). The compatibility between the constituents of the mix and the type of SP effects the required SP dosage[27]. Due to dispersing effect, the gradual addition of SP to the mix is more effective rather than adding SP once. SP dosage of 1.4% to 2.4% was recommended by Wille et al[26].

**Aggregate:** Cracking in the concrete typically initiates in the proximity of the aggregates. Cement-aggregate interfacial zone (ITZ) is the weakest link in the normal concrete. The major portion of the fracture paths in the normal concrete presents along the interface between coarse aggregate particles and cementitious matrix called ITZ. This is may be due to the inherent weakness of ITZ or due to stress concentration induced by rigid aggregates embedded in the cementitious matrix. ITZ have high w/b ratio as compared to surrounding matrix due to internal bleeding around the elongated and flat coarse aggregate particles and hence characterized by the highly porous region affect the durability of concrete. Therefore, above-mentioned weaknesses induced by ITZ can be reduced by eliminating the coarse aggregates from the mixture of UHPFRC[28]. Fine aggregates like quartz sand are used in UHPFRC mixture which plays a key role in reducing the maximum plate thickness (MPT). MPT is an important factor in the mixture design of UHPFRC. Wille et al. reported an optimum sand to cement ratio of 1.4 for a quartz particle size of 0.8 mm[26].

**Fibers:** UHPFRC exhibits the ductility and as the specimen begins to crack, the small scale fibers reinforced the cementitious matrix causing smaller and less damaging cracks to form. Fibers are either metallic, polymeric or natural. Generally, metallic (Steel) fibers are used for structural and non-structural purposes. The steel fibers bridge the crack due to which UHPFRC shows strain hardening behavior under tensile loading. The size, shape, and type of steel fibers affect the workability and energy dissipation capacity during crack bridging. For economical and workable UHPFRC mixture, Richard and Cheyrezy recommended 2% by mixture volume of steel fibers[29].

### 2.3.3 Mechanical properties:

Sufficient data has been published about the properties of UHPFRC and sufficient information is available to establish a range of material properties [30]. The range of UHPFRC material properties is listed in Table 2-2.

**Table 2-2 Range of UHPFRC material properties**

| Property | Range | |
|---|---|---|
| Compressive strength | 20 – 30 ksi | 140 – 200 MPa |
| Tensile strength | 0.9 – 1.5 Ksi | 6 – 10 MPa |
| Modulus of Elasticity | 6000 – 10000 Ksi | 40 – 70 GPa |
| Poisson’s ratio | 0.2 | 0.2 |
| Coefficient of thermal expansion | 5.5 – 8.5 millionths/$^{o}$F | 10 – 15 millionths/$^{o}$C |
| Creep coefficient | 0.2 – 0.8 | 0.2 – 0.8 |
| Specific creep | 0.04 – 0.3 millionths/psi | 6 to 45 millionths/Mpa |
| Total shrinkage | Up to 900 millionths | Up to 900 millionths |

### 2.3.4 Compatibility of NC and UHPFRC:

Miguel Angel Carbonell Munoz studied the bond characteristics of UHPFRCC and NCSS by conducting the different bond tests such as slant shear test with bond interface inclined at 55$^{o}$, 60$^{o}$ and 70$^{o}$, pull off and splitting prism tests. The role of surface preparation treatment, pre-wetting conditions and freeze-thaw cycles in the development of bond were herein investigated. Different NCSS of samples for the split tensile test is shown in Figure 2-14 and for slant shear, and pull off tests are shown in Figure 2-15. The samples prepared for all bond tests and test setup are shown in Figure 2-16.

*(a) Chipped surface, slightly brushed.* *(b) Smooth surface, slightly brushed.* *(c) Smooth surface, no dust removal treatment applied.*

*(d) Sandblasted surface.* *(e) Brushed surface.* *(f) Grooved surface.*

**Figure 2-14 NSC substrate surfaces for Split tensile samples**

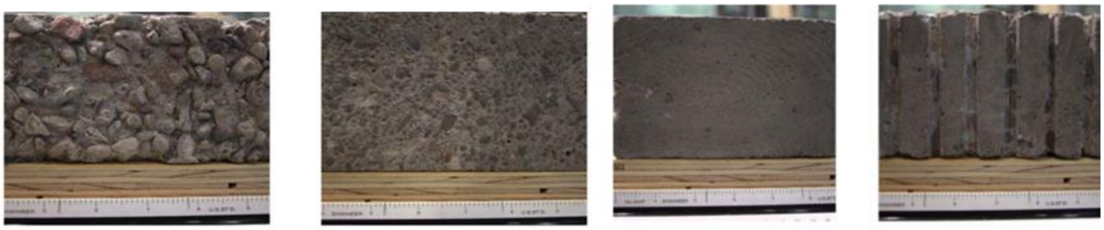

*(a) Rough surface.* *(b) Sandblasted* *(c) Brushed surface.* *(d) Grooved surface.*

**Figure 2-15 NCSS for Slant Shear and Pull off samples**

(a) The set-up for the splitting tensile test.

(b) Composite samples in the chamber.

(c) Determining the fundamental longitudinal frequency of the composite specimen.

(a) Compressive machine for the slant-shear test

(b) Specimen with rough surface during loading test

(c) Specimen with grooved surface during loading test

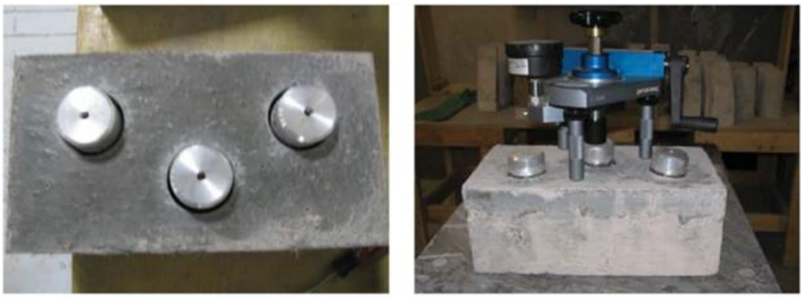

(a) Steel disks glued to the UHPC surface

(b) The set up for the pull off test

**Figure 2-16 Test Setup of split tensile, slant-shear and pull off tests**

It was reported that the bond performance between NCSS and UHPFRCC is successful. Results showed that saturated conditions of NCSS resulted into an excellent bond performance. The roughness degree of NCSS became irrelevant to obtain a good bond strength if appropriate wetting conditions took place[31].

Al-Osta et al. [32] evaluated the bond strength between UHPFRC and normal concrete by conducting the bond test such as split cylinder tensile strength test and slant-shear test.

Epoxy bonded (EP), plane surface and sandblasted (SB) hybrid cylinder specimens were tested in the current research work. The author concluded that specimens whose NC substrate surfaces was made rough through sandblasting had higher slant-shear strength than epoxy bonded or plane surface specimens and failure was observed in the interface plus partial concrete substrate. The values of split tensile strength test for both techniques (EP and SB) showed that the bond between UHPFRC and NSC fall under excellent bond quality regardless of surface preparation.

## 2.4 Application of UHPFRC in Strengthening the RC Beams:

Katrin et al. (2007) [33] experimentally investigated the rehabilitation potential of UHPFRC and conventional concrete structural members. The experimental work consists of 12 full scale 5.4 m long flexural beams with UHPFRC layer on the tensile face. The beams were comprised of conventional reinforced concrete substrate and UHPFRC layer as shown in Figure 2-17.

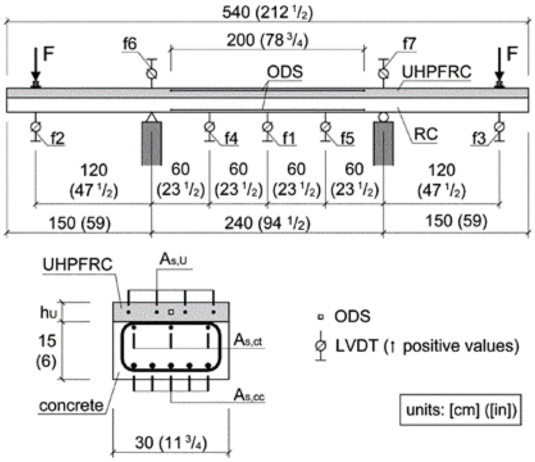

**Figure 2-17 Hybrid UHPFRC-RC Beam Test [33]**

These composite beams were tested under displacement control four-point loading system. Different thickness of UHPFRC layer (hu) and the presence of steel reinforcement in

UHPFRC layers were the experimental parameters. Beams without reinforcing bars in UHPFRC layer (NR) and Beams with reinforcing bars in UHPFRC layers (R) were under investigation. The results indicated that the use of rebars in UHPFRC layer increased the ultimate load carrying capacity by two times for R5 beams with $h_u$= 50 mm. this value was five times more for R10 beams with $h_u$= 100 mm in comparison with NR beams. The application of UHPFRC layer on the conventional RC beams enhanced the stiffness, reduced the deformations, minimize the crack spacing, crack width and delay the development of localized macro-cracks.

Martinola et al. [13] studied the performance of RC beams strengthened with HPFRC. For this purpose, total 3 full-scale 4.55 long beams had been tested in the current research work. Beam without any reinforcing bars and beam with very low 0.03 % reinforcement ratio had been strengthened with an HPFRCC jacket having a thickness of 40 mm as shown in Figure 2-18. The third beam without HPFRCC jacket but with the same reinforcement ratio had been used as a control specimen. After sandblasting the surface of normal concrete, HPFRCC jacket was applied. HPFRCC was reinforced with straight steel fibers.

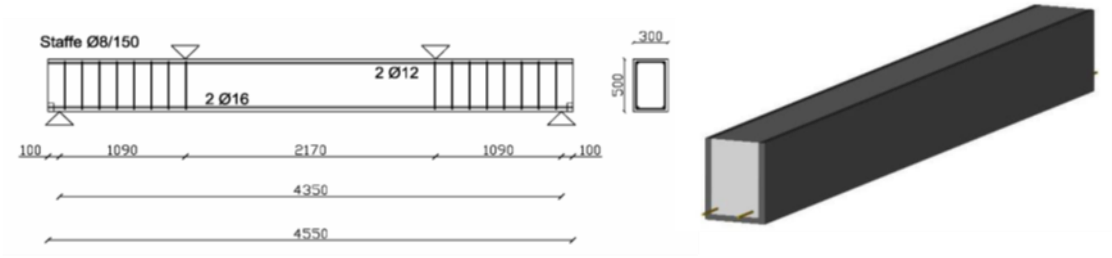

**Figure 2-18 Strengthening Scheme of Beams** [13]

It was reported that the strength of a beam with jacketing was increased by 2.15 times than the beam without strengthening. The proposed strengthening technique significantly increased the beam stiffness and consequently, mid-span deflection of beam strengthened with HPFRCC was reduced to from 6 mm to 0.5 mm at service load of 80 kN. Experimental results evidently showed that there is no need of any primer adhesive product for application of HPFRC. Sandblasting with the surface roughness of 1-2 mm is enough for proper bonding.

Serena et al. [34] experimentally evaluated the increment in the bearing capacity of RC members under shear action which is the challenging issue in repairing field. The test matrix consisted of 4 full scale 2.85 m long beams. One of the beams was used as a benchmark while all other beams were strengthened with HPFRC. The beam specimens had been strengthened with longitudinal reinforcement only. Stirrups and inclined reinforcement had not been used to ensure shear failure. The surface of other beams was made rough by sandblasting technique and U bent wire mesh was placed within HPFRC jacket. A different configuration of HPFRC jacket and specimen characteristics are shown in Figure 2-19.

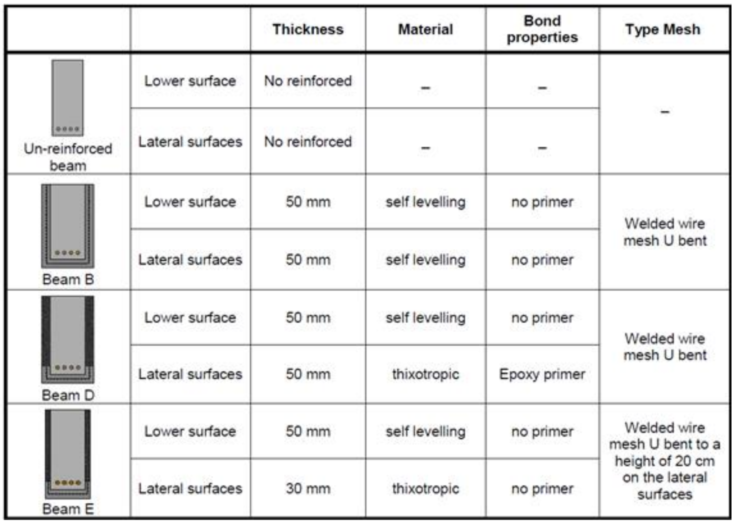

| | | Thickness | Material | Bond properties | Type Mesh |
|---|---|---|---|---|---|
| Un-reinforced beam | Lower surface | No reinforced | – | – | – |
| | Lateral surfaces | No reinforced | – | – | |
| Beam B | Lower surface | 50 mm | self levelling | no primer | Welded wire mesh U bent |
| | Lateral surfaces | 50 mm | self levelling | no primer | |
| Beam D | Lower surface | 50 mm | self levelling | no primer | Welded wire mesh U bent |
| | Lateral surfaces | 50 mm | thixotropic | Epoxy primer | |
| Beam E | Lower surface | 50 mm | self levelling | no primer | Welded wire mesh U bent to a height of 20 cm on the lateral surfaces |
| | Lateral surfaces | 30 mm | thixotropic | no primer | |

**Figure 2-19 Specimen Characteristics [34]**

Experimental results showed that the thickness of jacket effect the maximum load capacity. Beams B and D had the same thickness of HPFRC jacket and equal to 50 mm. Their capacities improved 1.7 times while beam E having a jacket of thickness 30 mm on the lateral surface, the maximum load increased 1.5 times. It was observed that HPFRCC jacket played the role of shear reinforcement and replaced it effectively.

Yehi et al. [35] investigated the flexural behavior of beams strengthened and retrofitted using the mixed steel fiber concrete jacket (MSFCJ) under short time repeated load. In the proposed research work, fourteen (14) 2.3 m long beams were cast and tested under three-point load configuration. Of these, two RC beams were constructed without retrofitting. One of them was tested under static load and other was tested under repeated load. The remaining 12 beams were strengthened and repaired. Of these, 6 beams were strengthened using U shape MSFCJ. MSFCJ was comprised of corrugated and end-hooked steel fibers. The other 6 beams were loaded up to 50% of ultimate static load then damaged beam was retrofitted using MSFCJ. Strengthening and retrofitting schemes are shown in Figure 2-20.

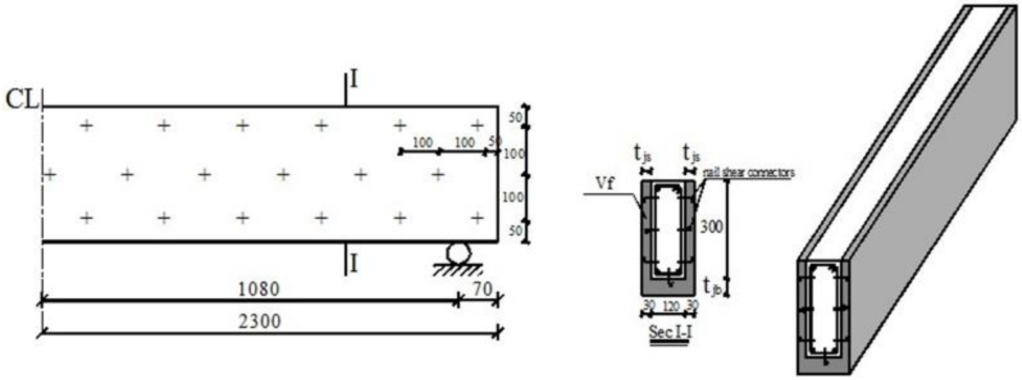

**Figure 2-20 Strengthening Schemes and Shear Connector Details [35]**

It was reported that the number of cracks had been reduced by using these types of strengthening and repairing techniques and cracks were concentrated in middle third portion of beams avoiding the formation of shear cracks. De-bonding failure had been prevented by use of shear connectors in MSFCJ. The stiffness of strengthened and retrofitted beams had been significantly enhanced. The addition of 1.5% fiber content in MSFCJ significantly increased the number of cycles and decreased the deflection and strains.

Prabhat et al. [36] studied the flexural behavior of damaged RC beams repaired using UHPC. The author experimentally evaluated the effectiveness of UHPC jacket in repairing the damaged RC beams. Total fifteen (15) 1.5 m long RC beams were fabricated having 100x200 mm X-section dimensions. Out of these 15 beams, 3 beams were tested without strengthening for finding the ultimate load carrying capacity of the reference beams. The remaining 12 beams were loaded up to 80-90% of ultimate load to induce distress in beams. Later on, these damaged specimens were repaired using UHPC strips of 20 mm thickness using an epoxy primer to take up the tensile stresses. In the current research work, the experimental parameter was curing type of retrofitted UHPC strips. Three different curing types namely hot air curing, steam curing and moist curing were used for curing of UHPC strips. All beams were tested under three-point loading system. It was observed that de-bonding failure had been prevented by the use of an epoxy primer. Results showed that UHPC strips cured with hot air treatment increased the failure load up to 30% while UHPC strips cured with steam curing increased load up to 10%. However, this value was equal to 20% for moist cured UHPC strips.

Al-Osta et al. [32] investigated the flexural behavior of RC beams retrofitted with UHPC. Two different techniques of strengthening of RC beams using UHPC with different configurations were assessed in this research. These two techniques are; i) NC surface was made rough by sandblasting and in-situ casting of UHPC around beams with different configurations. ii) Epoxy primer was used to attach the precast UHPC plates with conventional RC beams. Total experimental work consisted of 8 RC beams. Of these, two beams were tested under four point loading configurations without strengthening and used as reference beams. Each technique of strengthening consisted of 3 beams with different strengthening schemes, as shown in Figure 2-21.

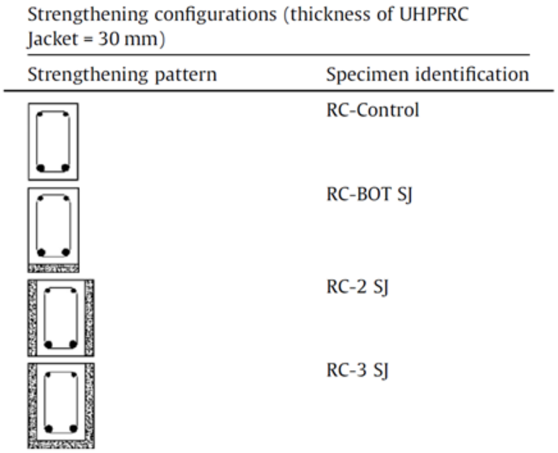

Strengthening configurations (thickness of UHPFRC Jacket = 30 mm)

| Strengthening pattern | Specimen identification |
|---|---|
|  | RC-Control |
|  | RC-BOT SJ |
|  | RC-2 SJ |
|  | RC-3 SJ |

**Figure 2-21 Strengthening Patterns and Specimen identifications [36]**

The author reported that there was no considerable difference in the results of two strengthening techniques. However, sandblasting interface preparation technique was more promising. It was reported that the stiffness and a cracking load of strengthened beams were increased, crack propagation was delayed and crack were concentrated in the middle third portion of the beam which reflected the increment in the shear strength of the beam.

From the review of literature presented above, it is observed that many research works have been conducted to study the efficiency of UHPFRC jacketing in strengthening the RC beams. However, very limited work is reported on the evaluation of the effectiveness of HPFRC jacketing in retrofitting the BCJs for making them capable of resisting the seismic loading. In the present research work, an attempt has been made to study the effectiveness of UHPFRC-jacketing for post-earthquake repairing and pre-earthquake strengthening of exterior BCJs, experimentally and numerically. The positive effect of the strengthening of BCJs using UHPFRC-jacketing was noticed against seismic loading due to the high compressive strength of UHPFRC coupled with strain hardening behavior under tensile stresses, high fracture toughness, and ductility.

# CHAPTER 3

# Experimental Program

## 3.1 Introduction

Experimental simulation is considered indispensable for getting insight into the response of structural members under earthquake-generated agitation to a structure. This chapter introduces the specimens tested at Heavy Equipment Reaction Floor Laboratory of KFUPM to investigate the effectiveness of UHPFRC jacket in repairing and strengthening the external RC BCJs with no stirrups in the joint region under monotonic and reversed cyclic loading protocols. The complete experimental matrix consists of seven (7) 1/3 scale exterior BCJs sub-assemblages and there were characterized by the same geometry and reinforcement detailing. Exterior BCJs are more susceptible to damage under seismic excitation due to less confinement, high torsional stresses and lower axial load on the column as compared to interior BCJs. The experimental campaign has been divided into two groups

1) Group # 1: Post-earthquake or post-damage repairing
2) Group # 2: Pre-earthquake or pre-damage strengthening

The following section will report detail description about the detailing and design of test specimens, fabrication of specimens, damaged specimens, and their retrofitting configurations, strengthening schemes of undamaged units, material properties of normal concrete, steel reinforcement, Sikadur® 32-LP and UHPFRC, the experimental test setup details, instrumentation and loading protocols.

## 3.2 Description of the specimens

A total of 7, 1/3 scale RC T-connections without any transverse reinforcement in their joint region were fabricated and tested under monotonic and reversed cyclic loading. Each specimen represents a part of the multi-story plane frame. As described earlier, these specimens had been divided into two groups. Group # 1 consisted of three damaged specimens repaired by using UHPFRC jacket and tested under monotonic loading. The effectiveness of UHPFRC jacket in repairing the damaged specimens under varying axial load had been studied in this group. The specimen were labeled as SP1-R, SP2-R, and SP3-R. Group # 2 comprised of four undamaged specimens. One of them was tested in as built condition and used as the reference unit, designated as TC. The remaining three specimens were strengthened by using UHPFRC jacket. Before jacketing, the normal concrete substrate surface (NCSS) of two specimens was made rough through sandblasting for the development of the full bond between normal concrete and UHPFRC jacket. After surface treatment, UHPFRC was cast around the BCJs inside the mold and these two specimens were designated as TS1 and TS2. However, for the fourth specimen, UHPFRC plates were cast and cured for 28 days. After cleaning the substrate concrete surface of the test unit, UHPFRC plates were attached to the surface of the unit, without any surface treatment, with the help of the epoxy primer. This specimen was designated as TSE. Specimens TC, TS1, TS2, and TSE were tested under reversed cyclic loading simulating the real loading event such as earthquake and CAL was kept constant and equal to 150 kN.

## 3.3 Design of specimen

All test units have same geometry and reinforcement detailing and they were designed such that failure would occur in the joint region due to shear without yielding of beam’s reinforcement. Concrete outline and reinforcement detailing of the specimen are shown in Figure 3-1 and Figure 3-2, respectively. Each specimen is comprised of an upper and lower column along with one orthogonal beam, coinciding in the joint region. According to the elastic lateral response of a moment-sway frame when subjected to lateral loads, the points of contra-flexural approximately occur at mid-height of columns and mid-length of beams. Therefore, the length of structural elements is representative of mid-story height for columns and mid-span of beams of the frame structure to simulate the boundary conditions at the extremity of elements. The column has rectangular 200 x 250 mm cross section and a length of 1200 mm whereas the beam has a rectangular 200 x 250 mm cross section and a length of 900 mm. Therefore, the joint panel has a square 250 x 250 mm plane section. Joint aspect ratio is kept 1 which is the most common case found in the literature. Two sets of four Φ20 (diameter of rebar is 20mm) deformed bars are selected for positive and negative reinforcement of beam. Reinforcement ratio for beam was kept high to promote joint failure mechanism without yielding of beam’s reinforcement. The anchorages of beam bars are conforming to current building code ACI 318-11[37] to ensure proper transfer of forces from beam to joint. As per code, bars are anchored in the joint by 90-degree standard hooks which are spotted within 500 mm from the face of the column. The hook tail length is 200 mm embedded into the joint. Φ8 transverse reinforcement in the beam is spaced at 50 mm. The first stirrup is provided at 10 mm from the face of the column in the beam. The flexural capacity of the column is kept around two times higher than demand imposed by the beam for all load combination used in the experiment. The column is designed by following the guidelines provided by ACI 318-11. Six Φ20 deformed bars are placed along the shorter dimension of the column as the column longitudinal reinforcement. The transverse reinforcement in column consists of Φ8 deformed bars spaced at 50 mm. The first tie in the column is placed at 25 mm from the face of the beam. No transverse reinforcement is placed in the joint area and all specimens are cast horizontally.

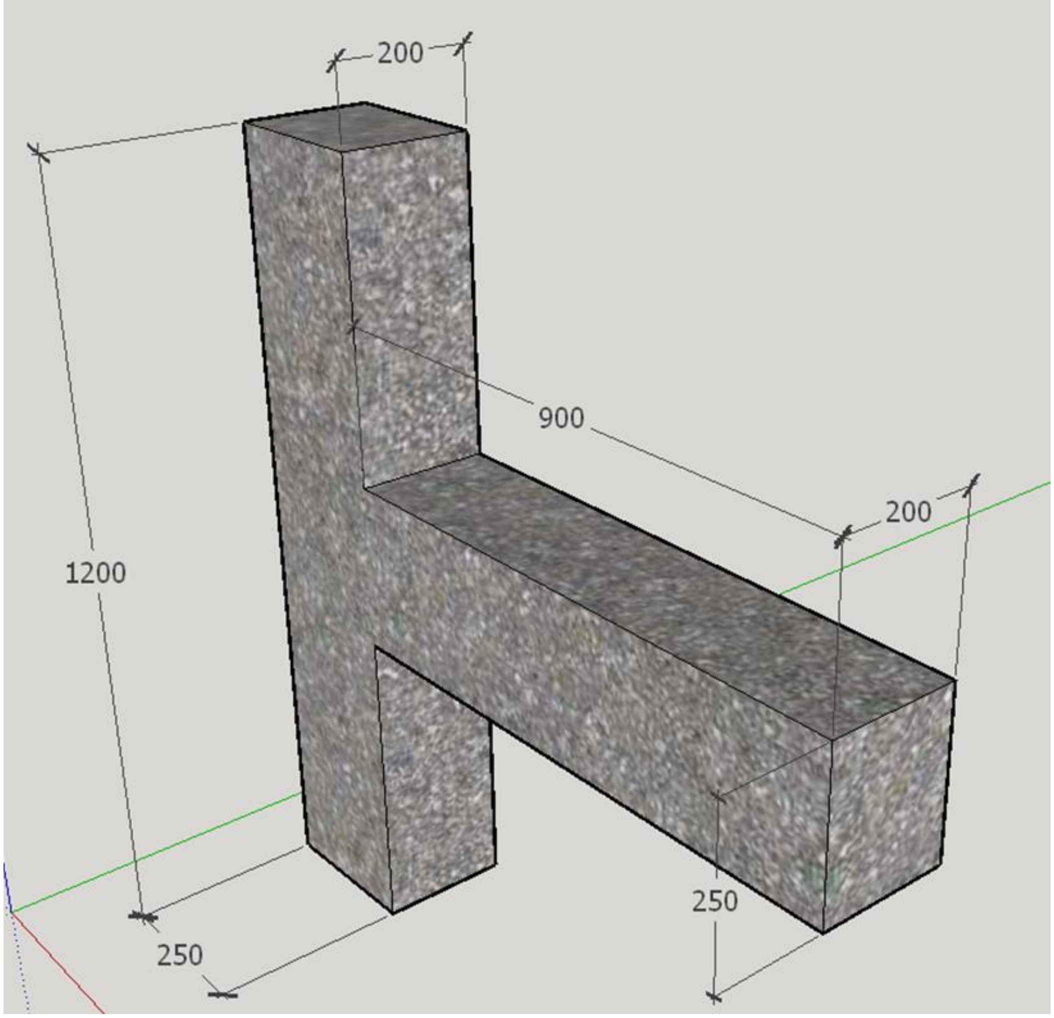

**Figure 3-1 Geometric details of BCJ (3-D view)**

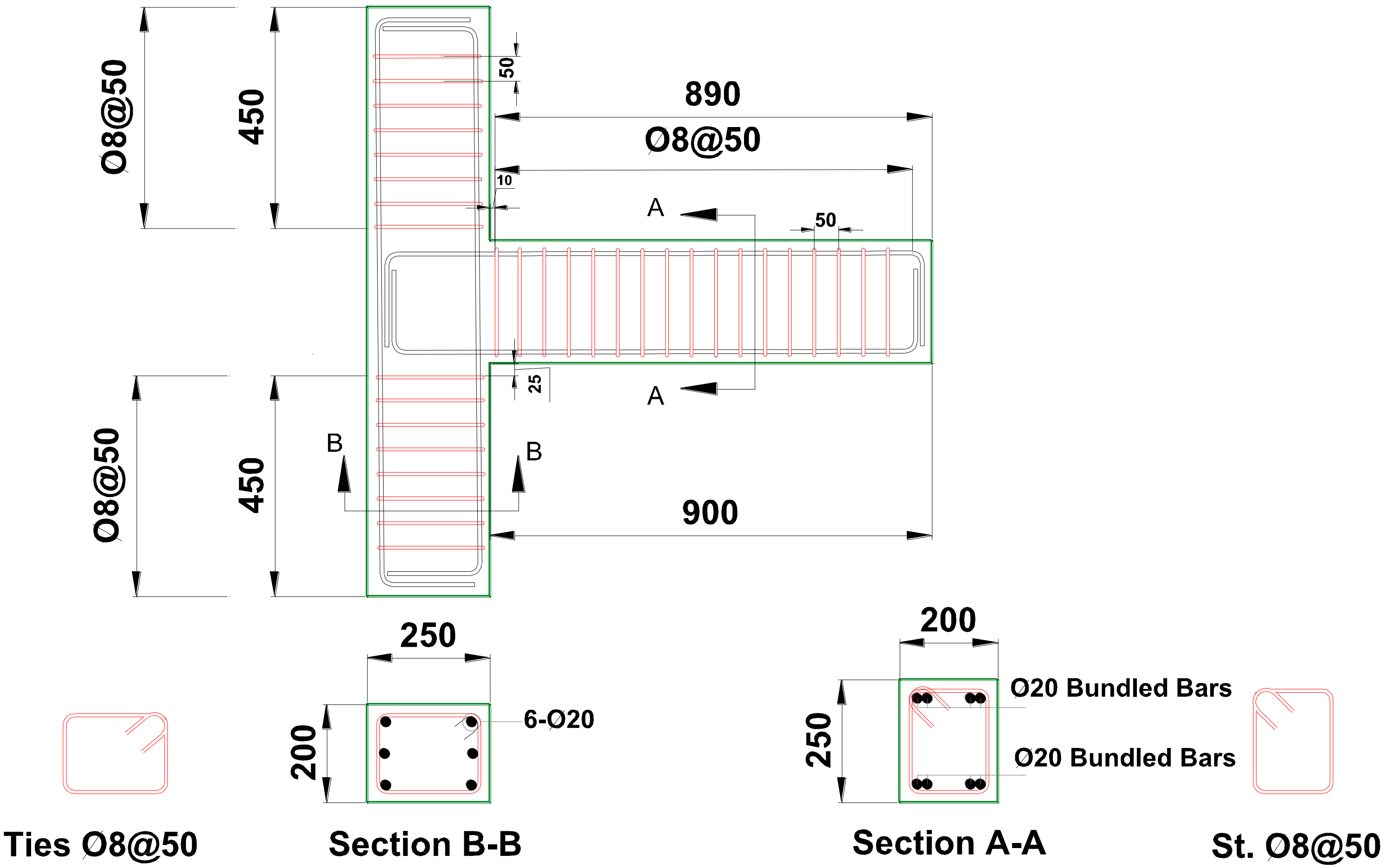

Figure 3-2 Reinforcement detailing of test specimen

## 3.4 Preparation of Specimen

The specimens were cast at “PRAINSA Precast Factory”. For the construction of specimens, wooden molds and steel cages were prepared at the same factory while the ready-mix concrete company supplied the concrete. The preparation of wooden molds and steel cages are described in the following sections.

### 3.4.1 Preparation of wooden molds:

New smooth surface plywood formwork of standard thickness 18 mm was used as a mold for casting the normal concrete. These molds were formed to produce specimens consisted of a column and beam with 200 x 250 mm cross section and the length of 1200 mm and 900 mm, respectively. In the formation of formwork, special attention was given to dimension, alignment and concrete cover. Before casting, inner sides of molds were properly cleaned and the gaps between the edges of formwork were sealed using silicon to prevent the flow of water from the concrete matrix. The preparation phase of the mold is shown in Figure 3-3. A thin layer of oil was sprayed on the inner sides of molds to facilitate the de-molding of RC specimens.

**Figure 3-3 Preparation of wooden molds**

### 3.4.2 Preparation of steel cages

The reinforcement was cut and bent by commercial steel supplier according to bar bending schedule provided to them. The steel cages were assembled in the factory. For the construction of steel cages, steel wires were used to hold the main bars and stirrups in their position. Plastic spacers attached to steel cage were used to ensure the required concrete cover. Complete steel cages are shown in Figure 3-4. After the construction of steel cages, the location of strain gauges for monitoring the strain in the rebar was marked appropriately on the main and transverse reinforcements. After their formation, they were placed in the wooden molds. Figure 3-5 shows the placement of steel cage inside the wooden mold. The steel cage, settled in the wooden mold before casting, is shown in Figure 3-6. Before casting the concrete, the strain gauges were installed on the main and transverse reinforcement after cleaning and sanding the surface of the rebar to provide the flat surface. Strain gauges were attached using super glue and covered them using waterproof tape to avoid their damage from water and protect them from the impact of aggregates and vibrator during casting.

**Figure 3-4 Steel cages for the test specimen**

**Figure 3-5 Placement of steel cages inside the wooden molds**

**Figure 3-6 Wooden molds with reinforcement cage before casting**

### 3.4.3 Casting and curing of the concrete

The conventional concrete for casting was provided by "Saudi Ready-Mix Concrete Company". All specimens were cast from the same batch. The concrete was poured directly into the molds from the truck. Small electrical poker vibrator was used to consolidate the concrete completely and leveling was done with the help of trowels to level an uneven surface as shown in Figure 3-7. For determining the material properties like concrete compressive strength and split tensile strength at the age of 28 days, standard size cylinders were cast from the same batch of concrete. After casting the concrete, BCJs and cylinders were covered with plastic sheets to prevent the loss of water that may result in the surface cracks. After de-molding, specimens were cured using wet jute to avoid shrinkage cracks and premature stresses in the concrete.

**Figure 3-7 Casting of test specimens**

After completion of curing period (28 days), specimens were transported from the precast factory to Heavy Equipment Reaction Floor Lab of KFUPM as shown in Figure 3-8.

**Figure 3-8 Test specimens at 28 days curing period**

## 3.5 Repairing and Strengthening Scheme

### 3.5.1 Repairing Strategy

The experimental work involves the post-damage repair and pre-damage strengthening of damaged and undamaged BCJs, respectively. In the former set, three severely damaged exterior BCJs designated as SP1, SP2, and SP3 were elected from a group of specimens that were tested in their virgin state in the ambit of the research program of MS thesis [38]. All specimens were similar regarding geometric and reinforcement detailing. The only difference between these specimens was Column Axial Load (CAL). For this group, Axial Load Ratio (ALR) varied from 0 to 0.57 and CAL was 0 kN, 200 kN, and 600 kN for units SP1, SP2, and SP3, respectively. These specimens were tested under monotonic loading and were loaded up to 100% of ultimate load carrying capacity at the beam tip in their virgin state to distresses their elements. These damaged specimens were repaired with state of the art magic material. These specimens were reinforced in the column, beam and joint region using UHPFRC jacket. The jacket was extended 250 mm from the joint region to the beam and columns, and this extension was equal to the depth of the element. Before application of UHPFRC jacket, the normal concrete substrate surface (NCSS) was made clean through brushing. For making the successful bond between NCSS and UHPFRC, some surface preparation techniques were available for the preparation of substrate surface such as chipped surface, sandblasted surface, and grooved surface. For the specimens of group 1, chipped surface slightly brushed with the dry condition was selected for surface preparation which includes the small holes produced by a hand drill. Figure 3-9 shows the NCSS after surface treatment.

**Figure 3-9 Chipped NCSS after surface treatment**

Smooth surface wooden molds were used for casting the UHPFRC jacket around the NC, as shown in Figure 3-10. The inner surface of the molds was cleaned and inside edges were sealed with silicon. To facilitate the demolding of UHPFRC jacket, a thin layer of oil was sprayed onto the inner surfaces before casting the UHPFRC. Figure 3-11 shows the damaged specimen after surface treatment positioned in the mold. The whole set-up of UHPFRC jacketing was placed on the vibrating table to provide small magnitude vibrations for the flow of UHPFRC if required. The equipment and material used for mixing and casting the UHPFRC will be discussed in section 3.6.3. Jackets were cast when specimens place horizontally. UHPFRC was poured around the damaged specimen inside the mold.

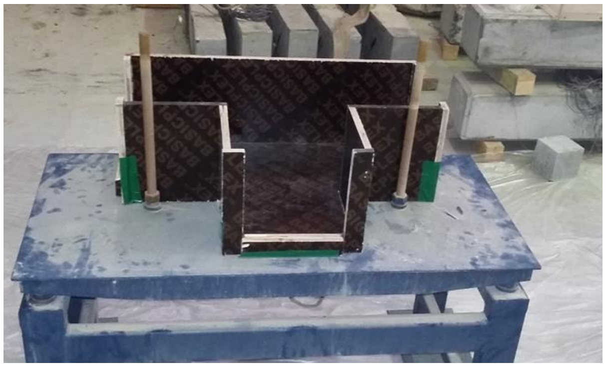

**Figure 3-10 Smooth surface wooden molds for jacketing with vibrating table**

**Figure 3-11 Specimen positioned inside the mold before UHPFRC jacketing**

The column, beam, and joint region were encased in UHPFRC jacket of 30 mm thickness. The geometry and reinforcement details of retrofitted specimens are shown in Figure 3-12 and Figure 3-13, respectively. After casting the jacket, test units were covered with plastic sheets to prevent rapid loss of water. Repaired specimens were de-molded after 24 hours of casting. These specimens were cured for 28 days with wet burlaps. The pictorial view of specimen's repairing, jacket casting, and curing is shown in Figure 3-14.

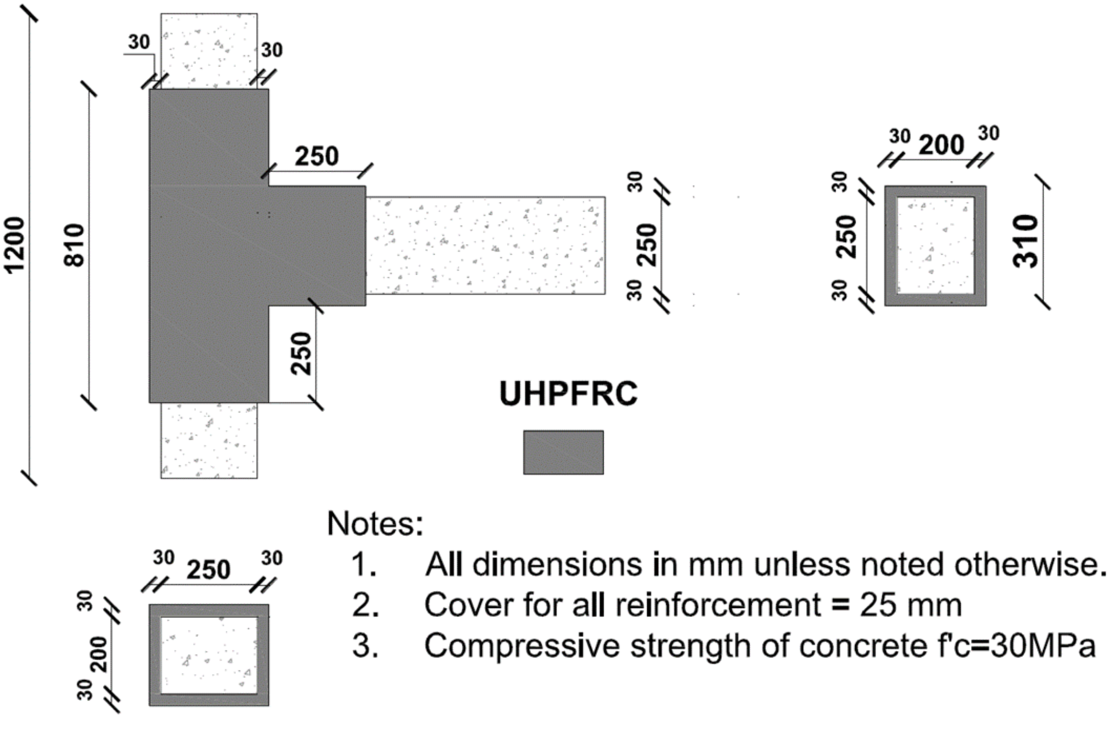

Notes:

1. All dimensions in mm unless noted otherwise.
2. Cover for all reinforcement = 25 mm
3. Compressive strength of concrete f'c=30MPa

**Figure 3-12 Geometric details of retrofitted specimens**

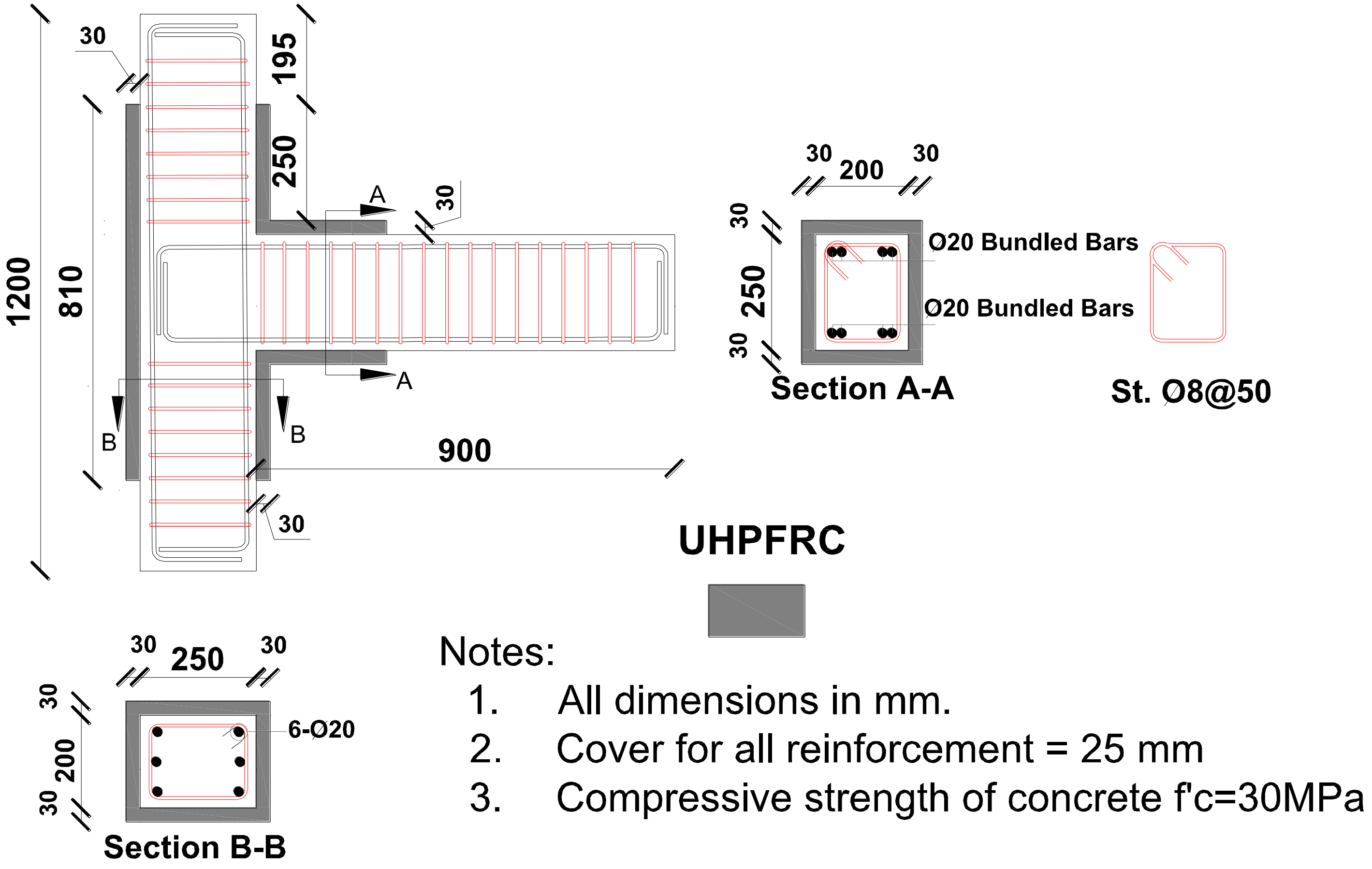

Notes:

1. All dimensions in mm.
2. Cover for all reinforcement = 25 mm
3. Compressive strength of concrete f'c=30MPa

**Figure 3-13 Reinforcement detailing of retrofitted specimens**

**Figure 3-14 Casting and curing of UHPFRC jacket of repaired specimens**

### 3.5.2 Strengthening Scheme

Group 2 consisted of four undamaged specimens. Of these, three specimens were strengthened using UHPFRC jacket before application of load, designated as TS-1, TS-2, and TSE. From the numerous surface preparation techniques, NCSS of specimens TS-1 and TS-2 was made rough through sandblasting technique up to medium level. Sandblasting of these specimens had been done at Prainsa Precast Factory, as shown in Figure 3-15. Figure 3-16 shows the strengthening process of units TS1 and TS2. The casting of UHPFRC jacketing was done in the same way as described in section 3.5.1. The geometry and thickness of UHPFRC jacket were same as described in section 3.5.1. Figure 3-12 shows the schematic view of strengthened specimen. Specimens upgraded using UHPFRC jackets were de-molded after 24 hours of casting. These specimens were cured for 28 days with wet burlaps.

**Figure 3-15 Sandblasting of BCJ's substrate surface**

**Figure 3-16 Strengthening process of units TS1 and TS2**

For the third specimen of this group, designated as TSE, the structural epoxy-bonding agent was used to attach the pre-fabricated UHPFRC plates without adopting any surface preparation technique. Instead of the in-situ casting of UHPFRC inside the molds, T, I and Square shape UHPFRC plates of 30 mm thick were cast using the wooden molds as shown in Figure 3-17 and cured for 28 days. These wooden molds were cleaned and sealed with silicon before casting. The wooden molds and UHPFRC-plates after de-molding are shown in Figure 3-17 and Figure 3-18, respectively. These UHPFRC plates were applied to NCSS using 2-parts structural epoxy bonding agent named as Sikadur®-32 LP. It is moisture tolerant, structural two part bonding agent based on a combination of epoxy resin and special fillers. NCSS was cleaned using an angle grinder to obtain the surface that was sound, clean, dry and free from any cement lattice. Any loose or friable particles were removed to achieve a contaminated free and open textured surface. Before application of these plates, the NCSS was also made clean through compressed air, as shown in Figure 3-19 and Figure 3-21. The components A and B of Sikadur®-32 LP were mixed for 3 minutes using spindle attached to an electric drill. After mixing the components of epoxy, I-shaped UHPFRC plate was attached to back face of the column, as shown in Figure 3-19 and Figure 3-22 (a), followed by the square-shaped strips that were bonded to column and beam portions, as shown in Figure 3-19 and Figure 3-22 (b). In the end, T-shape plates were applied to the specimen covering beam, column, and joint region. Figure 3-19 shows the retrofitting process of specimen TSE. Figure 3-20 displays the 3-D view of TSE. The ambient conditions and temperature, as stated in product data sheet provided by the epoxy supplier, were maintained using two 500 watts halogen bulb, as shown in Figure 3-23.

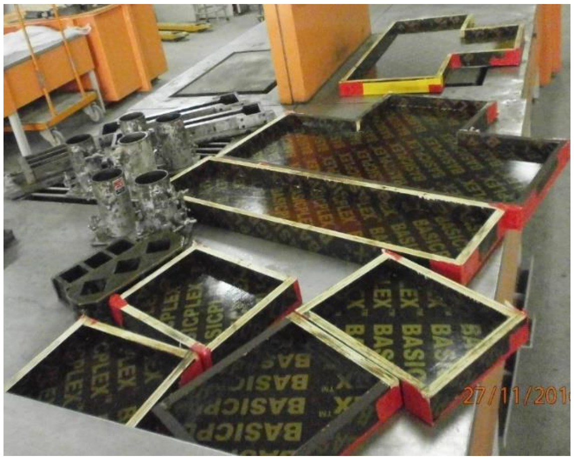

**Figure 3-17 Molds used for casting the UHPFRC plates**

**Figure 3-18 Precast UHPFRC plates**

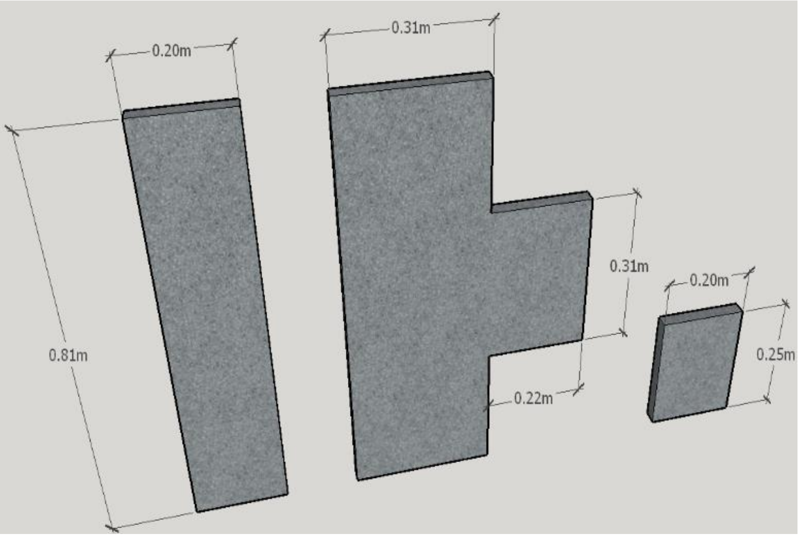

**Step 1:** Casting of UHPFRC plates of required geometry

**Step 2:** Cleaning the NCSS

**Step 3:** Mixing the components of structural bonding agent

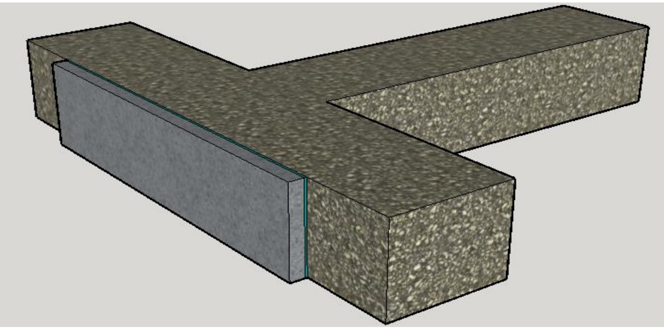

**Step 4:** Attachment of I-plate by using epoxy bonding agent on the outer face of column

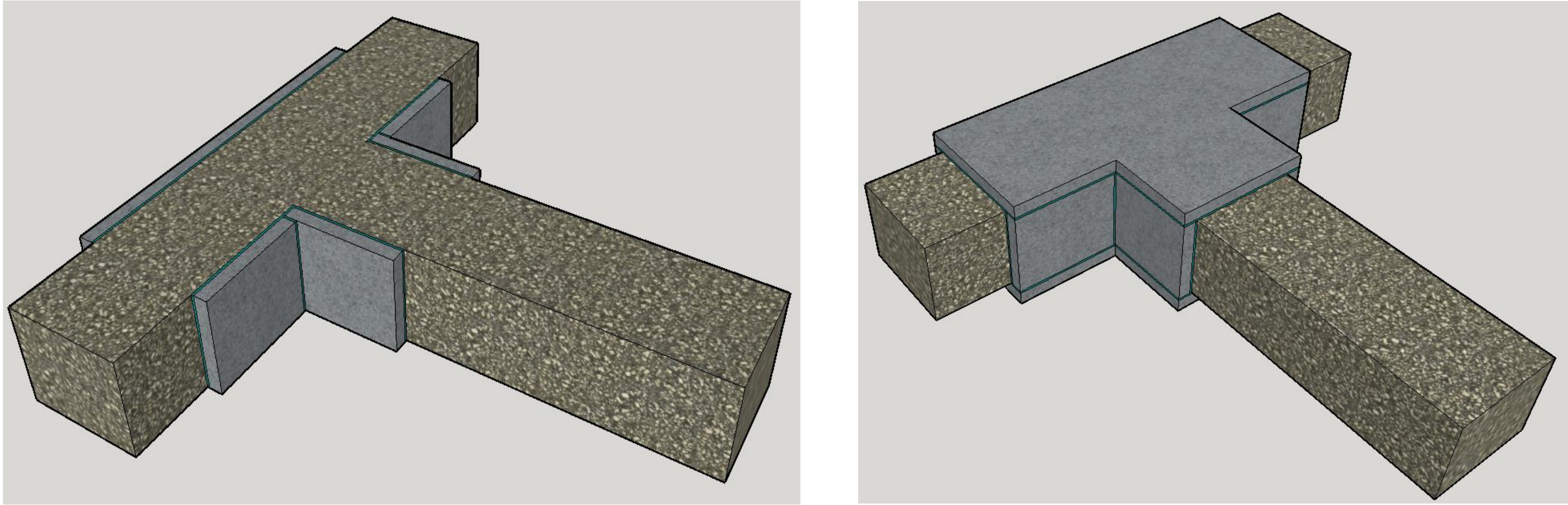

**Step 5:** Attachment of square plates by using epoxy bonding agent on the inner face of column and upper and lower face of beam

**Step 6:** Attachment of T-plates by using epoxy bonding agent on the front and back face of column and beam

**Figure 3-19 Strengthening process of unit TSE**

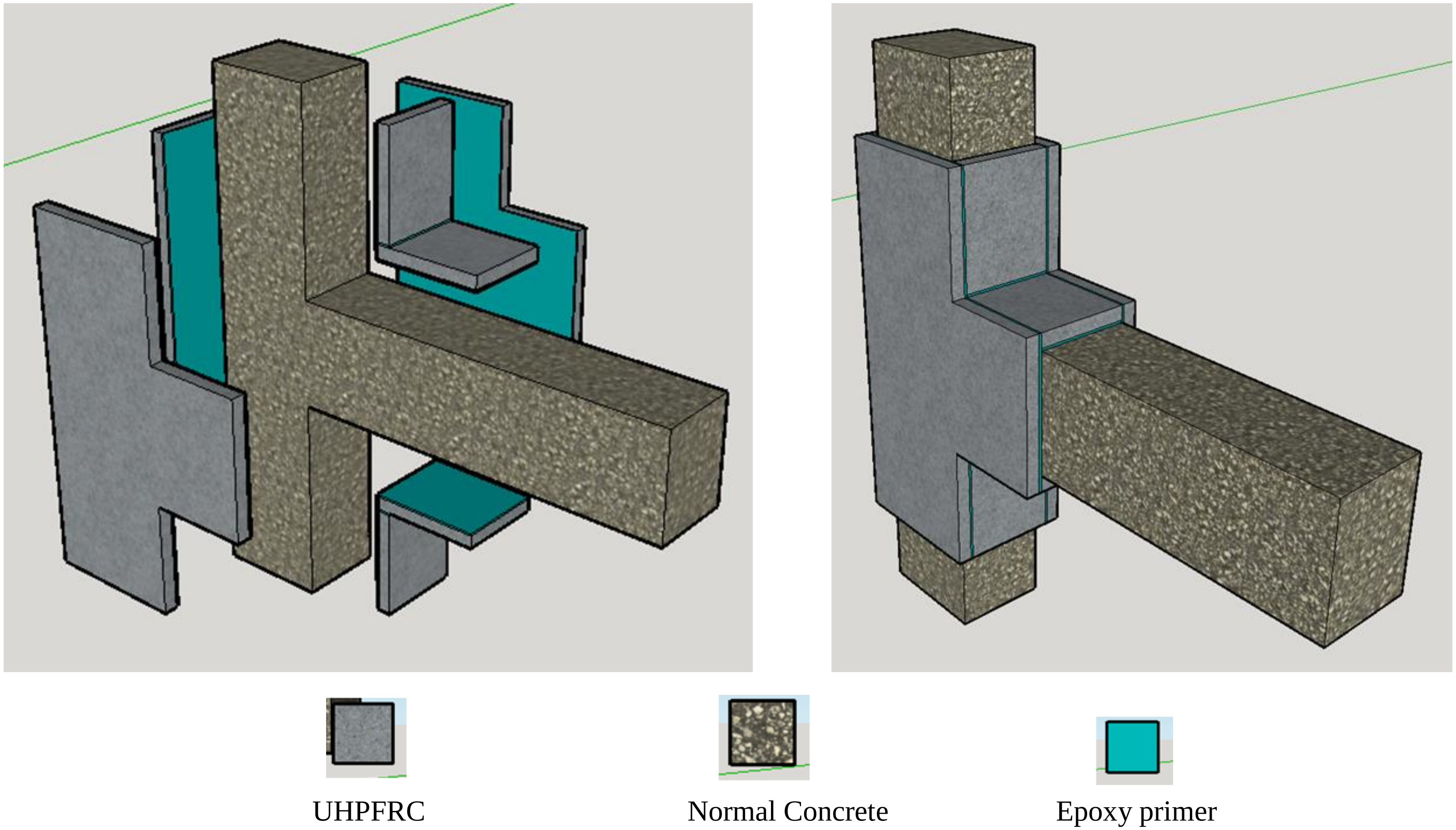

**Figure 3-20 3-D views of Specimen TSE**

Figure 3-21 Cleaning process of NCSS before application of plates

(a) Attachment of I-plate

(b) Attachment of rectangular plate

Figure 3-22 Strengthening of BCJ with pre-fabricated UHPFRC plates

**Figure 3-23 Curing of epoxy adhesive using halogen lights**

## 3.6 Material Properties

Four materials were used in fabrication, repairing and strengthening of damaged and undamaged test units. To characterize these materials, different tests had been performed according to standard test methods given in the literature. The material characteristics of following four materials were determined.

1. Normal concrete
2. Steel reinforcement
3. Ultra-High Performance Fiber Reinforced Concrete
4. Sikadur 32 Lp ®

### 3.6.1 Normal Concrete

Saudi Ready-mix Concrete Company provided the Normal concrete with a minimum design strength of 25 MPa. The slump of concrete before casting was 110 mm and the maximum aggregate size used was 25 mm. During the casting of BCJs, multiple cylindrical specimens of 75mm x 150 mm were cast from the same batch, as shown in Figure 3-24, for characterization and material modelling. For modelling the concrete in Finite Element solver, uniaxial compression test under monotonic and cyclic loading was performed. From this test, stress-strain behavior of the material, modulus of elasticity and Poisson's ratio were calculated which were used to characterize and model the material. In addition to compression testing, split cylinder strength test was also performed to determine the indirect tensile strength of concrete.

**Figure 3-24 Sampling of concrete during Casting**

#### 3.6.1.1 Compressive strength test

For determining the compressive strength and stress-strain behavior of normal concrete, cylindrical of 75 mm diameter and 150 mm height were tested, on test date of BCJs, in compression as per ASTM C39 [39] at a loading rate of 0.25 MPa/sec. Before testing the cylinders, sulphur capping was done to obtain the smoothness at the top and bottom surfaces. Compression strength test was performed using a digital compression-testing machine with a maximum loading capacity of 3000 kN. For this purpose, a frame of 87 mm gauge length with two LVDT's and load cell of 1000 kN capacity attached to portable data logger TDS-303 was used to record load-deformation data. Figure 3-25 shows the whole test setup and specimen after failure. Compressive strength was calculated by dividing the load at the failure to X-sectional area of the specimen. The compressive strength values of concrete used for casting the specimens of group 1 (damaged specimens) and group 2 (undamaged specimens) are tabulated in Table 3-1 and Table 3-2, respectively. Figure 3-26 shows the stress-strain behavior of concrete used for casting the specimens of group 2.

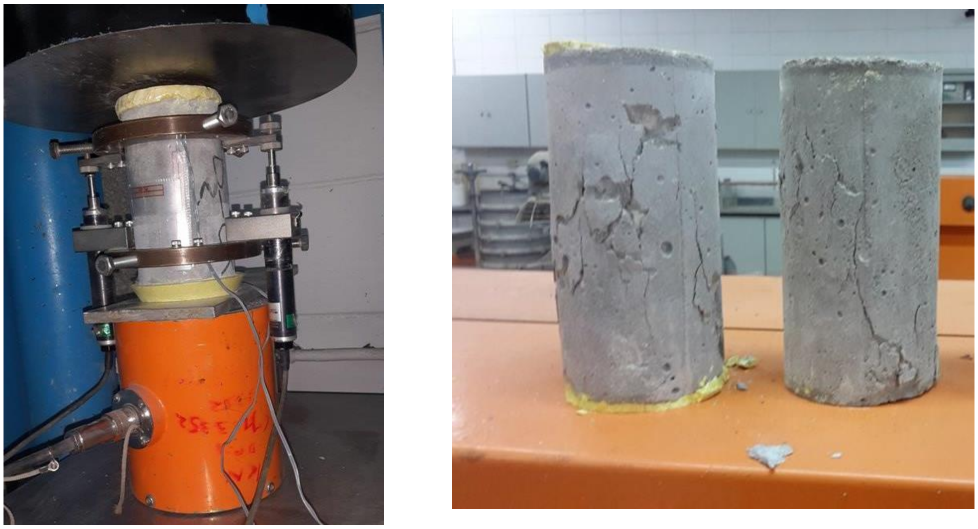

**Figure 3-25 Test Setup for compression testing (Left), ultimate failure in cylinders (Right)**

**Table 3-1 Compressive Strength of Normal Concrete (Group 2)**

| Specimen | Ultimate Load | X-sectional Area | Strength | Average Strength |
|---|---|---|---|---|
| | kN | $mm^2$ | MPa | MPa |
| Cylinder 1 | 134.61 | 4417.86 | 30.47 | 30.09 |
| Cylinder 2 | 131.25 | 4417.86 | 29.71 | |

**Table 3-2 Compressive Strength of Normal Concrete (Group 1)**

| Specimen | Ultimate Load | X-sectional Area | Strength | Average Strength |
|---|---|---|---|---|
| | kN | $mm^2$ | MPa | MPa |
| Cylinder 1 | 88.4 | 4417.86 | 20.01 | 20.47 |
| Cylinder 2 | 89.73 | 4417.86 | 20.31 | |
| Cylinder 3 | 93.17 | 4417.86 | 21.09 | |

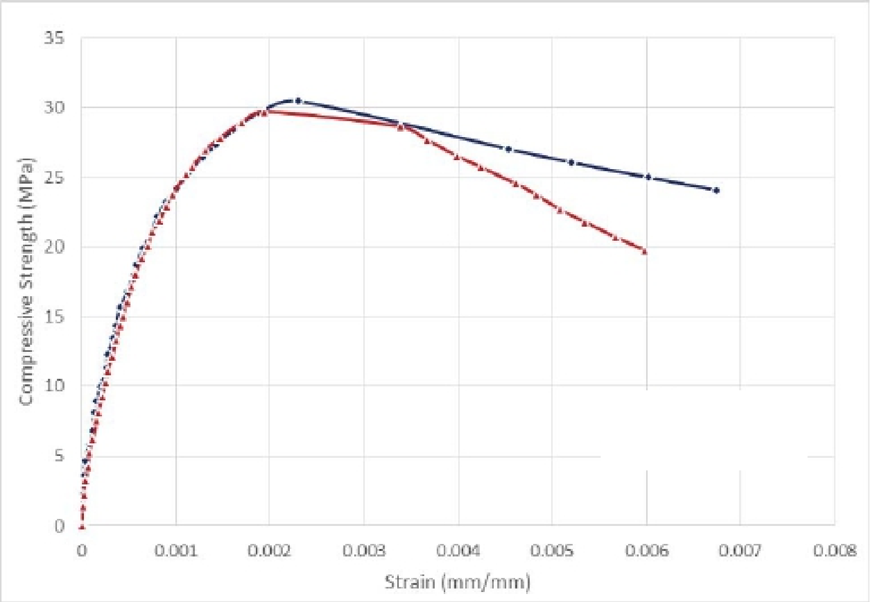

**Figure 3-26 Normal concrete stress-strain behavior of group 2 specimens**

#### 3.6.1.2 Modulus of elasticity and Poisson's ratio

The Experimental test setup used for the measurements of the modulus of elasticity and Poisson’s ratio was same as used in compression strength test. The only difference between them was the application of load. The compression strength test was performed under monotonic loading while in this setup, the test was performed under cyclic compression loading. For the measurements of strains in concrete, in addition to LVDTs, two strain gauges were installed on a concrete surface in horizontal and vertical direction. MOE (E) and Poisson’s ration (µ) were calculated by using the following formula reported in ASTM C469 [40].

$$\mathrm{E} = \frac{S_2 - S_1}{\epsilon_2 - 0.00005} \tag{3.1}$$

$$\mu = \frac{\epsilon_{t2} - \epsilon_{t1}}{\epsilon_2 - 0.00005} \quad (3.2)$$

Where:

E = Modulus of elasticity (MPa)

S2 = Stress corresponding to 40 % of Ultimate Load

S1 = Stress corresponding to longitudinal strain of 0.00005

$\epsilon_2$ = Longitudinal strain corresponding to stress $S_2$

$\epsilon_{t2}$ = Transverse strain corresponding to stress $S_2$

$\epsilon_{t1}$ = Transverse strain corresponding to stress $S_1$

The behavior of normal concrete used for casting the specimens of group 2 under cyclic loading is shown in Figure 3-27.

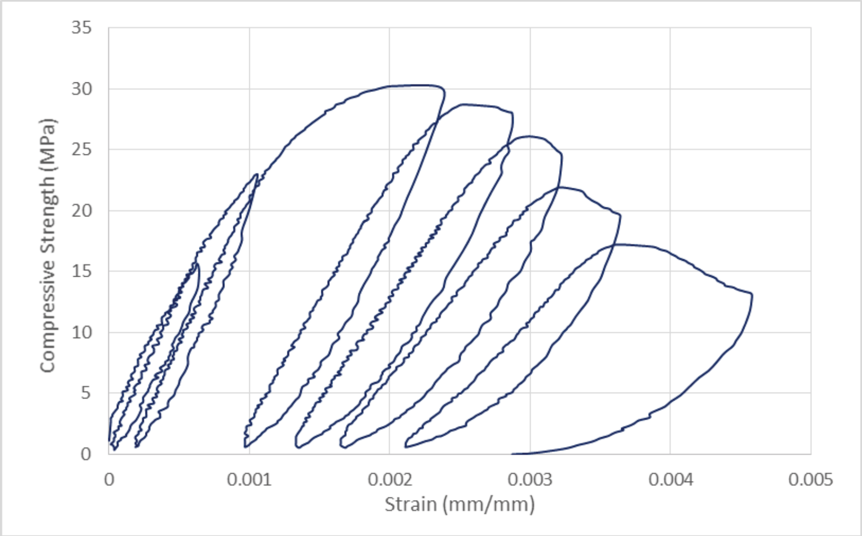

**Figure 3-27 Response of Normal concrete under cyclic compressive loading**

MOE and Poisson’s ratio of normal concrete used for casting the specimens of group 1 were reported by the research program of MS thesis [38] and for specimens of group 2, these values were calculated as per ASTM C 469 and given in Table 3-3.

**Table 3-3 MOE and Poisson’s ratio of normal concrete**

| Group No. | MOE<br>MPa | Poisson’s ratio |
|---|---|---|
| Group 1 | 21542 | 0.2 |
| Group 2 | 25700 | 0.19 |

#### 3.6.1.3 Split tensile test

Split tensile strength test was carried out on three cylinders for the measurement of the indirect tensile strength of concrete used for casting the specimens of group 2 while for the specimens of group 1, split tensile strength values were reported in MS thesis [38]. The test setup used for testing and specimen after testing is shown in Figure 3-28.

**Figure 3-28 Test setup for Split tensile test (left) and failure mode (right)**

The strength value was determined in according to ASTM C496 [41]. Compression testing machine with a maximum capacity of 3000 kN was used for this test. Peak failure load was obtained from the machine and following formula was used to determine the indirect tensile strength of the concrete.

$$f_t = \frac{2\,P}{\pi\, l\, d} \tag{3.3}$$

where:

$f_t$ = Split tensile strength (MPa)

P = Peak failure load (N)

$l$ = Length (mm)

d = Diameter (mm)

Split tensile strength values of concrete used for casting the specimens of group 1 and group 2 were calculated using Eq. 3.3 and given in Table 3-4.

**Table 3-4 Split tensile strength of normal concrete**

| **Group No.** | **Tensile Strength** |
|---|---|
| | **MPa** |
| Group 1 | 2.81 |
| Group 2 | 3.08 |

### 3.6.2 Steel reinforcement

The uniaxial tensile strength test was carried out on the deformed rebar used in BCJ subassembly, as per ASTM A615, by using Universal Tension Machine available in Structural Mechanics Lab of KFUPM. 20 mm bars were used as longitudinal reinforcement and 8 mm bars were used as transverse reinforcement in all specimens. The test setup used for tensile test of rebar and failure mode of 20 mm bar is shown in Figure 3-29

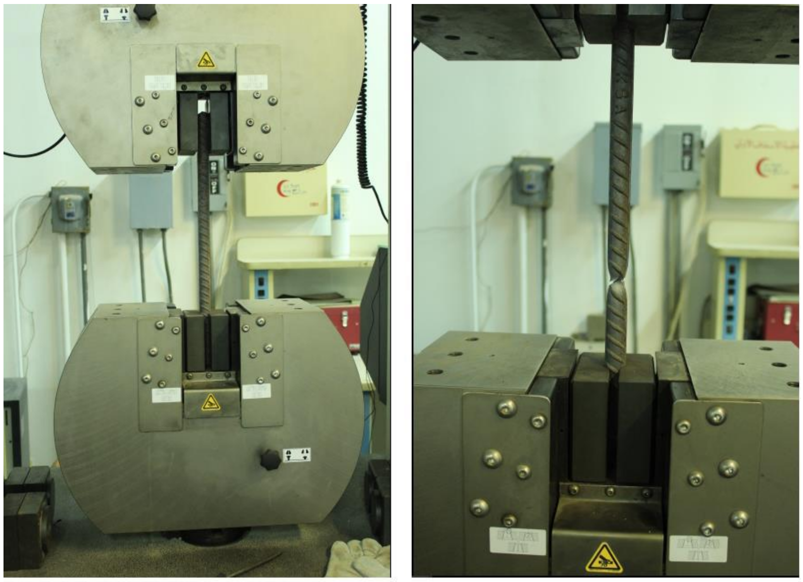

**Figure 3-29 Uniaxial tensile test setup (Left) and failure mode of rebar (Right)**

By performing the tensile test on steel bars, average values of 605 and 695 MPa were determined for the yield tensile strength and ultimate tensile strength of the longitudinal reinforcement at the strain of 0.0031 mm/mm and 0.0106 mm/mm, respectively with an elastic modulus of 195161 MPa. Figure 3-30 displays the stress-strain behavior of longitudinal bar under tensile loading. However, transverse reinforcement had the yield strength and ultimate tensile strength of 580MPa and 667 MPa at the strain of 0.003 mm/mm and 0.0105 mm/mm, respectively with an elastic modulus of 193600 MPa. Figure

3-31 shows the stress-strain behavior of transverse reinforcement under tensile loading. The result data of tensile test for longitudinal and transverse reinforcement is given in Table 3-5.

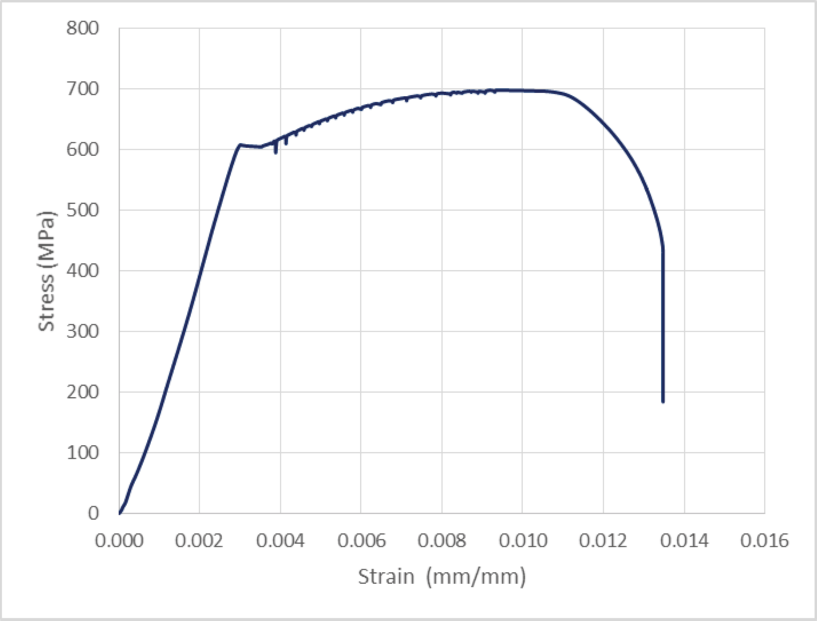

**Figure 3-30 Stress-strain behavior of longitudinal reinforcement (Ø20)**

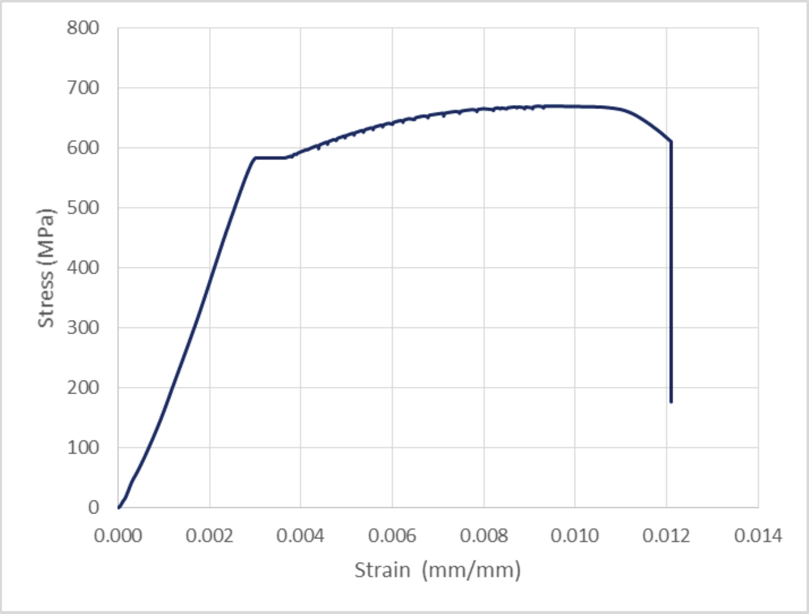

**Figure 3-31 Stress-strain behavior of transverse reinforcement (Ø8)**

**Table 3-5 Result data of tensile test performed on steel reinforcement**

| Bar Size | Stress | | Strain | | Modulus of Elasticity |
|---|---|---|---|---|---|
| | $f_y$ | $f_u$ | $\in_y$ | $\in_u$ | E |
| | MPa | MPa | mm/mm | mm/mm | MPa |
| Ø20 | 605 | 695 | 0.0031 | 0.0106 | 195161 |
| Ø8 | 580 | 667 | 0.0030 | 0.0105 | 193600 |

## 3.6.3 Ultra-High Performance Fiber Reinforced Concrete

### 3.6.3.1 Components of UHPFRC mixture

UHPFRC composition consists of a combination of cementitious materials such as Portland cement and silica fume, fine aggregate, high-range water reducing admixtures, fibers and water. Depending on its application and use, different dosages of these materials can be used. UHPFRC was prepared in Concrete Lab of KFUPM with the help of the planetary mixer.

### Cement

In UHPFRC mixture, Type I ordinary Portland cement with a specific gravity of 3.15 was used. The chemical composition of used cement is given in Table 3-6.

### Silica Fume

Silica fume is mineral additive, acts chemically as a highly reactive pozzolan due to its fineness, and physically optimize the particle packing density. It was obtained from the local suppliers Elkem. Elkem is the Norway’s largest industrial company and Elkem

Materials is the world largest suppliers of Micro-Silica. Elkem micro-silica is a byproduct of silicon and ferrosilicon alloy obtained from the carbothermic reduction quartz and quartzite in the electric furnace with a specific gravity of 2.25. The chemical composition of Elkem micro-silica obtained from product data sheet is given in Table 3-6.

**Table 3-6 Chemical Composition of Cement and Silica fume**

| **Constituents** | **% by mass** | |
|---|---|---|
| | **Type I Cement** | **Silica Fume** |
| CaO | 64.35 | 0.48 |
| $SiO_2$ | 22.00 | 92.5 |
| $Al_2O_3$ | 5.64 | 0.72 |
| $K_2O$ | 3.80 | 0.84 |
| MgO | 2.11 | 1.78 |
| $Na_2O$ | 0.19 | 0.5 |
| Equivalent alkalies Na2O + 0.658K2O | 0.33 | - |
| Loss on Ignition | 0.7 | 1.55 |
| C3S | 55 | - |
| C2S | 19 | - |
| C3A | 10 | - |
| C4AF | 7 | - |

## Aggregate

Dune sand with a specific gravity 2.56 was used as fine aggregate in the mixture. The absorption value was 0.4 %. The grading of the sand used is given in Table 3-7.

**Table 3-7 Sieve analysis of fine aggregate**

| ASTM sieve Number | Sieve size | Percentage Passing |
|---|---|---|
| # | mm | % |
| 4 | 4.75 | 100 |
| 8 | 2.36 | 100 |
| 16 | 1.18 | 100 |
| 30 | 0.6 | 75 |
| 50 | 0.3 | 10 |
| 100 | 0.15 | 5 |

### Superplasticizer

Polycarboxylic ether based new generation high range water reducing/superplasticizer concrete admixture named as Master Glenium®51, the product of chemical company BASF, was used as HRWR agent which is consistent with ASTM C494 Type F. Its color is amber and structure is polycarboxylic ether based. Its density varies from 1.082 – 1.142 Kg/liter. Chloride contents are less than 0.1% as per EN 480-10 and alkaline contents are less than 3% as per EN 480-12.

### Steel Fibers

Steel fibers with two different shapes in equal ratio were used in UHPFRC mixture having a different role in improving the properties of the fresh and hardened mixture. Shapes of steel fibers affect the ductility, crack bridging, energy dissipation around the crack, and workability. To improve the quality of mixture, hooked end and straight fibers were used in the ratio of 1:1. The product name of straight fibers is Micro Steel Fibers. Micro Steel

Fibers had 0.2 mm diameter, 13 mm length and aspect ratio of 65 with tensile strength more than 2500 MPa. The product name of hooked end fibers is Brass Coated Hooked End Fibers. These fibers were 0.35 mm in diameter, 25 mm in length and had an aspect ratio of 71 with tensile strength more than 2500 MPa.

The components of UHPFRC mixture are shown in Figure 3-32

**Figure 3-32 Constituents of UHPFRC mixture**

### 3.6.3.2 UHPFRC mixture design

UHPFRC mixture was prepared by using the mixture design developed by Hakeem et al. (2011) [42]. The strengthening material utilized in repairing and strengthening of damaged and undamaged specimens, had the composition per cubic meter as follows: ASTM Type I Portland cement 900 kg; Elkem Micro-silica 220 kg, dune sand 991 kg; steel fibers 157 kg (about 2% by volume of UHPFRC); 40.3 kg Master Glenium®51 and water 168 kg representing water-binder ratio of 0.15. The UHPFRC mixture design yielded compressive strength more than 170 MPa on 50 mm cube and flexural strength exceeding 31 MPa.

#### 3.6.3.3 UHPFRC mixture Preparation

Locally developed and optimized mixture was used for strengthening and repairing of all BCJ specimens. Special equipment and procedure were used for the preparation of UHPFRC mixture. For the preparation of strengthening material, a high shear capacity mixer was required. The casting of UHPFRC was carried out in Concrete Lab, using horizontal pan mixer and average flow diameter was measured using flow table test, as shown in Figure 3-33.

Following procedure was adopted for the preparation of strengthening material

- Weight the superplasticizer and water in the start and mix them. Leave this mix for around 20 minutes.
- Start weighing the remaining components in the order of lighter component first followed by heavier components. This precaution is taken in order to avoid the loss of material due to the spilling of constituents in dry mixing.
- Put these constituents one after the other into the mixing drum except fiber which was added at the end.
- Run the mixer for 2-3 minutes for dry mixing.
- Add 50% of water and superplasticizer mix with small discharge so that it can be thoroughly mixed rather than being concentrated and forming the lumps.
- Note the time when water and superplasticizer mix is added.
- Keep monitoring the mix for observing the sign of cohesiveness
- After 8-10 minutes of first pouring of water and HRWR agent mix, add 20 % more of this mix into the mixing drum.

- Around 13 minutes of first addition of water and HRWR agent mix, signs of the cohesive mix will be prominent and moisture traces will be visible in the mixture. Now add remaining water and HRWR agent mix and mix them for another 2 minutes. The mixture will start to flow at this stage.
- Dispense the steel fibers into the matrix and keep mixing for another 3-5 minutes until all fibers seem to be evenly mixed. The UHPFRC mixture is ready to perform spread flow test and strengthening the BCJs.

**Figure 3-33 Planetary mixer (Left), UHPFRC mixture (Center) Flow Table Test (Right)**

#### 3.6.3.4 Trial Mixes

UHPFRC jacketing around all sides of BCJ specimens was one of the challenging tasks due to lower water-binder ratio. Four trial mixes had been prepared using the mixture design developed by Hakeem et al. (2011) [42] to obtain the maximum spread flow without compromising the mechanical properties. The variable parameters in these mixtures were the dosage of super plasticizers and water-binder ratio. Spread flow values were determined through flow table test and compression strength test was conducted on 50 mm cubes. For this purpose, UHPFRC mixture was prepared and 50 mm cubes were cast, as shown in Figure 3-34. Trial mixtures were tested for consistency. ASTM C1437 standard test method for measuring the flow of hydraulic cement was used to comply with the recommendation outlined in Ductal reference TOO6 (Operating Procedure Flow Test). For this, the mini cone was filled with the mixture and removed slowly to allow the mixture to flow evenly on the table and then flow table was dropped 20 times and its average flow diameter was recorded, as shown in Figure 3-34.The compression strength test was conducted on 50 mm cubes. The details of these mixes and test results are given in Table 3-8.

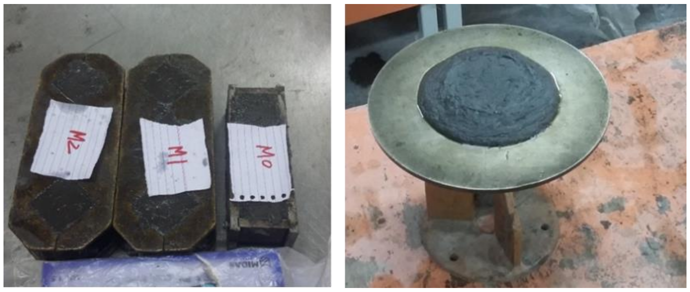

**Figure 3-34 Casting of cubes (Left) and Flow table test (Right)**

**Table 3-8 Average flow diameter and compressive strength of trial mixes**

| **Mix No.** | **Water-Binder ratio** | **Dosage of superplasticizer** | **Avg. flow diameter** | **Cube Compressive Strength** | | | **Avg. Compressive Strength** |
|---|---|---|---|---|---|---|---|
| | | % | mm | MPa | MPa | MPa | MPa |
| 1 | 0.145 | 3.6 | 162 | 170 | 169 | 167 | 168.67 |
| 2 | 0.15 | 3.6 | 170 | 165 | 162 | 157 | 161.33 |
| 3 | 0.145 | 3.7 | 180 | 156 | 149 | 144 | 149.67 |
| 4 | 0.15 | 3.7 | 190 | 139 | 150 | 140 | 143 |

Mixture # 2 had been selected for the preparation of strengthening the material. As these mixtures had been prepared in small mixers, so these properties such as Avg. flow diameter and cube compressive strength would be enhanced when they were prepared in big horizontal pan mixers as described in section 3.6.3.2. The procedure used for the preparation of UHPFRC mixture had already been described in section 3.6.3.3.

### 3.6.3.5 Evaluation of mechanical properties of UHPFRC

Compressive strength test on cubes and cylinders, uniaxial tensile strength test on dog-bones and flexural strength test on prisms had been performed to determine the characteristics of retrofitting material,

#### 3.6.3.5.1 Compressive Strength and Modulus of Elasticity

For determining the stress-strain behavior of UHPFRC under compression, three cylinders of 75 mm diameter and 150 mm height were tested according to ASTM C39 using the setup, as explained in section 2.6.1.1 and shown in Figure 3-36. The strength of UHPFRC is more than Sulphur, so for the smoothness of ends, if Sulphur capping is done will result in the failure of capping before the failure of UHPFRC. Therefore, sulphur capping will not work for this material. One side of the cylinder was made smooth by cutting a thin layer of rough surface with the help of an electrical cutter. The results of compression testing on cubes and cylinders is presented in Table 3-9 and Table 3-10, respectively. Figure 3-35 displays the average stress-strain behavior of UHPFRC under compression. Figure 3-36 shows the failure mode of cubes and cylinder of UHPFRC under compression.

**Table 3-9 Cube compressive strength of UHPFRC**

| Specimen ID | Compressive strength | Average Cube Compressive Strength |
|---|---|---|
| | MPa | MPa |
| Cube 1 | 170 | 170.33 |
| Cube 2 | 171 | |
| Cube 3 | 171 | |

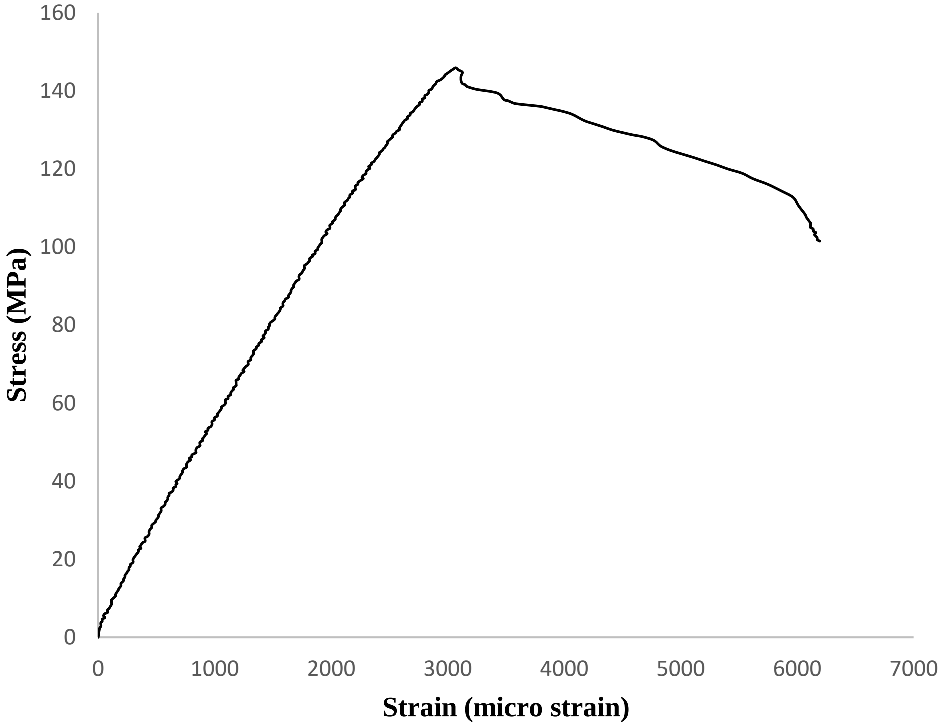

**Figure 3-35 Stress-Strain behavior of UHPFRC under compression**

**Figure 3-36 Test set-up for Compressive strength test (left) and Failure modes of specimens (right)**

The load-deformation data acquired from compression testing was used to determine the modulus of elasticity of UHPFRC according to ASTM C469. The procedure and equations adopted to determine the MOE as per ASTM C469 discussed in detail in section 2.6.1.2. The test results of MOE is presented in Table 3-10.

**Table 3-10 Compressive strength test results of UHPFRC**

| Specimen ID | Compressive strength | Average Cylinder Compressive Strength | MOE | Average MOE |
|---|---|---|---|---|
| | MPa | MPa | GPa | GPa |
| Cylinder 1 | 145.9 | 145.1 | 52.9 | 52.4 |
| Cylinder 2 | 140.8 | | 49.7 | |
| Cylinder 3 | 148.6 | | 54.6 | |

#### 3.6.3.5.2 Flexural strength or Modulus of Rupture

Flexural strength of concrete was commonly represented by a parameter named as modulus of rupture. According to ASTM C78, four points flexural loading was applied on the prism having size 40x40x160 mm. The test was performed using Instron 1196 Universal testing machine with a maximum capacity of 250 kN. LVDT was placed at the center of prism for measuring the mid-span deflection. Figure 3-37 displays the complete test setup for finding the flexural strength. The test was displacement control and the load was applied at the rate of 0.5 mm/minute. The load-deflection data was recorded using TDS-303 portable data logger. Figure 3-38 shows the load-deflection response of prism specimen under four point flexural loading. MOR was calculated using Eq. 3.4 and the results are presented in Table 3-11.

$$R = \frac{PL}{b\,d^2} \tag{3.4}$$

where:

$R =$ Split tensile strength (MPa)

P = Peak load (N)

$L =$ Length (mm)

b = Width of prism (mm)

d = Depth of prism (mm)

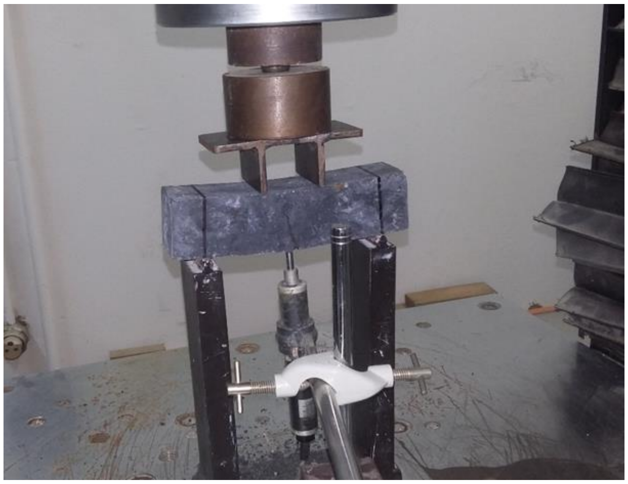

Figure 3-37 Test setup for flexural strength test of UHPFRC

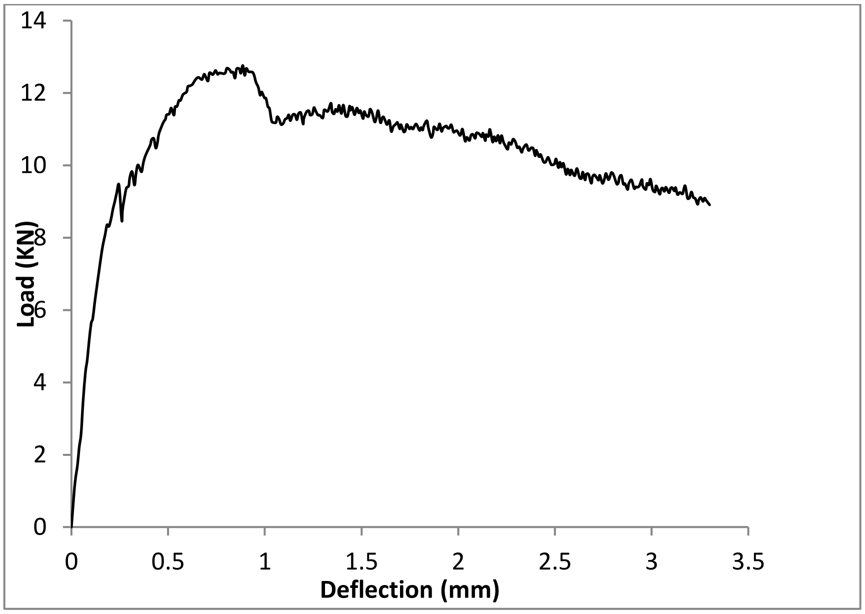

Figure 3-38 Load-deflection response of prism under four point bending

Table 3-11 Modulus of rupture of UHPFRC

| Specimen ID | Modulus of Rupture | Average Modulus of Rupture |
|---|---|---|
| | MPa | MPa |
| Prism 1 | 31.9 | 31.22 |
| Prism 2 | 30.34 | |
| Prism 3 | 31.43 | |

### 3.6.3.5.3 Direct tensile test

The direct tensile test was executed on dog-bone specimens to characterize the retrofitting material in tension. The specimen geometry is shown in Figure 3-39. The direct tensile test was performed using Instron 5589 Universal testing machine available in structural mechanics lab of KFUPM. Figure 3-39 shows the complete test setup. The concrete is characterized by average direct tensile strength of 8.51 MPa. Figure 3-40 displays the stress-strain behavior of retrofitting material under uniaxial tensile loading. Stress-strain behavior highlighted the growth of micro cracking up to 2000 μϵ. After peak stress, strain value represented the crack mouth opening. Stress-strain behavior highlighted strain hardening up to 2000 μϵ followed by stable and gradually degrading softening behavior.

**Figure 3-39 Test setup for direct tensile strength test**

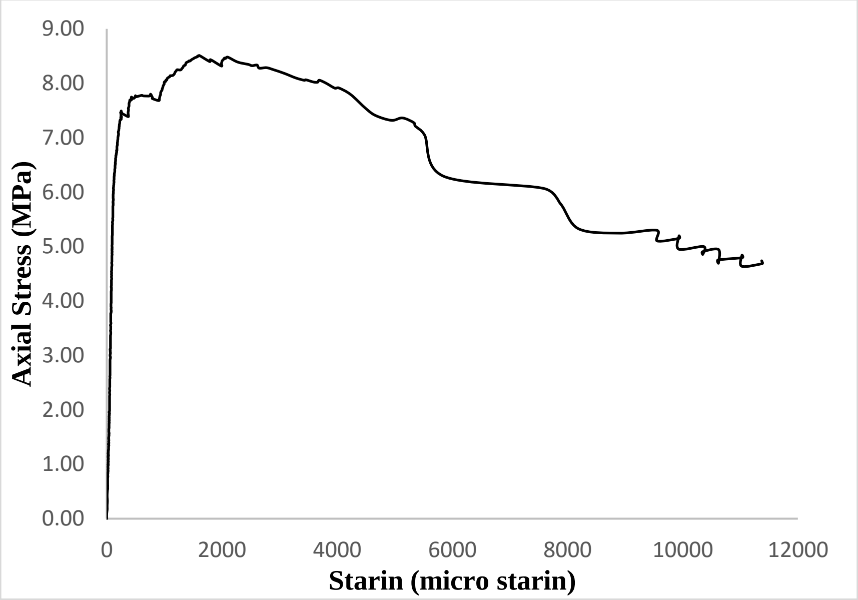

**Figure 3-40 Stress-strain behavior of UHPFRC under tension**

### 3.6.4 Sikadur® -32 LP

For upgrading the BCJ sub-assembly, pre-fabricated UHPFRC plates were attached to NCSS using Sikadur®-32 LP. It is available in 5kg (A+B) package, as shown in Figure 3-41. It is 2-part structural epoxy bonding agent and adhesive for concrete elements. The mechanical properties, as given in product data sheet are described in Table 3-12

**Figure 3-41 Packaging of Sikadur® -32 LP**

**Table 3-12 Mechanical properties of epoxy primer**

| Properties | Curing time | Curing temperature | | |
|---|---|---|---|---|
| | | +23$^0$C | +30$^0$C | +40$^0$C |
| Compressive Strength (MPa) | 14 days | ~39 | ~43 | ~56 |
| Flexural strength (MPa) | 14 days | ~38 | ~38 | ~42 |
| Tensile Strength (MPa) | 14 days | ~22 | ~24 | ~25 |
| Bond Strength (MPa) | 7 days | >3 | - | - |
| Tensile E-modulus (MPa) | 14 days | ~2750 | - | - |
| Flexural E-modulus (MPa) | | ~2600 | | |
| Compressive E-modulus (MPa) | | ~2100 | | |

## 3.7 Test setup details

A special test setup and devices were designed and mounted to achieve the idealized boundary and loading conditions as much as possible to which BCJ was subjected during ground motion. So, for simulating the three inflection points in the actual structure, as shown in Figure 3-42, moment release was provided at the top and bottom end of columns and at the end of the beam. Figure 3-43(a) and (b) shows the deformed shape of BCJ sub-assemblies under seismic shocks. Figure 3-43(a) represents the deformed shape of BCJ sub-assemblages when the structure is subjected to ground movement from right to left. However, Figure 3-43(b) accounts for the deformed shape of BCJ sub-assemblages when the structure is subjected to ground movement from left to right ignoring the P-Δ effect which does not affect the performance of BCJ as per ACI 318-14.

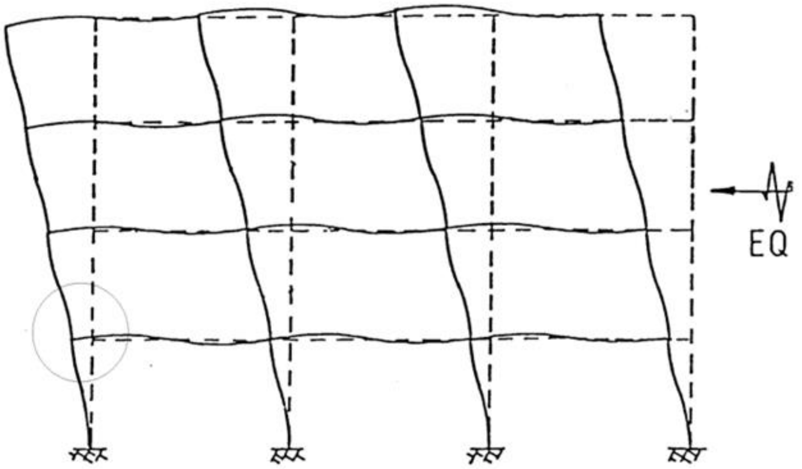

**Figure 3-42 Deformed shape of RC frame under seismic activity**

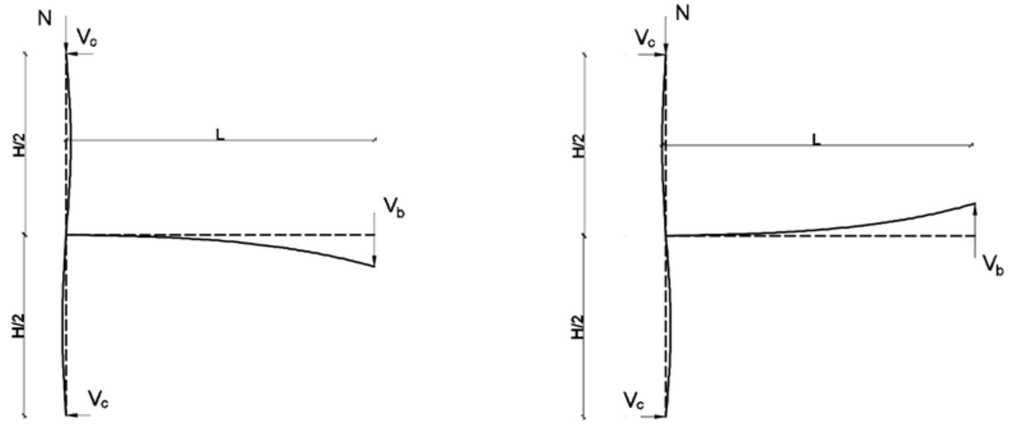

(a) (b)

**Figure 3-43 Idealized BCJ sub-assemblages**

Figure 3-44 shows the schematic view of test specimen inside the self-reaction steel loading frame with the loading apparatus and load measuring devices mounted to characterize the performance of specimens in its original state. The test specimens were loaded in the vertical position to simulate the real-time event as earthquake resulted in a repeated and an alternating tensile and compressive stresses in the structural elements which were achieved by the application of alternate push and pull at the beam tip. The specimen was held in place by pin supports at the top and the bottom ends of the column through steel rods and plates. The BCJ sub-assemblies were tested under a displacement control multipurpose testing system with a loading capacity of 1200 kN and 300 kN in the vertical direction. For specimens of group 1, CAL of different magnitude according to their loading protocol and for specimens of group 2, CAL of 150 kN (10% of column axial load capacity) was applied at the start of test by using the Hydraulic Jack A of capacity 1200 kN positioned between the column top end and load cell A, which had a direct contact with steel loading frame. The lower column was fixed to strong epoxy coated floor by a pin support. CAL load was measured through Load Cell A placed over the hydraulic jack A. The cyclic load was applied at the end of the beam using Hydraulic Jack B of 300 kN capacity. The hydraulic jack was mounted vertically and reacted against a steel frame from one end and applied load through steel plates. Two load cells labeled as Load Cell B and Load Cell C were used between the face of beam and load transferring element of Hydraulic Jack B for measuring the reaction developed at beam tip in push and pull actions.

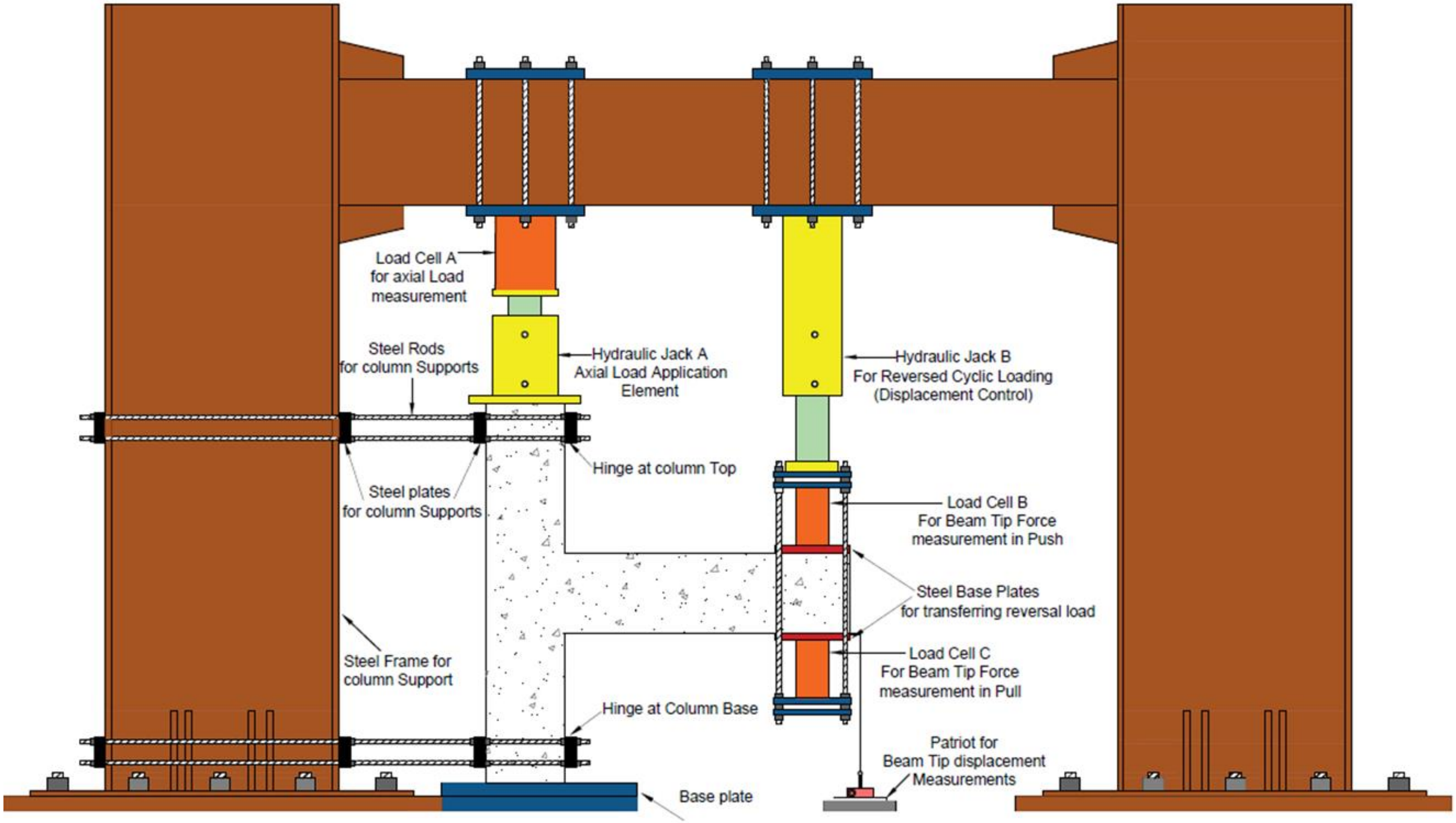

**Figure 3-44 Schematic view of Test setup**

## 3.8 Instrumentation

### 3.8.1 Introduction

Test units were highly equipped with external and internal instruments to monitor beam shear and column axial forces, beam tip displacement, the global translation of the system, strains in concrete, strains of reinforcing bars and crack monitoring. Beam shear and column axial forces were applied through hydraulic jacks and monitored through load cells. Beam tip displacement was captured through Linear motion transducer, steel, and concrete strain gauges were mounted to monitor strains in UHPFRC and steel reinforcement, the global motion of the complete system was captured through LVDT's mounted at the top and bottom end of the column and crack mouth opening was measured using LVDT's and displacement transducers.

### 3.8.2 Beam Shear and column axial Forces

The two hydraulic jacks of capacity 1200 kN and 300 kN were used to apply column axial load and beam shear force, respectively. Hydraulic jack used to apply force at beam tip was operated under displacement control. However, hydraulic jack A for column axial load was driven by force control. These forces were monitored through load cells. Three load cells were used to measure column axial and beam shear forces. These load cells were calibrated before testing. The capacities of load cell A, B, and C are 200 tf, 100 tf and 50 tf, respectively. Figure 3-44 displays the location of these load cells in the test setup.

### 3.8.3 Beam tip displacement

Beam tip displacement, which was used to plot load-displacement response of test units or hysteresis behavior of specimen, was monitored through linear motion string transducer manufactured by Patriot Sensors and Controls Corporation.

### 3.8.4 Global translation

The global translation was monitored through two LVDT's which were installed at steel plates used in hinge support system at the top and bottom ends of columns, as shown in Figure 3-45. The readings of these LVDT's were subtracted from the imposed displacement monitored through string transducer to find the actually imposed displacement at beam tip.

### 3.8.5 Joint Shear deformation and crack monitoring

To measure shear deformations in the joint, in addition to strain gauges, two LVDT's were installed diagonally on the joint front and back face in case of a reference specimen, designated as TC. However, for upgraded specimens, these LVDT's were shifted to the beam-joint interface to monitor the crack mouth opening. So, two different arrangements of LVDT's were adopted for reference and upgraded specimens, as shown in Figure 3-45 and Figure 3-46, respectively. In the case of upgraded units, crack opening was monitored through two LVDT's and two TML PI-2-50 displacement transducers which were mounted to the beam-joint interface, as shown in Figure 3-46 (a) and (b). Figure 3-45 shows the setup for reference specimen and Figure 3-46 shows the set up for the upgraded specimens. The differences between two instrumentations were the location of LVDT's and the use of displacement transducers for crack monitoring which were not used for reference specimen.

### 3.8.6 Concrete Strain gauges

A total of 11 concrete strain gauges were mounted on each specimen to measure the deformations and strains in the concrete at critical locations, as shown in Figure 3-45 and Figure 3-46. Of these, two concrete strain gauges were mounted in the vertical direction on the front and back face of the top column to ensure the concentric application of axial load, as far as possible because P-Δ had not been considered in the present research work. The joint area was gauged with four strain gauges mounted diagonally, at the front and back face of joint, to monitor the shear deformation and strains. Top and bottom faces of the beam near the joint area which is the most crucial flexural zone were gauges with two strain gauges. One concrete strain gauge was mounted at the face of column opposite to beam to measure the strain at the onset of reinforcement rotation or slip.

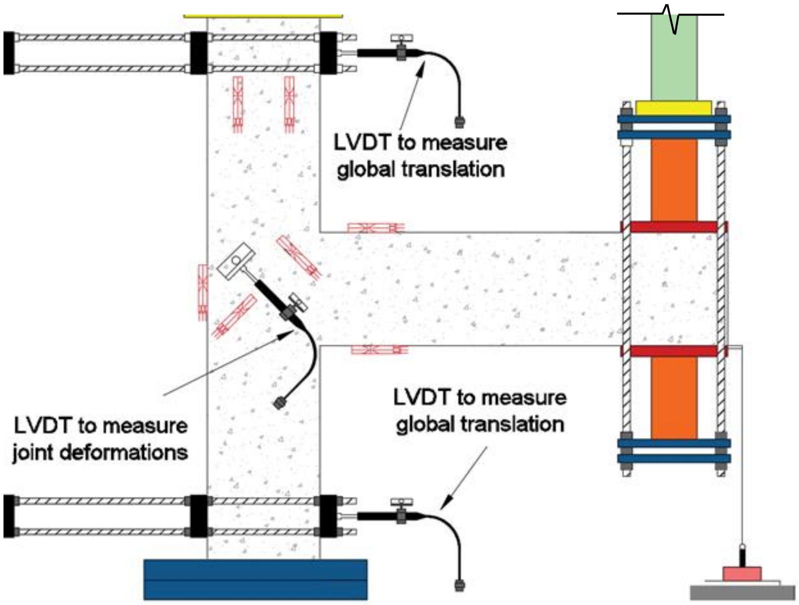

**a) Front view**

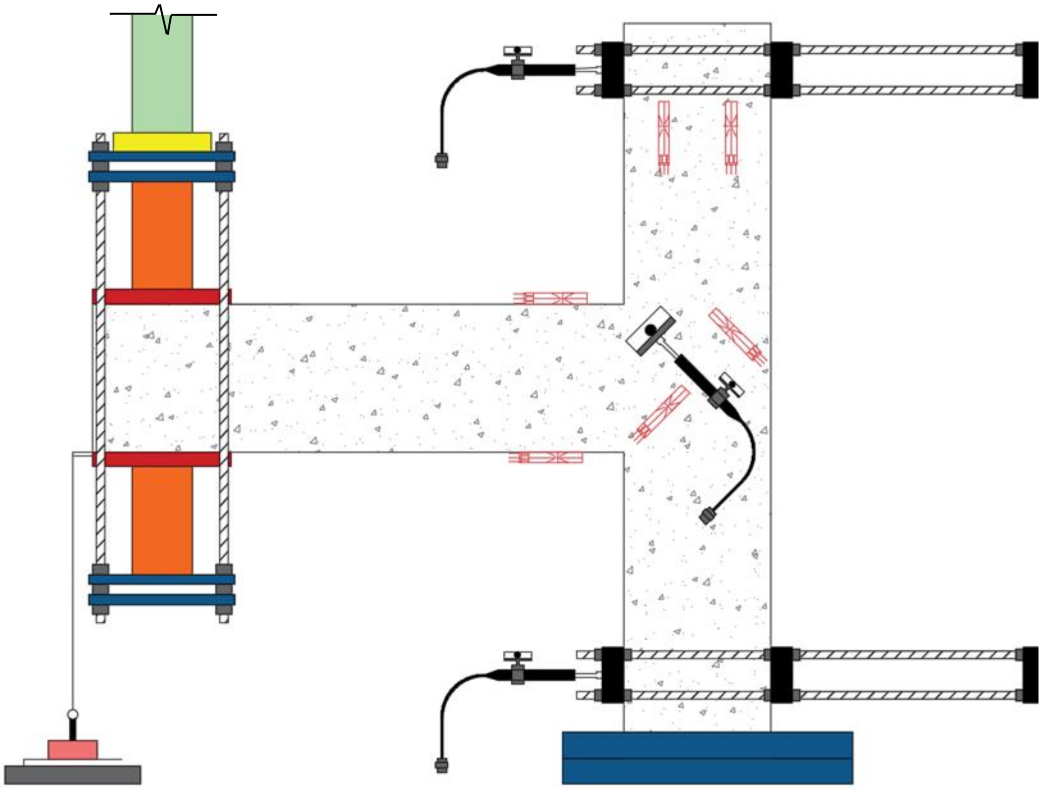

**b) Back view**

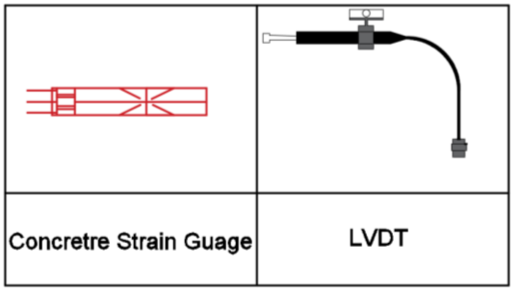

Figure 3-45 Schematic diagram of external instrumentation of control specimen

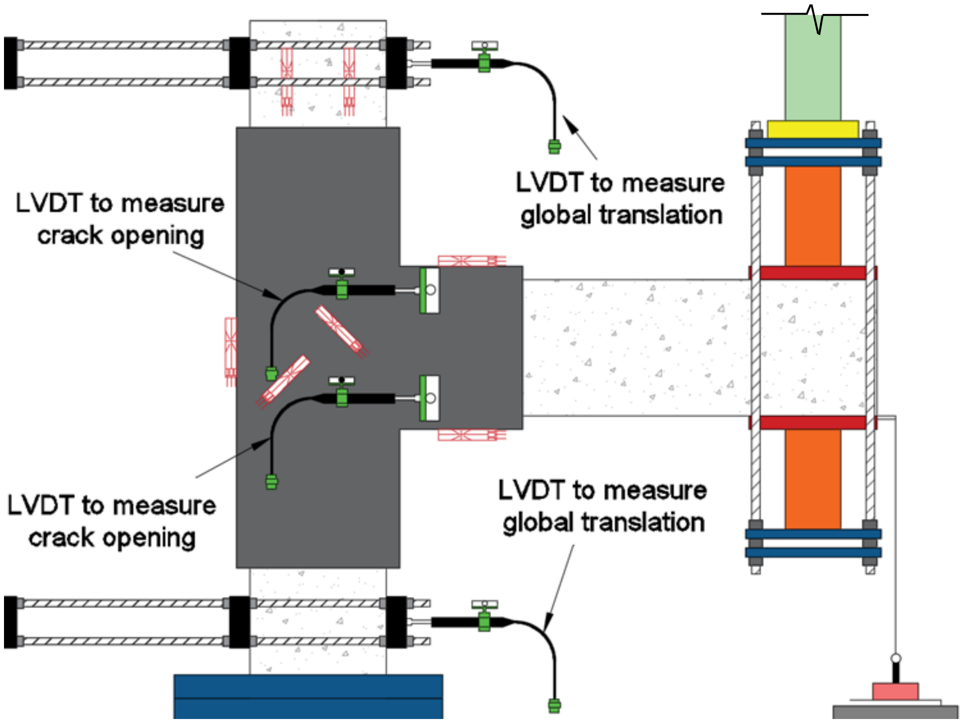

a) **Front view**

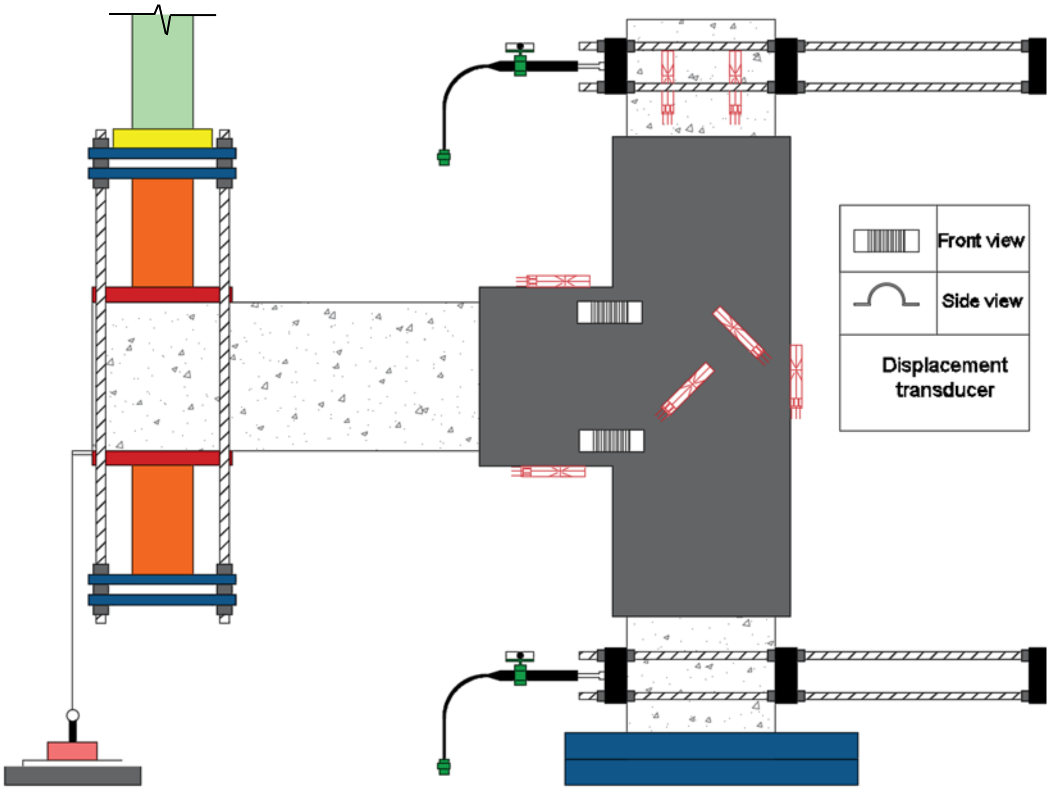

b) **Back view**

**Figure 3-46 Schematic diagram of external instrumentation of upgraded specimen**

### 3.8.7 Steel strain gauges

A total of seven strain gauges with 120 Ω electrical resistance were installed on longitudinal and transverse reinforcement of beam and column longitudinal reinforcement. Strain gauges were attached by means of super glue and covered them using waterproof tape to avoid their damage from water and protect them from the impact of aggregates and vibrator during casting. Among the beam reinforcement, four strain gauges were installed at the beam top and bottom reinforcement which is the most crucial flexural zone for beam reinforcement to investigate the onset and propagation of the yielding to judge the failure mechanism. Only one stirrup was instrumented with one strain gauge at the shear critical section of the beam because shear failure was not expected to occur in the beam. Column longitudinal bars were equipped with strain gauges just above and below the joint, a critical flexural zone for column's reinforcement. Figure 3-47 displays the layout of strain gauges on the column and beam's reinforcement.

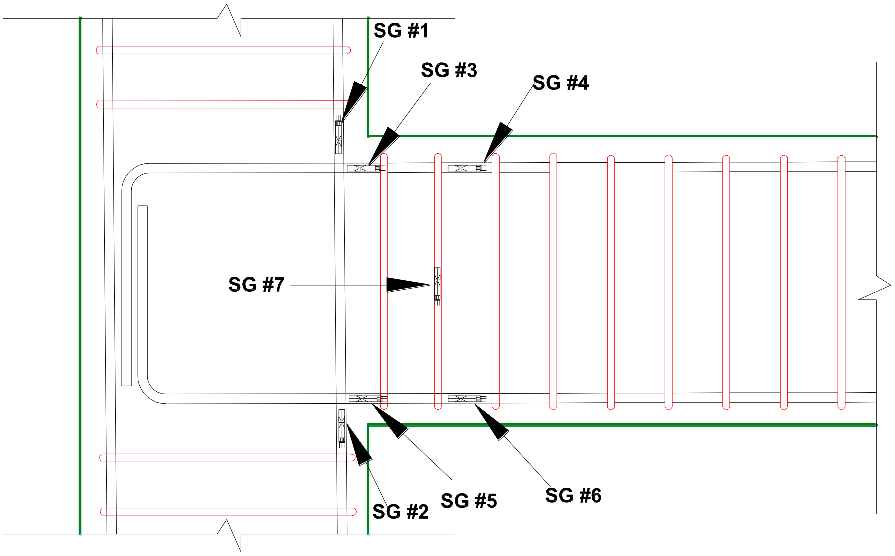

**Figure 3-47 Layout of Steel strain gauges on Column and beam's reinforcement**

## 3.9 Test Program

The experimental program consisted of two groups. Group 1 consisted of three damaged specimen retrofitted using UHPFRC-jacket and tested under monotonic loading for evaluating the efficiency of UHPFRC-jacket in repairing the damaged specimens in terms of strength, stiffness, ductility and energy dissipation capacity. However, group 2 consisted of four specimens and tested under the reversed cyclic loading to simulate the seismic activity.

### 3.9.1 Loading history for specimens of group 1

The same loading history and axial load in the column used for testing the virgin specimens were implemented for testing the repaired units. Three repaired specimens SP1-R, SP2-R and SP3-R with same retrofitting scheme were subjected to a different magnitude of the axial load on column according to axial load protocol, as tabulated in the Table 3-13. Incremental displacement amplitudes were applied at the free end of the beam until the load dropped to 75% of its peak value.

**Table 3-13 Loading history for Group 1**

| **Sr. No.** | **Specimen ID** | **Magnitude of Axial Load** | **Axial Load ratio** |
|---|---|---|---|
| | | kN | $\frac{\boldsymbol{N}}{\boldsymbol{A_g\, f'_c}}$ |
| 1 | SP1-R | 0 | 0.00 |
| 2 | SP2-R | 200 | 0.19 |
| 3 | SP3-R | 600 | 0.57 |

### 3.9.2 Loading history for specimens of group 2

Group 2 consisted of four specimens. Of these, three specimens were strengthened using UHPFRC-jacket before application of load, designated as TS1, TS2, and TSE. The fourth specimen was used as a reference specimen, labeled as TC. To simulate the seismic simulation, the loading protocol for this group comprised of simultaneous column constant axial load of 150 kN, corresponding to 10% of the nominal axial strength of column, and reversed cyclic loading applied at the free end of the beam through a hydraulic jack mounted on the self-reaction frame. The axial load in the column was maintained at the required level throughout the loading phase by adjusting the hydraulic pressure imposed by a hydraulic jack. The displacement-controlled cyclic load was applied slowly to eliminate dynamic effect until the failure of the specimen or up to the yielding of longitudinal reinforcing bars. The displacement-controlled loading pattern consisted of a sequence of cycles with target drift reversals indicated as a function of drift ratio, defined as the percentage of imposed displacement at beam free end to the length of the beam, according to loading history, as shown in Figures 3-48 and Figures 3-49. All cycles were started with the push direction first then went into the pull direction. There were two loading patterns adopted under reverse cyclic loading. Figure 3-48 and Table 3-14 represent the loading history used for units TC, TS2 and TSE, where $d_b$ is the imposed displacement at the free end of the beam and $d_b^P$ is the peak displacement for the corresponding cycle. Figure 3-49 and Table 3-15 show the loading history used for unit TS1. These two loading patterns were same up to drift of ~±5%. Specimens TC, TS2, and TSE were loaded up to drift of ~±5%. However, specimen TS1 was loaded up to drift of 8.7%, until the yielding of the longitudinal reinforcement.

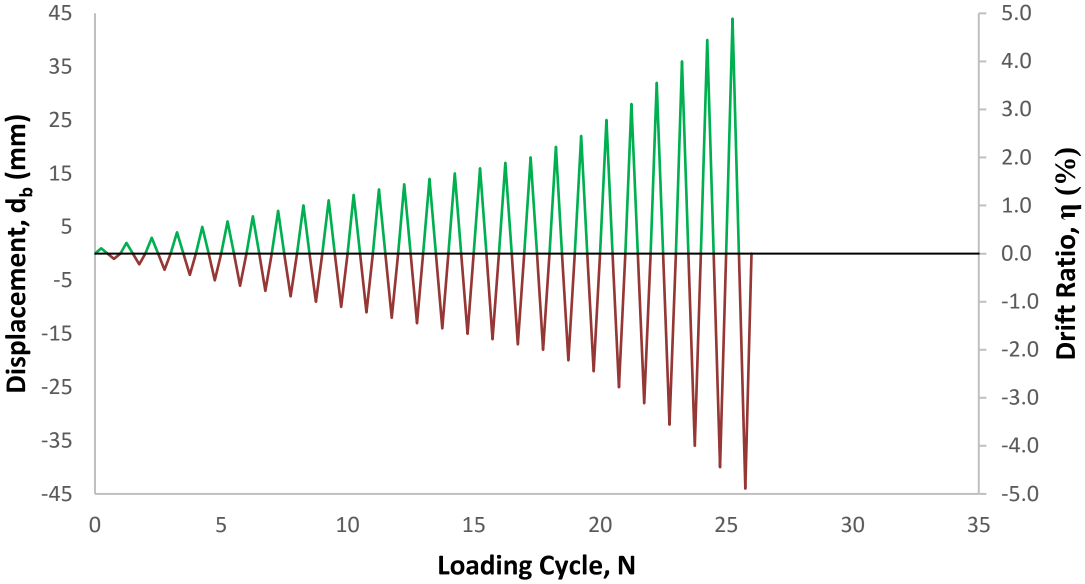

Figure 3-48 Loading protocol adopted for specimens TC, TS2 and TSE

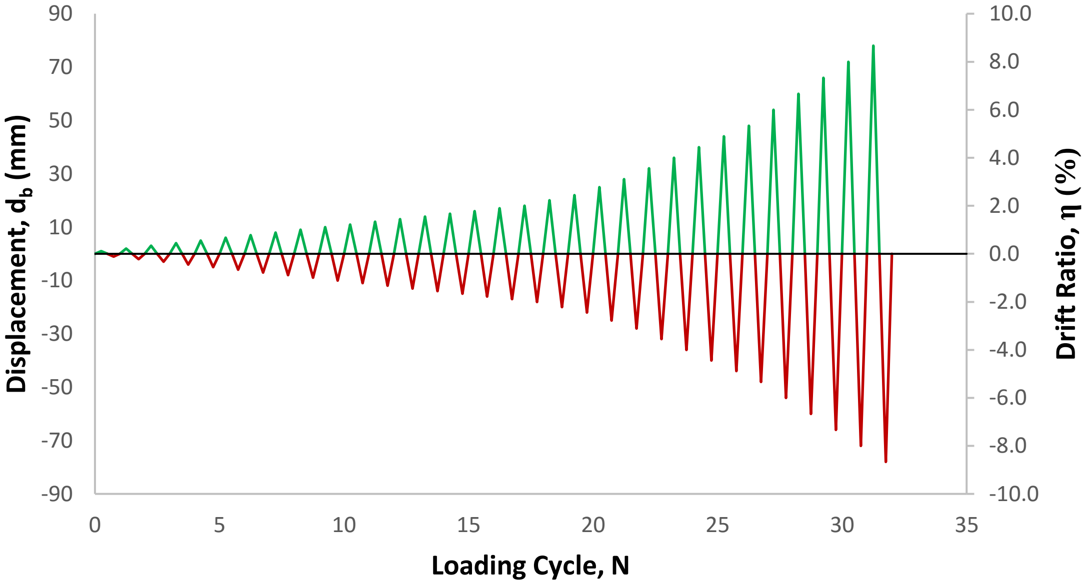

Figure 3-49  Loading protocol adopted for specimens TS1

**Table 3-14 Loading history adopted for specimens TC, TS2 and TSE**

| Loading Cycle, N | $d_b^P$ | Max drift, η |
|---|---|---|
| | mm | % |
| 1 | ±1 | 0.11 |
| 2 | ±2 | 0.22 |
| 3 | ±3 | 0.33 |
| 4 | ±4 | 0.44 |
| 5 | ±5 | 0.56 |
| 6 | ±6 | 0.67 |
| 7 | ±7 | 0.78 |
| 8 | ±8 | 0.89 |
| 9 | ±9 | 1.00 |
| 10 | ±10 | 1.11 |
| 11 | ±11 | 1.22 |
| 12 | ±12 | 1.33 |
| 13 | ±13 | 1.44 |
| 14 | ±14 | 1.56 |
| 15 | ±15 | 1.67 |
| 16 | ±16 | 1.78 |
| 17 | ±17 | 1.89 |
| 18 | ±18 | 2.00 |
| 19 | ±20 | 2.22 |
| 20 | ±22 | 2.44 |
| 21 | ±25 | 2.78 |
| 22 | ±28 | 3.11 |
| 23 | ±32 | 3.56 |
| 24 | ±36 | 4.00 |
| 25 | ±40 | 4.44 |
| 26 | ±44 | 4.89 |

**Table 3-15 Loading history adopted for specimens TS1**

| Loading Cycle, N | $d_b^P$ | Max drift, η |
|---|---|---|
| | mm | % |
| 1 | ±1 | 0.11 |
| 2 | ±2 | 0.22 |
| 3 | ±3 | 0.33 |
| 4 | ±4 | 0.44 |
| 5 | ±5 | 0.56 |
| 6 | ±6 | 0.67 |
| 7 | ±7 | 0.78 |
| 8 | ±8 | 0.89 |
| 9 | ±9 | 1.00 |
| 10 | ±10 | 1.11 |
| 11 | ±11 | 1.22 |
| 12 | ±12 | 1.33 |
| 13 | ±13 | 1.44 |
| 14 | ±14 | 1.56 |
| 15 | ±15 | 1.67 |
| 16 | ±16 | 1.78 |
| 17 | ±17 | 1.89 |
| 18 | ±18 | 2.00 |
| 19 | ±20 | 2.22 |
| 20 | ±22 | 2.44 |
| 21 | ±25 | 2.78 |
| 22 | ±28 | 3.11 |
| 23 | ±32 | 3.56 |
| 24 | ±36 | 4.00 |
| 25 | ±40 | 4.44 |
| 26 | ±44 | 4.89 |
| 27 | ±48 | 5.33 |
| 28 | ±54 | 6.00 |
| 29 | ±60 | 6.67 |
| 30 | ±66 | 7.33 |
| 31 | ±72 | 8.00 |
| 32 | ±78 | 8.67 |

### 3.9.3 Test loading scheme

Seven specimens were tested under monotonic and reversed cyclic loading protocols. These specimens include control and retrofitted/strengthened specimens. Table 3-16 shows the loading schemes of all specimens.

**Table 3-16 Summary of test loading scheme**

| S. No. | Specimen ID | Description | Magnitude of Axial Load (kN) | Axial Load ratio $\frac{N}{A_g f'_c}$ | Loading Type |
|---|---|---|---|---|---|
| Group 1 | | | | | |
| 1 | SP1-R | Repaired | 0 | 0 | Monotonic |
| 2 | SP2-R | Repaired | 200 | 0.19 | Monotonic |
| 3 | SP3-R | Repaired | 600 | 0.57 | Monotonic |
| Group 2 | | | | | |
| 4 | TC | Control | 150 | 0.1 | Reversed cyclic |
| 5 | TS1 | Strengthened | 150 | 0.1 | Reversed cyclic |
| 6 | TS2 | Strengthened | 150 | 0.1 | Reversed cyclic |
| 7 | TSE | Strengthened | 150 | 0.1 | Reversed cyclic |

# CHAPTER 4

# Experimental Results Observations and Discussions

This chapter presents the experimental investigation of the seismic behavior of damaged and undamaged RC exterior BCJs repaired and strengthened by using UHPFRC jacket. The efficiency of implemented retrofitting scheme is evaluated quantitatively based on the comparisons of hysteretic response, load-displacement envelopes, maximum strength, strength degradation, strains in steel reinforcement, damage evolution and failure modes, secant stiffness characteristics, cumulative energy dissipation capacity and displacement ductility. The effectiveness of the UHPFRC jacket in post-damage repairing of the exterior BCJs evaluated through testing three exterior BCJs (Group #1). Test variable includes the amount of axial load. The efficiency of retrofitting technique in the pre-damage strengthening of exterior BCJs evaluated through testing the four BCJs sub-assemblages (Group #2). Test variable includes the strengthening methods.

## 4.1 Response of repaired specimens under monotonic loading

### 4.1.1 Load-displacement response

Test units SP1-R, SP2-R and SP3-R were rehabilitated with UHPFRC by using the repairing scheme described in section 3.5.1. The retrofitted units SP1-R, SP2-R and SP3-R were subjected to displacement-controlled loading phase with CAL equals to 0 kN, 200 kN and 600 kN, respectively throughout the test. Figures 4-1, 4-2 and 4-3 show the load-displacement response of both virgin and repaired specimens in terms of beam shear and beam tip displacement, registered at the free end of the beam. Retrofitting technique resulted in the successful repairing solution in comparison with the results retrieved by testing the corresponding specimens in the virgin state. For retrofitted specimens, the shape of the curves delineates the behavior of a section comprised of NC core and UHPFRC jacket. The peak value of load corresponds to the maximum tensile strength in the outer fibers of UHPFRC jacket.

### Specimen SP1-R

Figure 4-1 expresses the results of specimens SP1 and SP1-R in terms of beam shear (F) vs. Beam tip displacement (Δ). The test unit SP1-R reached a peak load of 71.37 kN, corresponding to a displacement of 36.41 mm. However, peak value registered for the same specimen in the virgin state was 37.55 kN at a displacement equals to 19.44 mm. In retrofitted specimen, peak load was sustained up to a displacement of 52.1 mm. The load starts decreasing gradually after displacement value 52.1 mm. The retrofitted specimen achieved a strength corresponds to 10% reduction in the peak strength at a displacement of 64.63 mm. The corresponding value for the virgin specimen was 31.52 mm. The load corresponds to which beam longitudinal reinforcement start yielding was found to be 69.56 kN at a displacement of 51.628 mm while the strain in the reinforcement of virgin specimen was well below the yield strain. The residual deflection of the beam tip was reported to be 43.93 mm at the end of testing.

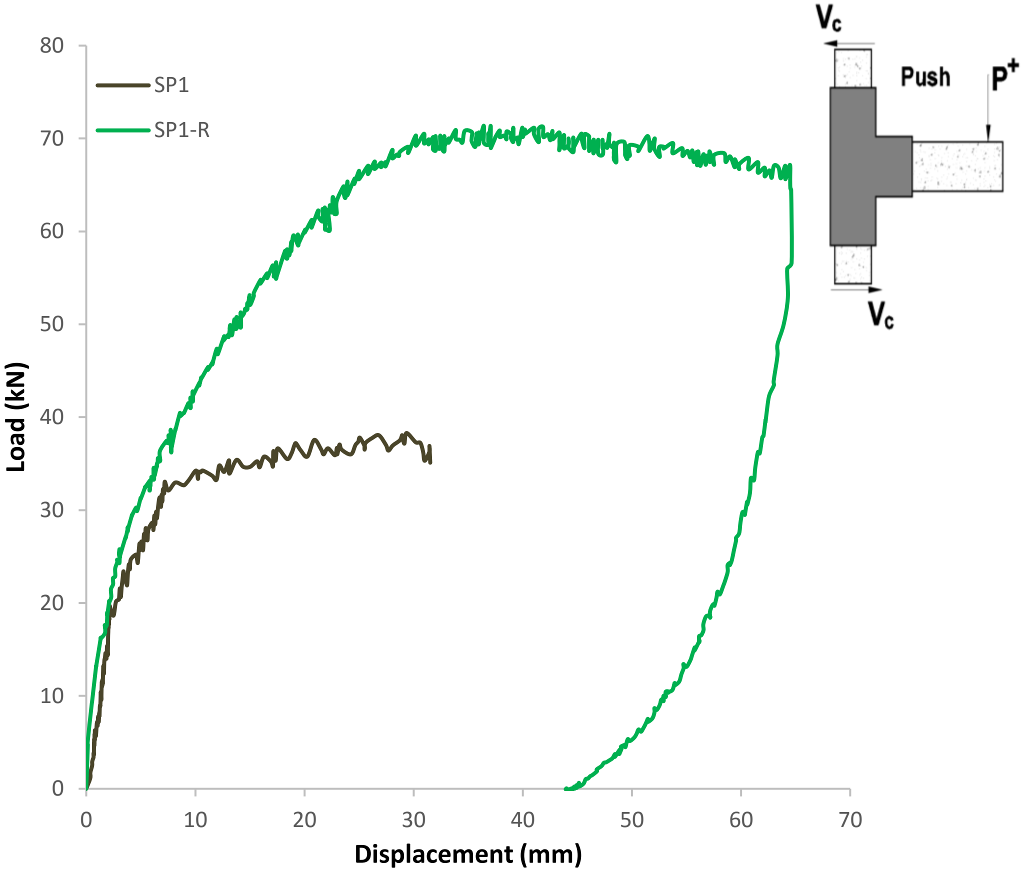

Figure 4-1 Load-displacement response of specimens SP1 and SP1-R

### Specimen SP2-R

Figure 4-2 displays the results of specimens SP2 and SP2-R in terms of beam shear (F) vs. Beam tip displacement (Δ). The test unit SP2-R reached a peak load of 94.19 kN, corresponding to a displacement of 30.433 mm. However, peak value registered for the same specimen in the virgin state was 51 kN at a displacement equals to 19.48 mm. The retrofitted specimen achieved a strength corresponds to 10% reduction in the peak strength at a displacement of 49.8 mm. The corresponding value for the virgin specimen was 28.66 mm. The load corresponds to which beam longitudinal reinforcement start yielding was found to be 79.71 kN at a displacement of 55.657 mm while the strain in the reinforcement of virgin specimen was well below the yield strain. The residual deflection of the beam tip was reported to be 43.12 mm at the end of testing.

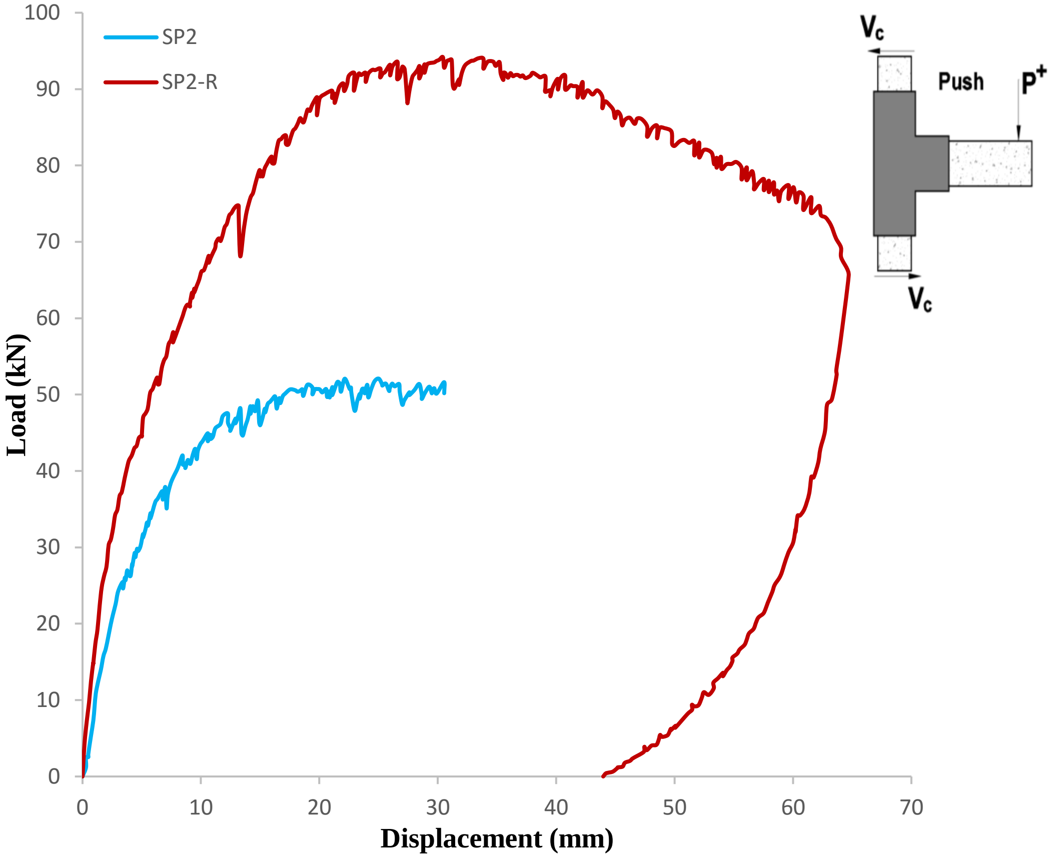

**Figure 4-2 Load-displacement response of specimens SP2 and SP2-R**

### Specimen SP3-R

Figure 4-3 depicts the results of specimens SP3 and SP3-R in terms of beam shear (F) vs. Beam tip displacement (Δ). The test unit SP3-R reached a peak load of 106.62 kN, corresponding to a displacement of 28.307 mm. However, peak value registered for the same specimen in the virgin state was 56.87 kN at a displacement equals to 17.86 mm. The retrofitted specimen achieved a strength corresponds to 10% reduction in the peak strength at a displacement of 52.7 mm. The corresponding value for the virgin specimen was 30.952 mm. The load corresponds to which beam longitudinal reinforcement start yielding was found to be 101.28 kN at a displacement of 37.1 mm while the strain in the reinforcement of virgin specimen was well below the yield strain. The residual deflection of the beam tip was reported to be 52.53 mm at the end of testing.

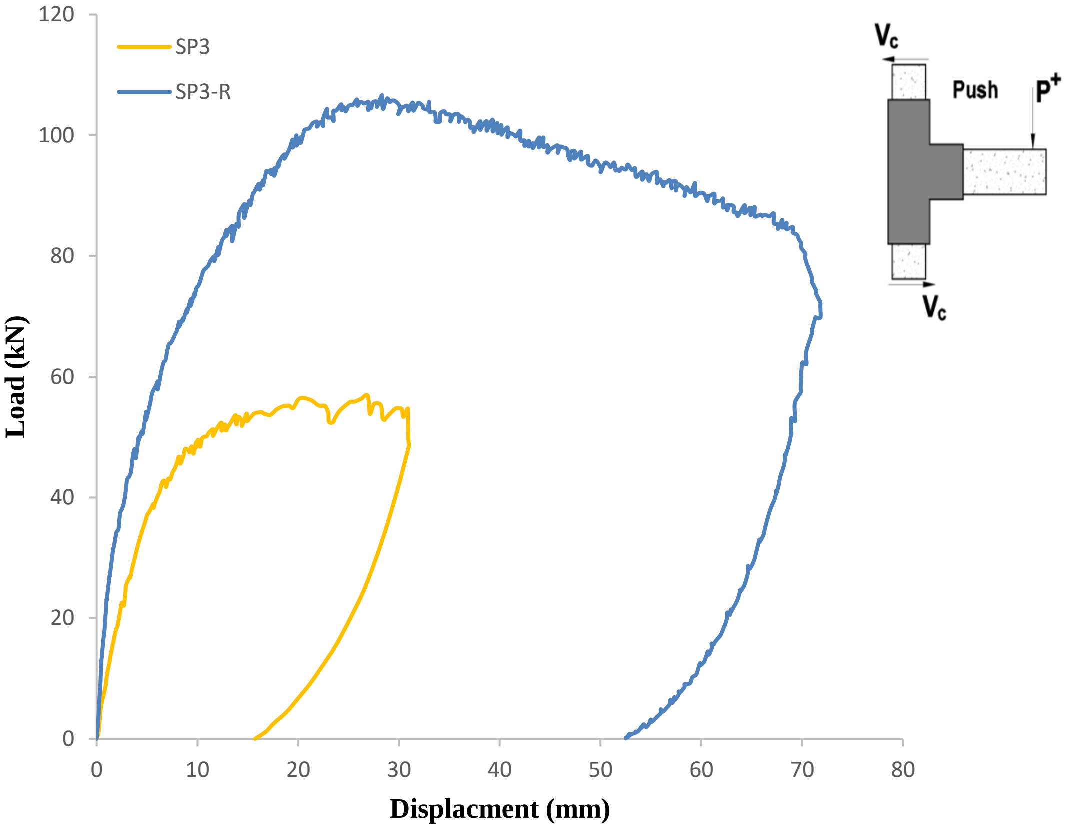

Figure 4-3 Load-displacement response of specimens Sp3 and SP3-R

### 4.1.2 Strength Factor and Displacement Index

Figure 4-4 represents the performance of retrofitted specimens against the specimens in the virgin state regarding their load-displacement response and highlighted the beneficial effects achieved by the implemented repairing system. The repairing system not only restored the performance of test units but also improved it in terms of strength, stiffness, energy dissipation capacity and ductility. The values registered for peak load ($F_P$), ultimate load ($F_u$), the load at which first yielding of longitudinal reinforcement started ($F_y$) and the corresponding displacements for specimens in the retrofitted and virgin states are listed in Table 4-1. According to available literature, displacement corresponding to 10% or 20% loss of peak load in the post-peak regime is taken as ultimate displacement [21]. In the present research work, ultimate displacement is taken as the displacement corresponds to 10% reduction in the peak load.

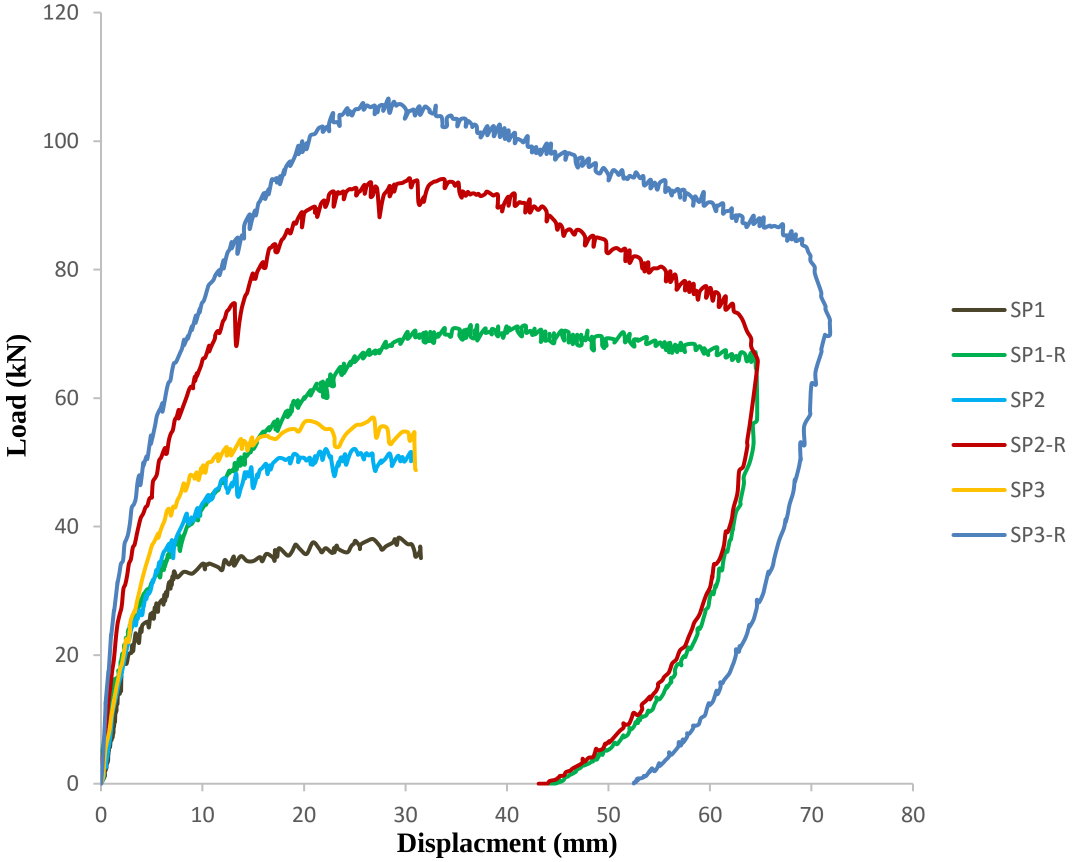

**Figure 4-4 Load-displacement response of specimens in retrofitted and virgin states**

**Table 4-1 Test results**

| Specimen ID | $F_p$ | $\Delta_p$ | $F_y$ | $\Delta_y$ | $F_u$ | $\Delta_u$ |
|---|---|---|---|---|---|---|
| | kN | mm | kN | mm | kN | mm |
| SP1-R | 71.37 | 36.41 | 69.56 | 51.628 | 64.618 | 64.518 |
| SP1 | 37.55 | 19.44 | - | - | 33.8 | 31.52 |
| SP2-R | 94.19 | 30.433 | 79.71 | 55.657 | 84.77 | 49.8 |
| SP2 | 51 | 19.48 | - | - | 45.9 | 28.66 |
| SP3-R | 106.62 | 28.307 | 101.28 | 37.1 | 95.96 | 52.7 |
| SP3 | 56.87 | 17.86 | - | - | 51.183 | 30.952 |

$F_p$ = Peak load (kN)

$\Delta_P$ = Displacement corresponds to peak load

$F_y$ = Load at which first yielding of longitudinal reinforcement started

$\Delta_y$ = Load corresponds to $F_y$

$F_u$ = Ultimate Load (load corresponds to 90% reduction in the peak load)

$\Delta_u$ = Ultimate displacement

Two indices were used to check the performance of retrofitting technique, strength index $I_F$ and displacement index $I_\Delta$. These indices were suggested by Roberto et al. [18] for examining the performance of strengthening systems. The definition of strength index and displacement index is shown in Eq. 4-1 and Eq. 4-2, respectively. The effectiveness of UHPFRC jacketing in repairing the damaged specimens can be evaluated by using these two ratios.

$$\text{Strength index} = I_F = \frac{(F_p)_{retrofitted}}{(F_p)_{virgin}} \tag{4-1}$$

$$\text{Displacement index} = I_\Delta = \frac{(\Delta_{90\%})_{retrofitted}}{(\Delta_{90\%})_{virgin}} \tag{4-2}$$

Table 4-2 showed that the repairing system not only restored the strength of damaged specimens but significantly improved their performance in terms of strength. According to the obtained results, the retrofitted system provided an increase of 90% and more than 100% in terms of peak load and deformation capacity of specimen SP1-R. The corresponding values for specimen SP2-R were 85% and 74% and for specimen SP3-R, UHPFRC jacket provided an increase of 87% and 70% in peak load and deformation capacity. It is important to notice that the increased axial load reduced the ductility of the test units.

**Table 4-2 Strength index and displacement index of retrofitted specimens**

| Specimen ID | $I_F$ | $I_\Delta$ |
|---|---|---|
| SP1-R | 1.9 | 2.05 |
| SP2-R | 1.85 | 1.74 |
| SP3-R | 1.87 | 1.7 |

### 4.1.3 Steel micro-strain Monitoring

For monitoring the strains in steel reinforcing bars of the retrofitted specimens, strain gauges were installed on stirrups, beam and column longitudinal reinforcement. The plots of imposed displacement vs. strain of steel reinforcement of retrofitted specimens SP1-R, SP2-R and SP3-R are shown in Figures 4-5, 4-6 and 4-7, respectively.

**Specimen SP1-R**

For specimen SP1, 660 µϵ was registered in beam's longitudinal reinforcement, which was well below the yield strain, while Figure 4-5 (a), (b) and (c) show the plot between strains in stirrups, beam and column main reinforcement vs. incremental displacement amplitudes for specimen SP1-R. The plots indicated the continuous increment in the micro-strain of all reinforcement but only longitudinal reinforcement of beam exceeded the limit of yield strain. The dotted line in each plot showed the limit of yield strain. However, stirrups and column's longitudinal reinforcement reached a value of 763 µϵ and 2550 µϵ, respectively. So the plot displayed in Figure 4-5 (b) indicated that retrofitted specimen performed efficiently.

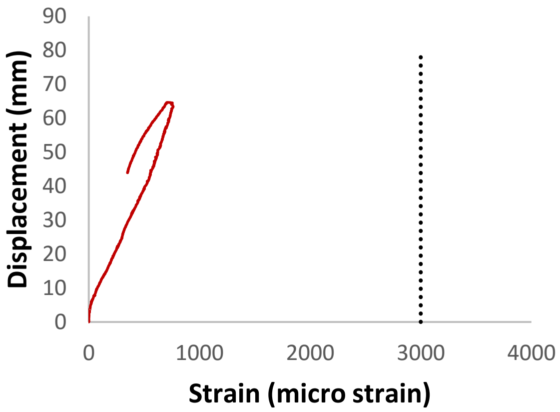

**a) Strains in Stirrups**

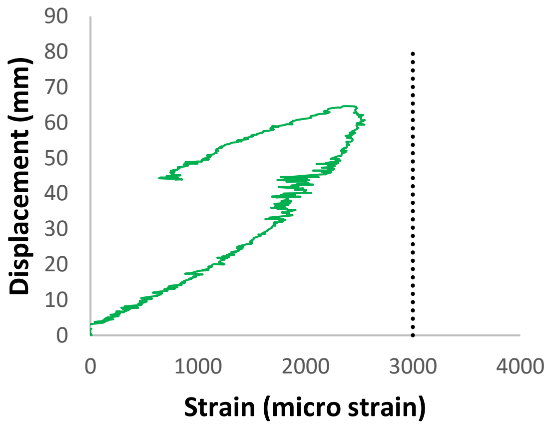

**b) Strains in column's longitudinal reinforcing bar**

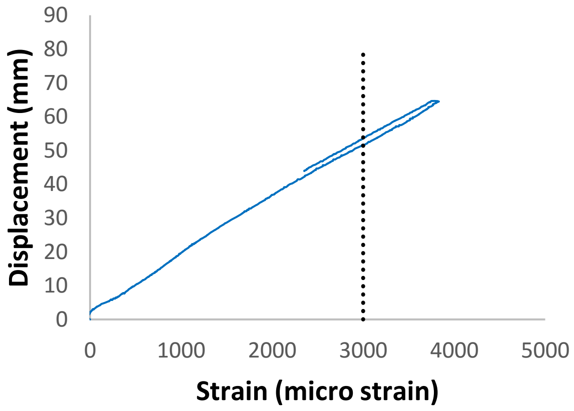

**c) Strains in Beam's longitudinal reinforcing bar**

**Figure 4-5 Imposed displacement vs. strain of steel reinforcement of retrofitted specimens SP1-R**

**Specimen SP2-R**

For specimen SP2, 810 μϵ was registered in beam's longitudinal reinforcement, which was well below the yield strain, while Figure 4-6 (a), (b) and (c) show the plot between strains in stirrups, beam and column main reinforcement vs. incremental displacement amplitudes for specimen SP2-R. Longitudinal reinforcement of beam exceeded the limit of yield strain. The dotted line in each plot showed the limit of yield strain. However, a value of 512 μϵ and 1165 μϵ was registered for stirrups and column's longitudinal reinforcement, respectively. Therefore, the plot presented in Figure 4-6 (b) indicated that retrofitted specimen performed adequately.

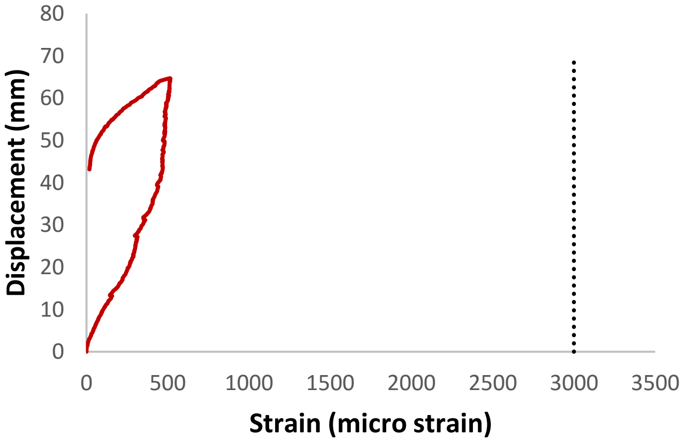

**a) Strains in Stirrups**

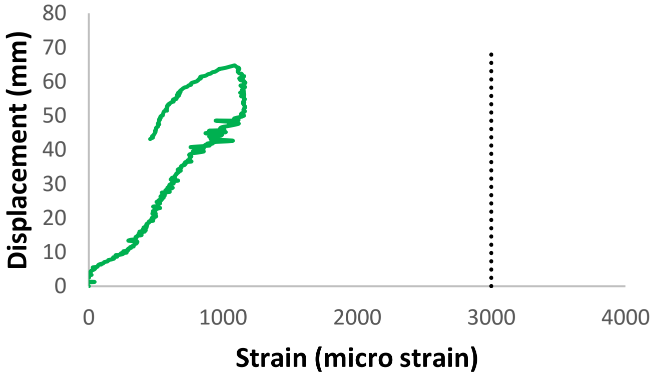

**b) Strains in column's longitudinal reinforcing bar**

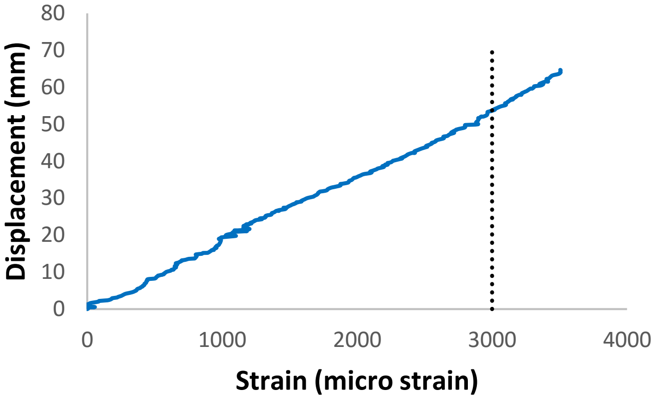

**c) Strains in Beam's longitudinal reinforcing bar**

**Figure 4-6 Imposed displacement vs. strain of steel reinforcement of retrofitted specimens SP2-R**

### Specimen SP3-R

For specimen SP3, 986 με was registered in beam's longitudinal reinforcement, which was well below the yield strain, while Figure 4-7 (a), (b) and (c) show the plot between strains in stirrups, beam and column main reinforcement vs. incremental displacement amplitudes for specimen SP3-R. The plots indicated the continuous increment in the micro-strain of all reinforcement but only longitudinal reinforcement of beam exceeded the limit of yield strain. The dotted line in each plot showed the limit of yield strain. However, stirrups and column's longitudinal reinforcement reached a strain of 718 με and 2381 με, respectively. Therefore, the plot in Figure 4-7 (b) showed that retrofitted specimen performed efficiently.

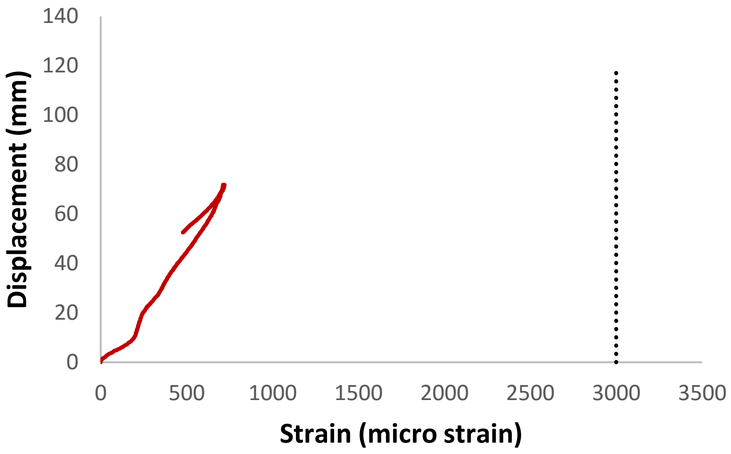

a) Strains in Stirrups

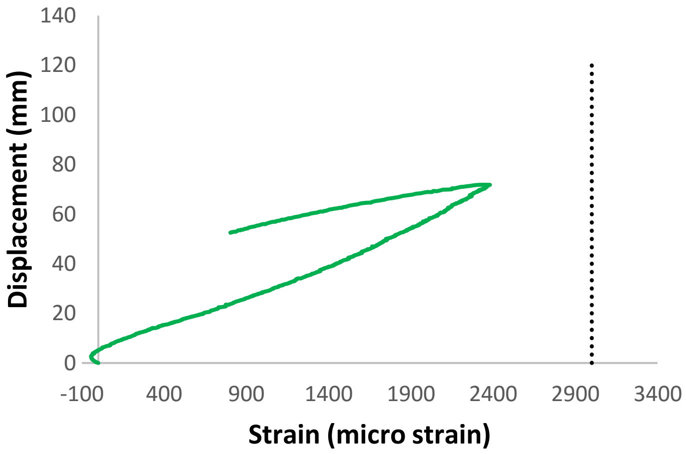

b) Strains in column’s longitudinal reinforcing bar

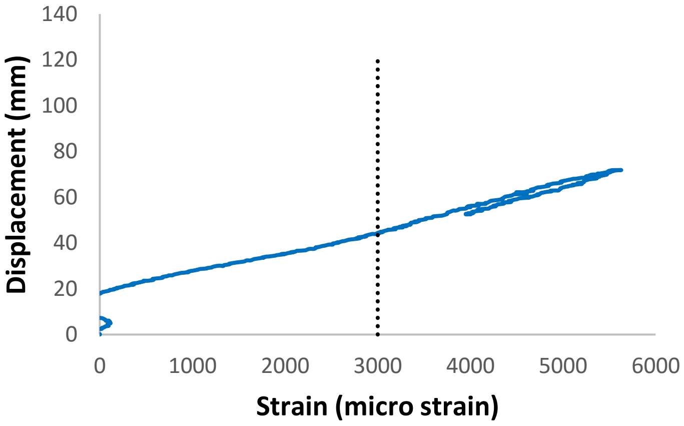

c) Strains in Beam’s longitudinal reinforcing bar

**Figure 4-7 Imposed displacement vs. strain of steel reinforcement of retrofitted specimens SP3-R**

### 4.1.4 Damage Evolution and failure mode

The gradual development of minor and major cracks and major damaged registered at the end of the test is depicted in Figures 4-8, 4-10 and 4-12 for specimens SP1-R, SP2-R and SP3-R, respectively. At the early stage of testing, it can be observed the formation of vertical and diagonal cracks on the beam, where it was not encased in the UHPFRC jacket, which was not developed significantly during the test. The major damaged was caused by the vertical flexural cracks in the beam and inside the joint panel. As test continued, diagonal cracks appeared in the column and inside the joint panel around the major cracks but did not contribute too much to failure.

**Specimen SP1-R**

The evolution of crack pattern for specimen SP1-R is shown in Figure 4-8. At the early stage of testing, hairline cracks on all sides of the beam, where it was not reinforced with UHPFRC, had been observed at an imposed load of 25 kN corresponding to a displacement of 3.1 mm. No further propagation of these cracks had been observed during the testing. The first sign of damage in the jacket in terms of vertical flexural cracks occurred in the beam at a load 26 kN corresponding to displacement 3.2 mm. Once the displacement reached to 5.4 mm, corresponding to the imposed load of 32 kN, new series of vertical flexural cracks appeared at the upper corner of joint. With the increment of beam tip displacement, this crack localized in the beam at beam-joint interface produced a significant opening increase up to a value of 10.4 mm at the end of the test. At peak load of 71.37 kN, the width of crack was found to be 3.1 mm and this value reached to 10.44 mm when the applied shear reduced to 80% of its peak value. At a displacement of 11.2 mm when the imposed load was 45 kN, further damage was observed in the beam in terms of flexural cracks, extended towards the bottom corner of joint at one end and joined the already developed flexural cracks on the other end in the subsequent loading history and appeared as the second major vertical flexural crack causing the failure of test unit. The specimen showed the first series of inclined cracks in the upper column near the upper corner of joint at a load 28 kN and at a displacement of 3.8 mm and propagated along the height of the column in the subsequent loading history. The width of this crack did not exceed from 0.9 mm. At an imposed load of 71 kN, corresponding to the displacement of 36.4 mm inclined cracks had been observed in the bottom column, which did not develop significantly. Test unit showed few cracks of minor importance around major cracks in the beam. At the end of the test, there was no sign of detachment or de-bonding between UHPFRC jacket and NCSS.

Contrariwise, in the virgin state, specimen SP1 showed diagonal crack inside the joint panel at a load 16 kN and a displacement of 1.34 mm reported by the research group [38]. This crack was extended towards the outer edge of the column at peak load of 37.55 kN and a displacement of 19.44 mm resulted in the brittle shear failure of joint. Maximum strain in the beam reinforcement was found to be 660 $\mu\epsilon$ which was considerably lower than the yield strain of reinforcement. In retrofitted specimen, not only the crack initiation was delayed but also the damage was shifted from typical diagonal tension cracks inside the joint panel to the vertical flexural cracks in the beam and beam joint-interface because UHPFRC-jacket had significantly improved the strength of the joint. The retrofitted specimen, designated as SP1-R, showed flexural failure in the beam at the beam-joint interface. UHPFRC jacket was able to shift the classical brittle joint shear failure to ductile flexural failure of beam at the beam-joint interface with the yielding of beam main reinforcement.

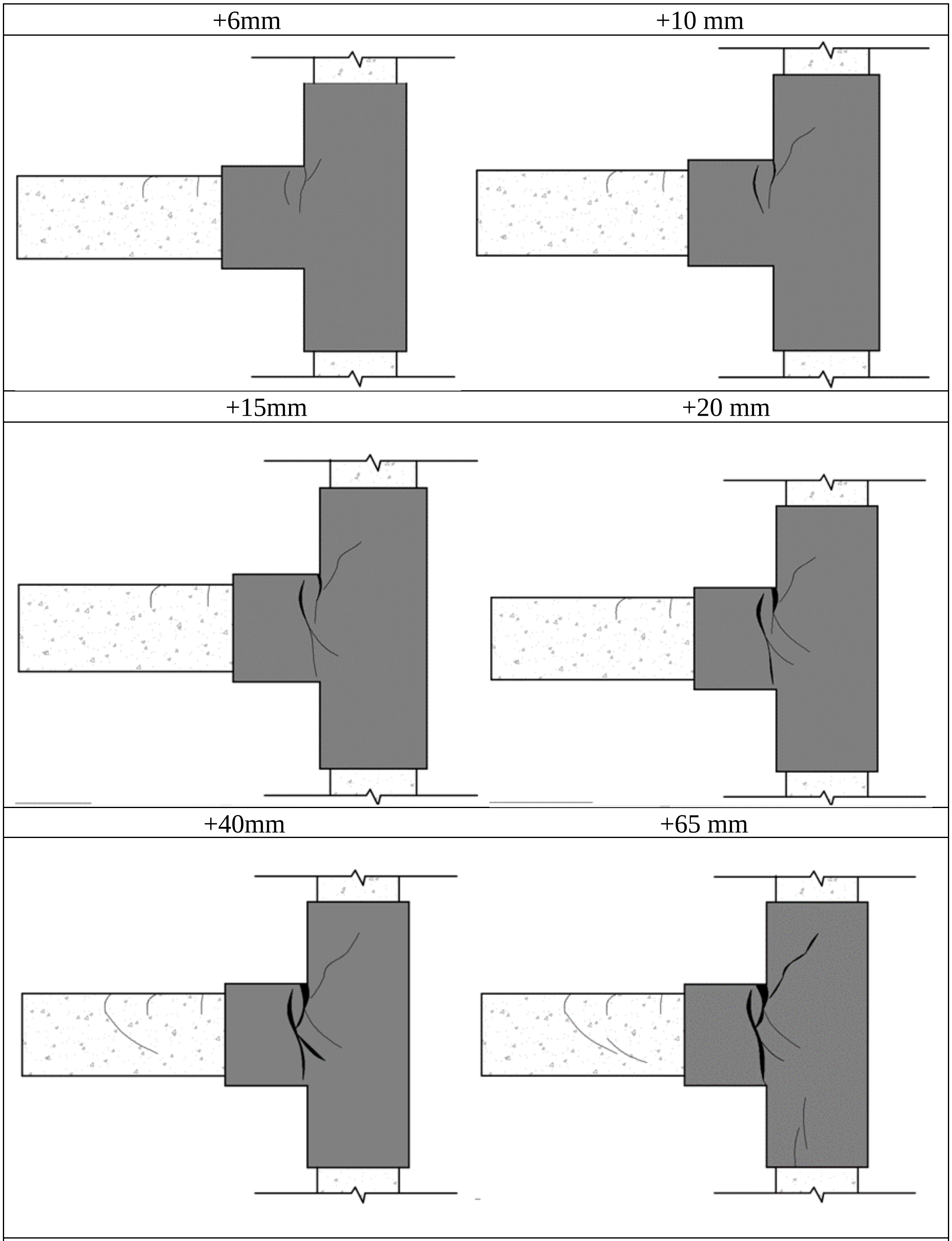

**Figure 4-8 Damage Evolution of specimen SP1-R**

**a)** **Crack pattern of Specimen SP1-R**

**b)** **Crack pattern of Specimen SP1**

**Figure 4-9 Crack pattern of Specimens SP1-R and SP1 at the failure load**

**Specimen SP2-R**

Specimen SP2-R was tested under monotonic loading with CAL of 200 kN. The crack evolution is depicted in Figure 4-10. The first vertical crack appeared in the beam at a displacement of 3.4 mm and an imposed load of 37 kN. Contrary to SP2-R, specimen SP2 in the virgin state showed the first diagonal crack at the center of joint at a load of 29 kN and a displacement of 3.8 mm. With the further increment of load, damage occurred in SP2 specimen with the formation diagonal cracks parallel to the first crack which increased in length and width until the peak load of 51 kN at a displacement of 19.48mm. However, for retrofitted specimen SP2-R, the second series of vertical flexural crack occurred in the beam at a load 43.3 kN and displacement of 4.6mm. The specimen showed the third flexural crack at the upper corner of joint at a load of 45 kN, corresponding to a displacement of 5 mm which propagated towards the opposite face of the column passing all along the width of the beam at the applied shear of 64.7 kN, corresponding to a displacement of 11 mm. At a displacement of 6.4 mm, corresponding to a load of 52.6 kN, an inclined crack appeared at beam-joint interface extended towards the bottom corner of joint. With the increment of beam tip displacement, further damage was observed when first and 3rd series of cracks extended towards each other and localized at the beam-joint interface which was monitored through displacement transducer. The crack width was 4.1 mm at peak load of 94.18 kN, corresponding to a displacement of 30.4 mm and crack width was increased up to 12.6 mm at a displacement of 60.27 mm, corresponding to an ultimate load of 75.15 kN. The second major damage was caused by the extension of second and fourth series of flexural cracks towards each other forming a single crack which increased in width and length with the increment of displacement. Few minor diagonal cracks appeared around the major cracks and on the face of the beam where it was not encased in the jacket at a load of 72 kN and displacement of 12 mm during did not develop significantly.

In the virgin state, test unit SP2 showed the diagonal cracks at the center of the joint panel with the increment of beam tip displacement and these diagonal cracks resulted in the brittle joint shear failure. The strain in the beam reinforcement was found to be 810 μϵ which was significantly lower than the yield strain of steel. However, specimen SP2-R showed vertical flexural cracks. Major failure and damage were registered due to the formation of vertical flexural cracks. The strain in the beam reinforcement was found to be 3500 μϵ which was more than the yield strain, showing the yielding of steel. No major crack had been found in the joint area and all cracks were shifted from the central joint area and localized in the beam at the beam-joint interface. Test unit SP2 and SP2-R after the completion of test is shown in Figure 4-12

Contrary to specimen SP1-R, specimen SP2-R showed cracks in the jacket on the inner face of the top and bottom columns at a load of 90 kN and displacement of 21.6 mm, as shown in Figure 4-11. The cracks also appeared on the bottom face of the beam near the edges at a load of 91 kN and displacement of 22.5 mm. Due to the development of these cracks, UHPFRC jacket was slightly de-bonded from NCSS, as shown in Figure 4-11. The reason behind detachment and additional cracking was the increased CAL. CAL enhanced the confinement of joint resulted in the increment in the joint strength and load carrying capacity from 71.37 kN to 94.19 kN when CAL was increased from 0 kN to 200 kN. It is essential to note that with the increase of CAL, the crack initiation was delayed. The first crack in beam appeared at 37 kN and a displacement of 3.4 mm as compared to specimen SP1-R where the first crack appeared at 26 kN and at a displacement of 3.2 mm.

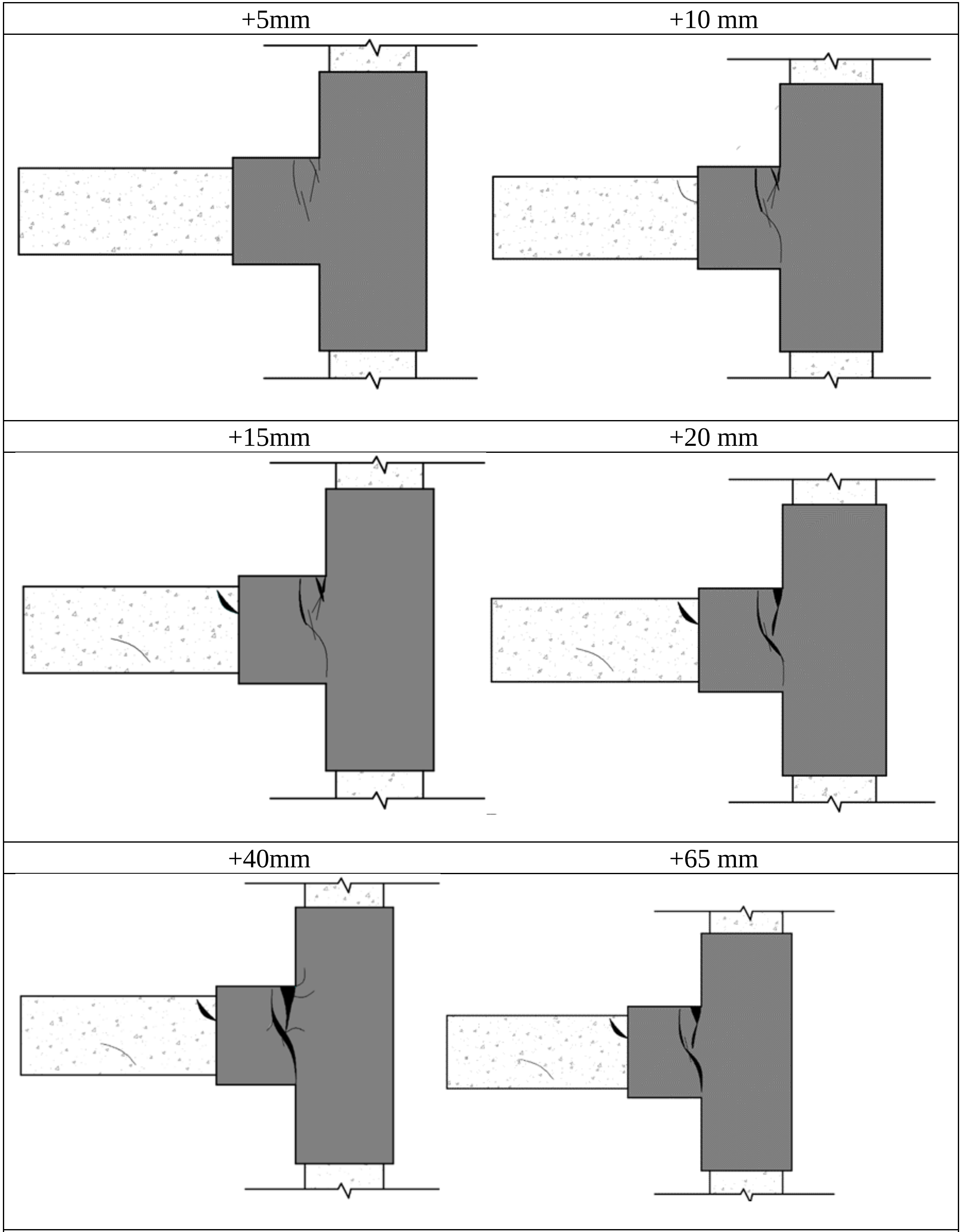
+5mm

+10 mm

+15mm

+20 mm

+40mm

+65 mm

**Figure 4-10 Damage Evolution of specimen SP2-R**

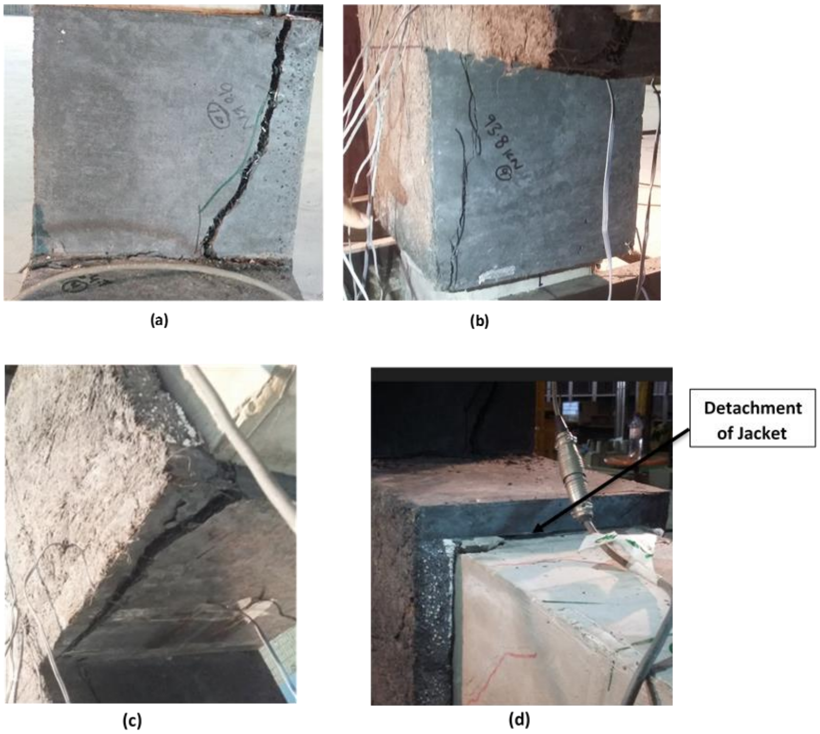

Figure 4-11 Development of cracks on the inner face of columns (a),(b); crack on beam bottom face (c); detachment of the UHPFRC jacket for test unit SP2-R

(a) Crack pattern of Specimen SP2-R (b) Crack pattern of Specimen SP2

Figure 4-12 Crack pattern at the failure load

### Specimen SP3-R

Specimen SP3-R was tested under monotonic loading with CAL of 600 kN. The crack evolution is depicted in Figure 4-13. The damage was registered in the jacket at a load of 55 kN and a displacement of 6.3 mm when vertical flexural cracks developed at the upper corner of joint. Later on, this crack was extended towards the opposite face passing all along the width of the beam at a load equals to 82 kN and a displacement of 14 mm, as shown in Figure 4-14. At a load of 73.5 kN corresponding to a displacement of 11.1 mm, horizontal cracks appeared in the beam which became vertical after passing through the beam-joint interface. Further damage was caused by the inclined cracks appeared in the top column at a load of 82 kN and a displacement of 14 mm. The vertical flexural crack caused the significant damage, appeared at the center of the beam-joint interface at a load of 100 kN and a displacement of 22 mm and extended towards the inclined cracks in the upward direction and extended towards the bottom corner of joint in the downward direction with the load increments. After joining, these cracks localized at the beam-joint interface in the subsequent loading history. The major portion of this crack was located at the beam-joint interface and monitored through LVDT's. Crack width was 5.8 mm at a peak load of 106.62 kN, corresponding to a displacement of 28.31 mm. This width was increased up to 13.37 mm at an ultimate displacement of 67.66 mm when the load was reduced to 80% of its peak load.

Test unit SP3-R showed horizontal cracks in the beam at load 68 kN and at 103 kN, corresponding to a displacement 9.8 mm and 25.3 mm resulting in the detachment or separation of the UHPFRC jacket from NCSS, as shown in Figure 4-14. These types of cracks had not been observed in specimen SP1-R and SP2-R and attributed to the increased

CAL. Increased CAL made the joint more confined than SP1-R and SP2-R due to which load carrying capacity had been increased and applied shear value was reached to 106.62 kN, which was 94.18 kN and 71.37 kN for specimen SP2-R and SP1-R, respectively resulting in the higher stresses at the interface of UHPFRC-jacket and NCSS.

In the virgin state, the first series of cracks appeared in the beam at a load of 17 kN corresponding to displacement 1.03 mm which did not develop significantly in the subsequent loading history. The Second series of cracks consisted of inclined cracks and occurred in the joint at a load of 38 kN and displacement of 4.11 mm. With the further increment of load, inclined cracks developed at $75^0$. These cracks increased in length and width and resulted in the failure of a joint in shear. Maximum strain in beam reinforcement was reported to be 986 $\mu\epsilon$ which was far less than the yield strain. Therefore, the specimen failure mode was brittle joint shear failure without yielding of beam reinforcement. Contrariwise, retrofitted specimen SP3-R, when tested under same loading history, showed vertical flexural cracks at beam joint interface and horizontal cracks near the edges of jacket. The major failure was registered due to vertical flexural cracks at the beam-joint interface. The maximum strain in the beam reinforcement was found to be 5629 $\mu\epsilon$. It is essential to notice that the application of 30 mm thick UHPFRC jacket delayed the initiation of cracks. Secondly, no major cracks had been found in the joint panel and cracks were shifted from the joint panel to beam or beam joint interface. Thirdly, the strain in the beam longitudinal reinforcement was more than the yield strain of the rebar resulting in the formation of a plastic hinge, concentrated at the beam-joint interface. The condition of specimens SP3 and SP3-R after the completion of the test is shown in Figure 4-15.

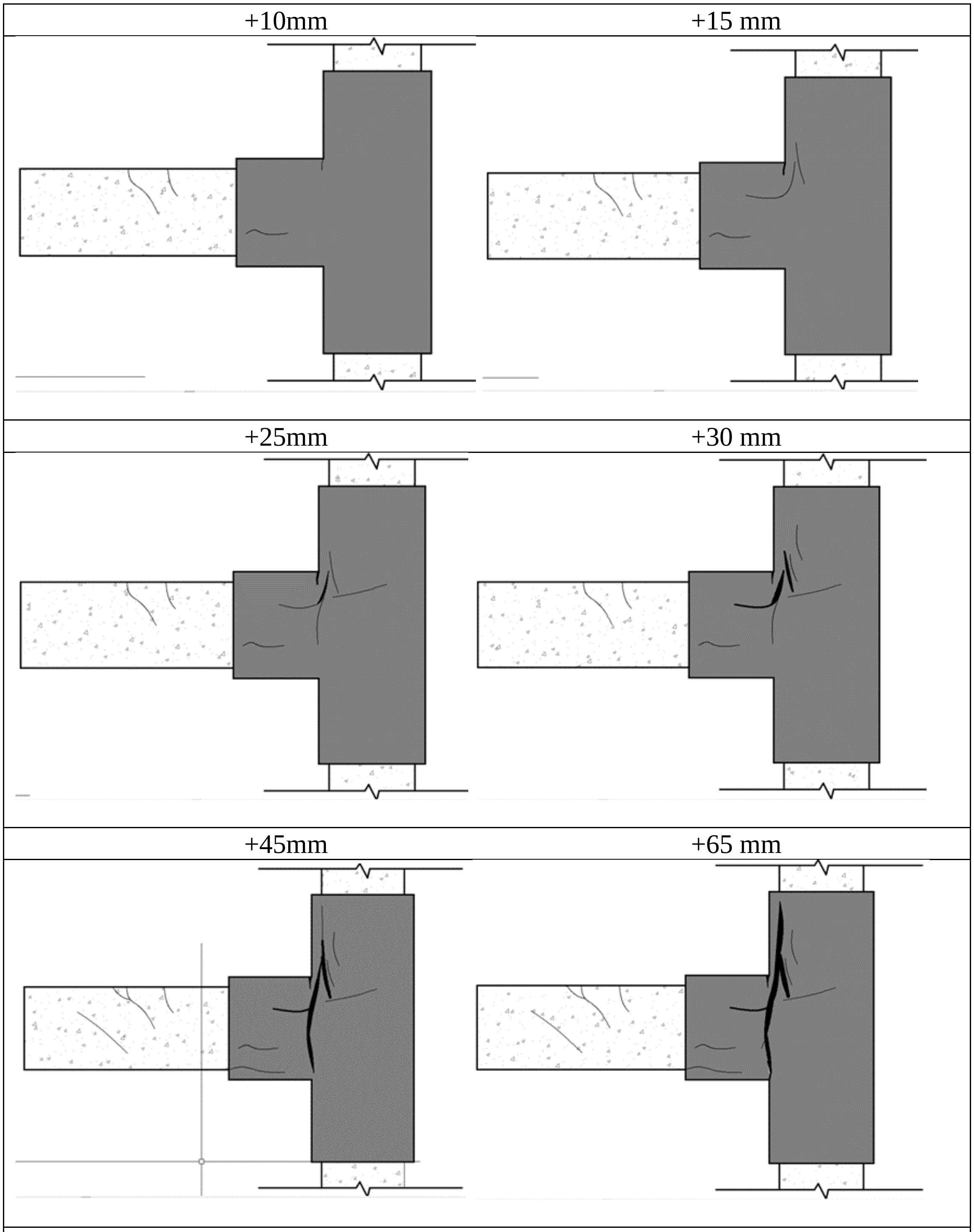
+10mm

+15 mm

+25mm

+30 mm

+45mm

+65 mm

**Figure 4-13 Damage Evolution of specimen SP3-R**

Figure 4-14 Horizontal cracking leads to detachment of UHPFRC from NCSS

a) Crack pattern of Specimen SP3-R

Figure 4-15 Continued

**b)** Crack pattern of Specimen SP3

Figure 4-15 Crack pattern of Specimens SP2-R and SP2 at the end of test

### 4.1.5 Initial stiffness and secant stiffness

Figures 4-1, 4-2 and 4-3 clearly indicate that retrofitted solution not only restored the stiffness of damaged specimen but also enhanced it. The retrofitting solution performed efficiently regarding stiffness restoration and stiffness enhancement. A better comparison of experimental data regarding stiffness can be made by calculating initial stiffness and secant stiffness of each specimen in the retrofitted and virgin state. Initial stiffness corresponds to the initial elastic part of the load-displacement curve and secant stiffness is calculated as a slope of the line passing through origin and peak force ($F_p$) in the load-displacement curve, as shown in Figure 4-16. Initial stiffness and secant stiffness corresponds to $F_p$ for each specimen is tabulated in Table 4-3.

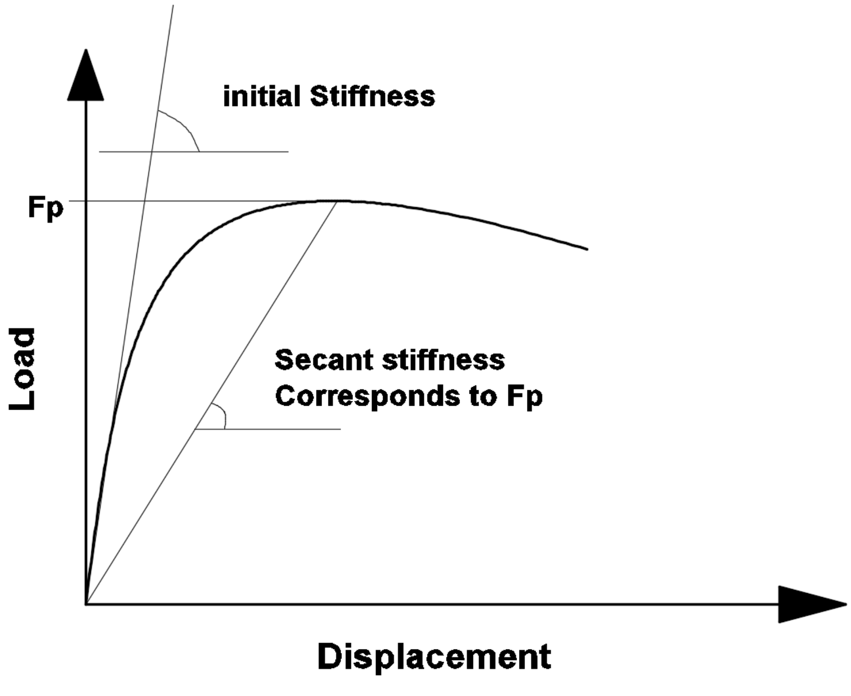

Figure 4-16 Illustration of initial and secant stiffness

**Table 4-3 Initial and secant stiffness of specimens in retrofitted and virgin state**

| Specimen ID | Initial stiffness | Secant stiffness correspond to $F_p$ | Increase in the initial stiffness |
|---|---|---|---|
| | kN/mm | kN/mm | % |
| SP1-R | 14.50 | 1.96 | 80 |
| SP1 | 8.06 | 1.93 | - |
| SP2-R | 15.45 | 3.1 | 83.7 |
| SP2 | 8.41 | 2.62 | - |
| SP3-R | 21.1 | 3.77 | 122 |
| SP3 | 9.49 | 3.18 | - |

The percentage increase in initial stiffness of retrofitted specimen relative to the corresponding specimen in the virgin state is listed in Table 4-3. The UHPFRC jacketing around the damaged unit recovered the stiffness of the test unit. Data indicated that the retrofitting solution was so efficient in recovering the stiffness that the initial stiffness of the test was not only restored but also improved. Specimen SP1 had an initial stiffness of 8.06 kN/mm. However, after retrofitting the damaged specimen, the same specimen showed the stiffness of 14.5 kN/mm. The improvement in the stiffness value is reported to be 80%. For specimen SP2-R, the percentage increase in initial stiffness is 83.7 %. The third retrofitted specimen SP3-R with CAL 600 kN, presented the maximum improvement in the initial stiffness value. The initial stiffness of SP3-R is 122% higher than the value registered in its virgin state. The enhancement in the initial stiffness amplified with the increment in the CAL With the increment of CAL, the specimens became stiffer. The secant stiffness of SP1-R, SP1, SP2-R, SP2, SP3-R and SP3 was 7.4, 4.18, 4.98, 3.21, 5.6 and 2.98 times less than the initial stiffness registered for the corresponding specimens. The reduction in the stiffness, due to deterioration in the specimen, was registered more in retrofitted specimens. However, secant stiffness value of the retrofitted specimen is either equal or more than the specimen in the virgin state.

### 4.1.6 Energy dissipation

The potential of lateral load resisting system to withstand the seismic shocks was assessed by the energy dissipation capacity over the elastic and plastic range and deterioration of energy dissipation capacity during inelastic deformation. Energy dissipation for each specimen was computed at each imposed displacement from the summation of the area under the load-displacement curve up to ultimate displacement, as shown in Figure 4-17. The ultimate displacement is taken as the post-peak displacement when maximum strength has undergone a slight reduction. According to available literature, displacement corresponding to 10% or 20% loss of peak load in the post-peak regime is taken as $\Delta_u$ [21]. In the present research work, displacement corresponds to 10% reduction in the peak load is considered as ultimate displacement. Integration of the dissipated energy with the increment in imposed displacement can provide the cumulative energy dissipation at the required displacement.

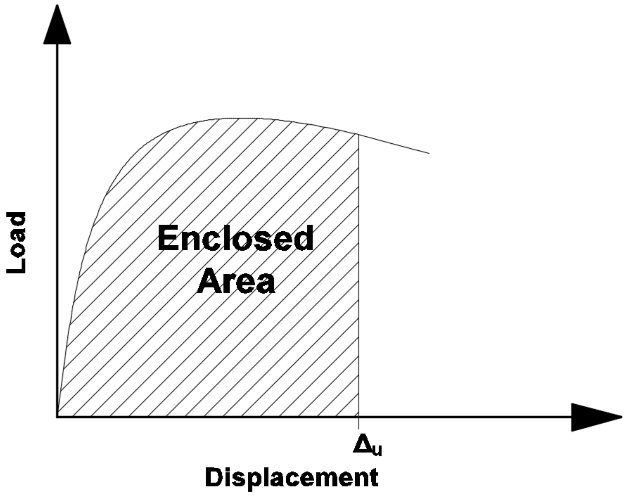

**Figure 4-17 Schematic representation of Area under load-displacement curve**

One of a desirable and distinctive feature of structure expected to sustain severe seismic shocks should have high energy dissipation capacities without considerable loss in its functional performance. Figures 4-18, 4-19, 4-20 and 4-21 show the energy absorption capacity of specimens in the virgin and retrofitted state. The relationship between energy dissipation capacity and imposed beam displacement of a retrofitted and virgin specimen is non-linear. During the early stage of testing, the slope of energy dissipation curve of retrofitted specimen is not increasing at higher rates but still more than the slope of energy dissipation curve of specimen in the virgin state, delineates that the retrofitted solution not only restored the performance of specimen in term of energy dissipation capacity but also improved it. However, this slope is increased significantly at higher displacement value. This increment is attributed to the contribution of UHPFRC jacket, higher level of confinement provided by jacket, higher toughness and crack bridging ability of UHPFRC, friction between cracks, opening and closing of cracks, localization of vertical flexural cracks at beam-joint interface, and the yielding of the beam’s main reinforcement which had not been observed in the corresponding specimens in the virgin state.

### Specimen SP1-R

For comparison, three feature points had been selected in energy dissipation vs. imposed displacement curves. At these points, dissipation capacity of the specimen in the virgin and retrofitted states was compared with each other to study the effectiveness of UHPFRC jacketing in repairing the damaged joints. The total energy dissipated by SP1-R at peak displacement point (point 1), ultimate displacement point (point 2) and ultimate displacement point of the virgin specimen (point 3) were 1912 kN-mm, 3848 kN-mm and 1590 kN-mm, as shown in Figures 4-22, 4-23 and 4-24. However, these values were 933 kN-mm, 1013 kN-mm and 1013 kN-mm for specimen SP1 indicated that energy dissipated by SP1-R at three feature points were 2.05, 3.8 and 1.6 times greater than those of SP1.

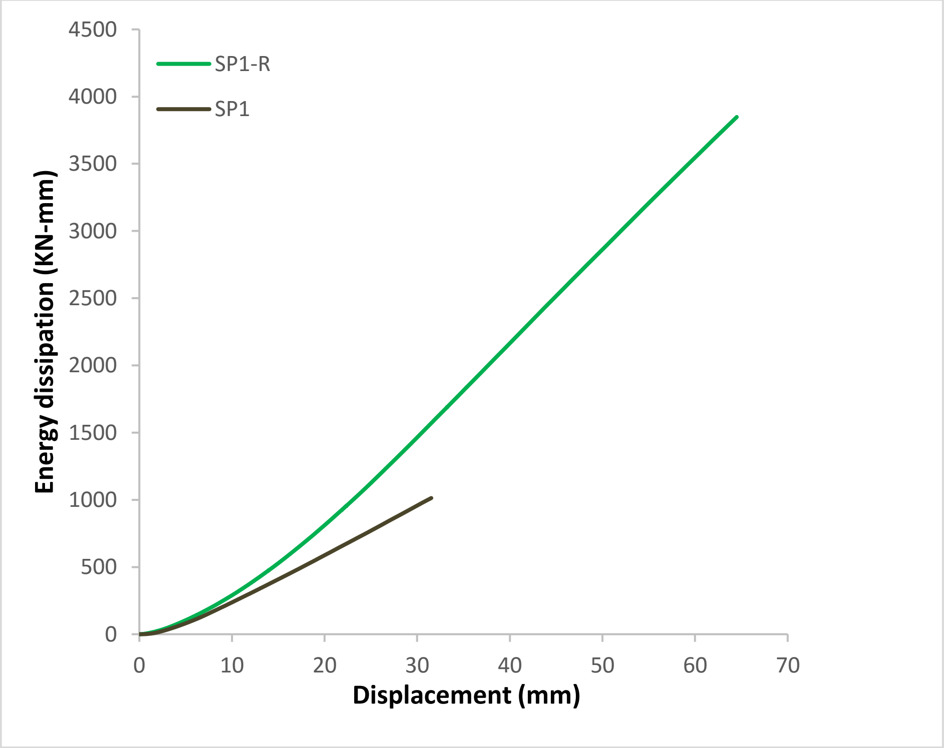

**Figure 4-18 Energy dissipation vs. displacement curves of specimens SP1-R and SP1**

### Specimen SP2-R

The energy dissipation capacity of specimen SP2-R was 2164 kN-mm, 3904 kN-mm and 2174 kN-mm at the three feature points, respectively as shown in Figures 4-22, 4-23 and 4-24. These values were higher than the values owned by specimen SP1-R. This increment was attributed to the increased ALR. It can be found from Figure 4-21 that the increase of CAL, such as SP1-R: SP2-R, resulted in a higher energy dissipation capacity. The total energy dissipated by specimen SP2 at three reference points were 1018 kN-mm, 1297 kN-mm and 1297 kN-mm. The energy dissipated by SP2-R at the three feature points were 2.13, 3 and 1.68 times more than those dissipated by SP2.

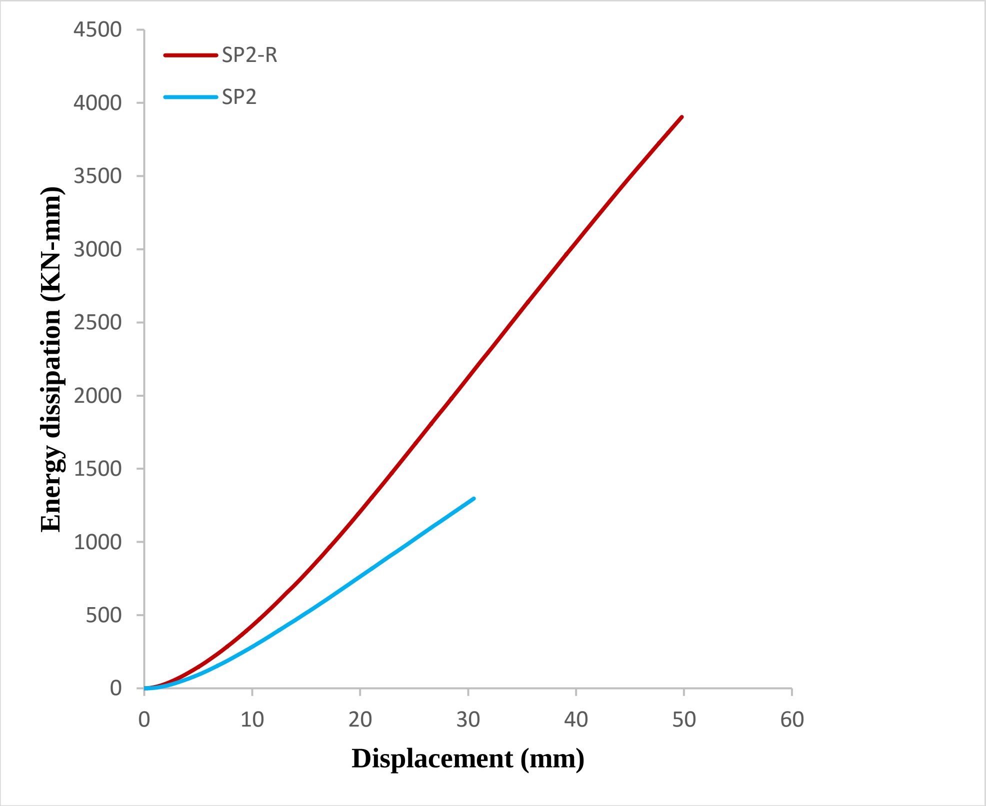

**Figure 4-19 Energy dissipation vs. displacement curves of specimens SP2-R and SP2**

## Specimen SP3-R

The energy absorption capacity of specimen SP3-R was 2245 kN-mm, 4692 kN-mm and 2545 kN-mm at the three feature points, respectively as shown in Figures 4-22, 4-23 and 4-24. These values were higher than the values owned by specimen SP1-R and SP2-R. This increment was attributed to the increased ALR. It can be found from Figure 4-21 that the increase of CAL, such as SP1-R: SP2-R: SP3-R, resulted in a higher energy absorption capacity. The total energy dissipated by specimen SP2 at three reference points were 1234 kN-mm, 1458 kN-mm and 1458 kN-mm. The energy absorption by SP3-R at the three feature points were 1.82, 3.2 and 1.74 times more than those dissipated by SP3.

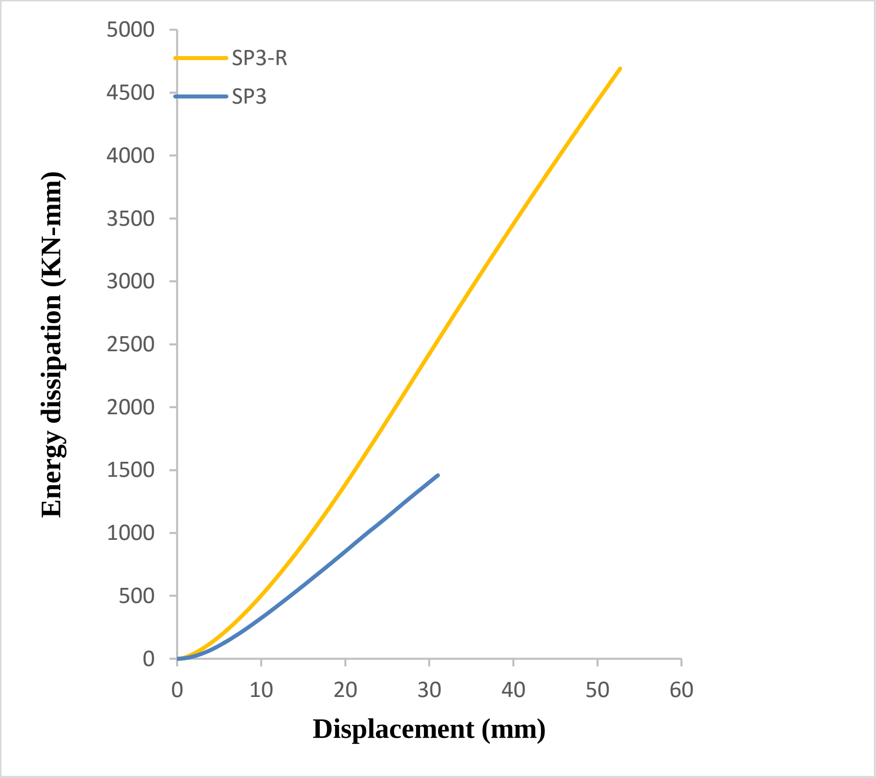

Figure 4-20 Energy dissipation vs. displacement curves of specimens SP3-R and SP3

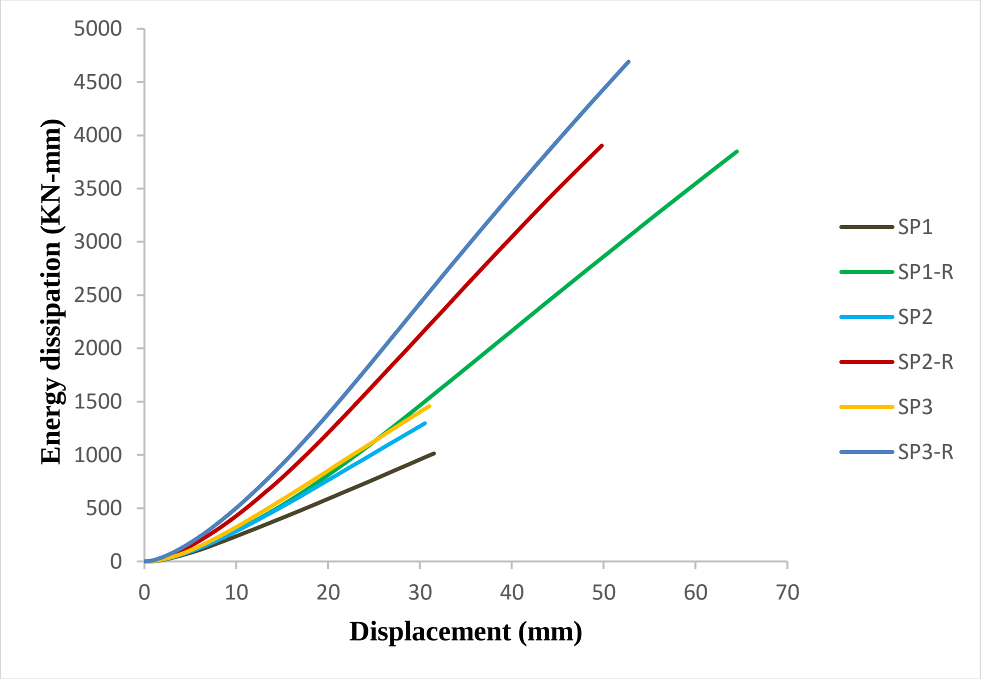

Figure 4-21 Energy dissipation vs. imposed displacement for specimens in retrofitted and virgin states

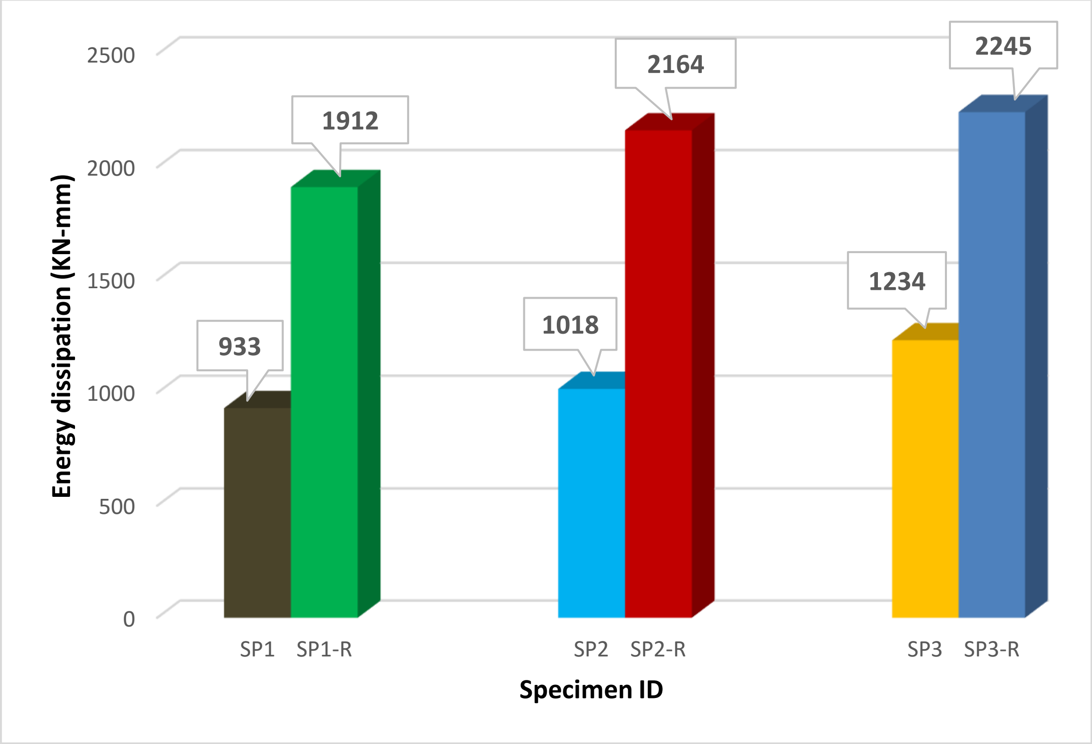

Figure 4-22 Total energy dissipation up to peak displacement of specimens

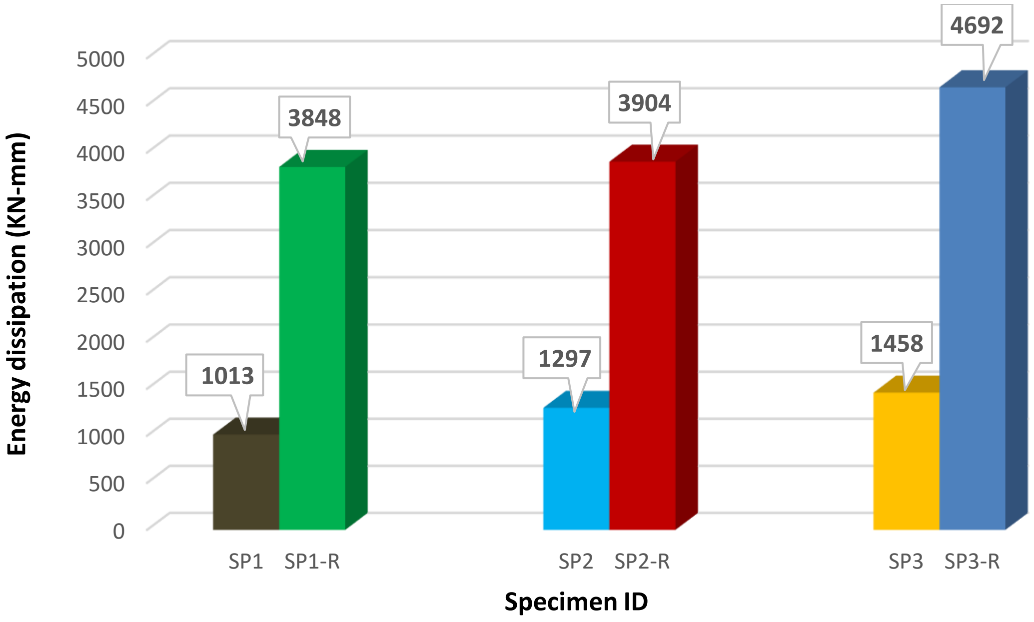

Figure 4-23 Total energy dissipation up to ultimate displacement of specimens

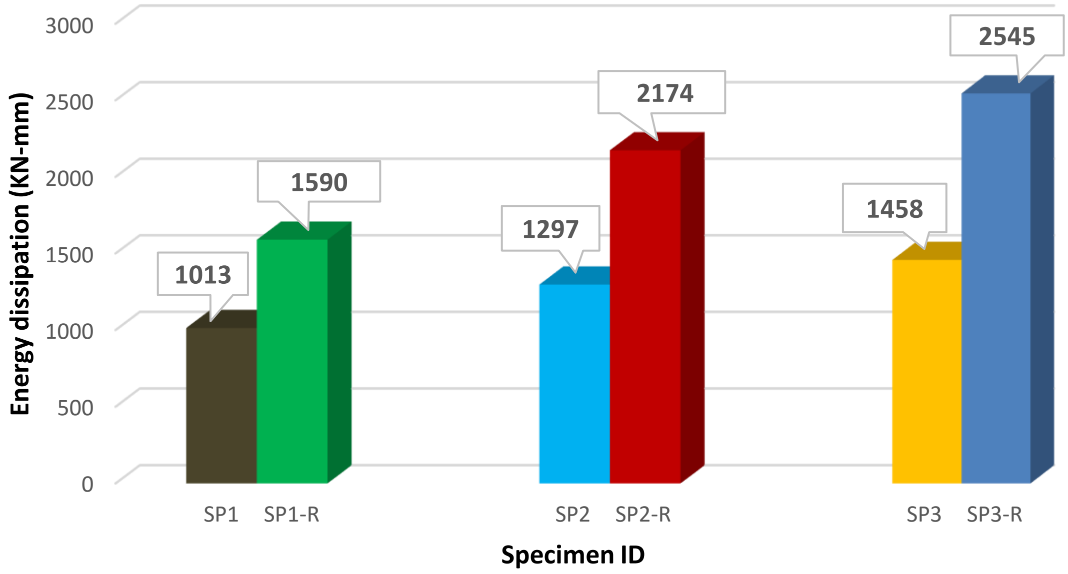

Figure 4-24 Energy dissipation corresponds to ultimate displacement of the virgin specimen

## 4.2 Seismic behavior of control and strengthened specimens

### 4.2.1 Hysteretic response

**Specimen TC**

Figure 4-25 shows the hysteretic response of the control specimen in terms of hysteretic load vs. beam tip displacement (and drift) registered at the free end of a beam. In the positive excursion (push), the beam upper face is in tension, whereas in the negative excursion (pull) tension occurs in the beam lower face. In the positive and negative load directions, the sub-assemblage response was governed by the shear damage in the joint core. In the positive direction, the test unit reached its maximum capacity, equal to 48.2 kN in the 19th cycle at a displacement equal to 18.5 mm (2% drift) whereas, in the negative direction, the maximum strength achieved was 41.5 kN at a displacement equal to 18.6 mm (2% drift). In the following cycles, the maximum strength declined at the gentle rate up to a drift of ±3% and the strength reduction was about equal to 8% of the peak load. However, with the further increase in the displacement, a sudden drop in the load occurred due to the formation of failure wedge or triangle inside the joint panel. After ±4%, when load sustained by the test unit dropped below 50%, the test was halted. The experimental results confirmed the high susceptibility of exterior BCJ, delineated by a shear damage in the joint panel.

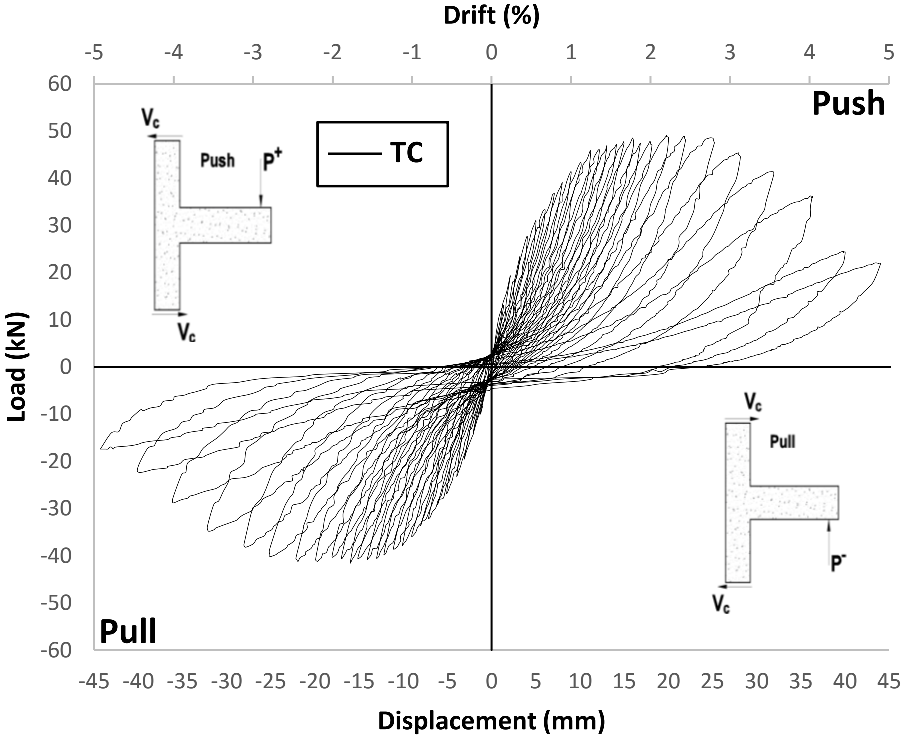

**Figure 4-25 Load-displacement hysteresis plot of Control Specimen TC**

### Specimens TS1 and TS2

Figure 4-26 and Figure 4-27 plot the results of upgraded specimens TS1 and TS2 in terms of hysteretic load vs beam tip displacement (and drift) registered at the free end of a beam. The shape of the curve delineates the behavior of a section comprised of NC core with UHPFRC jacket. The maximum value of load corresponds to the tensile strength in the outer fibers of UHPFRC jacket.

In the positive excursion, specimen TS1 achieved a maximum strength, equal to 105.6 kN in the 13th cycle at a displacement of 12.9 mm (1% drift), while for test unit TS2 the peak load was 103.9 kN at 13.6 mm displacement (1.5%). In the negative excursion, test unit TS1 reached a maximum strength of 100.5 kN in the 14th cycle at a displacement of 14 mm (1.5% drift). However, test unit TS2 achieved the maximum strength of 92.3 kN at 18mm displacement. For specimen TS1, after the peak strength was achieved, load dropped suddenly and decreased to the strength of RC core-subassembly. It leveled out around the value of 45 kN at a displacement of 54 mm (6% drift). This strength reduction was attributed to the localization of vertical flexural cracks at the beam-joint interface and partial detachment of UHPFRC layer from the normal concrete substrate surface. This reduction questioned the post peak deformation capacity and ductility of strengthened specimens. But as the strength reduced to the strength of RC core-subassembly, it was sustained for high drift values due to the yielding of beam's main reinforcement and confinement provided by the UHPFRC jacket and the specimen reached a high drift of ±8.7%. So, UHPFRC jacket played a key role in yielding the beam's longitudinal reinforcement, preventing the classical brittle joint shear failure and forming the plastic hinge localized at the beam-joint interface. UHPFRC jacket performed efficiently and promoted the ductile failure. The post-peak behavior of the test unit strengthened by using UHPFRC jacket was characterized by a sudden drop of strength followed by the plateau in the curve delineates the excellent post peak deformation capacity of the test unit. However, for specimen TS2, as the strength reduction was about equal to 60% of its peak load at 4.9% drift, the test was terminated. Both specimens showed similar behavior up to 4.9% drift.

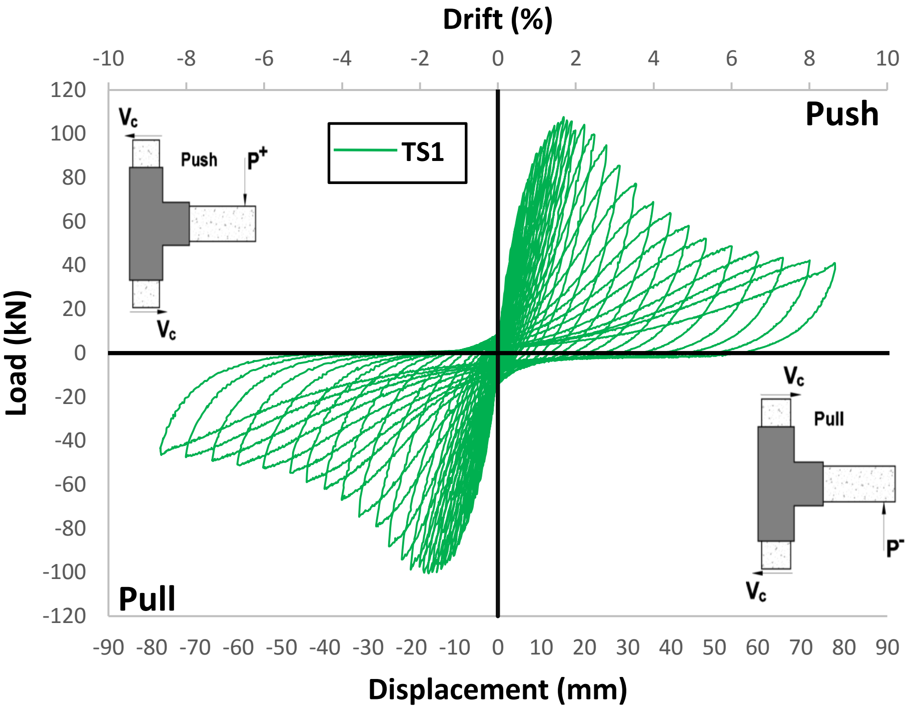

**Figure 4-26 Load-displacement hysteresis plot of Specimen TS1**

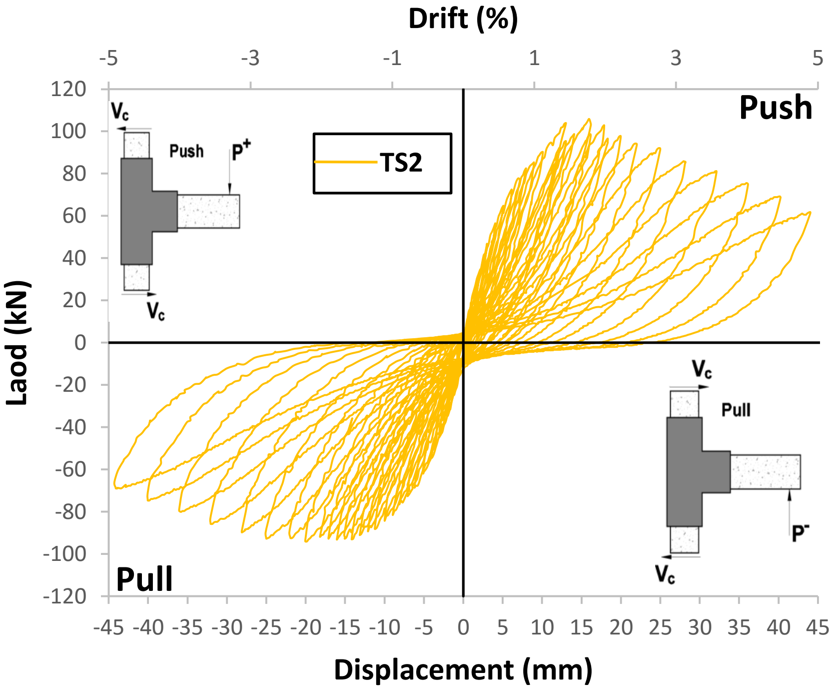

**Figure 4-27 Load-displacement hysteresis plot of Specimen TS2**

### Specimen TSE

Figure 4-28 represents the curve of the cyclic load versus beam tip displacement of specimen TSE. The specimen exhibited different hysteretic load responses in positive and negative excursions. The structural epoxy bonding agent was used to attach the pre-fabricated UHPFRC plates without adopting any surface preparation technique for strengthening the test unit. In the positive excursion, specimen TSE reached its maximum capacity, equals to 98.7 kN in the 17th cycle at a displacement equals to 17 mm (1.9% drift). However, in the negative excursion, the maximum strength achieved was 120.3 kN at a displacement equal to 15.2 mm (1.7% drift). In the following cycles, the load suddenly dropped. This reduction in the strength was attributed to the severe cracking at the edges of UHPFRC plates, cracking in epoxy adhesive and detachment of UHPFRC plates from the NCSS. At the end of the test, UHPFRC plates were completely detached with the cover of NC core-subassembly. The specimen showed the brittle failure due to detachment of UHPFRC plates. Contrary to test unit TS1, the load carrying capacity of test unit TSE decreased continuously even after reaching the strength of RC core-subassembly because de-bonding of the UHPFRC plates severely damaged the NCSS and removed the concrete cover from the test unit resulting in the brittle failure. Although this technique of retrofitting enhanced the maximum load carrying capacity, secant stiffness and energy dissipation but test unit showed early rupture and loss of load carrying capacity before the achievement of high ductility. In the positive excursion, the strength was reduced from 98.7 kN at a drift of 1.9% to 36 kN at a drift of 4%.

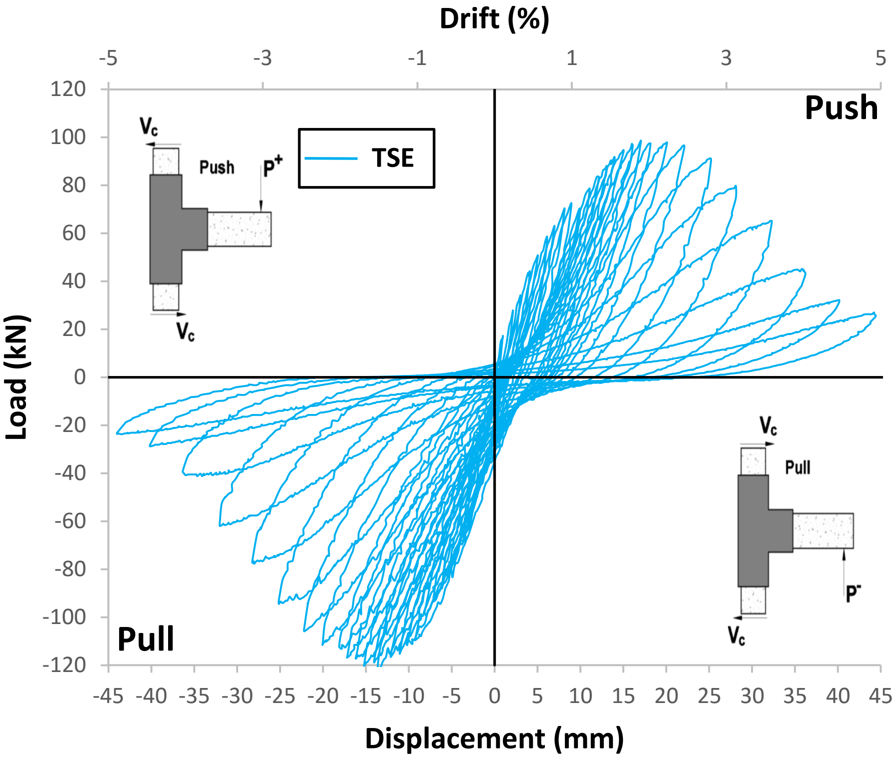

**Figure 4-28 Load-displacement hysteresis plot of Specimen TSE**

### 4.2.2 Comparison in terms of Hysteretic response of Control and strengthened specimens

Hysteretic responses of both control and strengthened BCJ sub-assemblages in terms of beam load vs. displacement (and drift) is subsequently compared in Figure 4-29, Figure 4-30, Figure 4-31and Figure 4-32 to evaluate the performance, efficiency and suitability of the implemented strengthening schemes for pre-earthquake retrofitting of the specimens. Improvement in strength, energy dissipation capacity, peak-to-peak stiffness and ductility is evident from Figure 4-29 and Figure 4-30 for the strengthened specimens TS1 and TS2.

Figure 4-31 presents the comparison between the load-displacement response of the specimens TSE and TC. It was observed that the implemented strengthening technique improved the maximum strength, energy dissipation capacity and secant stiffness but the behavior of strengthened specimen was unsymmetrical in push and pull directions. In addition, the performance of upgraded specimen was inefficient in the post peak regime and showed early fracture and loss of strength without yielding of beam's main reinforcement due to detachment of UHPFRC plates with the NC cover. Contrary to specimen TS1, the post-peak behavior of specimen was only characterized by the sudden reduction in the strength resulting in the brittle failure of the specimen.

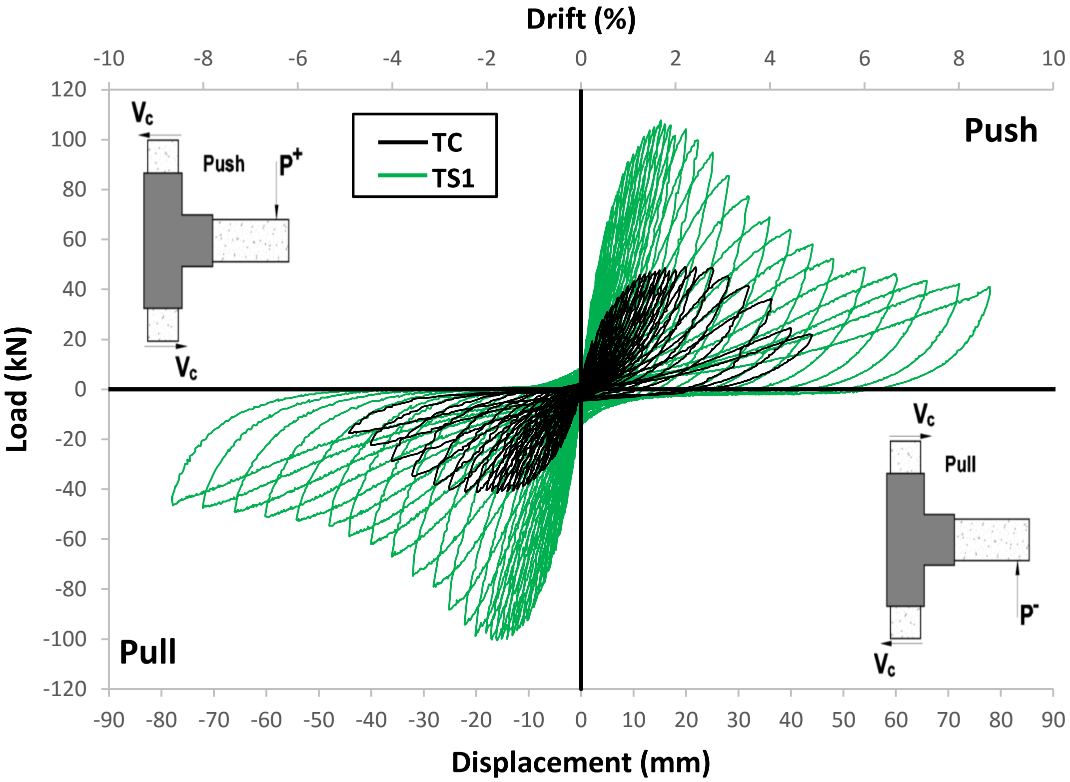

**Figure 4-29 Load-displacement hysteresis plot of Specimens TC and TS1**

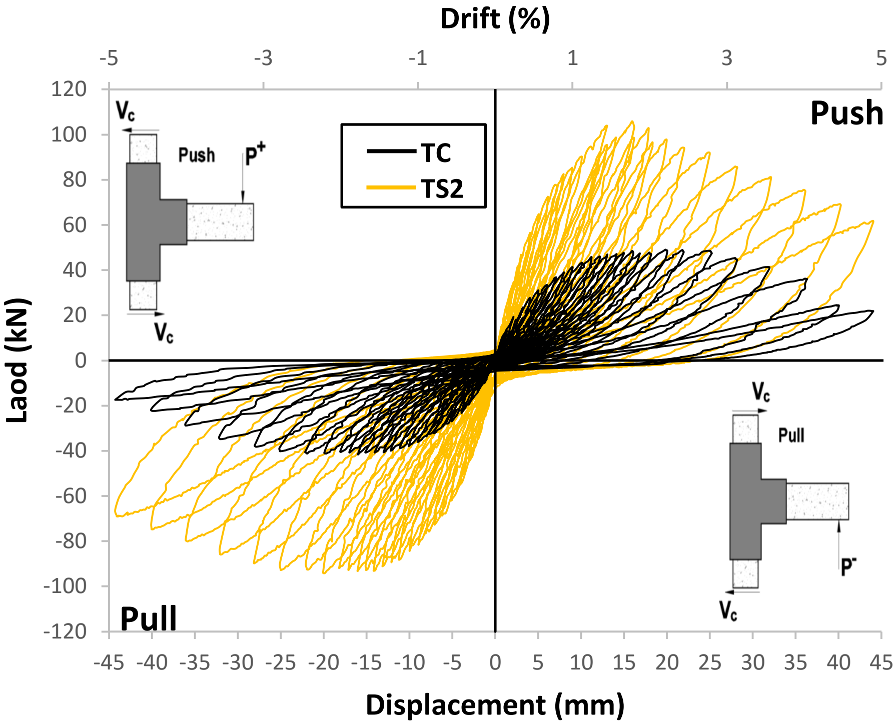

Figure 4-30 Load-displacement hysteresis plot of Specimens TC and TS2

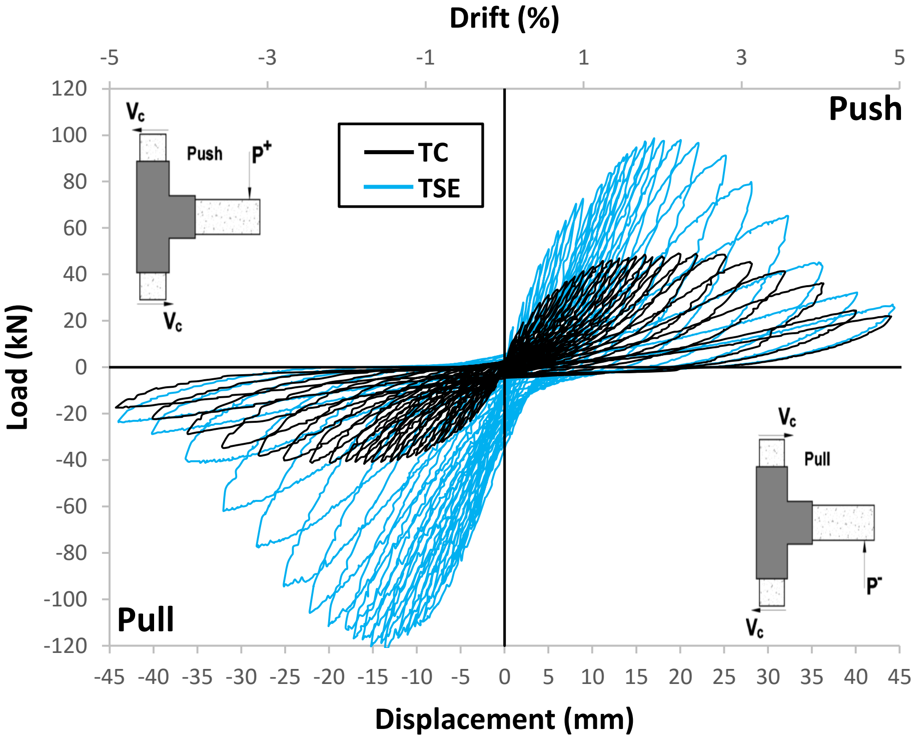

Figure 4-31 Load-displacement hysteresis plot of Specimens TC and TSE

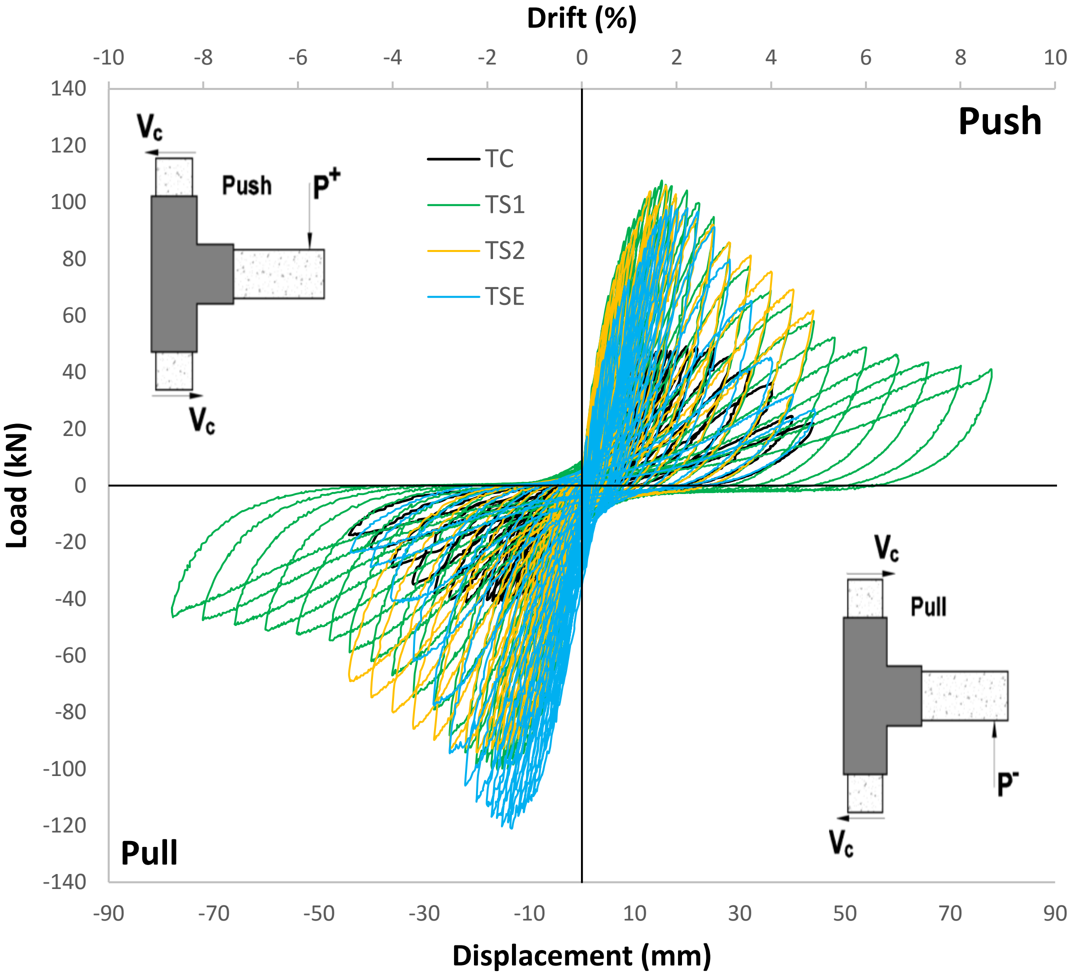

Figure 4-32 Comparison of hysteretic response of control and strengthened specimens

### 4.2.3 Load-Displacement Envelopes

Envelope curve is a load-deformation curve that envelopes the hysteretic response of structural component that is subjected to reverse cyclic loading and obtained by joining the peak points of each cycle of load-displacement hysteresis plot. The Cyclic envelope of the hysteresis loop of hysteretic load versus beam tip displacement (and drift) for control and strengthened specimens are shown in Figure 4-33. To study the efficiency of implemented retrofitting technique in terms of load carrying capacity (strength), displacement capacity, strength degradation, ultimate displacement (displacement corresponding to 20% reduction in the peak load) and post peak deformation capacity (ductility), envelope curves for control and strengthened specimens are plotted.

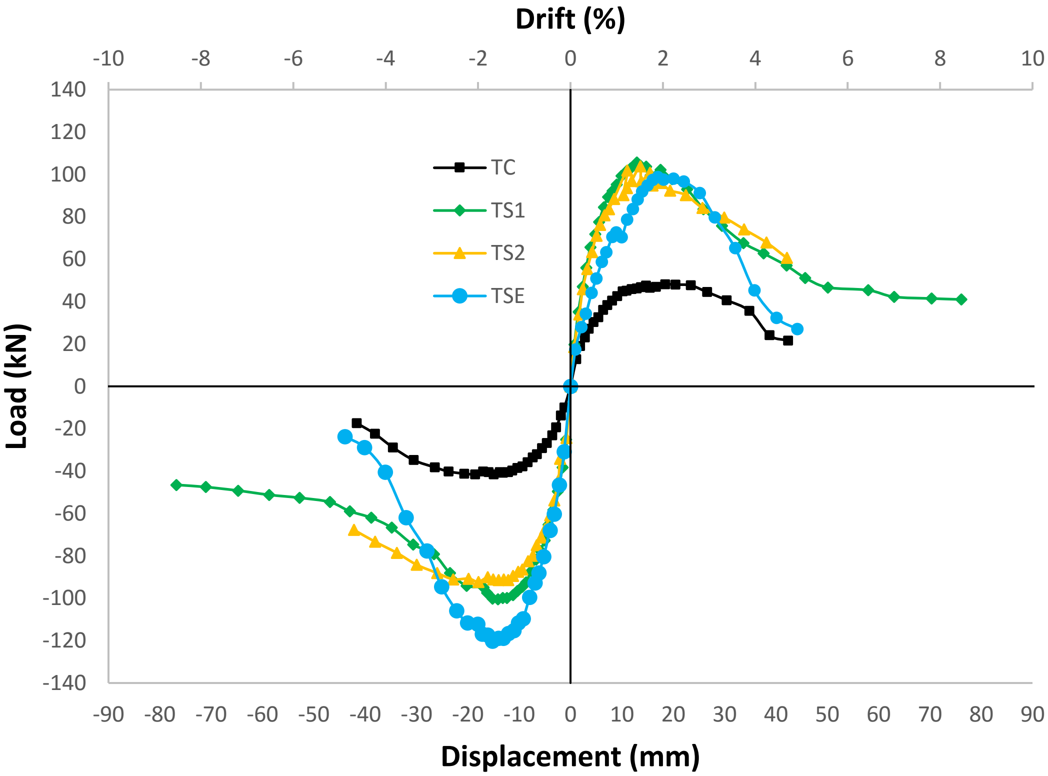

**Figure 4-33 Envelope curves of control and strengthened specimens**

The value registered for the peak load ($F_P$) and corresponding displacements ($\Delta_p$) for control and strengthened specimen are given in Table 4-4. For a better comparison of load carrying capacity, a strength index $I_F$ was calculated using the following equation and tabulated in the same table. The values reported for ultimate load and corresponding displacement were tabulated in the Table 4-6 which were used for estimation of displacement ductility.

$$\text{Strength index} = I_F = \frac{(F_{avg})_{strengthened}}{(F_{avg})_{control}} \qquad 4\text{-}3$$

$F_{avg}$ is the average value of the peak load in the positive and negative directions of loading.

From Table 4-4, it is observed that the in-situ casting of 30 mm thick UHPFRC jacket around the sandblasted NCSS provided the increase of load carrying capacity of about 2.3 and 2.2 times w.r.t the control specimen and this value is 2.44 for specimen TSE where 30 mm thick pre-fabricated UHPFRC plates were attached to RC core-subassembly using epoxy adhesive.

As a result of cyclic load reversal, test unit experiences a reduction in the strength. Cyclic strength degradation or deterioration was computed by comparing the registered peak strength to the residual load carrying capacity at 4.5% drift. The degradation in the peak strength was calculated for control, strengthened specimen using the following equation, and listed in Table 4-5.

$$\text{Strength degradation} = \lambda = \left[1 - \frac{F_{4.5\%}}{(F_{avg})_{peak}}\right] \text{x } 100 \qquad 4\text{-}4$$

The residual load carrying capacity of control specimen was less than 50% of its peak strength and this strength reduction was attributed to the brittle joint shear failure. It is observed that strength degradation was 73.4% for specimen TSE which was much higher and it was associated with the de-bonding of UHPFRC plates. For specimens TS1 and TS2, these values were 43.8% and 34.6%, respectively. Strength deterioration was much lower than the value registered for specimen TSE.

Specimen TS1 reached a drift equal to 8.7% against the 5% drift reached by the control specimen and specimen TSE could reach a drift of 5% only and exhibited the brittle failure due to detachment of UHPFRC plates. So, the in-situ casting of UHPFRC jacket around the sandblasted surface of normal concrete showed significant improvement in the displacement capacity of BCJ sub-assembly resulted into the ductile failure.

**Table 4-4 Data for the evaluation of strength factor**

| **Specimen** | **Positive direction** | | **Negative direction** | | **Strength Factor** |
|---|---|---|---|---|---|
| | $\boldsymbol{F_P^+}$ | $\boldsymbol{\Delta_P^+}$ | $\boldsymbol{F_P^-}$ | $\boldsymbol{\Delta_P^-}$ | **$I_F$** |
| | **kN** | **mm** | **kN** | **mm** | **%** |
| TC | 48.2 | 18.5 | -41.5 | -18.6 | - |
| TS1 | 105.6 | 12.9 | -100.5 | -14 | 2.3 |
| TS2 | 103.9 | 13.6 | -92.3 | -18 | 2.2 |
| TSE | 98.7 | 17 | -120.3 | -15.2 | 2.44 |

**Table 4-5 Data for the evaluation of strength degradation factor**

| Specimen | $(F_{avg})_{peak}$ | $F_{4.5\%}$ |  | $(F_{4.5\%})_{avg}$ | Strength degradation |
|---|---|---|---|---|---|
|  |  | Positive direction | Negative direction |  | λ |
|  |  | kN | kN | kN | % |
| TC | 44.85 | 21.6 | 17.4 | 19.5 | 56.5 |
| TS1 | 103.05 | 57 | 58.9 | 57.95 | 43.8 |
| TS2 | 98.1 | 60.6 | 67.7 | 64.15 | 34.6 |
| TSE | 109.5 | 30.1 | 28.2 | 29.15 | 73.4 |

**Table 4-6 Ultimate loads and corresponding displacements**

| Specimen | Positive direction |  | Negative direction |  |
|---|---|---|---|---|
|  | $F_u^+$ | $\Delta_u^+$ | $F_u^-$ | $\Delta_u^-$ |
|  | kN | mm | kN | mm |
| TC | 38.512 | 32.6 | -33.2 | -31.85 |
| TS1 | 84.5 | 25.65 | -80.4 | -26.1 |
| TS2 | 83.1 | 26.6 | -73.84 | -37.6 |
| TSE | 78.97 | 28.3 | -96.24 | -24.75 |

### 4.2.4 Damage Evolution and failure mode

**Control specimen TC**

The damage registered in terms of minor and major cracks for control specimen TC is depicted in Figure 4-34. The major damage occurred due to the formation of extensive concrete wedge mechanism followed by the spalling of the concrete. The specimen showed the classic joint shear failure mode combined with the slippage of beam's longitudinal bars within the joint region. It is observed that in the positive excursion, the beam upper face is in tension and upper corner of joint tends to open, whereas in the negative excursion, tension occurs in the beam's lower face and bottom corner of joint tends to open. The vertical cracks initiated at the upper and lower corner of the joint at a drift of ±0.5%, corresponding to a load of 18 kN and 23 kN during the positive and negative excursion, respectively. In the following cycles, these cracks did not develop.

During the 9th cycle at +1% drift, diagonal cracks appeared inside the joint panel. The two major diagonal tension cracks occurred inside the joint panel at -1% drift, corresponding to 38.2 kN load in the opposite direction forming an X-pattern and concrete wedge started to take shape. These diagonal cracks extended at both ends towards the outer and inner edge of columns, at higher displacement amplitudes. Crushing of concrete in the joint panel continued with the opening and closing of the cracks with further increase in the drift ratio. At -3.5% drift, corresponding to 34.8 kN load, the concrete cover on the inner face of the column just above the joint and at the sides of the beam near beam-joint interface spalled out. At the 26th cycle at ~±5% drift, the developed concrete wedge spalled out resulting in the significant reduction in the strength of a test unit. The two failure mechanisms are well highlighted: classical joint shear failure with severe diagonal cracks inside the joint core without yielding of main reinforcement and extensive concrete wedge mechanism. The condition of the specimen at the end of a test is shown in Figure 4-35.

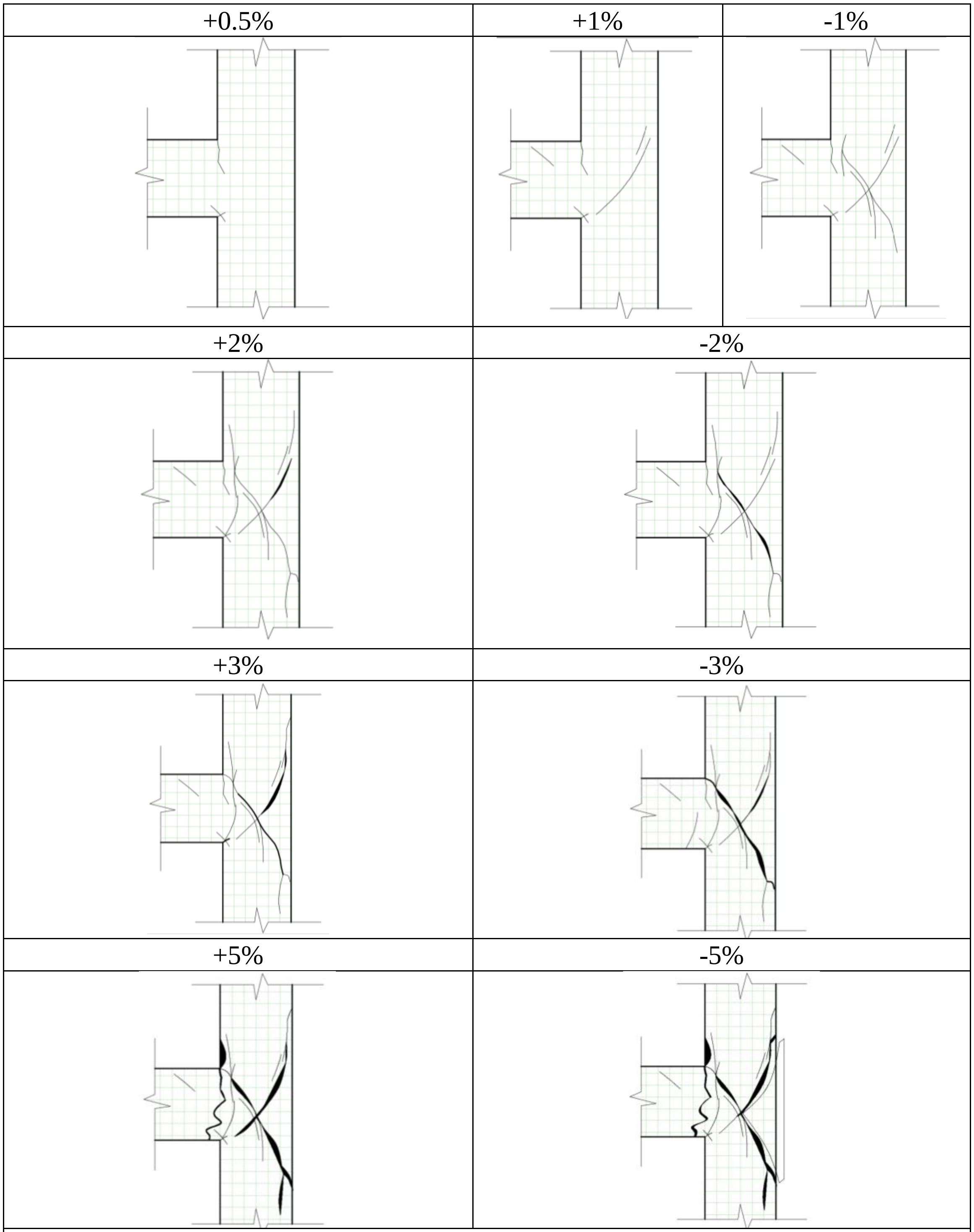

**Figure 4-34 Damage evolution of specimen TC**

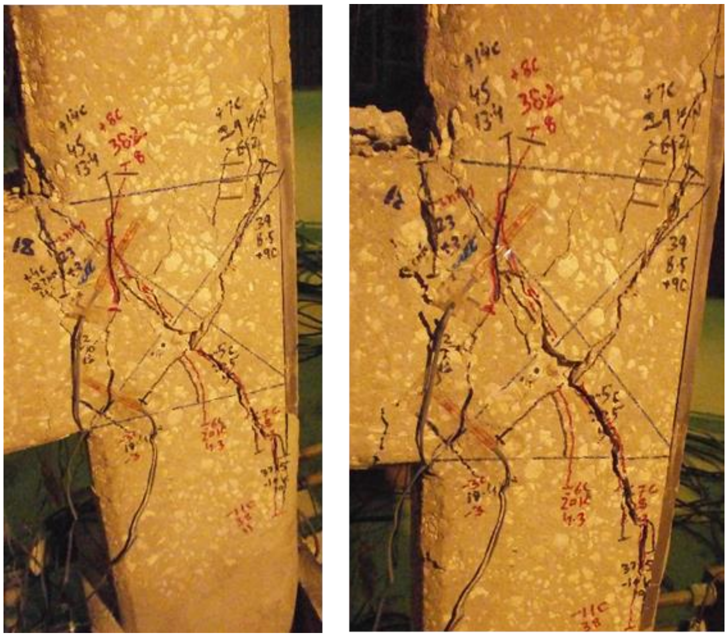

**Figure 4-35 Development and propagation of cracks in specimen TC**

## Specimen TS1 and TS2

The gradual development of minor and major cracks and major damage registered at the end of the test for specimens TS1 and TS2 is depicted in Figure 4-36 and Figure 4-38. At the early stage of testing, minor shear cracks appeared in the beam where it was not reinforced with UHPFRC. These cracks did not develop, as test continued. The significant damage was registered due to the formation of vertical flexural cracks in the beam and beam-joint interface. During the test, cracks had been observed at the edges and corners of UHPFRC jacket at the peak load resulting in the detachment of UHPFRC jacket from the RC core-subassembly in the subsequent loading history.

### Specimen TS1

The test unit showed the minor diagonal cracks in the beam where it was not encased in the UHPFRC-jacket up to a drift of ±1%. These cracks did not play the significant role in the disintegration of the specimen. In the negative excursion, the first sign of damage in UHPFRC-jacket in terms of vertical flexural cracks had been observed in the beam near the lower corner of joint at a drift of -0.22% corresponding to a load of 37.5 kN. However, at the third cycle at +0.33% drift, the first vertical flexural crack, in the positive excursion, occurred in the beam, corresponding to a load of 47.3 kN. In the following cycles, these vertical cracks were extended towards each other and localized in the beam at the beam-joint interface. The crack opening and closing were monitored through displacement transducers. The crack width was less than 1 mm up to a drift of ±1%. In the 14th cycle, at a drift of ±1.6%, when the maximum load was imposed at the beam tip, the crack width was 4.1 mm. The crack width was reported to be 22.5 mm at a drift closer to ±5%. Strain monitoring data showed the yielding of beam's longitudinal reinforcement at a drift of ±6.5%. Few diagonal cracks of minor importance appeared around major cracks.

At the 14th cycle at ±1.6% drift, when the specimen reached the peak strength, the damage was observed on the edges and corners of UHPFRC-jacket surrounding the inner face of upper and lower column and upper and lower face of the beam, as shown in Figure 4-37. These cracks developed in the subsequent load history. As a result, the detachment of UHPFRC-jacket started to occur at a drift of about ±2.5%.

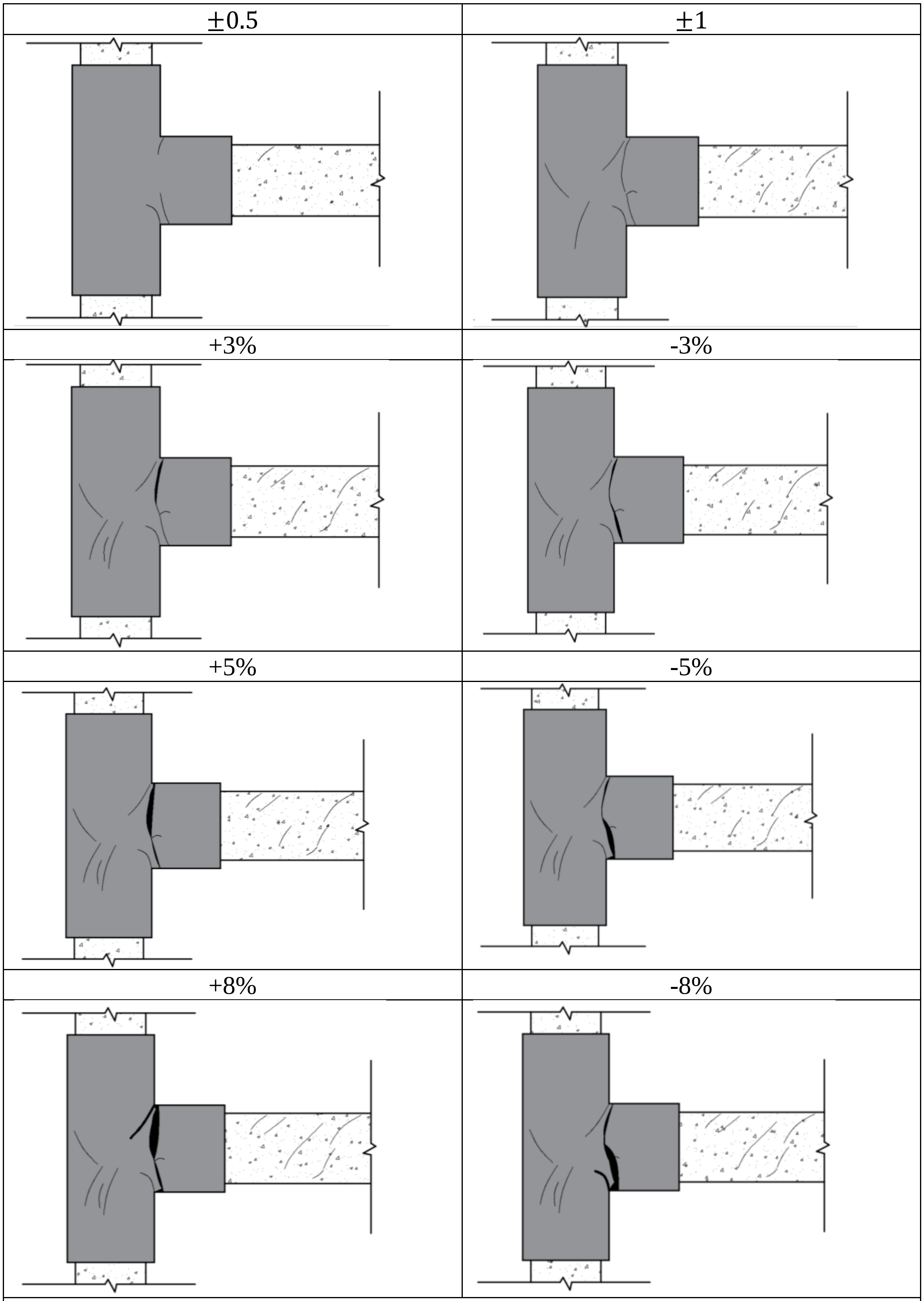

±0.5

±1

+3%

-3%

+5%

-5%

+8%

-8%

**Figure 4-36 Damage evolution of specimen TS1**

**Figure 4-37 Development and propagation of cracks in specimen TS1**

### Specimen TS2

The minor damage seemed in terms of diagonal shear cracks in the beam where it was not encased in the UHPFRC-jacket up to a drift of ±1.22%. These cracks did not cause too much damage to the specimen as they were not developed significantly in the subsequent loading history. In the positive excursion, the first sign of damage in UHPFRC-jacket in terms of vertical flexural cracks had been observed at the beam-joint interface near the upper corner of joint at a drift of +0.5% corresponding to a load of 47.6 kN. However, at the fifth cycle at -0.5% drift, the first vertical flexural crack, in the negative excursion, occurred in the beam-joint interface near the lower corner of joint, corresponding to a load of 61.3 kN. In the following cycles, the third flexural crack formed at the center of the beam-joint interface at +1% drift. These vertical cracks were extended towards each other and localized in the beam at the beam-joint interface. The crack opening and the closure was monitored through displacement transducers. The crack width was less than 1 mm up to a drift of ±1%. In the fifteenth cycle, at a drift of±1.9%, when the maximum load was imposed at the beam tip, the crack width was 3.9 mm. As test continued, a significant crack opening was observed and the crack width was reported to be 20.2 mm at a drift closer to±5%. Few diagonal cracks of minor importance appeared around major cracks. The properties of tested specimens are given in Table 4-7.

At the 17th cycle at ±1.9% drift, when the specimen reached the peak strength, cracks had been observed on the edges and corners of UHPFRC-jacket covering the inner face of upper and lower column and side faces of the beam, as shown in Figure 4-39. These cracks developed in the subsequent load history. As a result, the detachment of UHPFRC-jacket started to occur at a drift of about ±2.7%. The de-bonding of the jacket is quite visible at the end of the test (drift equal to ±5%), as shown in Figure 4-39. The condition of a specimen after the completion of the test is shown in Figure 4-40.

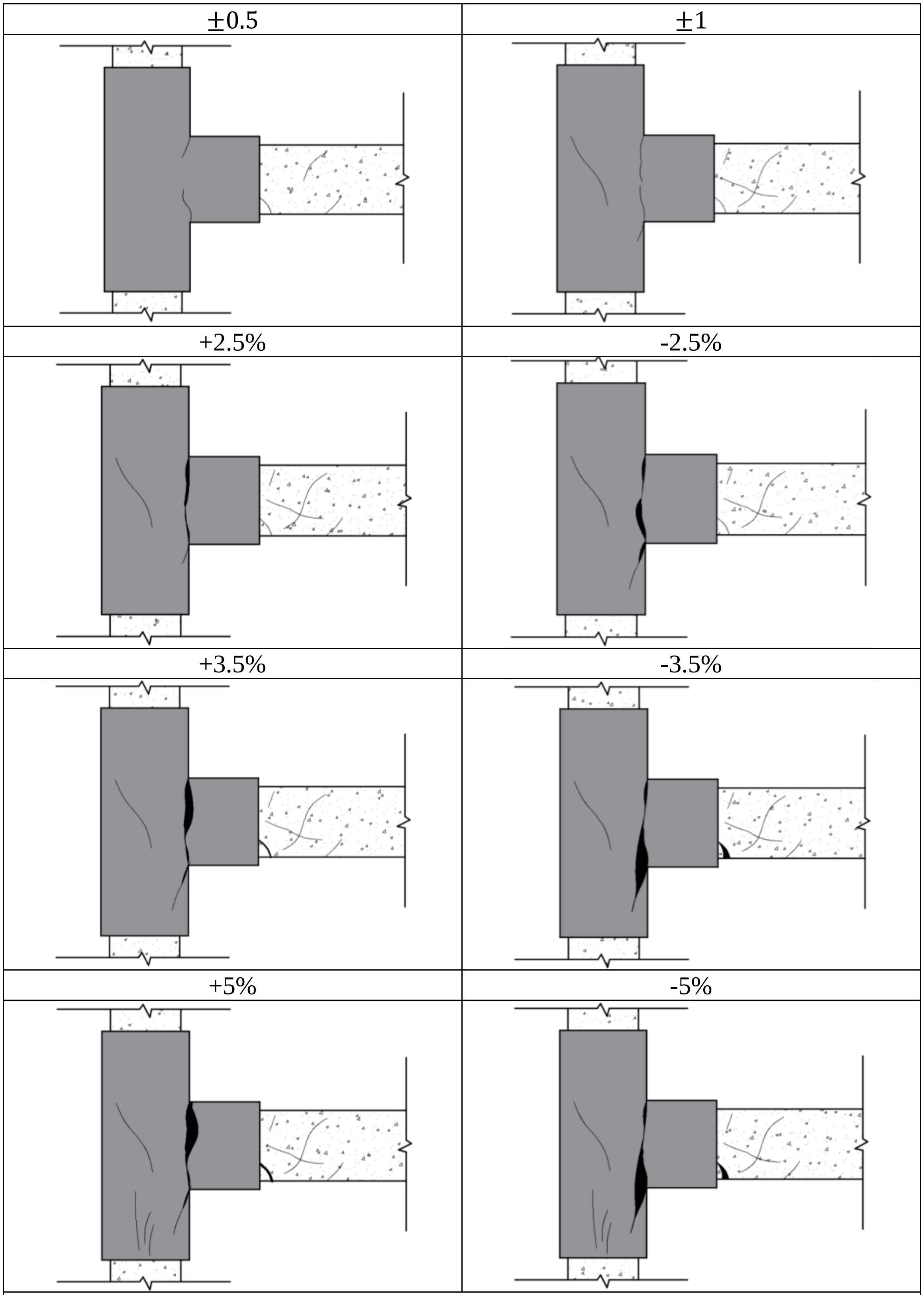

±0.5

±1

+2.5%

-2.5%

+3.5%

-3.5%

+5%

-5%

**Figure 4-38 Damage evolution of specimen TS2**

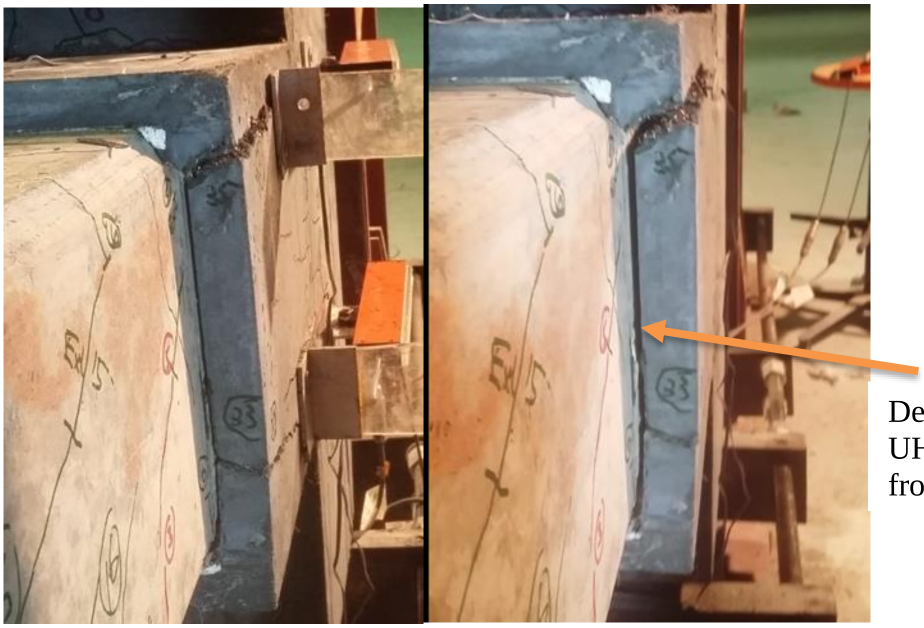
Detachment of UHPFRC jacket from NCSS

**Figure 4-39 Back side of the beam after the test completion and detachment of UHPFRC for test unit TS2**

**Figure 4-40 Specimen TS2 at the end of the test**

### Specimen TSE

Specimen TSE was subjected to reverse cyclic loading according to the loading protocol given in Table 3-14. The evolution of damage under cyclic loading is depicted in Figure 4-44. During testing, the first major damage was registered in terms of localized vertical flexural crack at beam joint interface, which developed in the subsequent loading history and monitored through displacement transducers. The second major damage occurred in the test unit due to the detachment of UHPFRC-plates from the NCSS resulting into the significant reduction in the strength of the test unit.

At the fifth cycle at ±0.5% drift, the portion of the beam, which was not reinforced with UHPFRC, showed diagonal cracks corresponding to the load of 80 kN, which did not develop, as the test continued. The second series of diagonal cracks of minor importance had been observed at the 18th cycle at ±2% drift.

The first series of vertical flexural cracks appeared at the lower corner of joint at a drift of -0.22%, corresponding to a load of 47 kN. At the 9th cycle at +1% drift, cracks had also seemed at the upper corner of joint. The major damage in terms of vertical flexural cracks occurred at the beam-joint interface at +1.5% drift, corresponding to a load of 87 kN. These cracks localized at the beam-joint interface and monitored through displacement transducers. The crack width was 0.5 mm at ±1% drift and increased up to 4.13 mm at a maximum strength of test unit at 1.9% drift. The crack width increased significantly after ±3% drift and reached to value of 25.2 mm at ±3.5% drift and this value increased up to 30 mm at the end of the test. A few cracks of minor importance had been observed in the column and inside the joint panel around the major cracks.

The major reason behind the sudden reduction in the strength of the test unit was the detachment/de-bonding of the UHPFRC prefabricated plates. This unit was strengthened with pre-fabricated T, I and small rectangular shape UHPFRC plates using epoxy adhesive. These plates have two types of contacts. At edges, each plate is joined with other UHPFRC plates with epoxy and in between edges, the plate has a contact with NCSS. The major problem occurred at the edges of T-plate. At one edge T-plate had a contact with the I-plate and on another edge, it had a contact with the small rectangular plate, as shown in Figure 4-41.

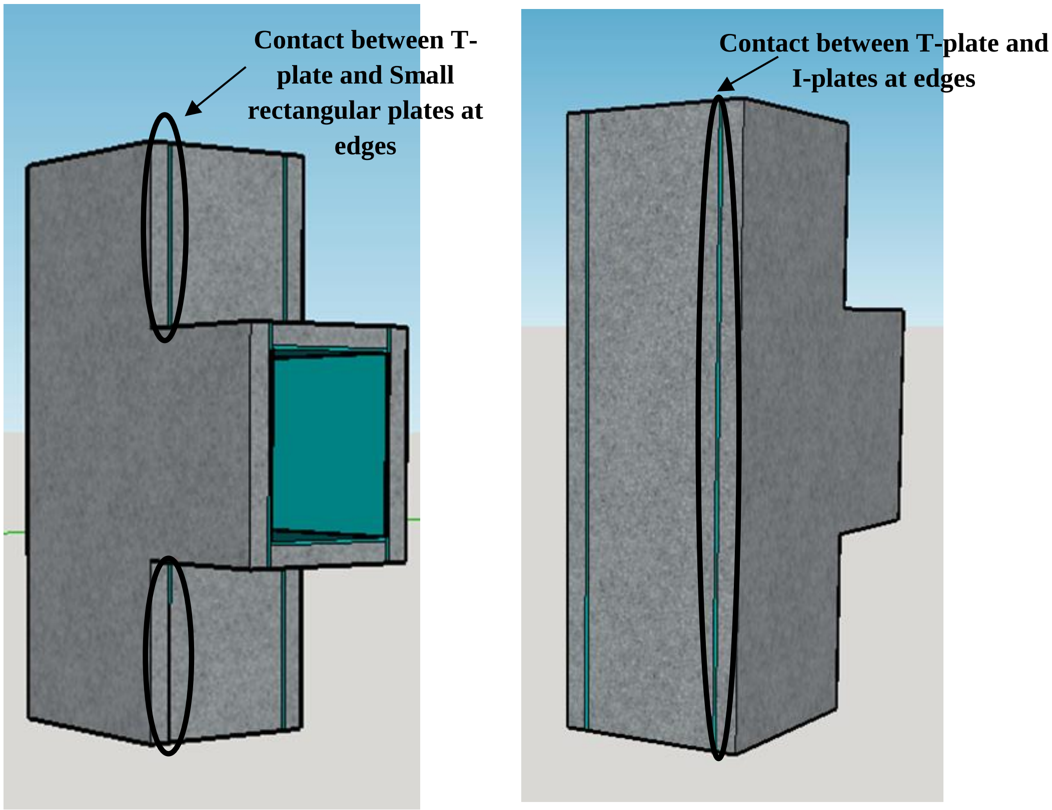

**Figure 4-41 Contacts of T-plate at edges**

These plates combined with RC core assembly performed their function efficiently up to ±2% drift. The whole assembly acted together and resist the forces and deformations developed due to the imposed displacement at beam tip as a single unit. At the 19th cycle at -2.22% drift, the contact between T-plate and rectangular plate over lower column was effected by the formation of cracks in the epoxy, as shown in Figure 4-42. This crack developed in the subsequent loading history and separation between UHPFRC plates started to occur at edges. In the positive excursion, at a 21st cycle at +2.8% drift, cracks appeared at the contact between T-plate and rectangular plate over an upper column, as shown in Figure 4-43. The performance of the whole assembly was severely damaged due to the formation of localized vertical cracks at the beam-joint interface and complete separation at one edge of T-plate from the other plates, as shown in Figure 4-45. As test continued, T-plate did not react and deform with the other assembly. Therefore, all stresses were taken up by the RC core assembly at front and back face of a unit at the 22nd cycle at ±3.1% drift, corresponding to a load of 79 kN. Control specimen TC showed the maximum capacity of 49.07 kN. RC core-assembly could not bear the stresses imposed by a load of 79 kN and T-plate with the cover of RC core assembly was pulled out with the thrust as it is resisted by the contact between T-plate and I-plate on the other edge. Therefore, a chunk of concrete along with UHPFRC plate was separated out from the assembly and resulted in the sudden reduction in the strength of the test unit. The small rectangular plates attached to the inner face of a top and a bottom column showed the same behavior. The condition of the specimen after the completion of the test and complete separation of UHPFRC plate with concrete cover is shown in Figure 4-45.

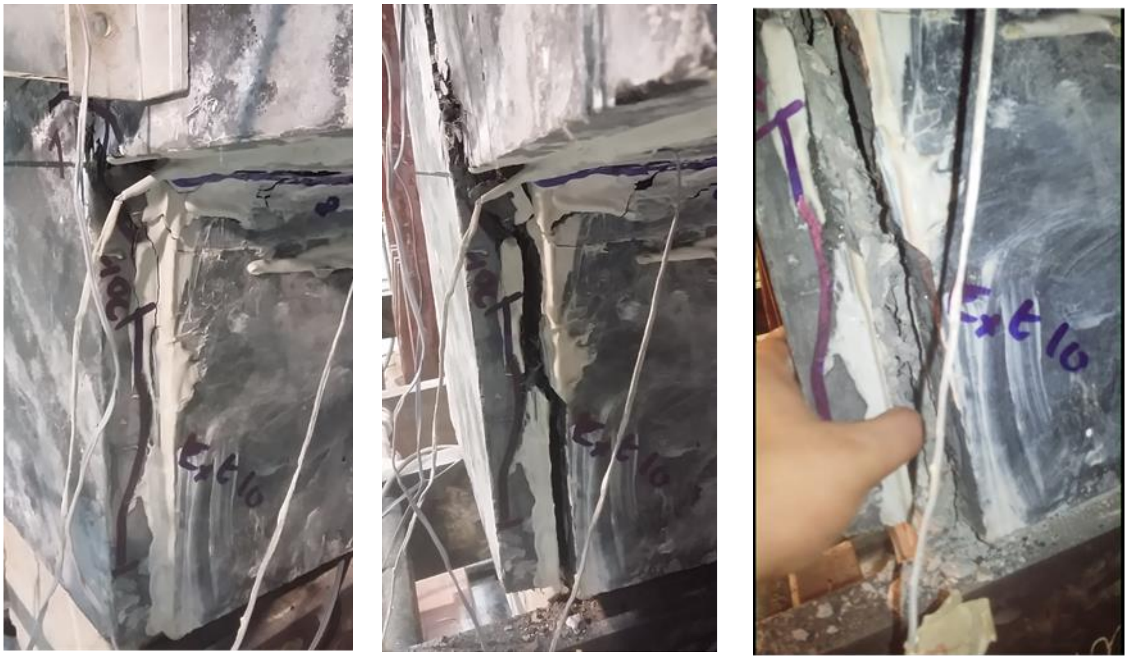

-2.2% -3% -4%

Figure 4-42 Development of crack at edges of T-plate and rect-plate in lower column

+2.8% +3% +4%

Figure 4-43 Development of crack at edges of T-plate and rect-plate in upper column

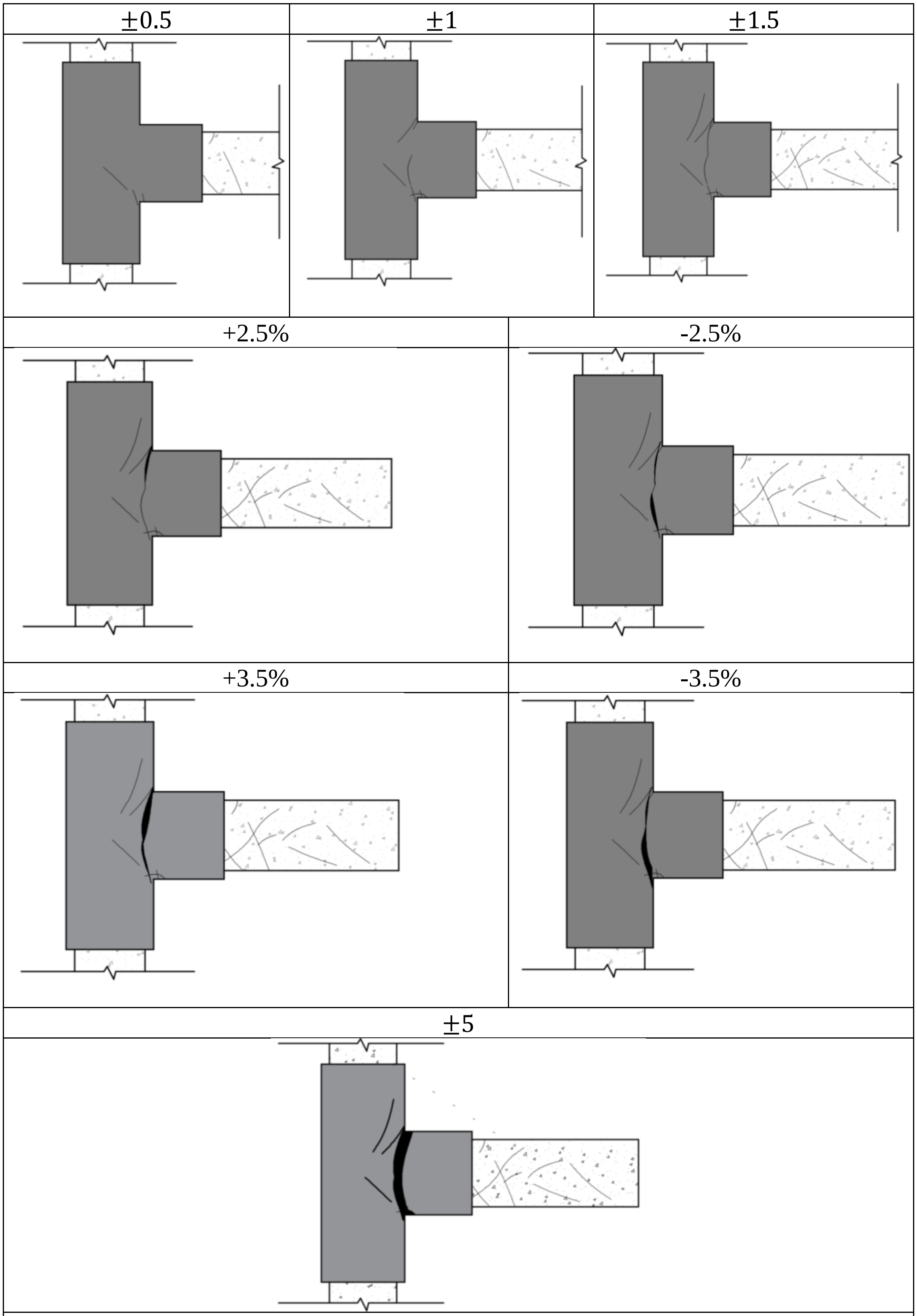

±0.5

±1

±1.5

+2.5%

-2.5%

+3.5%

-3.5%

±5

**Figure 4-44 Damage evolution of specimen TSE**

**Figure 4-45 Specimen TSE after test completion (LEFT) and Separation of plates with concrete cover (Right)**

**Table 4-7 Properties of tested BCJs**

| **Specimen** | **Cracking load** | **Crack width at peak load** | **Crack opening at the end of test** | **Failure crack type** | **Failure type** |
|---|---|---|---|---|---|
| | **kN** | **mm** | **mm** | | |
| TC | 18 | 1.2 | 5.1 | Diagonal shear | Brittle |
| TS1 | 37.5 | 4.1 | 18.5 | Vertical flexural | Ductile |
| TS2 | 47.6 | 3.9 | 15.2 | Vertical flexural | Ductile |
| TSE | 47 | 4.3 | 20.1 | Debonding | Brittle |

### 4.2.5 Secant stiffness characteristics

Beam-column assembly, when subjected to large cyclic load reversals, will exhibit the gradual degradation in stiffness. Stiffness degradation in reinforced concrete components is attributed to inelastic deformations, cracking, loss of concrete strength, loss of bond, bar slip or high axial and shear stresses. The level of stiffness degradation depends on the geometry of the structure, material properties, reinforcement detailing and loading protocol such as the number of cycles, the sequence of cycles and intensity of loading in each cycle. For each test unit, secant stiffness is evaluated during the drift evolution and gleaned in Figure 4-47. The secant stiffness is taken as the slope of the straight line joining the peaks of the positive and negative cycles, as shown in Figure 4-46. Secant stiffness for each hysteresis loop can be evaluated using the relationship given in the Eq. 4-5.

$$\text{Secant stiffness of ith cycle} = K_i = \frac{\left|F_{P,i}^{+}\right| + \left|F_{P,i}^{-}\right|}{\left|\Delta_{P,i}^{+}\right| + \left|\Delta_{P,i}^{-}\right|} \qquad \text{4-5}$$

Where $K_i$ is the secant stiffness of specimen at ith cycle; $F_{P,i}^{+}$ and $F_{P,i}^{-}$ are peak loads in positive and negative excursion at ith cycle, respectively; $\Delta_{P,i}^{+}$ and $\Delta_{P,i}^{-}$ are the corresponding imposed displacement at the ith cycle.

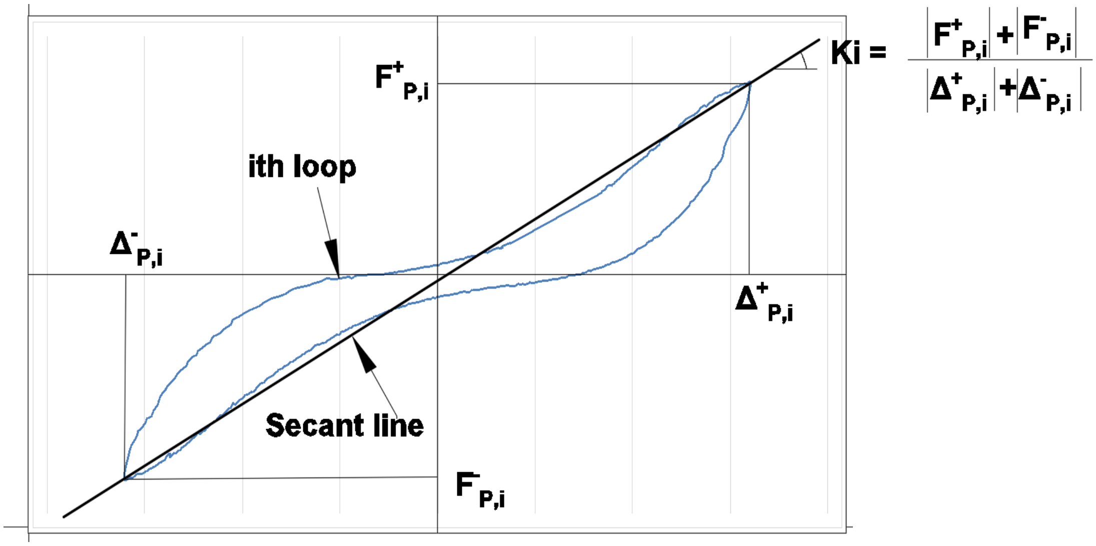

**Figure 4-46 Schematic representation of secant stiffness**

According to the secant stiffness-displacement evolution curve, strengthened specimens TS1 and TS2 presented higher secant stiffness than TC. However, during the evolution of drift, secant stiffness of TSE remained higher than TC at least up to ±4% drift. Later on, it matches with the stiffness of control specimen indicating higher stiffness degradation of TSE. For better comparison between the performance of two adopted strengthening solutions and control specimen, secant stiffness at three feature points is compared. The initial secant stiffness of TS1, TS2 and TSE was 2.73, 2.86 and 2.2 times higher than the value registered for the control specimen. This increment is attributed to larger section comprised of UHPFRC and NC and a higher level of joint confinement because of UHPFRC jacketing. The reduction in the initial secant stiffness of specimens in the virgin and retrofitted states was reported to be more than 12%, 26.3%, 35.1% and 30.4% for specimens TC, TS1, TS2 and TSE, respectively when the specimen showed the first crack. The strengthened specimens showed higher degradation in the stiffness. This is attributed to crack concentration at the beam-joint interface. At peak load point, the secant stiffness of specimens in the retrofitted state provided an increase of about 3.3, 3.0 and 2.6 times for specimens TS1, TS2 and TSE with respect to control specimen. The implemented retrofitting solution assured the increment of about 2.8, 2.9 and 2.5 times in secant stiffness at the ultimate load point for specimens TS1, TS2 and TSE over control specimen TC.

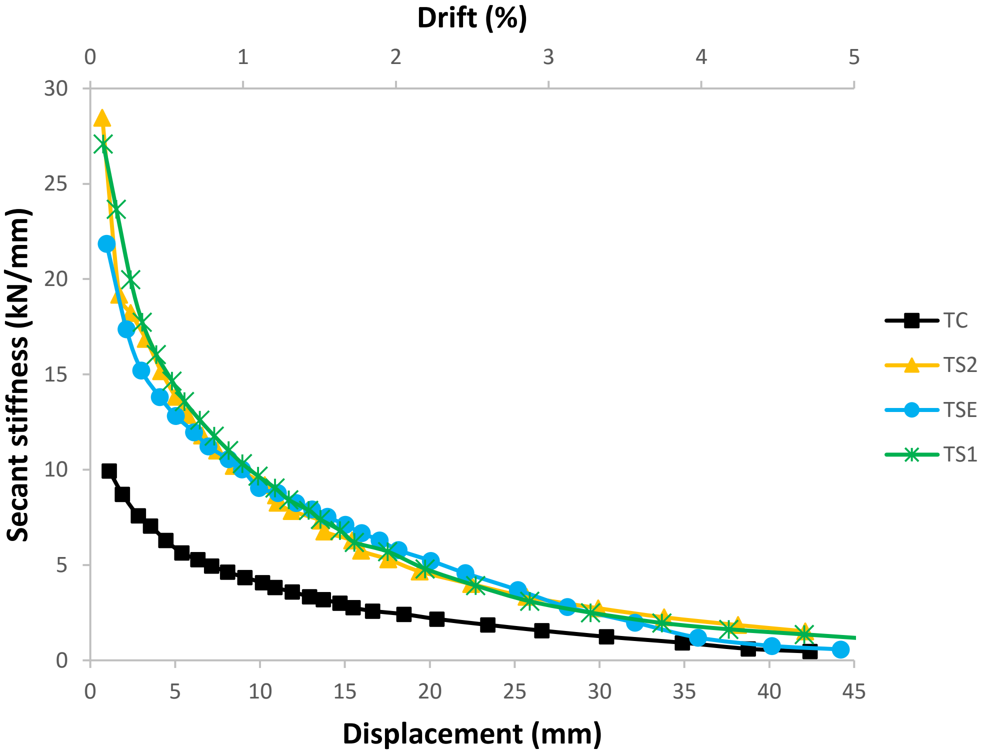

Figure 4-47 Secant stiffness evolution in specimens TC, TS1, TS2 and TSE

### 4.2.6 Energy dissipation

One of the most promising approaches for establishing the efficient method for improving the lateral load resisting system is by predicting the response of structures to earthquake loading through an energy. The total energy input to the structure due to earthquake ground motion can be resisted by the sum of K.E, the elastic strain energy, the energy dissipated through inelastic deformations and the energy dissipated through equivalent viscous damping. In order to make the economical earthquake resistant structure, the major portion of the input energy should be dissipated either through plastic deformations or by viscous damping systems. The use of inelastic deformations of structural materials and structural components in dissipating the energy is achieved by making the structure ductile with ductile materials and ductile type structural components.

The amount of energy dissipation per cycle ($E_i$), is calculated from the enclosed area in each loading cycle, as presented by the hysteretic response of hysteretic load-imposed displacement, as shown in Figure 4-48. The summation of the dissipated energy w.r.t the increment in the drift results into the cumulative energy dissipation at each given level of drift. Figure 4-49 presents the evolution of energy dissipation capacity of control and strengthened specimens with the increasing level of drift and imposed displacement at the free end of the beam. It can be interpreted from Figure 4-49 that the strengthening solutions had significantly improved the energy dissipation capacity of the test units. The strengthened specimen TS1, in which the strengthening solution involves the in-situ casting of UHPFRC around the sandblasted NCSS had provided much higher energy dissipation capacity than the specimen TSE which was strengthened with prefabricated UHPFRC plates and epoxy resins.

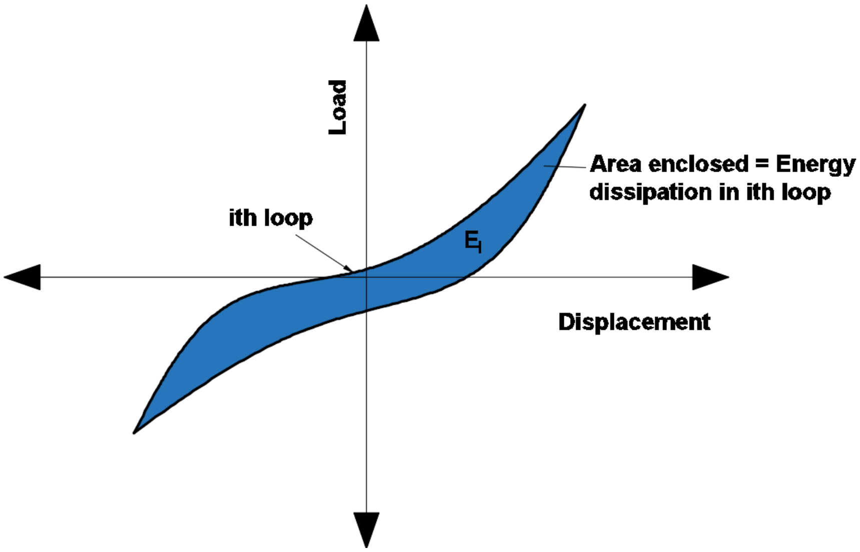

**Figure 4-48 Representation of energy dissipation per cycle**

For a better comparison between two strengthening solutions and the control specimens, three feature points have been selected. These feature points are peak load point (point 1), the ultimate load point (point 2), and the collapse load point (point 3). The cumulative energy dissipated by the control specimen TC at feature point 1, point 2 and point 3 were 2392 kN-mm, 5251 kN-mm and 6346 kN-mm, respectively. The corresponding values were 4117 kN-mm, 11897 kN-mm, 32779 kN-mm and 4025kN-mm, 11180 kN-mm, 17882kN-mm and 6053kN-mm, 12538 kN-mm, 16976 kN-mm for specimens TS1, TS2 and TSE, respectively. Cumulative energy dissipated by TS1 at feature point 1, point 2 and point 3 were 1.72, 2.27 and 5.17 times greater than those of TC, indicating that strengthening the BCJ by the in-situ casting of UHPFRC around the rough NCSS had significantly improved the energy dissipation capacity. This behavior was mainly attributed to the contribution of UHPFRC jacket, higher level of confinement provided by jacket, higher toughness and crack bridging ability of UHPFRC, friction between cracks, opening and closing of cracks, localization of plastic hinge at beam-joint interface, and above all the yielding of the beam's main reinforcement which had not been observed even in case of specimen TSE. The cumulative energy dissipated by TSE at the three feature points were 2.5, 2.4 and 2.7 times greater than those dissipated by the control specimen TC.

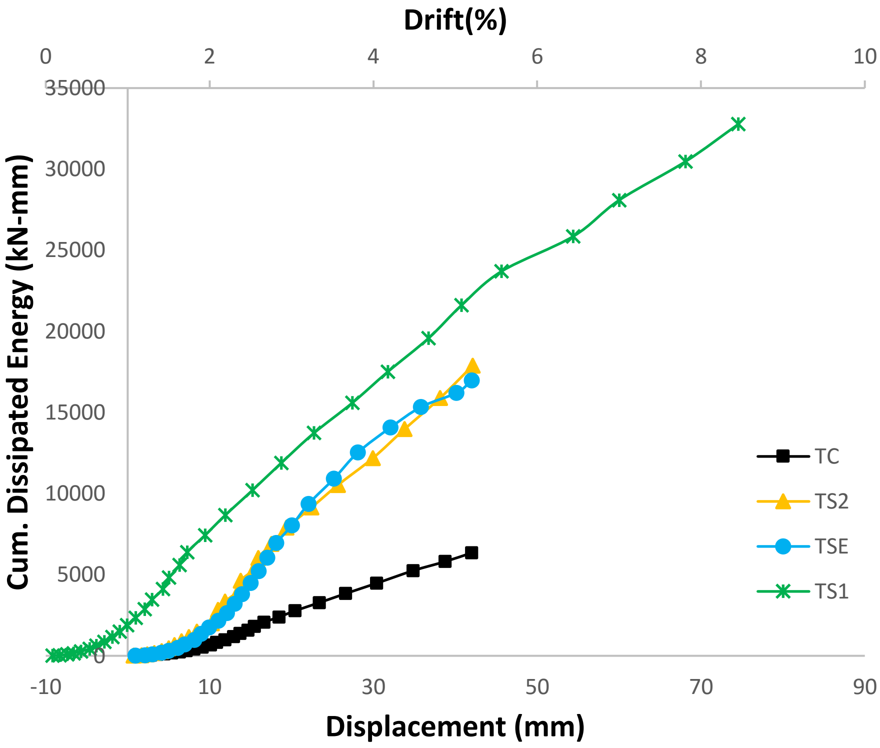

**Figure 4-49 Evolution of cumulative energy dissipation in specimens TC, TS1, TS2 and TSE**

The energy dissipated by specimens TC and TS1 during each loading cycle is shown in Figure 4-50. The comparison showed that in every cycle, specimen TS1 dissipated more energy than specimen TC. The amount of energy dissipation in a cycle is more than the value registered in the previous cycle. This trend is attributed to the large inelastic deformations. However, this trend was continued up to 24th cycle for specimen TC and later on this value started to reduce due to significant strength degradation. However, specimen TS1 showed the same trend till the end of the test. TS1 could reach the drift of 8.7% due to the formation of localized plastic hinge at the beam-joint interface with the yielding of beam’s main reinforcement resulting into the ductile failure of the beam at the beam-joint interface. Therefore, specimen TS1 exhibited excellent energy dissipation capacity among all the specimens. The same trend was found between specimen TC and TS2, as shown in Figure 4-51.

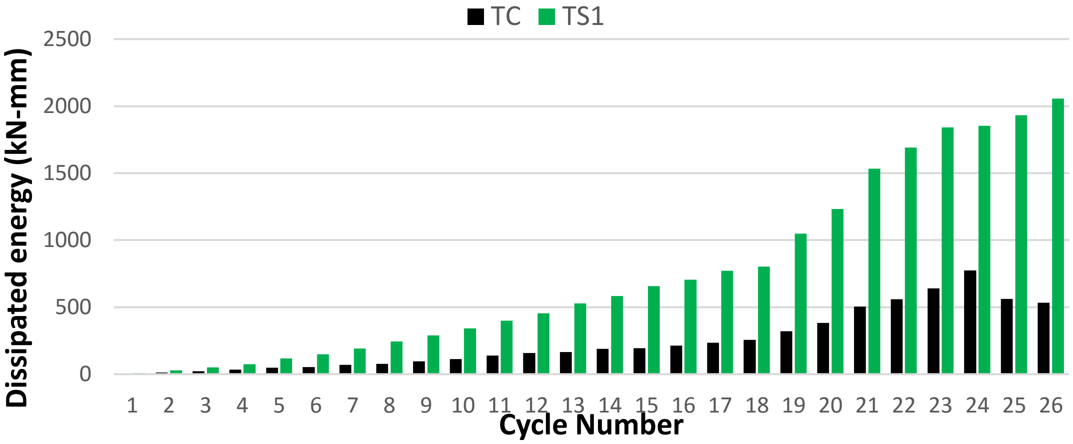

**Figure 4-50 Dissipated energy in each cycle of specimens TC and TS1**

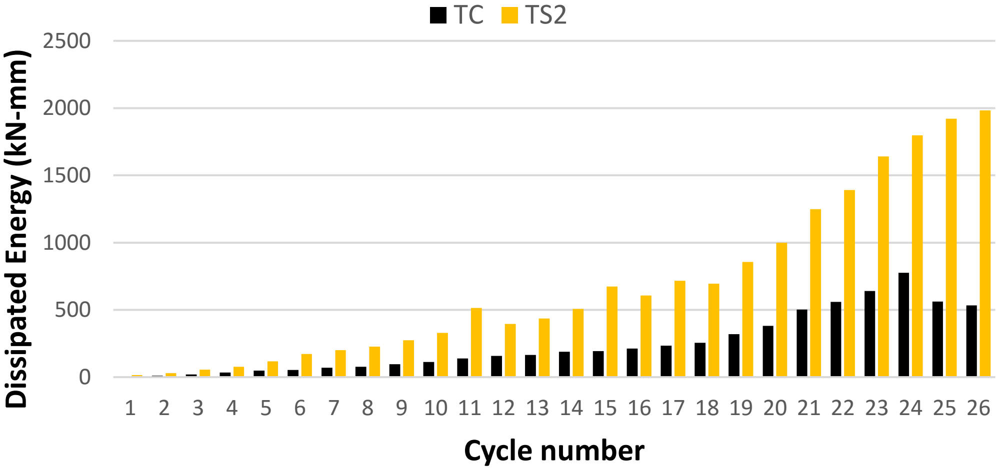

**Figure 4-51 Dissipated energy in each cycle of specimens TC and TS2**

Figure 4-52 shows the performance of specimens TC and TSE in terms of energy dissipation capacity during each cycle. Specimen TSE dissipated more energy than unit TC during each cycle. After the 22nd cycle, the dissipated energy start reducing due to high strength degradation of specimen TSE. The same trend was observed in specimen TC after 24th cycle.

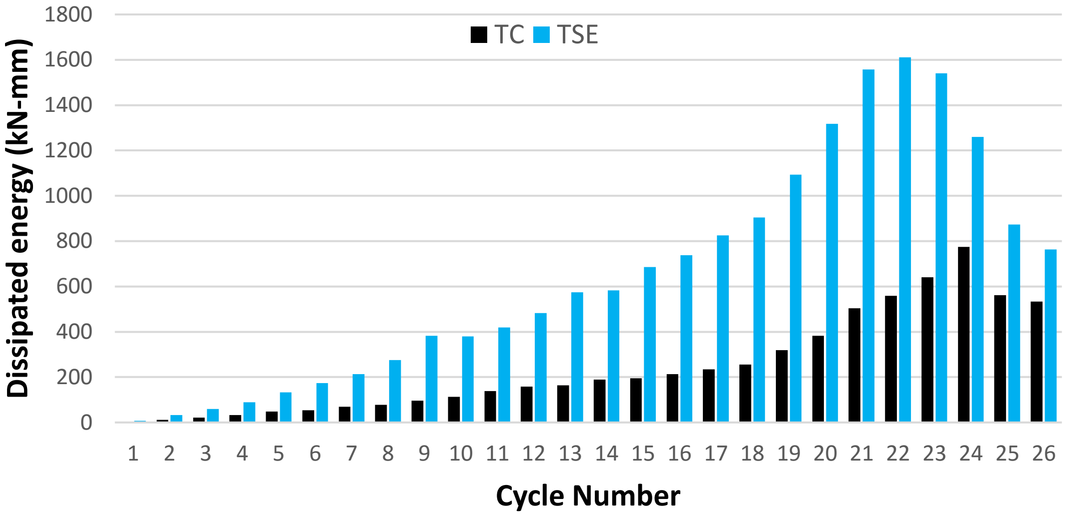

**Figure 4-52 Dissipated energy in each cycle of specimens TC and TSE**

The performance of Specimen TS1 and TSE, strengthened using different techniques, in terms of energy dissipation capacity is compared in Figure 4-53. Both specimens dissipated almost same energy up to 22nd cycle. The energy dissipation capacity of specimen TSE starts reducing after 22nd cycle. This reduction was so abrupt that at 22nd cycle, test unit dissipated 1610 kN-mm and this value was reduced to 763 kN-mm at 26th cycle. This reduction is attributed to a sudden reduction in the strength of specimen due to detachment of prefabricated UHPFRC plates from RC core sub-assembly with the concrete cover. This strength degradation made the specimen unstable and resulted in the brittle failure of the test unit. The high dissipation capacity up to 22nd cycle is attributed to the contribution of

UHPFRC jacket, higher level of joint core confinement provided by the jacket, higher toughness, ductility, strain hardening behavior and crack bridging ability of UHPFRC, friction between cracks, opening and closing of cracks. However, specimen TS1 performed efficiently under reversed cyclic loading and dissipated higher energy in each cycle as compared to the value registered in the previous cycle. This trend was continued until the end of the test. The additional factors that played a key role in energy dissipation were the plastic hinge formed in the beam at the beam-joint interface and the yielding of beam's main reinforcement.

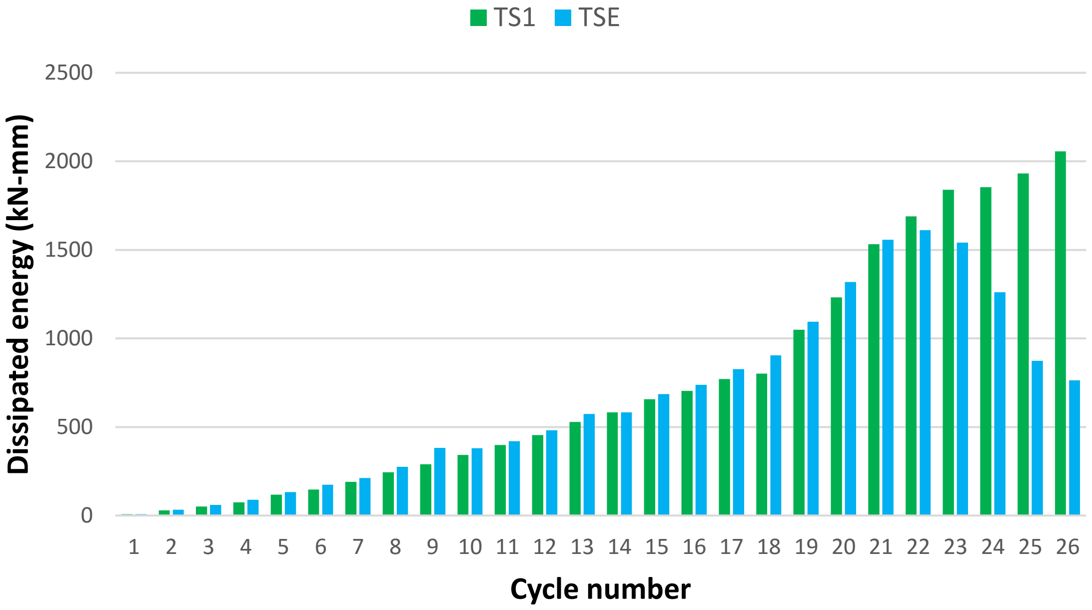

**Figure 4-53 Dissipated energy in each cycle of specimens TS1 and TSE**

### 4.2.7 Displacement Ductility

It is not viable to keep the structure under elastic range in the event of severe earthquake ground motion and it undergoes large inelastic deformations. These deformations will increase significantly and stiffness of structure can degrade dramatically if not properly designed. Under these large inelastic deformations, the structure should have a potential to remain stable without collapse i.e. it should not exhibit the strength degradation. Ductility specifies the aptitude of structure to undergo large inelastic cyclic deformation during its post-peak regime under severe seismic shocks without excessive deterioration in its peak load. A ductile structure has a potential to sustain several cycles of inelastic deformations with a slight reduction in the strength. Various response parameters of deformations are used to express the ductility ratios, such as displacement, rotation and curvature. The displacement ductility ratio in hysteretic loading is based on the load-displacement envelope curve of hysteretic loops that delineates the relation between strength and displacement.

Ductility index is calculated as the ratio of the ultimate displacement and the corresponding displacement present when yielding occurs.

$$\text{Displacement ductility ratio}= \mu_{\Delta} = \frac{\Delta_u}{\Delta_y} \qquad 4\text{-}5$$

When calculating ductility index the definition of the yield displacement often causes difficulties since load-displacement envelope may not have a well-defined yield point. This may happen due to the inelastic response of the material or due to the formation of plastic hinges in different components of the structure at different load values or due to longitudinal bars yield at different load levels [43]. To estimate the yield displacement alternate definitions have been proposed by the researchers and illustrated in Figure 4-54.

R. Park recommends the calculation of yield point based on reduced stiffness equivalent elasto-plastic yield method. Because it is the most realistic definition for reinforced concrete structures and it includes the reduction in the stiffness due to cracking near the end of the elastic range. In the present research work, yield displacement is calculated based on reduced stiffness equivalent elasto-plastic yield method.

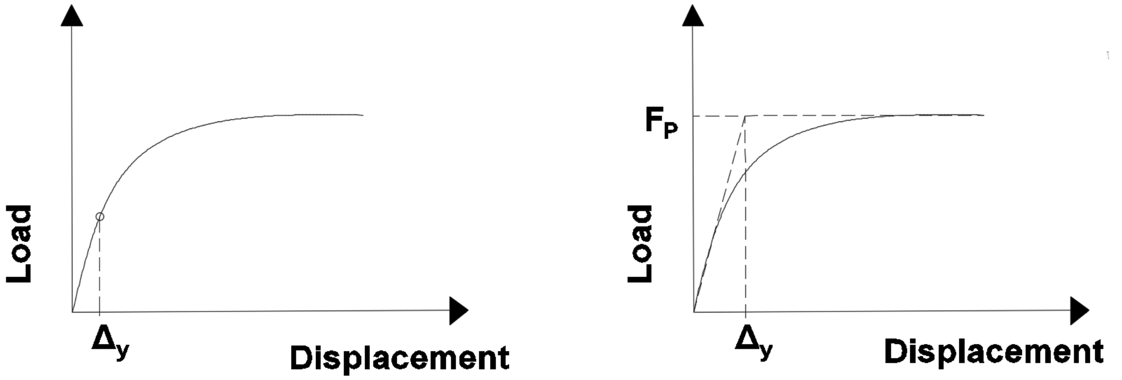

**a) Based on first yield**

**b) Based on Equivalent Elasto-plastic Yield**

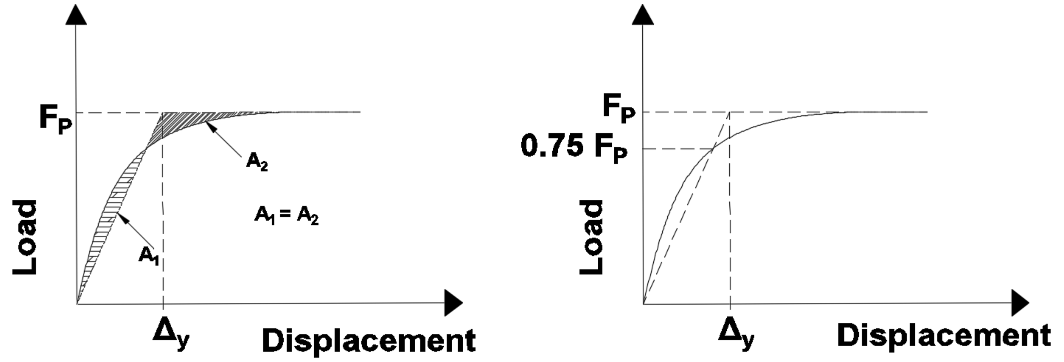

**c) Based on Equivalent Elasto-plastic Energy Absorption**

**d) Based on Reduced Stiffness Equivalent Elasto-plastic Yield**

**Figure 4-54 Definitions of yield displacement** [43]

The ultimate displacement is taken as the post-peak displacement when maximum strength has undergone a slight reduction. According to available literature, displacement corresponding to 10% or 20% loss of peak load in the post-peak regime is taken as $\Delta_u$ [21]. In the present research work, displacement corresponds to 20% reduction in the peak load is considered as ultimate displacement. For calculation of displacement ductility ratio, the yield and ultimate displacements for the positive and negative loading for control and strengthened specimen are given in Table 4-8. The listed ductility ratio is calculated as the mean ductility in positive and negative displacements. It is observed that the yield displacement for specimens TS1 and TS2 has reduced when compared to the value registered for the control specimen, in positive and negative direction. This reduction is attributed to the lower stiffness degradation during the early stage of loading history, assured by the implemented retrofitting technique. However, the yield displacement registered for specimen TSE is more than the values reported for control specimen due to higher stiffness degradation among all specimens. According to the values reported for average displacement ductility ratio in Table 4-8, the ductility of strengthened specimens TS1, TS2 and TSE were reduced by 8.3%, 1.5% and 36.6% from the ductility of control specimen. The post-peak load-displacement response of specimen TS1 was different from the response of other specimens. After reaching the peak load, the strength of the test unit TS1 was degraded. This degradation was not smooth and reflected in the displacement ductility value which was less than the ductility of control specimen. The reduction in the load was stopped as it reached to the strength of RC core sub-assembly and the load was sustained up to the drift of 8.7% due to the localization of vertical flexural crack at the beam-joint interface and the yielding of beam’s main reinforcement. This behavior is evident from the plateau in the load-displacement envelope curve for the drift greater than 5%. In load-displacement envelope curve, the post peak regime of specimen TS1 was characterized by the sudden reduction in the strength followed by the plateau in the curve. The former characteristic was highlighted in ductility value, but the latter character was not incorporated in the displacement ductility ratio. Due to this unique behavior, specimen TS1 performed efficiently in terms of overall ductility of the test unit, as compared to specimen TSE. It was observed that specimen TSE was failed due to detachment of prefabricated UHPFRC plates with the concrete cover from the RC core sub-assembly and the failure was brittle in nature without yielding of beam's reinforcement due to which prefabricated UHPFRC plates enhanced the maximum load carrying capacity but could not maintain the ductility of the structural component.

**Table 4-8 Data for the evaluation of displacement ductility ratio**

| **Specimen** | **Positive direction** | | **Negative direction** | | **Displacement ductility** |
|---|---|---|---|---|---|
| | $\boldsymbol{\Delta_y^+}$ | $\boldsymbol{\Delta_u^+}$ | $\boldsymbol{\Delta_y^-}$ | $\boldsymbol{\Delta_u^-}$ | $\mu_{\boldsymbol{\Delta}} = \frac{\boldsymbol{\Delta_u}}{\boldsymbol{\Delta_y}}$ |
| | mm | mm | mm | mm | |
| TC | 8.48 | 32.6 | 8.27 | 31.85 | 3.85 |
| TS1 | 7.74 | 26.65 | 7.2 | 26.3 | 3.53 |
| TS2 | 8 | 26.6 | 7.07 | 30.10 | 3.79 |
| TSE | 13.93 | 28.3 | 8.67 | 24.75 | 2.44 |

# CHAPTER 5

# Numerical Modelling of BCJs

## 5.1 Introduction

Numerical modelling becomes a useful tool these days to study the response of complex problems. Many studies have been carried out on RC BCJs using finite element solver to simulate the behavior of experimental studies. The response of BCJs has been studied by the researchers, in the recent years, using a wide range of non-linear finite element packages such as DIANA, ANSYS, ABAQUS and VECTOR 2, etc. In the present research work, commercially available non-linear FE software ABAQUS 6.13 was used to simulate the behavior of control and strengthened units.

In this chapter, FE model is discussed in which different models to simulate cracking in concrete are discussed. Among these models, the appropriate model is selected which takes into account the numerical computational difficulties, convergence and solution degradation problems. Modeling of normal concrete, UHPFRC, steel reinforcement and their bond behavior is then presented. ABAQUS 6.13 has a wide range of constitutive models for metals, concrete and other materials. Finally, ABAQUS 6.13 was used to validate the developed FE model with the experimental results of control and strengthened test units presented in the previous chapter.

## 5.2 Finite element model

The model presented below explains the modelling to simulate normal concrete and UHPFRC followed by the modelling of reinforcing steel and its bond with concrete and modelling the bond between UHPFRC and normal concrete using linear elastic traction-separation law.

### 5.2.1 Models to Simulate Damage in Concrete

According to the available literature, various conceptual models are available to simulate the quasi-brittle nature of reinforced concrete which includes discrete crack model, smeared crack model and inner softening band. Discrete crack model (DCM) and smeared crack model (SCM) are mostly used for numerical modelling of concrete cracking. In DCM and SCM, crack openings are physically modelled which arises due to cracking in concrete and taken as geometrical identity. Since crack is modelled along the surface of the element, it creates mesh bias. Many researchers attempt to resolve this issue had been done to resolve this issue by developing the FE codes capable of generating remeshing[44]-[45]. But Borst et al.(1985) had found the computational difficulties associated with remeshing and it is still a great challenge[46]. However, in the case of smeared crack model strain localization phenomenon leads to zero energy utilization during the crack opening when element size approaches zero. This phenomenon results in a non-mesh objective case due to which solution does not converge.

In the present research work, the Damage Plasticity Model (DPM) has been utilized to model the behavior of concrete. Cracking and crushing of concrete and yielding of reinforcement are the non-linear mechanisms that are considered in modelling. In damage plasticity model, the development of yield surface was controlled by the two hardening variables that are tension and compression. The damage was modelled by stiffness degradation approach using continuum damage mechanics which essentially means that elasticity is deteriorated in the concrete where it cracks.

### 5.2.2 Beam-Column Joint Modelling in ABAQUS

3D non-linear finite element models were generated for the control and strengthened test units using ABAQUS 6.13. The geometry, reinforcement detailing and boundary conditions were kept similar to the specimens tested under the experimental program. Figure 5-1 shows the assembly of control specimen TC in ABAQUS. The assembly of strengthened specimens TS1, TS2 and TSE is shown in Figure 5-2.

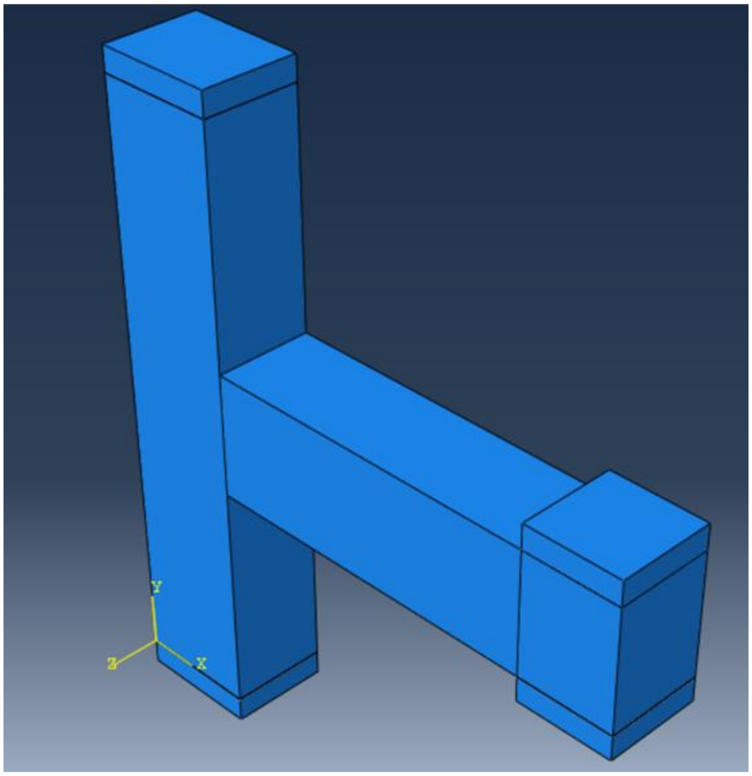

**Figure 5-1 Model of Control specimen in ABAQUS**

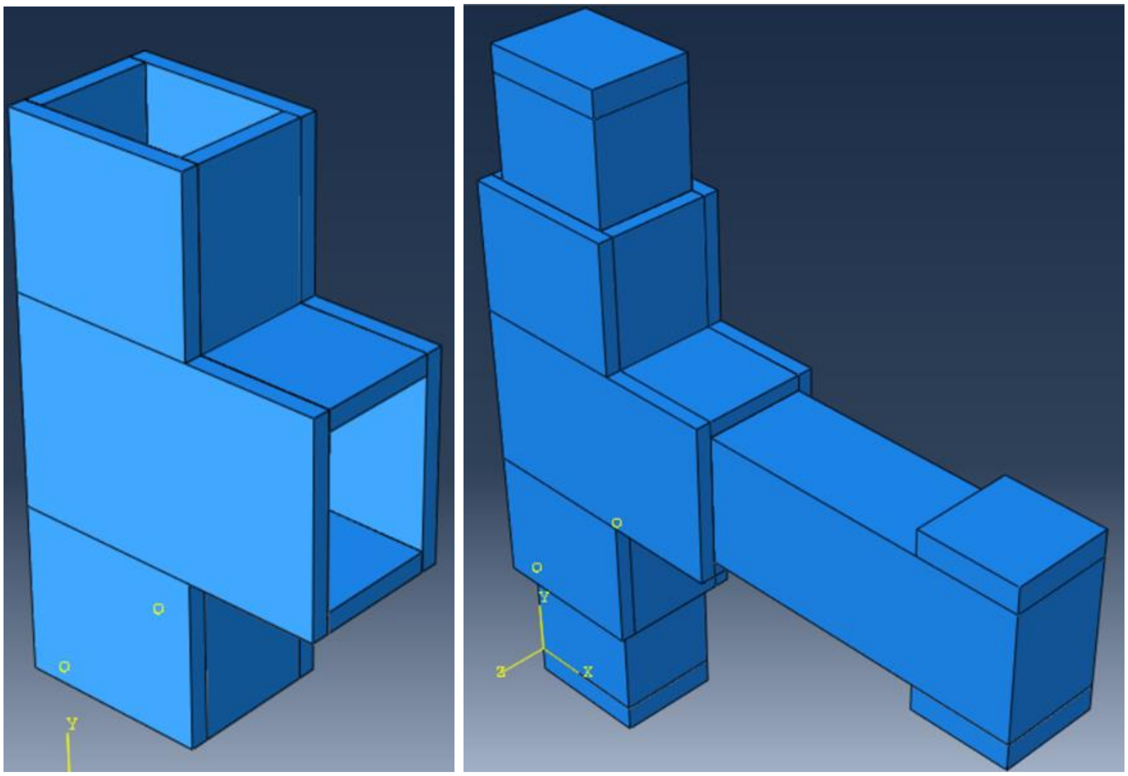

**Figure 5-2 Model of UHPFRC jacket and Strengthened specimens in ABAQUS**

## 5.2.3 Material Models

### 5.2.3.1 Concrete Damage Plasticity Model (CDPM)

The CDP model was adopted to simulate the nonlinear behavior of both normal concrete and UHPFRC in ABAQUS which requires the following material functions:

a) Uniaxial stress-strain relation of concrete under compression and tensile loading.

b) Concrete compression damage and tension damage parameters under compression and tensile loading.

The fib model code for concrete structure [47] has been adopted because this model can control ascending as well as the post-peak behavior of stress-strain curve for concrete by using advanced parameters. The stress-strain relationship under compression is as follow:

$$\frac{\sigma_c}{f_{cm}} = \frac{k.\eta - \eta^2}{1 + (k-2).\eta} \qquad 5\text{-}1$$

$$\eta = \frac{\epsilon_c}{\epsilon_{c1}} \qquad 5\text{-}2$$

$$k = \frac{E_{ci}}{E_{c1}} \qquad 5\text{-}3$$

where

fcm = Concrete compressive strength; $\epsilon_c$= Concrete compressive strain; $\epsilon_{c1}$=strain corresponding to max. Compressive stress; $E_{ci}$ = Elastic modulus at 28 days; $E_{c1}$= Secant modulus; k = Plastic number

The stress-strain relationship with above prescribed parameters is depicted in the Figure 5-3.

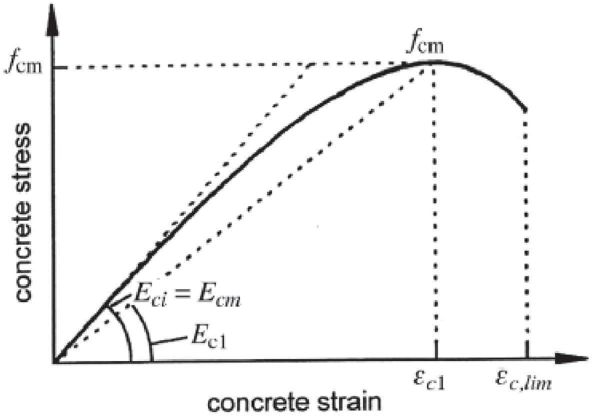

**Figure 5-3 Stress-strain relationship under compression for concrete modelling** [47]

Bilinear stress-strain relationship used for the tensile behavior of concrete is as given below:

$$\mathrm{\sigma_{ct}} = E_{ci}\,\epsilon_{ct}\ for\ \ \mathrm{\sigma_{ct}} \leq\ 0.9\,\mathrm{f_{ctm}} \qquad 5\text{-}4$$

$$\frac{\mathrm{\sigma_{ct}}}{\mathrm{f_{ctm}}} = 1 - 0.1\,\frac{0.00015 - \epsilon_{ct}}{0.00015 - 0.9\,\frac{\mathrm{f_{ctm}}}{E_{ci}}}\ for\ \ 0.9\mathrm{f_{ctm}}\ \leq\ \mathrm{\sigma_{ct}} \leq \mathrm{f_{ctm}} \qquad 5\text{-}5$$

where

$\epsilon_{ct}$ = Tensile strain; $\mathrm{\sigma_{ct}}$ = Tensile stress; $\mathrm{f_{ctm}}$= Tensile strength

Tensile stress-strain relationship with related parameters is depicted in Figure 5-4.

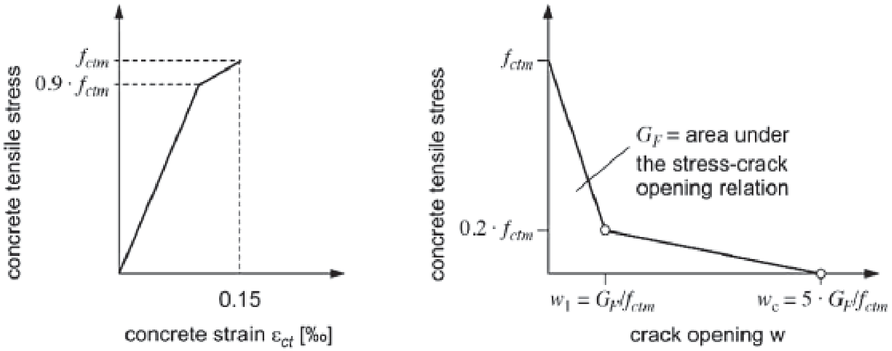

**Figure 5-4 Stress-strain relation in tension and Crack opening relation** [47]

The expression for concrete compression damage parameter that is used in modelling the material is given in Eq. 5-6 [48].

$$d_c = 1 - \frac{\mathrm{\sigma_c}\,E_c^{-1}}{\epsilon_c^{pl}\,\left(\frac{1}{b_c} - 1\right) + \mathrm{\sigma_c}\,E_c^{-1}} \qquad 5\text{-}6$$

where: $d_c =$ Concrete compression damage parameter; $\mathrm{\sigma_c}$= Compressive stress; $\mathrm{E}_c$= Elastic Modulus of concrete; $\epsilon_c^{pl}$= Plastic strain corresponding to compressive strength; $b_c$= Constant factor use for curve fitting upon unloading and ranges from $0\ < b_c > 1$

The compression damage parameter defines the stiffness after damage in non-linear part of stress-strain curve in uniaxial compression, as depicted in Figure 5-5

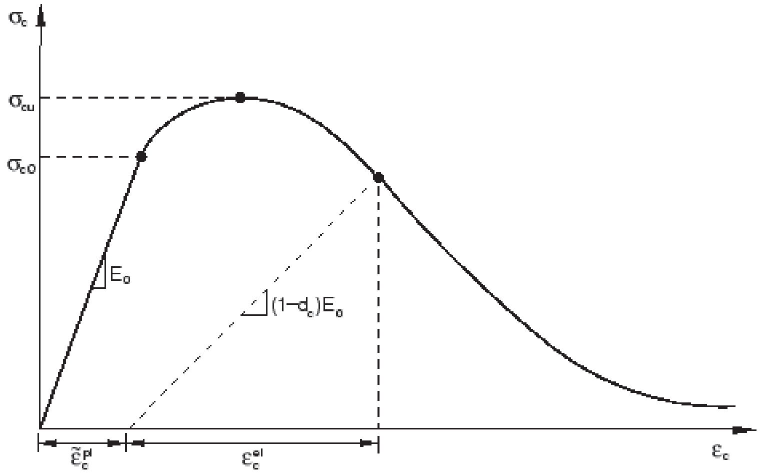

**Figure 5-5 Damage parameter for uniaxial compression** [49]

The evolution of the tension damage component was obtained using Eq. 6-7 [48].

$$d_t = 1 - \frac{\sigma_t\, E_c^{-1}}{\epsilon_t^{pl}\left(\frac{1}{b_t} - 1\right) + \sigma_t\, E_c^{-1}} \tag{5-7}$$

Where: $d_t =$ Concrete tension damage parameter; $\sigma_c$= Tensile stress; $\text{E}_c$= Elastic Modulus of concrete; $\epsilon_c^{pl}$= Plastic strain corresponding to tensile strength; $b_t$= Constant factor use for curve fitting upon unloading and ranges from $0 < b_t > 1$.

Figure 5-6 depicts the physical interpretation of tension damage parameter in expressing the stiffness after damage in softening part of the stress-strain curve of concrete in uniaxial tension.

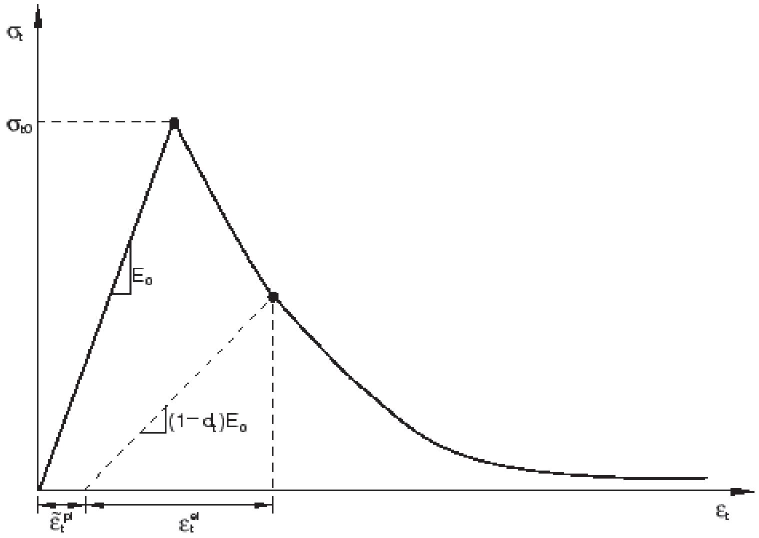

**Figure 5-6 Damage parameter for uniaxial tension** [49]

It has been observed that several functional parameters are required to perform the simulation of concrete material in the ABAQUS using CDP model. These parameters were determined experimentally. The non-linear behavior of normal concrete and UHPFRC was modelled by directly inputting the CDP model parameters listed in Table 5-1. To simulate the plastic response of the normal concrete and UHPFRC, uniaxial stress-strain data under compression and tension have been used in CDP model. The stress-plastic strain behavior of NC and UHPFRC under compression is shown in Figure 5-7 and Figure 5-9, respectively and was obtained by conducting uniaxial compression test on the cylinders, as already described in section 2.6.1.1 and section 3.6.3.5.1. The tensile behavior of NC was determined by performing the flexural strength test on prism specimen and given in Figure 5-8, whereas the stress-plastic strain data for UHPFRC used in CDP model was obtained by conducting the direct tensile strength test on dog-bones specimens, as described in section 3.6.5.3 and data is shown in Figure 5-10.

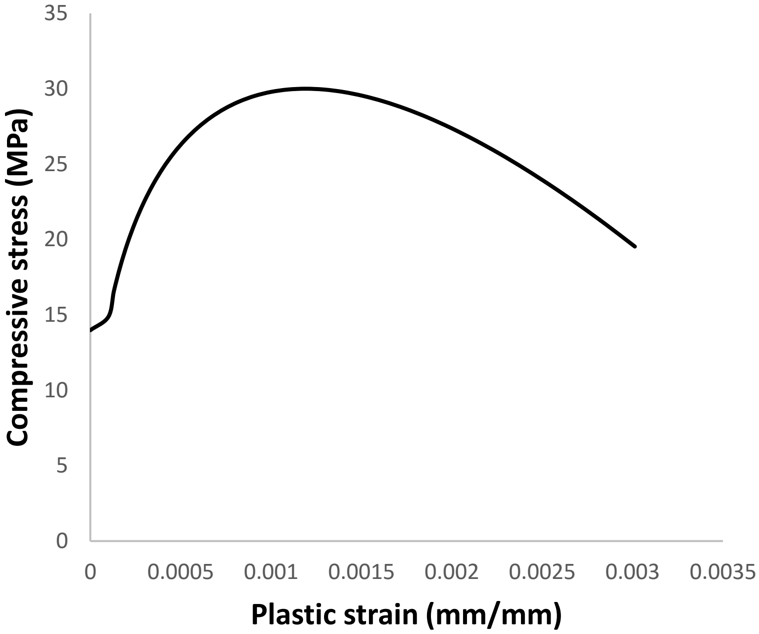

**Figure 5-7 Stress vs. plastic strain in compression for NC**

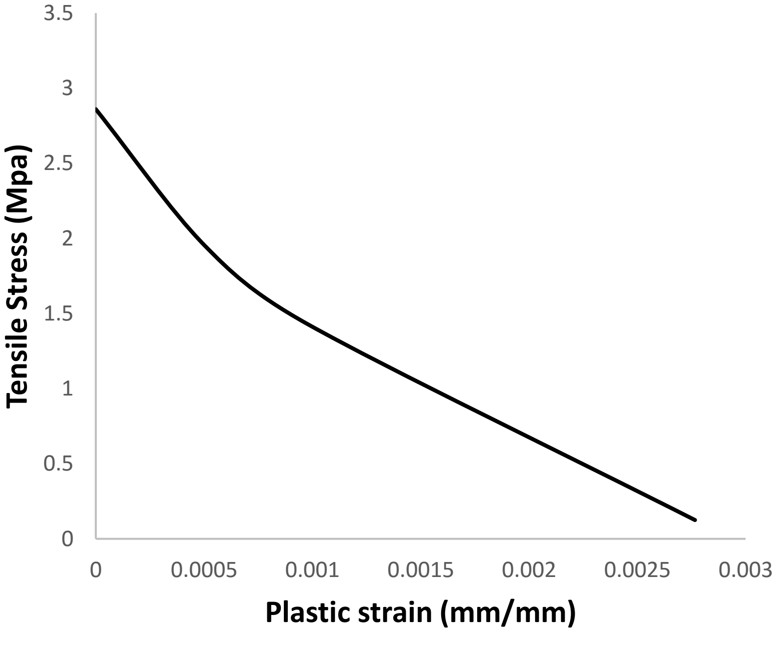

**Figure 5-8 Stress vs. plastic strain in tension for NC**

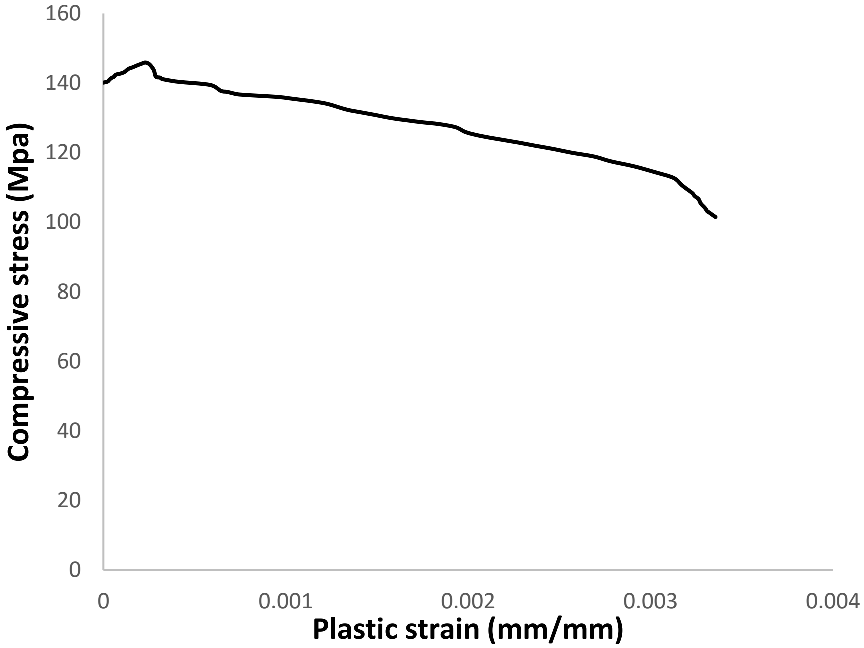

Figure 5-9 Stress vs. plastic strain in compression for UHPFRC

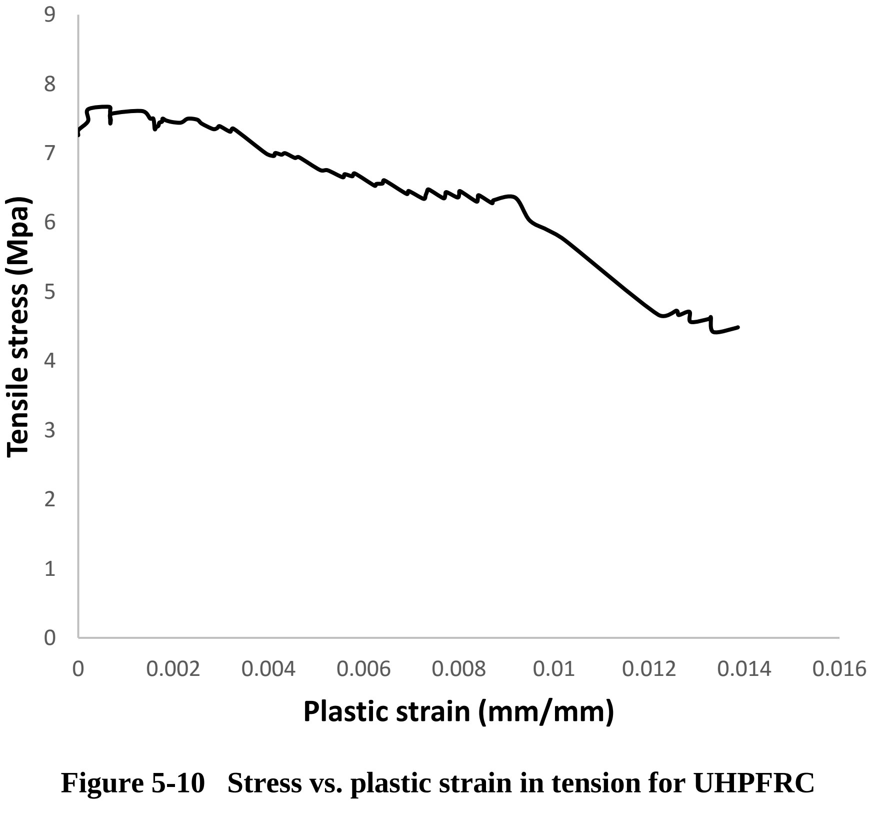

Figure 5-10   Stress vs. plastic strain in tension for UHPFRC

Table 5-1 Concrete Parameters used in CDP model

| Material | Mass Density | Young's Modulus | Poisson's ratio | Dilation angle (ψ) | Eccentricity (ϵ) | $\frac{f_{bo}}{f_{co}}$ | K |
|---|---|---|---|---|---|---|---|
| | Tone/mm$^3$ | MPa | | degree | | | |
| NC | 2.4E-009 | 25700 | 0.19 | 36 | 0.1 | 1.16 | 0.67 |
| UHPFRC | 2.4E-009 | 52400 | 0.18 | 36 | 0.1 | 1.16 | 0.67 |

#### 5.2.3.2 Steel reinforcement

Steel bars are simulated with metal plasticity model and modelled by an elastic-plastic with strain hardening relationship whose parameters were determined through uniaxial tension test on a steel bar. The stress-strain curve input in ABAQUS for steel reinforcement is shown in Figure 5-11. The other parameters that are used to define rebar are listed in Table 5-2.

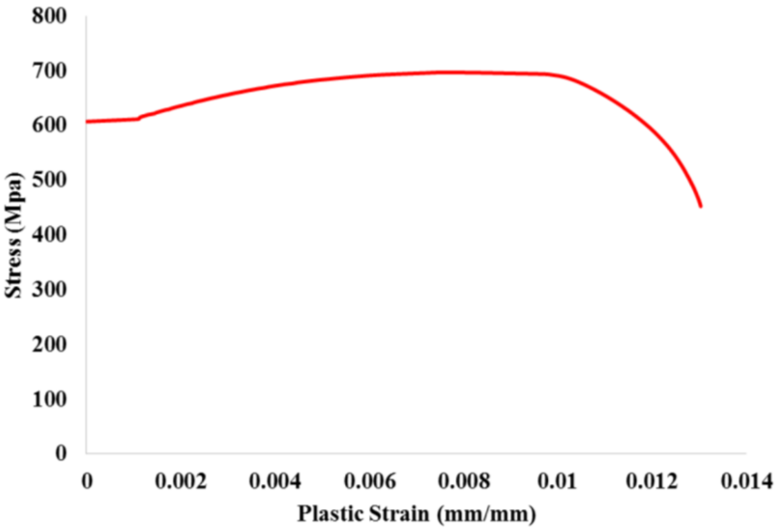

Figure 5-11 Stress-plastic strain relation of rebar used in ABAQUS

**Table 5-2 Parameters used to model reinforcing steel**

| Material | Mass Density | Elastic modulus | Poisson's ratio | Yield Stress |
|---|---|---|---|---|
| | tonne/mm$^3$ | MPa | | MPa |
| Steel rebar | 7.85E-009 | 195161 | 0.3 | 605 |

### 5.2.4 Element type, Boundary conditions, Loads and Meshing

Four parts were made to make the assembly of the model and the element used to make these parts are listed in Table 5-3.

In order to mimic the experimental conditions, the top end of the upper column was constrained in x and z-direction and the bottom end of the lower column was constrained in x, y and z-direction. The free end of the beam was constrained in y-direction for imposing the displacement which was taken as 40 mm at which the test was stopped. A constant pressure load of 3 MPa, which is equal to axial load 150 kN, was applied on the column. The load and boundary conditions of the model are depicted in Figure 5-12. The steel reinforcement was modelled as a linear element in ABAQUS as shown in Figure 5-13. The meshing of retrofitted specimen is shown in Figure 5-14.

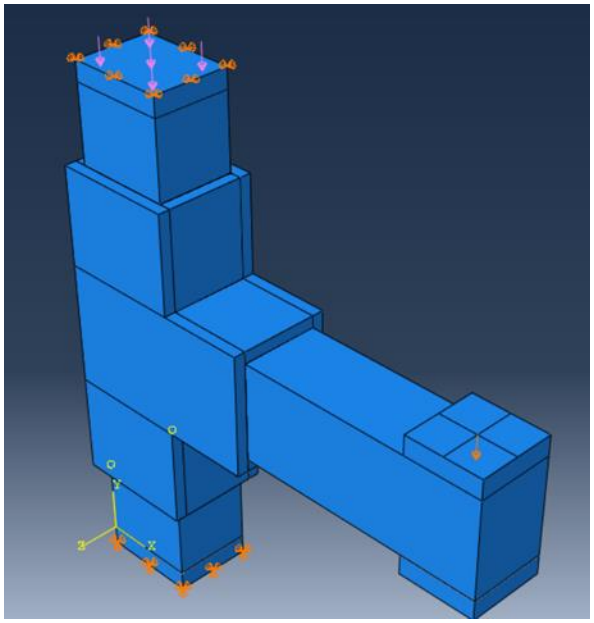

Figure 5-12 Load and boundary conditions of the model

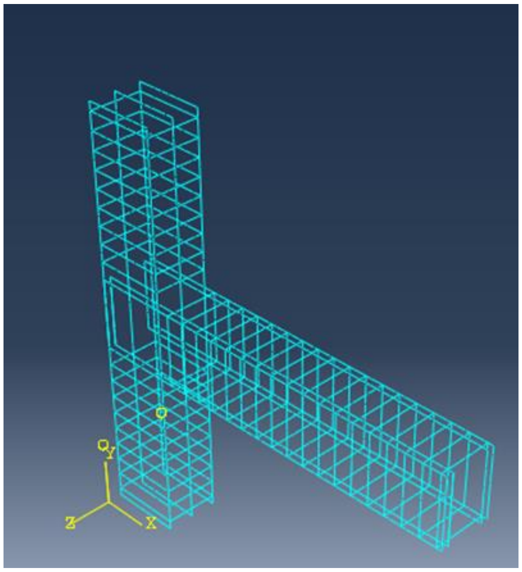

Figure 5-13 Model of steel reinforcement

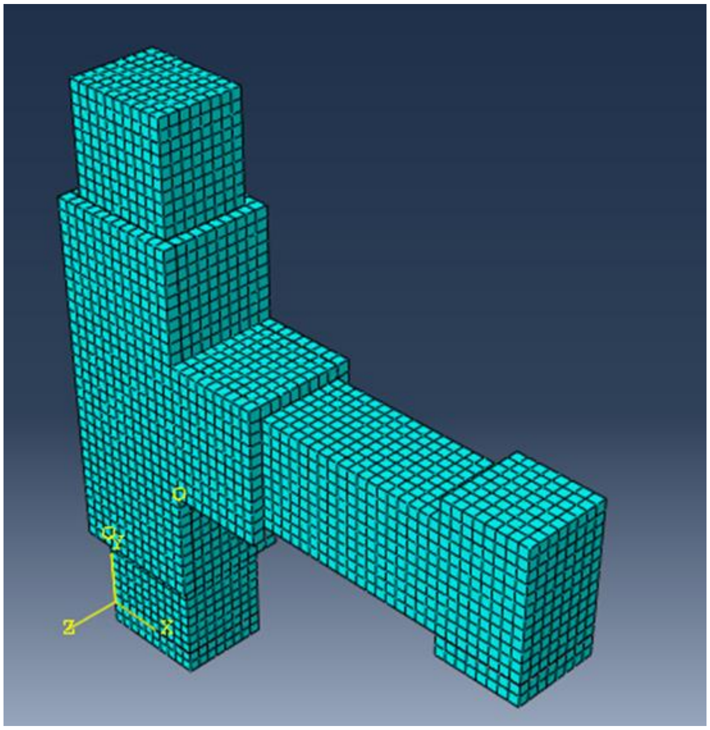

**Figure 5-14 Meshing of retrofitted specimen**

**Table 5-3 Description of elements used in modelling**

| Part | Element | Element Description |
|---|---|---|
| Normal concrete | C3D8R | 8-noded linear brick reduced integration element |
| UHPFRC | C3D8R | 8-noded linear brick reduced integration element |
| Rebar | T3D2 | 2-noded truss element |
| Steel plates | C3D8R | 8-noded linear brick reduced integration element |

### 5.2.5 Constraints between concrete and steel reinforcement

Reinforcement bars was bonded with concrete as an embedded element in ABAQUS. Many researchers had successfully used embedment technique and it is very powerful FE tool which allows the number of elements to be embedded inside the host element. There is no need to model interaction surface between the embedded and host element which eliminates numerically costly iterations linked with the surface formulation.

### 5.2.6 Interface Contact Element

The contact between the normal concrete substrate surface and UHPFRC jacket was modelled as a surface-to-surface cohesive contact. The contact surfaces are the outer surface RC core sub-assembly and the inner surface of UHPFRC jacket. Linear elastic traction-separation law with uncoupled behavior, as depicted in Eq. 5-8, damage initiation criteria and damage evolution laws were used to govern the surface-based cohesive behavior. Before the initiation of damage, linear elastic traction-separation law pertains the normal and shear stresses to normal and shear separations across the interface through a full populated stiffness matrix in the coupled low. In the linear elastic traction-separation model, the behavior can be coupled or uncoupled behavior is represented by the setting the off-diagonal terms of stiffness matrix to be zero, as depicted in Eq. 5-8.

$$\begin{Bmatrix} t_n \\ t_s \\ t_t \end{Bmatrix} = \begin{bmatrix} K_{nn} & 0 & 0 \\ 0 & K_{ss} & 0 \\ 0 & 0 & K_{tt} \end{bmatrix} \begin{Bmatrix} \delta_n \\ \delta_s \\ \delta_t \end{Bmatrix} = K\delta \qquad 5\text{-}8$$

Normal stiffness ($K_{nn}$), shear and tangential stiffness ($K_{ss}$ and $K_{tt}$) are required to define the linear elastic behavior of uncoupled traction-separation behavior. The values for stiffness matrix in the uncoupled low were determined through the bond test, as explained below.

### 5.2.6.1 Bond Strength Evaluation

For the assessment of bond strength between the normal concrete substrate and UHPFRC and for the assessment of tangential stiffness (Kss), the bi-surface shear test or pull out test was selected from the various bond test presented by Ariel D. Espeche et al.(2011) [50]. These tests were categorized into three main classes depending on the stress measured and shown in Figure 5-15.

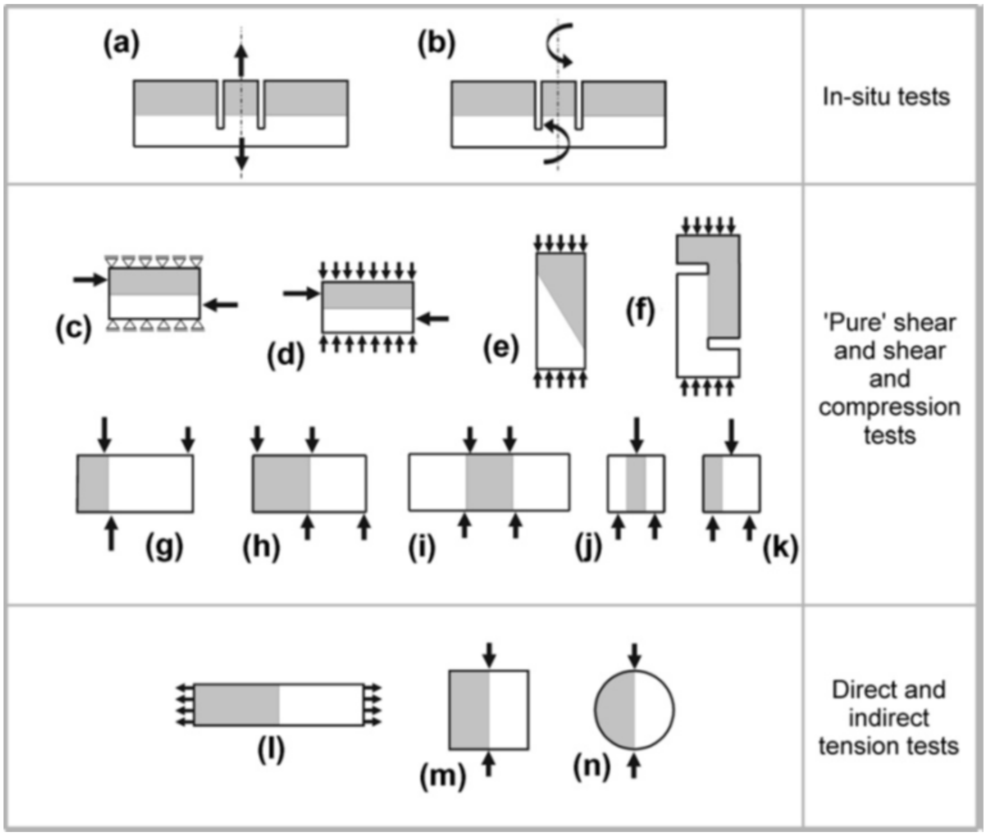

**Figure 5-15 Schematic representation of different bond test** [50]

Three composite specimens were prepared for the push out test and composed of UHPFRC and ordinary concrete. Composite specimens consist of UHPFRC block with 150x150x50 dimensions, sandwiched between two normal concrete blocks with 150x150x75 dimensions, as shown in Figure 5-16. For the preparation of three composite specimens, the surface of normal concrete blocks was made rough through sandblasting followed by the in-situ casting of UHPFR block of dimensions as mentioned above using the wooden molds, as shown in Figure 5-17, to simulate the surface conditions as adopted for the strengthening of specimens TS1 and TS2. The variable parameters were normal, shear and tangential stiffness and their values are listed in Table 5-4. These parameters were determined through pull out test and calibrated by using the experimental results. Figure 5-18 presents test setup adopted for pull out test.

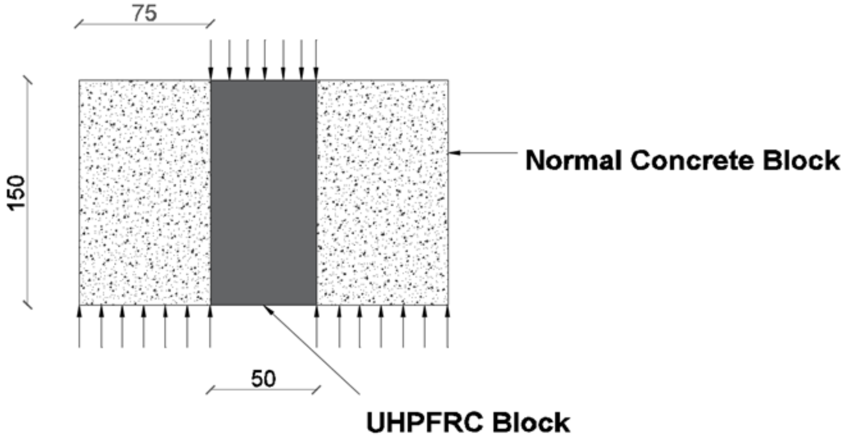

**Figure 5-16 Schematic representation of Bond test**

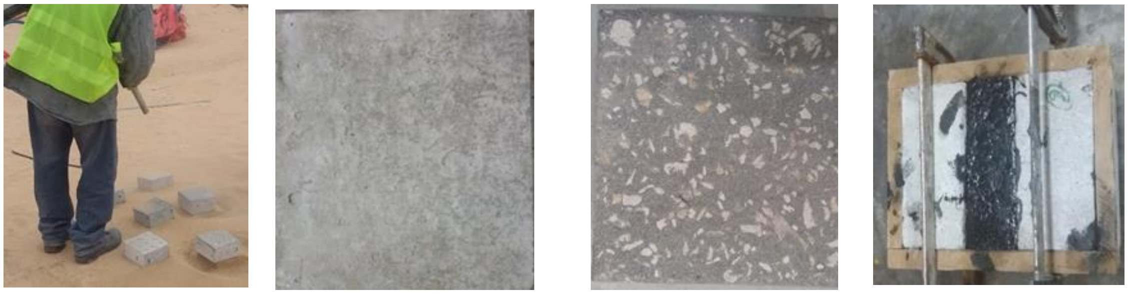

a) Sandblasting b) NCSS before sandblasting c) NCSS after sandblasting d) Composite specimen

**Figure 5-17 Preparation of Composite specimens for pull out test**

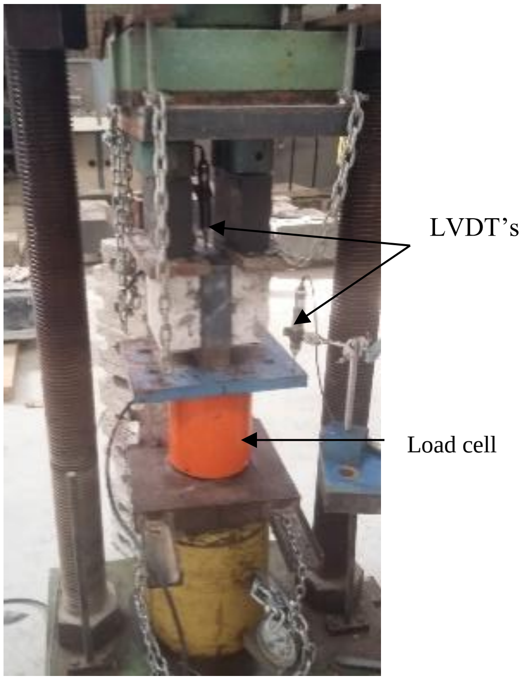

**Figure 5-18 Test setup of push out test**

**Table 5-4 Stiffness coefficient of cohesive interface**

| $K_{nn}$ | $K_{ss}$ | $K_{tt}$ |
|---|---|---|
| **MPa/mm** | **MPa/mm** | **MPa/mm** |
| 0.01 | 0.001 | 0.001 |

## 5.3 Numerical simulation of Control Specimen TC

Figure 5-19 depicts the load-displacement response of specimen TC registered experimentally and as predicted by FEM. The peak load of 44.8 kN was achieved at a displacement of 18.1 mm in FEM model, whereas the corresponding experimental values were 48.2 kN and 18.5 mm in push direction and in pull direction these values were -41.5 kN and -18.6 mm. In general, load-displacement curve predicted by FE solver is in good agreement with that of the experiment.

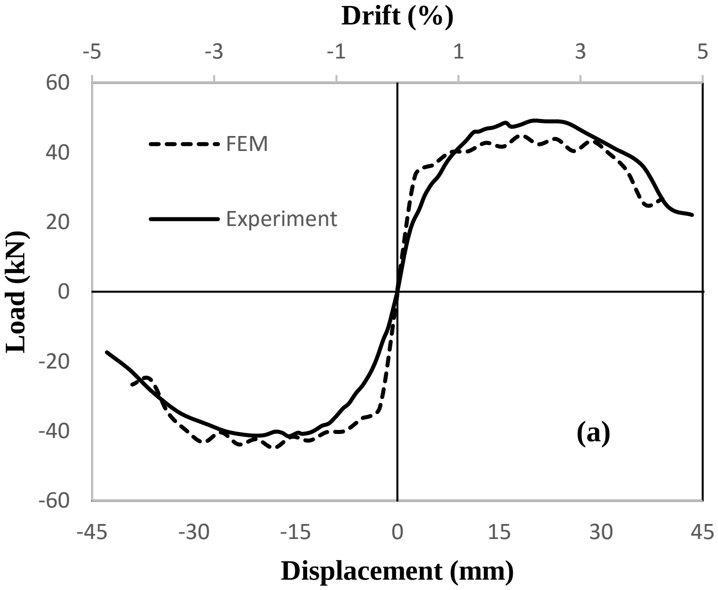

**Figure 5-19 Load-displacement response of Control specimen TC**

The evolution of damage in the model and its comparison with the cracks registered in the experimental program is shown in Figure 5-20. The failure mode predicted by FEM model is the joint failure without yielding of beam's reinforcement and it is in good agreement with the experimental results. The stresses in the steel are shown in Figure 5-21. The maximum stress registered in the beam longitudinal reinforcement was 178.5 MPa, which was much less than the yield stress of reinforcement. Figure 5-22 displays the steel strain.

The average maximum strain in beam’s longitudinal reinforcement was registered as 0.00089 mm/mm against the experimental value of 0.0012 mm/mm.

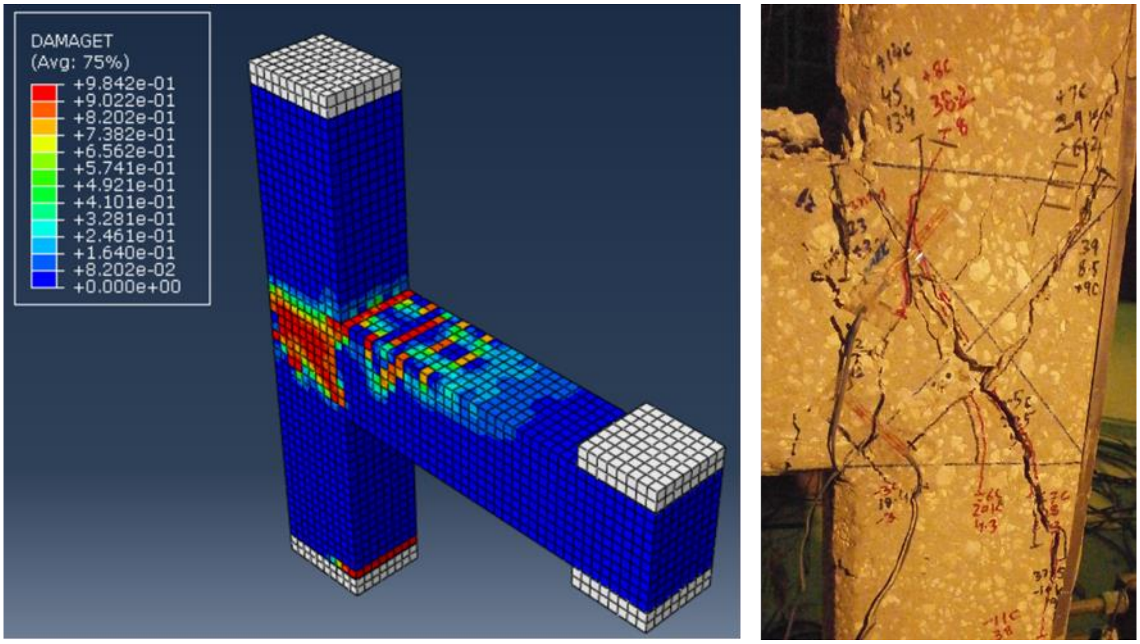

Figure 5-20 FEM and experimental crack pattern

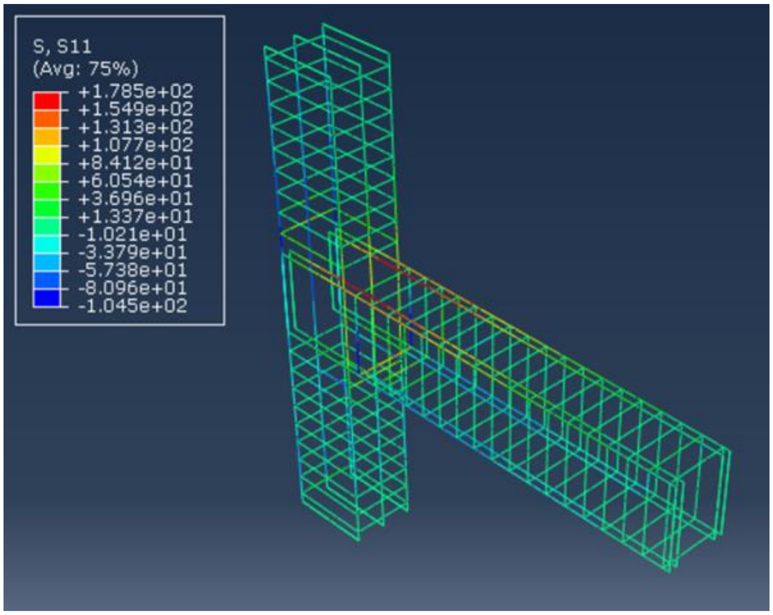

Figure 5-21 Steel stresses at failure load of control specimen TC

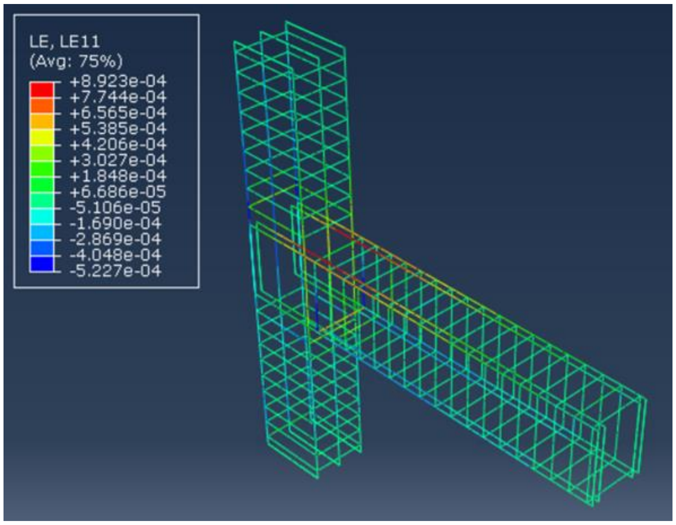

**Figure 5-22 Steel strain at failure load of specimen TC**

## 5.4 Numerical simulation of Retrofitted Specimen

Figure 5-23 shows the load-displacement response of strengthened specimens registered experimentally and as predicted by FEM. The peak load of 103.3 kN was obtained, in case of specimen TS1, at a displacement of 15.5 mm in FEM model, whereas the corresponding experimental values were 105.6 kN and 12.9 mm in positive excursion and in the negative excursion, these values were -100.5 kN and -14 mm. In general, load-displacement curve predicted by FE solver is in good agreement with that of the experiment.

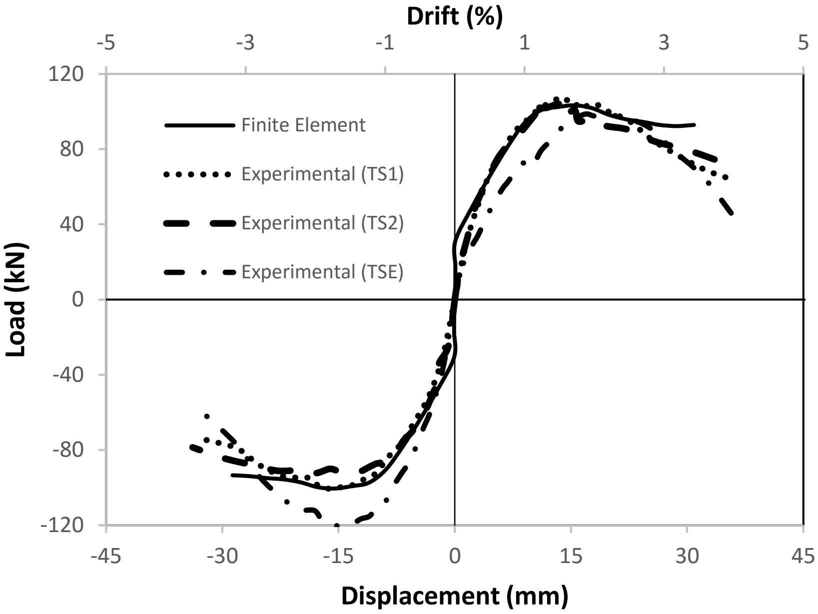

**Figure 5-23 Load-displacement response of Retrofitted specimen**

The evolution of cracks in the model and its comparison with the cracks registered in the experimental program is shown in Figures 5-24 and 5-25. A detachment of UHPFRC jacket from NCSS was observed at the peak load during the experiment. It was also verified by the FE model, as shown in Figure 5-26. The stresses in the steel is shown in Figure 5-27. The maximum stress registered in the beam longitudinal reinforcement was 339 MPa at peak load, which was much less than the yield stress of reinforcement.

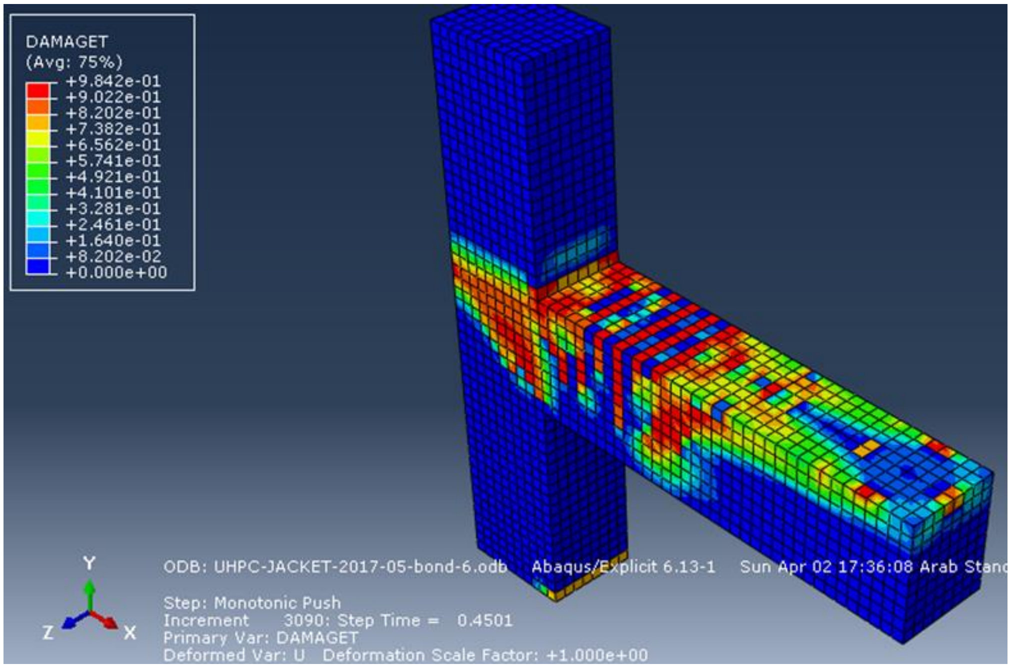

Figure 5-24 FEM crack pattern of NC core sub-assembly

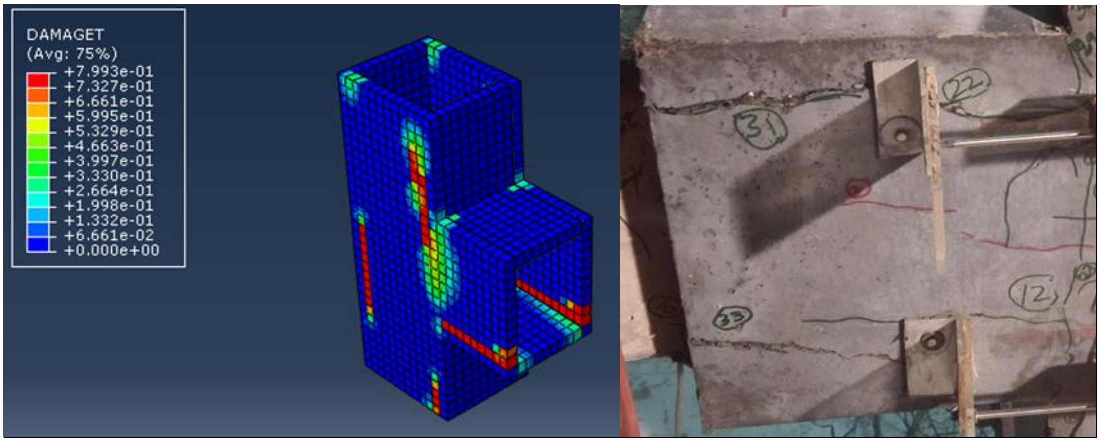

Figure 5-25 FEM and experimental crack pattern in UHPFRC jacket at peak load

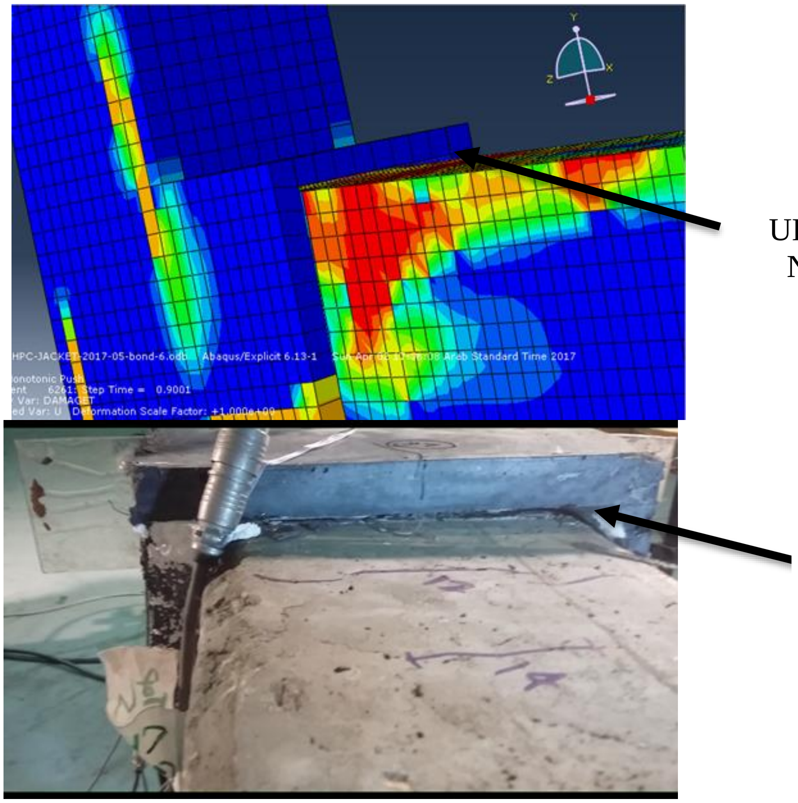
Detachment of UHPFRC jacket from NCSS at peak load

Detachment of UHPFRC jacket from NCSS at peak load

**Figure 5-26 Detachment of UHPFRC jacket from NCSS**

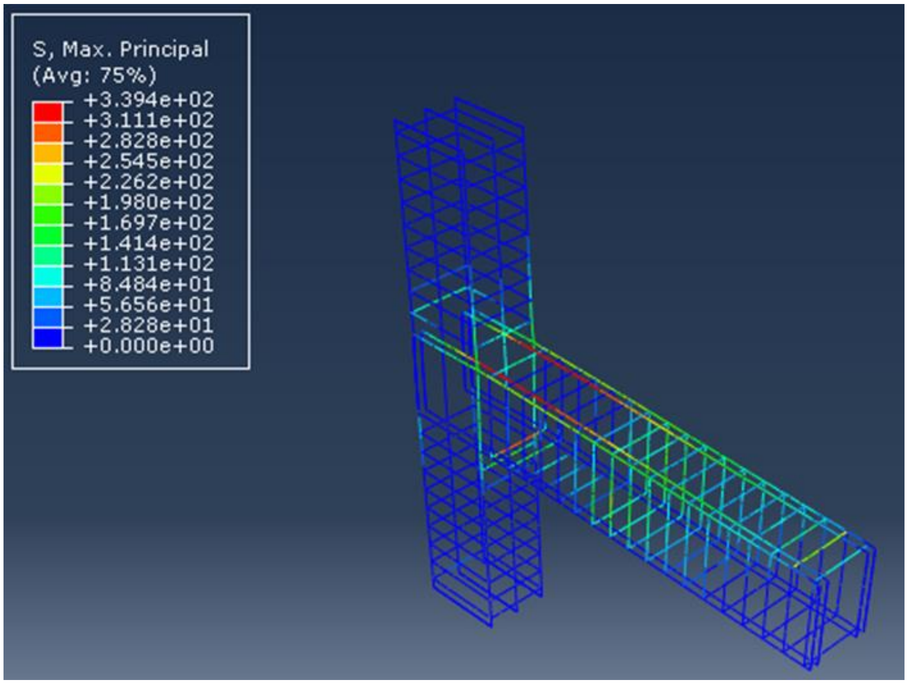

**Figure 5-27 Steel stresses at failure load of retrofitted specimen**

# CHAPTER 6

# CONCLUSIONS AND RECOMMENDATIONS

## 6.1 Conclusions

An experimental program was conducted to evaluate the effectiveness of UHPFRC jacketing in repairing the damaged reinforced concrete exterior BCJs (post-earthquake repairing) and strengthening the undamaged exterior BCJs (pre-earthquake up gradation). UHPFRC is modern era concrete possessing excellent mechanical properties (high compressive strength, fracture toughness), crack bridging ability and excellent durability.

The former group consists of three damaged specimens with CAL equal to 0 kN, 200 kN and 600 kN. In the experimental investigation, it was explored that how effectively repairing can be done for damaged test units which can be re-used without compromising the safety issues. Repaired specimens showed excellent performance in terms load-displacement response, maximum strength, displacement ductility, initial stiffness, secant stiffness and energy dissipation capacity than the corresponding values registered when these specimens were tested in their virgin state. The application of 30 mm thick UHPFRC jacketing not only restore the strength, stiffness, ductility and energy dissipation capacity of severely damaged specimens but also improved their performance. The following conclusions can be drawn based on the results obtained from the experimental investigation.

- Three severely damaged exterior BCJs designated as SP1, SP2, and SP3 were elected from a group of specimens that were tested in their virgin state in the ambit of the research program of MS thesis. The research group reported the significant shear damage of the joint panel in their virgin state and specimens showed the classical joint shear failure.
- The up-gradation of damaged specimens through 30 mm UHPFRC layer delayed the crack initiation and the damage was shifted from the typical diagonal tension cracks inside the joint panel to the vertical flexural cracks in the beam at the beam-joint interface.
- It was reported that test units exhibited brittle joint shear failure without yielding of beam’s main reinforcement in their virgin state. However, the application of UHPFRC thin jacketing promoted the yielding of beam’s main reinforcement. In the retrofitted sub-assemblies, the major damage was registered in terms of vertical flexural crack localized at the beam-joint interface. The plastic hinge was formed at the beam-joint interface. The proposed retrofitting solution was able to shift the classical joint shear failure to ductile flexural failure of the beam at the beam-joint interface.
- When the retrofitted specimens SP2-R and SP3-R reached a level of maximum load, UHPFRC jacket was slightly de-bonded from the NCSS. The detachment of UHPFRC jacket was more prominent in unit SP3-R where CAL was 600 kN. Increased CAL enhanced the confinement of the joint due to which load carrying capacity of retrofitted specimens was increased. This higher value of load resulted into higher stresses at the interface of UHPFRC and NCSS.

- The UHPFRC jacket efficiently confined the joint and significantly improved the maximum strength of the retrofitted sub-assembly. Retrofitted specimen SP1-R achieved a maximum strength of 71.37 kN against the strength of 37.55 kN achieved by the test unit in the virgin state. However, a value of 94.2 kN for maximum load carrying capacity was registered for specimen SP2-R against a value of 51 kN reported for the unit in the virgin state. Specimen SP3-R reached a maximum strength of 106.6 kN whereas, test unit could reach a value of 56.9 kN in a virgin state.
- The application of UHPFRC jacketing provided an increase of joint strength of about 1.9, 1.85 and 1.87 times for retrofitted specimens SP1-R, SP2-R and SP3-R, respectively with respect to the un-retrofitted sub-assemblies. Implemented retrofitting scheme not only restored the strength but also improved it to the significant value. This is mainly associated to the confinement provided by UHPFRC jacket at the joint region, high mechanical properties of UHPFRC due to its ability to distribute the stresses by developing the fine cracks, crack bridging ability due to the presence of steel fibers, excellent ductility and strain hardening behavior under tensile stresses.
- The retrofitted technique significantly improved the displacement capacity of the test units. The retrofitted unit SP1-R reached an ultimate displacement of 64.5 mm against the 31.5 mm displacement reached by the specimen in the virgin state. The corresponding values were 49.8 mm and 28.7 mm for specimens SP2-R and SP2, respectively. Specimen SP3-R could reach an ultimate displacement of 52.7 mm against the value of 30.9 mm achieved by the specimen in the virgin state. Hence,

ductility index showed that the deformation capacity of SP1-R is 100% more than the specimen in the virgin state. Specimens SP2-R and SP3-R showed an increase of deformation capacity over corresponding specimens in the virgin state equal to 74% and 70 %, respectively. This is mainly attributed to a significant increment in the initial stiffness, damage localization out of repaired region, excellent ductility and strain hardening behavior of UHPFRC.

- The deformation capacity of retrofitted specimens was decreased with the increase of CAL. Hence, the increased CAL reduced the ductility of the test unit.
- The implemented retrofitting solution not only restored the initial stiffness of test unit but also improved it. The initial stiffness of SP1-R, SP2-R and SP3-R were 80%, 83.7% and 122% higher than the corresponding values registered in the virgin state. This increase is attributed to larger section comprised of UHPFRC and NC and the higher level of joint confinement because of UHPFRC jacketing. In addition, it is essential to mention that with the increment of CAL, specimens became stiffer.
- The retrofitted specimens dissipated the much higher amount of energy as compared to the corresponding specimens in the virgin state. It is attributed to the contribution of UPFRC by distributing the stresses with the formation of closely spaced cracks prior to the localization of cracks, fibers crack bridging ability, localization of larger width cracks at the beam-joint interface and the yielding of beam’s main reinforcement.

The second group of the experimental program consists of four seismically deficit BCJ sub-assemblies. In this experimental investigation, it was explored the seismic behavior of seismically deficit joint and the efficiency of UHPFRC jacketing in strengthening the seismically deficit sub-assemblies. Two different techniques were used for strengthening the sub-assemblies. Control and strengthened specimens were tested under reversed cyclic loading with constant axial load and the performance of these specimens in terms of hysteretic response, maximum strength, strength degradation, deformation capacity, secant stiffness characteristics, energy dissipation capacity and displacement ductility ratio is evaluated and following conclusions can be drawn:

- The test confirmed that control specimen showed the classical joint shear failure mode combined with the slippage of beam’s longitudinal bars within the joint region. The major damage occurred due to the formation of extensive concrete wedge mechanism followed by the spalling of concrete.
- The application of 30 mm UHPFRC jacket on exterior BCJs delayed the crack initiation and implemented retrofitting solution was able to shift the typical diagonal tension cracks in the joint panel to the vertical flexural cracks in the beam at the beam-joint interface. The UHPFRC jacket successfully confined the joint region to avoid the extensive concrete wedge expulsion.
- The major damage was registered in terms of vertical flexural cracks concentrated at beam-joint interface and beam’s longitudinal reinforcement showed the yielding at higher drift values in the case of Specimen TS1. However, in the case of test unit TSE, the major damage occurred due to detachment of UHPFRC plates with the concrete cover from the RC core sub-assembly and test unit showed brittle failure.
- For strengthened specimens, TS1, TS2 and TSE, the application of 30 mm thick UHPFRC jacket provided a significant increase in strength of about 2.3, 2.2 and

2.44 times, respectively over a reference specimen. This is mainly associated to the higher level of confinement provided by UHPFRC jacket at the joint region, high mechanical properties of UHPFRC due to its ability to distribute the stresses by developing the fine cracks, crack bridging ability due to the presence of steel fibers, excellent ductility and strain hardening behavior under tensile stresses.

- The degradation in the strength at ±4.5% drift was reported to be 56.5%, 43.8%, 34.6% and 73.4% for control and strengthened specimens TC, TS1, TS2 and TSE, respectively. Specimen TSE showed the highest reduction in the peak strength due to detachment of UHPFRC plates. However, control specimen showed higher value because of brittle joint shear failure.
- Specimen TS1 reached a drift equal to 8.7% against the 5% drift reached by the control specimen and specimen TSE could reach a drift of 5% only and exhibited the brittle failure due to detachment of UHPFRC plates. So, the in-situ casting of UHPFRC jacket around the sandblasted surface of normal concrete showed significant improvement in the displacement capacity of BCJ sub-assembly resulted into the ductile failure. This is mainly attributed to a significant increment in the initial stiffness, damage localization out of the joint region, excellent ductility and strain hardening behavior of UHPFRC.
- The initial secant stiffness of TS1, TS2 and TE was 2.73, 2.86 and 2.2 times higher than the value registered for the control specimen. This increment is attributed to larger section comprised of UHPFRC and NC and a higher level of joint confinement because of UHPFRC jacketing.

- Strengthened specimens dissipated the much higher amount of energy due to inelastic deformations as compared to control specimen. The strengthening solutions of specimens TS1 and TSE assured an increase of energy dissipation capacity of about 5.17 and 2.7 times over control specimen. Specimen TS1 dissipated maximum energy which is associated to the contribution of UHPFRC jacket, higher level of confinement provided by jacket, higher toughness and crack bridging ability of UHPFRC, friction between cracks, opening and closing of cracks, localization of vertical flexural cracks at beam-joint interface, and the yielding of the beam's main reinforcement which had not been observed even in case of specimen TSE.
- The ductility of strengthened specimens TS1, TS2 and TSE were reduced by 1.5%, 8.3% and 36.6%, respectively from the ductility of control specimen. This reduction is attributed to high strength and stiffness degradation. In load-displacement envelope curve, the post peak regime of specimen TS1 was characterized by the sudden reduction in the strength followed by the plateau in the curve. The former characteristic was highlighted in ductility value but the latter characteristic was not incorporated in the displacement ductility ratio. Due to this unique behavior, specimen TS1 performed efficiently in terms of overall ductility of the test unit, as compared to specimen TSE and TC.
- It was observed that specimen TSE was failed due to detachment of prefabricated UHPFRC plates with the concrete cover from the RC core sub-assembly and the failure was brittle in nature without yielding of beam's reinforcement due to which prefabricated UHPFRC plates assured the maximum load carrying capacity and

energy dissipation capacity but could not maintain the ductility of the structural component and showed higher degradation in strength and stiffness.

- The numerical model successfully predicted load-displacement envelope curves and the damage in concrete with very high level of accuracy. The FEM predicted peak load is very close to experimental values.

## 6.2 Future Recommendations

1. In the present research work, exterior BCJs were repaired and strengthened with 30 mm layer of UHPFRC jacket. The study can be extended to other types of a joint like Knee, interior and corner joints.
2. In the present research work, NCSS was made rough through sandblasting technique only. A number of surface preparation techniques were available in the literature for the preparation of NCSS such as chipped surface, sandblasted surface and grooved surface with dry or wet conditions. The work can be extended to study the effect of the roughness of NCSS on the performance of UHPFRC jacketing in retrofitting the BCJs with dry or wet conditions.
3. NCSS was made rough through sandblasting up to different levels. The research work can be extended to determine the optimum value of NCSS roughness to avoid the detachment of UHPFRC jacket from the NCSS at higher axial load.
4. The research study can be extended to study the effect of jacket thickness on the efficiency of UHPFRC jacketing in strengthening the BCJs.
5. Future studies will be addressed to avoid the issues of pre-fabricated UHPFRC plate detachment which led to strength degradation and sudden reduction in the ductility

of the unit. The adoption of High modulus epoxy or mechanical anchorage between the concrete substrate surface and UHPFRC plates may be useful in this regard.

# References

[1] J. F. Bonacci and R. T. Leon, “Recommendations for Design of Beam-Column Joints in Monolithic Reinforced Concrete Structures (ACI 352R-76),” *ACI J.*, vol. 73, no. 7, pp. 375–393, 1976.

[2] P. Beres, A.; Pessiki, S. P.; White, R. N.; and Gergely, “Implications of Experiments on the Seismic Behavior of Gravity Load Designed RC Beam-to-Column Connections,” *Earthq. Spectra*, vol. 12, no. 2, pp. 185–198, 1996.

[3] A. Sharma, G. Genesio, G. R. Reddy, R. Eligehausen, S. Pampanin, and K. K. Vaze, “14 th Symposium on Earthquake Engineering EXPERIMENTAL INVESTIGATIONS ON SEISMIC RETROFITTING OF REINFORCED CONCRETE BEAM-,” vol. 2, 2010.

[4] S. Z. Korkmaz, “Observations on the Van Earthquake and Structural Failures,” vol. 29, no. Inan 2010, pp. 1–25, 2015.

[5] F. Lanning, A. G. Haro, M. K. Liu, A. Monzón, H. Monzón-despang, A. Schultz, A. Tola, T. Council, G. Guillermo, N. Antonaki, X. Vera-grunauer, R. Gilsanz, V. Diaz, H. Stone, B. Ahmed, S. C. Chian, F. Hughes, and N. Jirouskova, *EERI Earthquake Reconnaissance Team Report :*, no. October. 2016.

[6] K. Acharya, “Building damage patterns in Kathmandu Valley due to 25th April Earthquake,” 2015.

[7] J. F. Bonacci and R. T. Leon, “Recommendations for Design of Beam-Column Connections in Monolithic Reinforced Concrete Structures,” *Concrete*, vol. 109, no. 1976, pp. 1–37, 2004.

[8] R. J. Stern and P. Johnson, “Continental lithosphere of the Arabian Plate: A geologic, petrologic, and geophysical synthesis,” *Earth-Science Rev.*, vol. 101, no. 1–2, pp. 29–67, 2010.

[9] A. M. Al-Amri, A. J. Rodgers, and T. A. Al-Khalifah, “Improving the level of

seismic hazard parameters in saudi arabia using earthquake location," *Arab. J. Geosci.*, vol. 1, no. 1, 2015.

[10] A. M. Al-bassam and F. K. Zaidi, "Natural Hazards in Saudi Arabia," no. MAY 2014, pp. 243–251, 2015.

[11] M. Engindeniz, L. F. Kahn, and A. Zureick, "Repair and Strengthening of Reinforced Concrete Beam-Column Joints : State of the Art," no. 102, 2006.

[12] J. B. D. P. Association, "Recent Development of Seismic Retrofit Methods in Japan," *English*, no. January, pp. 1–94, 2005.

[13] G. Martinola, A. Meda, and G. A. Plizzari, "An application of high performance fiber reinforced cementitious composites for R/C beams strengthening," *Fram. Catania (Italy), Proc.*, 2007.

[14] Y. A. Al-Salloum, S. H. Alsayed, T. H. Almusallam, and N. A. Siddiqui, "Seismic behavior of FRP-upgraded exterior RC beam-column joints," *2nd Int. Conf. Concr. Repair, Rehabil. Retrofit. ICCRRR 2008*, vol. 14, no. 2005, pp. 405–406, 2009.

[15] M. Kazem Sharbatdar, A. Kheyroddin, and E. Emami, "Cyclic performance of retrofitted reinforced concrete beam-column joints using steel prop," *Constr. Build. Mater.*, vol. 36, pp. 287–294, 2012.

[16] B. Li, E. S. S. Lam, B. Wu, and Y. Y. Wang, "Experimental investigation on reinforced concrete interior beam-column joints rehabilitated by ferrocement jackets," *Eng. Struct.*, vol. 56, pp. 897–909, 2013.

[17] M. N. S. Hadi and T. M. Tran, "Retrofitting nonseismically detailed exterior beam-column joints using concrete covers together with CFRP jacket," *Constr. Build. Mater.*, vol. 63, pp. 161–173, 2014.

[18] R. Realfonzo, A. Napoli, and J. G. R. Pinilla, "Cyclic behavior of RC beam-column joints strengthened with FRP systems," *Constr. Build. Mater.*, vol. 54, pp. 282–297, 2014.

[19] E. Esmaeeli, J. A. O. Barros, J. Sena-Cruz, L. Fasan, F. R. Li Prizzi, J. Melo, and H. Varum, “Retrofitting of interior RC beam-column joints using CFRP strengthened SHCC: Cast-in-place solution,” *Compos. Struct.*, vol. 122, pp. 456–467, 2015.

[20] G. Campione, L. Cavaleri, and M. Papia, “Flexural response of external R.C. beam-column joints externally strengthened with steel cages,” *Eng. Struct.*, vol. 104, pp. 51–64, 2015.

[21] E. Esmaeeli, J. A. O. Barros, J. Sena-Cruz, H. Varum, and J. Melo, “Assessment of the efficiency of prefabricated hybrid composite plates (HCPs) for retrofitting of damaged interior RC beam-column joints,” *Compos. Struct.*, vol. 119, pp. 24–37, 2015.

[22] E. Esmaeeli, F. Danesh, K. F. Tee, and S. Eshghi, “A combination of GFRP sheets and steel cage for seismic strengthening of shear-deficient corner RC beam-column joints,” *Compos. Struct.*, vol. 159, pp. 206–219, 2017.

[23] M. S. Prof, H. Universit, E. F. Prof, I. Universit, and M. S. Prof, “Ultra-High-Performance Concrete : Research , Development and Application in Europe Ultra-High-Performance Concrete :,” no. September, 2015.

[24] E. Ghafari, M. Arezoumandi, H. Costa, and E. Júlio, “Influence of nano-silica addition in the durability of UHPC,” *Constr. Build. Mater.*, vol. 94, no. September, pp. 181–188, 2015.

[25] I. Talebinejad, A. Iranmanesh, S. A. Bassam, and M. Shekarchizadeh, “Optimizing Mix Proportions of Normal Weight Reactive Powder Concrete with Strengths of 200-350 MPa,” *Proc. Int. Symp. UHPC Kassel, Ger.*, pp. 133–141, 2004.

[26] K. Wille, A. E. Naman, and G. J. Parra-Montesinos, “Ultra - High Performance Concrete with Compressive Strength Exceeding 150 MPa (22ksi) : A Simpler Way,” *ACI Mater. J.*, vol. 108, no. 1, pp. 46–53, 2011.

[27] P. Rougeau and B. Borys, “Ultra high performance concrete with ultrafine

particles other than silica fume," *Int. Symp. Ultra High Perform. Concr.*, pp. 213–225, 2004.

[28] J. J. Park, S. T. Kang, K. T. Koh, S. W. Kim, and E. Fehling, "Influence of the Ingredients on the Compressive Strength of UHPC as a Fundamental Study to Optimize the Mixing Proportion," *2nd Int. Symp. Ultra High Perform. Concr.*, pp. 105–112, 2008.

[29] P. Richard and M. Cheyrezy, "Composition of reactive powder concretes," *Cem. Concr. Res.*, vol. 25, no. 7, pp. 1501–1511, 1995.

[30] H. Russel, G and B. a. Graybeal, "Ultra-High Performance Concrete : A State-of-the-Art Report for the Bridge Community," no. June, p. 171, 2013.

[31] M. Á. C. Muñoz, "Compatibility of ultra high performance concrete as repair material : bond characterization with concrete under different loading scenarios," MICHIGAN TECHNOLOGICAL UNIVERSITY, 2012.

[32] M. K. R. M.A. Al-Osta, M.N. Isa, M.H. Baluch, "Flexural behavior of reinforced concrete beams strengthened with ultra-high performance fiber reinforced concrete," *Constr. Build. Mater.*, vol. 134, pp. 279–296, 2016.

[33] K. Habel, E. Denarié, and E. Brühwiler, "Experimental Investigation of Composite Concrete and Conventional Concrete Members," *ACI Struct. J.*, no. 104, pp. 93–101, 2007.

[34] S. Mostosi, A. Meda, P. Riva, and S. Maringoni, "Shear Strengthening of Rc Beams With High Performance Jacket," *Symp. A Q. J. Mod. Foreign Lit.*, pp. 1–9, 2011.

[35] Yehia A. Hassanean;Kamal Abas Assaf; Shehata E. Abdel Raheem; and Ahmed. N.M. Arafa, "Flexural behavior of strengthened and repaired R.C. beams by using steel fiber concrete jacket under repeated load," vol. 3, no. 3, pp. 564–578, 2013.

[36] B. H. B. and N. R. I. Prabhat Ranjan Prem, A. Ramachandra Murthy, G. Ramesh, "Flexural Behaviour of Damaged RC Beams Strengthened with Ultra High

Performance Concrete," *Adv. Struct. Eng.*, vol. Matsagar, pp. 2057–2069, 2015.

[37] ACI committee 318, *Building Code Requirements for Structural Concrete and Commentary (ACI 318M-11)*. 2011.

[38] U. Khan, "Effect Of Variation Of Axial Load On Seismic Performance Of RC Exterior BCJs," King Fahd Univeristy of Petroleum and Minerals, 2016.

[39] T. D. Cores, C. Testing, and ASTM:C39/C39M-12a, "Standard Test Method for Compressive Strength of Cylindrical Concrete Specimens 1," *ASTM Int.*, vol. i, no. C, pp. 1–8, 2012.

[40] C. C. Test, T. Drilled, and C. C. Test, "Standard Test Method for Static Modulus of Elasticity and Poisson ' s Ratio of Concrete," vol. 4, pp. 1–5, 2015.

[41] ASTM C496/C496M, "Standard Test Method for Splitting Tensile Strength of Cylindrical Concrete Specimens," *Am. Soc. Test. Mater.*, pp. 1–5, 2011.

[42] I.Y.A. Hakeem, "Characterization of an Ultra-High Performance Concrete," King Fahd University of Petroleum and Minerals, 2011.

[43] R. Park, "Ductility evaluation from laboratory and analytical testing," *Proceedings of the 9th World Conference on Earthquake Engineering, 2-9 August*. pp. 605–616, 1988.

[44] Z. J. Yang, J. F. Chen, and D. Proverbs, "Finite element modelling of concrete cover separation failure in FRP plated RC beams," *Constr. Build. Mater.*, vol. 17, no. 1, pp. 3–13, 2003.

[45] Z. J. Yang and J. Chen, "Finite element modelling of multiple cohesive discrete crack propagation in reinforced concrete beams," *Eng. Fract. Mech.*, vol. 72, no. 14, pp. 2280–2297, 2005.

[46] R. de Borst and P. Nauta, "Non-orthogonal cracks in a smeared finite element model," *Eng. Comput.*, vol. 2, no. 1, pp. 35–46, 1985.

[47] "fib Model Code for Concrete Structures," *Int. Fed. Struct. Concr.*, vol. 1, 2010.

[48] V. Birtel and P. Mark, “Parameterised Finite Element Modelling of RC Beam Shear Failure,” *Ababqus User’s Conf.*, pp. 95–108, 2006.

[49] Dassault Systèmes Simulia, “Analysis User’s Manual: Volume 5:Prescribed Conditions, Constraints & Interactions,” *Abaqus 6.12*, vol. V, 2012.

[50] Ariel D. Espeche and Javier León, “Estimation of bond strength envelopes for old-to-new concrete interfaces based on a cylinder splitting test,” *Constr. Build. Mater.*, vol. 25, no. 1, pp. 1222–1235, 2011.

# Vitae

Name : Muhammad Irfan Khan

Nationality : Pakistani

Date of Birth : 22-04-1991

Email : muhammadi1991@hotmail.com

Address : House # 42-B, Street # 13, Mujahidabad

Mughal pura Lahore, Pakistan

Academic Background : Bachelor of Engineering Science, Major Civil Engineering, University of Engineering and Technology, Lahore, Pakistan, 2013.

: Master of Science, Major Structural Engineering King Fahd University of Petroleum and Minerals, Dhahran, Saudi Arabia, 2017.